Title
Slow photoelectron imaging and infrared dissociation spectroscopy of ionic clusters

Author
Garand, Etienne

Publication Date
2010

Peer reviewed|Thesis/dissertation

Slow photoelectron imaging and infrared dissociation spectroscopy of ionic clusters

by

Etienne Garand

A dissertation submitted in partial satisfaction of the

requirements for the degree of

Doctor of Philosophy

in

Chemistry

in the

Graduate Division

of the

University of California, Berkeley

Committee in charge:

Professor Daniel M. Neumark, Chair
Professor Stephen R. Leone
Professor Dmitry Budker

Spring 2010

Abstract

Slow photoelectron imaging and infrared dissociation spectroscopy of ionic clusters

by

Etienne Garand

Doctor of Philosophy in Chemistry

University of California, Berkeley

Professor Daniel M. Neumark, Chair

The anion slow photoelectron velocity-map imaging (SEVI) technique, a high resolution (~1 cm^{-1}) variant of anion photoelectron spectroscopy, is applied to the study of open-shell anions and neutral species. First, SEVI is used to study the C_nH (n=5-9), $C_{2n}N$ (n=1-3), C_nO (n=2-3) and C_nS (n=2-3) heteroatom doped carbon clusters. The SEVI spectra are assigned with the help of electronic structure calculations and Franck-Condon simulations. Precise electron affinities, term energies and vibrational frequencies are determined for these species. These studies also yield evidence of vibronic coupling in the ground states of C_6H, C_8H, C_9H and CCS. Futhermore, it is found that the ground states of the C_5H^-, C_7H^-, C_9H^-, C_4N^- and C_6N^- anions are linear $^3\Sigma^-$ states, contrary to previous theoretical studies that reported bent structures.

In addition, the strong vibronic coupling between the very close-lying $^2A_1$ and $^2B_2$ states of the HCO_2 and DCO_2 radicals is studied using SEVI. The complex photodetachment spectra are simulated and assigned using a quasidiabatic Hamiltonian approach. The strong vibronic coupling is highlighted by the observation of several nominally forbidden transitions.

The SEVI technique is also applied to the study of the weakly bound ArO and KrO van der Waals complexes. The interaction potential and spin-orbit splitting of the neutral and anion states are determined and compared with high-level electronic structure calculations. Finally, the SEVI spectra of the ClH_2^- and ClD_2^- anions are used to characterized the electronic and nuclear coupling in the pre-reactive region of the $Cl(^2P)+H_2$ reaction and to understand the reactivity of the excited spin-orbit state of chlorine. The SEVI spectra are compared to simulations with and without non-adiabatic couplings between the Cl spin-orbit states. The non-adiabatic effects are found to be small but their inclusion improves agreement with experiment.

The second part of this work concerns the structure of ionic clusters which is studied with infrared multiple photon dissociation (IRMPD) spectroscopy. The stepwise solvation of the bicarbonate anion is probed by acquiring the IRPMD spectra of $HCO_3^-(H_2O)_{1-10}$ clusters in the gas-phase. Electronic structure calculations have been performed on the n=1-8 clusters to identify the structure of the low-lying isomers and to assign the observed spectral features. It is found that the water molecules preferably bind to the negatively charged CO_2 moiety of the HCO_3^- anion. A binding motif consisting of a four-membered ring with each water forming a single H-bond with the CO_2 moiety is found for clusters with n=4 or larger. In addition, the structure of the small $(SiO)_{3-5}^+$ clusters have been studied with IRPMD and electronic structure calculations. The onset for the formation of the first Si-Si bond is observed for the n=5 cluster.

Table of Contents

List of Figures

List of Tables

Acknowledgments

First I would like to thank Prof. Daniel Neumark for accepting me in his research group and giving me the wonderful opportunity to work on the SEVI project. I am especially grateful to him for giving me the liberty to explore some of my own research ideas.

I was very fortunate to work closely with Jia Zhou and Tara Yacovitch on the SEVI project. Jia, the "godmother of SEVI", brought the technique to its current state-of-art status during the first years of my Ph. D and left me with a machine ready to "turn-and-burn" data. Tara has been a great apprentice; I wish her the best of luck with the SEVI project, even though I am sure she will not need any.

My graduate years were greatly facilitated by Michelle Haskins who helped me navigate through the impenetrable fog of Berkeley's bureaucracy. On the technical side, Eric Granlund and the staff of the chemistry department machine shop transformed many of my crazy ideas into reality. I'm also grateful to Phil Simon of the student shop who taught me how to do it myself.

I want to thank Dr. Knut Asmis and the members of his research group for allowing me to join them for the IRMPD experiments at FELIX. I spent great times with them in Nieuwegein, in the basement of the FOM Institute and at the adjacent "Cafe de Zwaan". I also thank the skillful and very friendly staff of the FOM Institute for their assistance during those experiments.

I acknowledge the contribution of several colleagues who helped with the theoretical interpretation of some of the SEVI spectra presented in this work. Prof. Millard Alexander (University of Maryland) and Prof. David Manolopoulos (Oxford University) worked on ClH_2^- and ClD_2^- spectra and its relationship to the $Cl+H_2$ reaction. Prof. Alexei Buchachenko (Moscow University) worked on the ArO^- and KrO^- spectra. Kirstin Klein (Johannes Gutenberg Universität Mainz) and Prof. John Stanton (University of Texas, Austin) helped interpret the otherwise incomprehensible HCO_2^- and DCO_2^- spectra. Collaborating and discussing with all of them have been very fruitful experiences and great pleasure.

I also want to acknowledge the support of the National Science and Engineering Research Council (NSERC) of Canada through a post-graduate scholarship. The work presented here has also been funded by the Air Force Office of Scientific Research (AFOSR) under grant No. F49620-03-1-0085.

And finally, un grand merci à tous mes amis et ma famille pour leur support inconditionel.

CHAPTER 1

Introduction

Free radicals are an interesting class of molecules, which are very reactive, owing to their open-shell electronic structure. These species are widely found as reactive intermediates in the fields of combustion,[1] atmospheric,[2] interstellar[3] and even biological[4,5] chemistry. Therefore, understanding their molecular properties, including their electronic and vibrational structure, and ultimately gaining a quantitative understanding of their reactivity, is an important goal in chemistry.

Over the past century, many spectroscopic techniques have been applied to identify and study free radicals. However, one problem that often arises in experimental studies is the difficulty in isolating these highly energetic and often short-lived species in sufficient number density. Free radicals are also a great challenge from the theoretical point of view. Their open-shell electronic structure leads to low-lying excited states, which can be difficult to treat accurately with the standard *ab initio* quantum chemical calculations techniques.[6]

One of the most powerful spectroscopic techniques used to study free radicals is anion photoelectron (PE) spectroscopy. In this technique, the neutral radicals are accessed through photodetachment of a corresponding stable and often closed-shell anion. Another advantage of working with anions is that they can be easily manipulated and mass-selected. Recently, the slow photoelectron velocity-map imaging (SEVI) technique, a high-resolution variant of PE spectroscopy, has been developed. It increases the energy resolution of PE spectroscopy by about two orders of magnitude, up to a few cm^{-1}. The SEVI technique, in combination with electronic structure calculations, thus yields quantitative information about the structure of free radicals that is complementary to other optical spectroscopy techniques.

Numerous other interesting molecular systems are often found as either positively or negatively charged species. In order to study the nature and structure of these systems in isolated conditions, a different approach needs to be used. Over the past two decades,

infrared dissociation has emerged as one of the preferred techniques.[7,8] It allows the well-known infrared absorption or vibrational spectroscopy to be extended to the study of isolated gas-phase ions with very low number density. In combination with electronic structure calculations, this technique yields structural information on these species.

1.1 Anion slow photoelectron velocity-map imaging spectroscopy (SEVI)

1.1.1 Principle of anion photoelectron spectroscopy.

In anion photoelectron (PE) spectroscopy, a molecular beam of mass selected anions is intersected with a laser beam. If the photon energy is sufficient, photoelectrons are ejected from the anions:

$$M^- + h\nu \rightarrow M + e^- \quad (1.1)$$

The distribution of electron kinetic energy (eKE) is measured and constitutes the PE spectrum. As shown schematically in Figure 1, the ejected photoelectron can only have eKE such that:

$$\text{eKE} = h\nu - \text{eBE} \quad (1.2)$$

where the electron binding energy (eBE) corresponds to the energy difference between the anion initial state and the various allowed neutral final states. The PE spectrum is often expressed in terms of eBE rather than eKE, because the former is independent of the photon energy used. Thus, the positions of the peaks in the anion PE spectrum convey information about the electronic and vibrational states of the corresponding neutral. Geometry information can also be obtained from the relative intensities of the different vibrational transitions.

Anion PE spectroscopy was first implemented in 1967[9] and has its roots in the photoelectron spectroscopy[10] of neutral species. Since then it has evolved into a widely applicable technique that can be used to probe the electronic and vibrational structure of any neutral molecule that can be accessed by photodetachment of an anion. Its application to the study of open-shell species,[11] metal clusters,[12,13] semiconductor clusters,[14] solvation complexes,[15] and transition state intermediates[16] has been well established over the past decades. PE spectroscopy is also a direct way to determine the electron affinity (EA) of atoms and molecules.[17] The adiabatic EA is defined as the energy difference between the anion and the neutral ground state.

In conventional anion PE spectroscopy, a laser source with fixed wavelength is used and the photoelectrons kinetic energy is measured with a field free time-of-flight,[18,19] a magnetic-bottle,[20] or hemispherical analyzer. The ultimate energy resolution of the PE spectrometer depends on the type of analyzer used and is usually limited to 5-10 meV in the best cases. This relatively low resolution is one of the major limitations of anion PE.

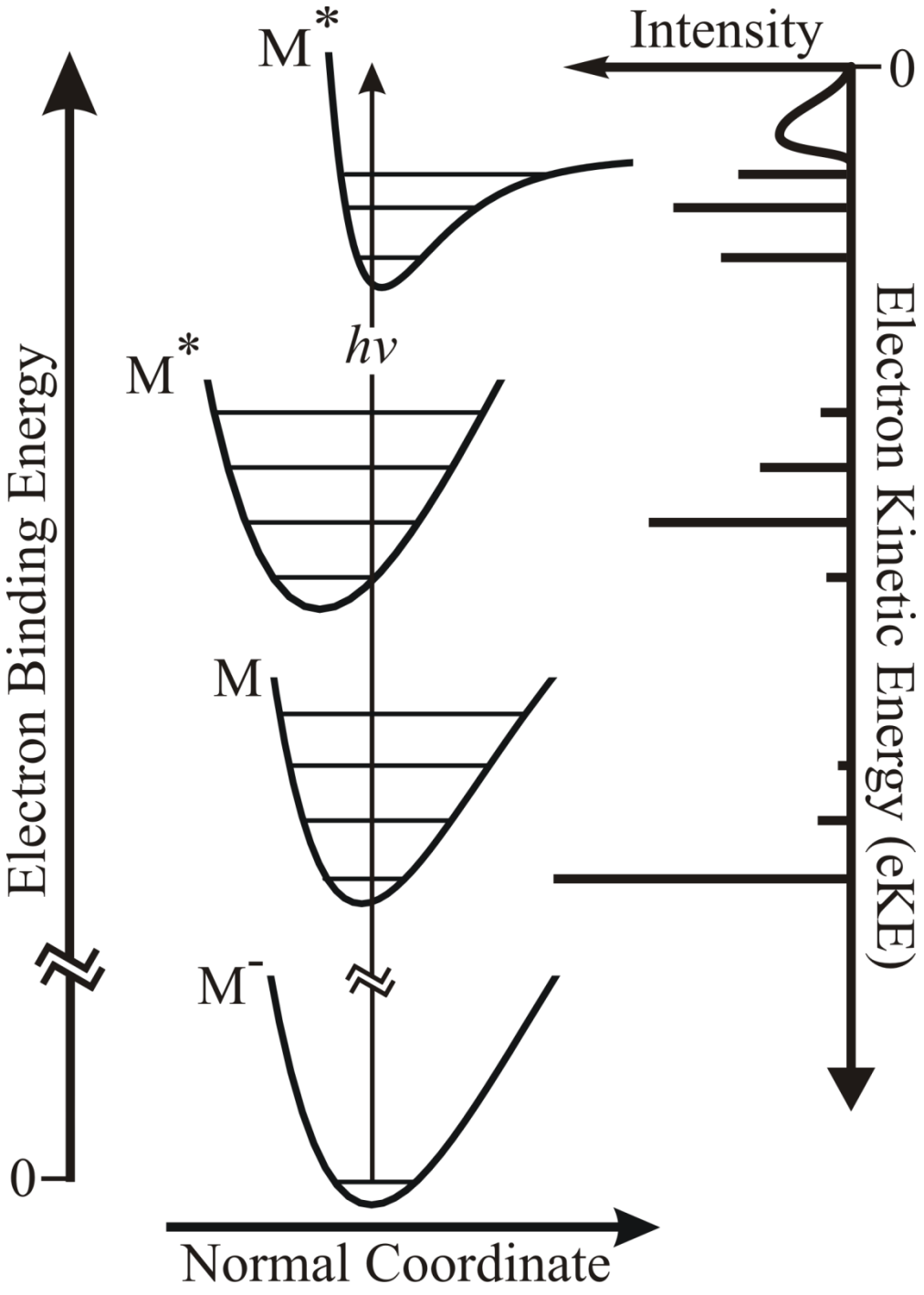

Figure 1.1 Principle of anion photoelectron spectroscopy.

Low-frequency vibrational transitions and spin-orbit fine structure cannot be resolved and the very congested spectra are difficult to analyze.

In order to improve the resolution of anion PE spectroscopy, the zero electron kinetic energy (ZEKE) spectroscopy scheme[21,22] has also been applied to anions.[23] In ZEKE, the photon energy is scanned and the electrons having nearly zero kinetic energy are selectively detected. While this technique has been used with great success from neutral molecules, it suffers from major limitations when applied to anions. The difference comes from the absence of high Rydberg states in anions which prevent the use of the pulse-field ionization ZEKE scheme.[24,25] This leads to very small detachment cross-sections at the threshold (see section 1.1.4) and renders many transitions unobservable. Nonetheless, anion ZEKE has been successfully applied to the study of halides van der Waals complexes[26-30] as well as small carbon[31] and semiconductor[32-36] clusters.

1.1.2 SEVI technique

The anion slow electron velocity-map imaging (SEVI) technique has been developed in recent years,[37,38] with the goal of increasing the resolution of PE spectroscopy while avoiding the intrinsic limitations of anion ZEKE. In SEVI, the photoelectron kinetic energy is measured using velocity-map imaging (VMI).[39] In this method, which is derived from the early photofragment imaging work of Chandler,[40,41] the charged particles are accelerated toward a 2-D position-sensitive detector by a set of electrostatic lenses such that all the particles having the same initial velocity vector are mapped on the same point on the detector. Over the past decade, the VMI scheme has been successfully applied to the detection of photoelectrons.[42,43]

The SEVI technique, illustrated in figure 1.2, takes advantage of the VMI detection scheme flexibility to achieve high resolution in PE spectroscopy. Low VMI potentials and a long flight tube are used in order to maximize the magnification the electron distribution image. This yields high resolution but means that only photoelectrons having low kinetic energy can be detected. In order to obtain the complete PE spectrum, several images acquired at different photon energies need to be stitched together and thus a tunable laser source is required. The laser tunability can also be used to select photon energies that are close to the detachment threshold, which yields the maximum achievable resolution of the VMI technique. Energy resolution as high as 0.1 meV can be achieved with the SEVI technique which is a large gain compared to the conventional PE spectroscopy. This means that for most molecular anions, the peak width is limited by the unresolved rotational contour. The SEVI technique also avoids the intrinsic limitations of anion ZEKE because the photon energy used is typically 5-25 meV above threshold.

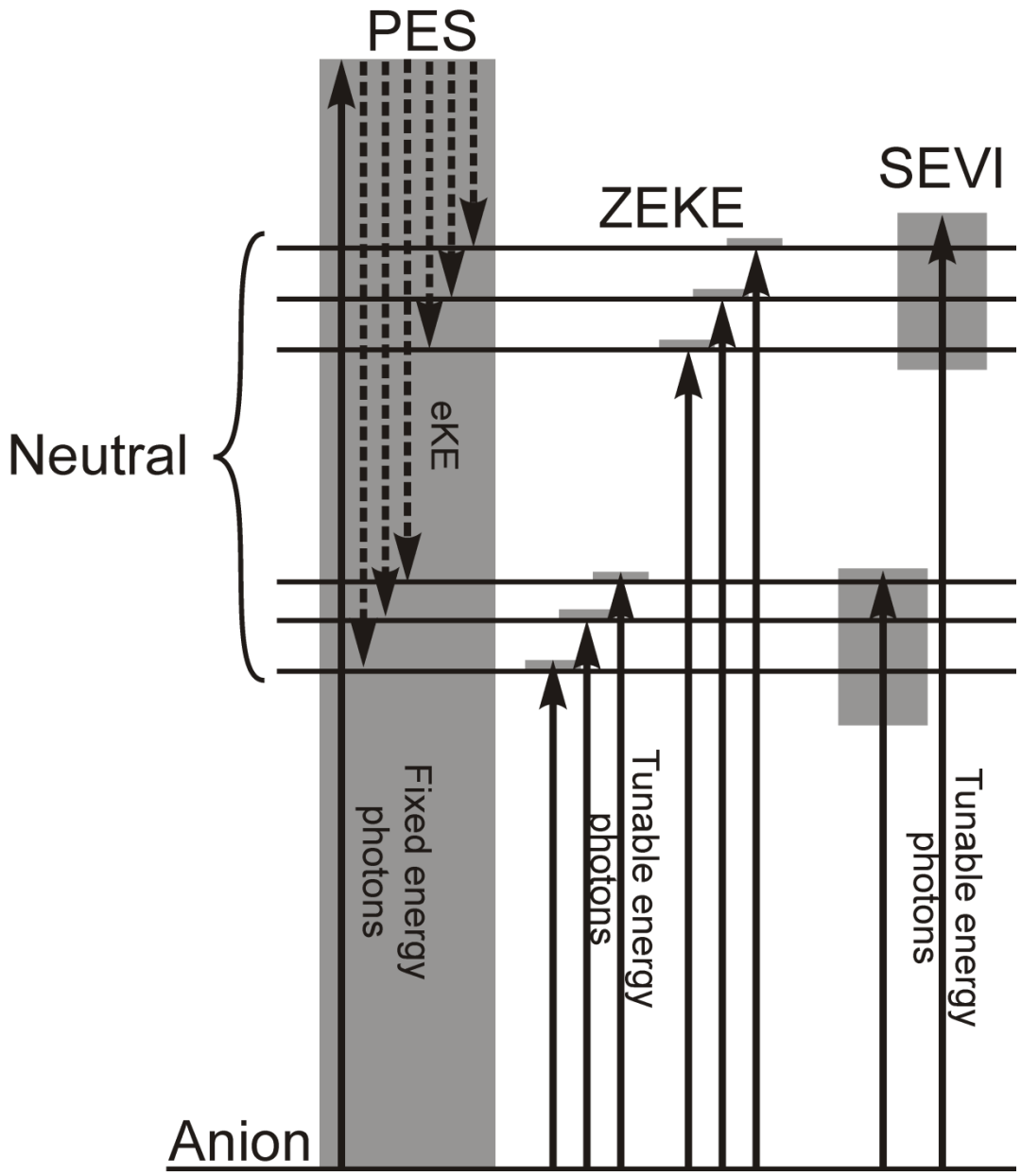

Figure 1.2 Comparison of the PES, ZEKE and SEVI scheme.

1.1.3 Photodetachment selection rules

The anion PE spectroscopy selection rules and the intensity of the various transitions can be derived from Fermi's Golden rule. If $\psi'$and $\psi''$are the total wavefunctions of the initial and final states, respectively, then the intensity (I) of a transition is defined by:

$$I = \frac{2\pi}{\hbar}\langle\psi'|M|\psi''\rangle^2\rho\delta(h\upsilon - \Delta E) \tag{1.4}$$

where M is the electric transition dipole moment, ρ is the density of final states and $h\upsilon$ is the photon energy. ψ' represent the anion total wavefunction while ψ'' is the total wavefunction comprising the neutral molecule and the outgoing free electron. ΔE is the energy difference between the initial and final states minus the kinetic energy of the ejected electron. This means that photodetachment can occur for any photon energy greater than the energy difference between the neutral and anion states. However, the density of final states for the ejected photoelectron has a kinetic energy dependence which leads to modulation of the cross-section as a function of photon energy (see section 1.1.4).

In order for a transition to be allowed ($I \neq 0$), the $\psi' M \psi''$ product needs to be totally symmetric for at least one orientation (x,y,z) of M. The selection rule can be further simplified by assuming that the Born-Oppenheimer approximation is valid, i.e, neglecting any interaction between the electronic and the nuclear motion. If the rotational motion is also neglected and the spin-orbit interaction is assumed to be small, the total wavefunction can be written as:

$$\psi = \psi_e\psi_v \tag{1.5}$$

where ψ_e and ψ_v represent the electronic and vibrational part of the total wavefunction. Similarly, the electric transition dipole moment can be resolved into:

$$M = M_e + M_n \tag{1.6}$$

where M_e and M_n are due to the electrons and nuclei, respectively. The transition probability thus becomes:

$$I \propto \langle\psi_e'\psi_v'|M_e + M_v|\psi_e''\psi_v''\rangle^2 \tag{1.7}$$

$$I \propto [\langle\psi_v'|\psi_v''\rangle\langle\psi_e'|M_e|\psi_e''\rangle + \langle\psi_v'|M_v|\psi_v''\rangle\langle\psi_e'|\psi_e''\rangle]^2 \tag{1.8}$$

The second term vanishes because the two electronic wavefunctions are orthogonal for a given position of the nuclei. Thus:

$$I \propto [\langle \psi_v' | \psi_v'' \rangle \langle \psi_e' | M_e | \psi_e'' \rangle]^2 \quad (1.9)$$

The first factor is the well-known Franck-Condon factor. Using the harmonic approximation and symmetry arguments, it can be shown that the allowed vibrational transitions are:

$\Delta v = 0, \pm 1, \pm 2, \ldots$ for totally symmetric modes (1.10)
$\Delta v = 0, \pm 2, \pm 4, \ldots$ for non-totally symmetric modes (1.11)

The relative intensities of the allowed vibrational transitions depend on the overlap between the vibrational wavefunctions of the anion and the neutral states. Within the harmonic oscillator approximation, it can be shown that this overlap mostly depends on the change of position between the initial and final states for the atoms involved in the vibrational motion. It also depends, to a lesser extent, on the change of vibrational frequency between the initial and final states for the mode. Thus only $\Delta v = 0$ transitions will have significant intensities if the anion and neutral states have very similar geometries. However, in most cases, the anion and neutral states have different geometries so that some $\Delta v \neq 0$ transitions are observed.

The second factor represents the electronic selection rule. In terms of the natural orbitals, the allowed transitions for a single photon photodetachment process are those involving the removal of a single electron, without any rearrangement of the other electrons. A few examples of allowed transitions are shown in Table 1.1. It can readily be seen from Table I that in anion PE spectroscopy, there are very few "dark states" among the lowest-lying neutral states. In the case of open-shell anions, neutral states with different spin multiplicities can be probed simultaneously. Thus, PE spectroscopy can be used to probe neutral states that cannot be observed in optical absorption spectroscopy.

Table 1.1 Examples of allowed one-photon photodetachment transitions

Initial anion states		Final neutral states	
MO's	State	MO's	State
$(a_2)^2(b_2)^2(a_1)^2$	$^1A_1$	$(a_2)^2(b_2)^2(a_1)^1$	$^2A_1$
		$(a_2)^2(b_2)^1(a_1)^2$	$^2B_2$
		$(a_2)^1(b_2)^2(a_1)^2$	$^2A_2$
$(\sigma)^2(\pi)^2(\pi)^1$	$^2\Pi$	$(\sigma)^2(\pi)^2(\pi)^0$	$^1\Sigma^+$
		$(\sigma)^2(\pi)^1(\pi)^1$	$^1\Delta$
		$(\sigma)^2(\pi)^1(\pi)^1$	$^3\Sigma^-$
		$(\sigma)^1(\pi)^2(\pi)^1$	$^1\Pi$
		$(\sigma)^1(\pi)^1(\pi)^1$	$^3\Pi$
$(\sigma)^2(\pi)^1(\pi)^1$	$^3\Sigma^-$	$(\sigma)^2(\pi)^1(\pi)^0$	$^2\Pi$
		$(\sigma)^1(\pi)^1(\pi)^1$	$^4\Sigma^-$

It should be noted that the selection rules presented here are only valid under the assumption that the electronic and vibrational wavefunctions are separable. In many cases, especially in open-shell species where the electronic states are in close proximity with each other, couplings between the electronic and nuclear motion lead to vibronic mixing and otherwise forbidden transitions can "borrow" intensity from allowed transitions.

1.1.4 Wigner threshold law

There is another factor modulating the intensity of the photodetachment transition arising from the long-range interactions between the ejected electron and the parent molecule. This effect is mostly important for photoelectrons ejected with low kinetic energy and thus greatly affects the intensity in the SEVI spectra. The cross-section can be derived from the Wigner threshold law[44] and for anion photodetachment, it has the form of:[45]

$$\sigma_{eKE} \propto (eKE)^{l+1/2} \tag{1.12}$$

where *eKE* and *l* are the kinetic energy and the angular momentum of the ejected photoelectron. The most common values of *l* for a one photon photodetachment process are 0 (*s-wave*), 1 (*p-wave*) and 2 (*d-wave*). Figure 1.3 shows the relative intensity of the transitions with *l*=0-2 as a function of the electron kinetic energy. At a photon energy very close to the detachment threshold (i.e eKE near zero) only transitions leading to the ejection of s-wave photoelectrons have significant intensities. This is a major limitation in the implementation of ZEKE spectroscopy to anion photodetachment. This is also somewhat of a limiting factor for the SEVI technique where the best resolution is achieved for low eKE electrons. However, transitions involving p-wave photoelectrons have enough intensity at photon energies of 200-300 cm^{-1} above threshold where good resolution is still achievable with SEVI.

1.1.5 Photoelectron angular distribution

In addition to the kinetic energy distribution, the photoelectron angular distribution (PAD) with respect to the polarization vector of the incident photon is also monitored in PE spectroscopy. With the VMI setup, this information is readily available because the entire photoelectron cloud is collected. For one-photon photodetachment from a randomly oriented ensemble of molecules, the PAD can be fitted with:[46,47]

$$\frac{d\sigma}{d\Omega} = \frac{\sigma_{total}}{4\pi}\left(1 + \beta\left(\frac{3}{2}\cos^2(\theta) - \frac{1}{2}\right)\right) \tag{1.13}$$

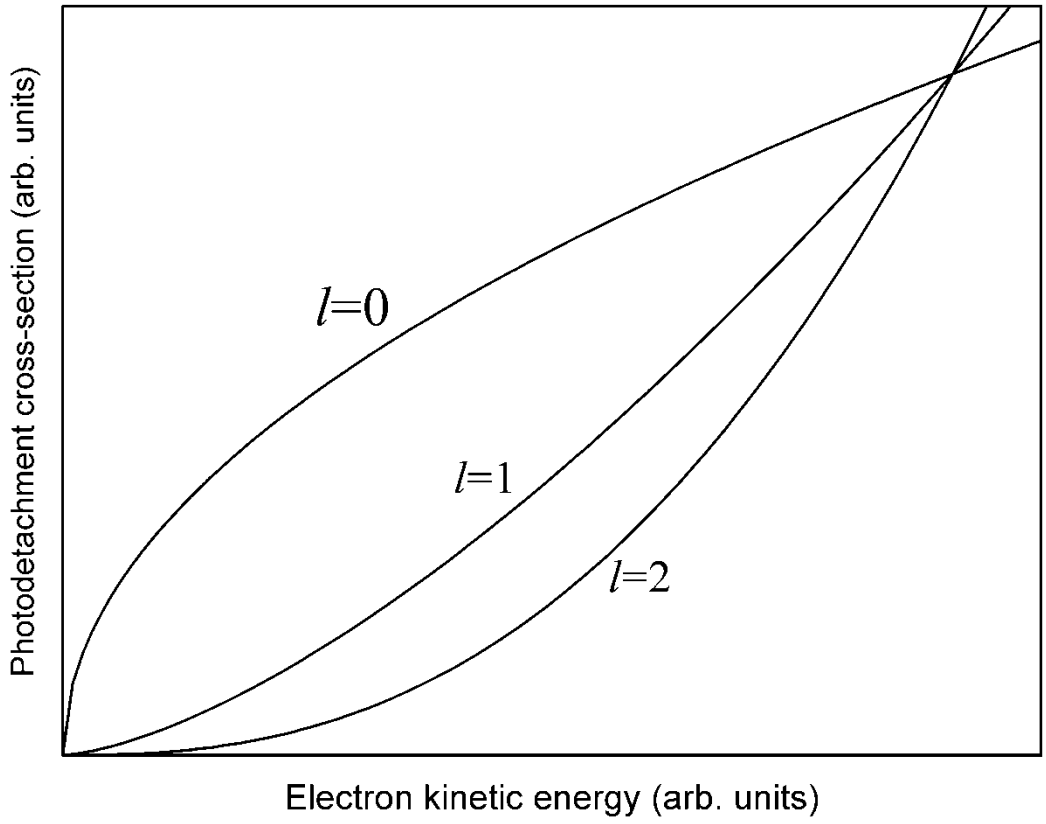

Figure 1.3 Relative intensity of the transitions with *l*=0-2 as a function of the electron kinetic energy.

where θ is the angle between the polarization vector of the photon and the momentum vector of the ejected photoelectron. The anisotropy parameter, β, lies between 2 and -1, corresponding to a $\cos^2(\theta)$ and $\sin^2(\theta)$ distribution, respectively. The value of β depends on the angular momentum of the ejected photoelectron such that *s*-wave (l=0) detachment leads to β=0, *p*-wave (l=1) leads to β=2 and *s*+*d*-wave (l=0,2) with equal phase and amplitude leads to β=-1. Intermediate values of β are obtained through the interference of several partial waves with different phases and amplitudes. However, it is impossible to retrieve the phases and amplitudes of the different partial waves from the β value in the case of one-photon photodetachment transition from a randomly oriented ensemble.

Because the probability of photodetachment leading to electrons with a particular angular momentum depends on the electron kinetic energy, the β value of a particular transition also varies with the photon energy used. In the case of SEVI, where several different photon energies are used to construct a complete spectrum, the exact value of β is thus not very meaningful. For this reason, the β values are usually simply denoted as "*p*-wave" for β>0, "*s*+*d*-wave" for β<0 and "*s*-wave" for $\beta \approx 0$.

The anisotropy parameter provides some information about the orbital from which the photoelectron was ejected. This can be easily understood for detachment from an atomic orbital where l is a good quantum number. Because the incident photon has an angular momentum of 1 and the total angular momentum of the system needs to be conserved, the ejected electron can only have l equal to the parent orbital angular momentum plus or minus 1. Thus, detachment from an atomic "s" orbital leads to a photoelectron having l=1 (*p*-wave) while detachment from a "p" orbital leads to l=0 and l=2 (*s*+*d*-wave). The problem becomes more complex for molecular orbitals, where l is no longer a good quantum number. However, the allowed photoelectron angular momentum for a given orbital symmetry can be derived from group theory. Some examples of this are shown in Table 1.2.

Table 1.2 Example of allowed partial-wave from common orbital symmetry.

Molecular Point group	Orbital symmetry	Allowed Partial-wave
$C_{\infty v}$	σ, π	*s,p,d*
$D_{\infty v}$	σ_u, π_u	*s,d*
	σ_g, π_g	*p*
C_{2v}	a_1,b_1,b_2	*s,p,d*
	a_2	*p*
C_{2h}	a_u,b_u	*s,d*
	a_g,b_g	*p*
C_s	a', a''	*s,p,d*

Therefore, in some cases, the PAD measured in PE spectroscopy can be used to assign transitions to a specific electronic state. Furthermore, each electronic state produces different PADs owing to the different amplitudes and phases of the partial waves and this can be used to distinguish transitions belonging to different electronic states. This is especially useful in the case of close lying electronic states producing overlapping vibrational transitions. Different PADs for vibrational transitions within the same electronic state is also used as a signature of vibronic coupling.

1.2 Infrared multiple photon dissociation (IRPMD)

1.2.1 Principle of IRMPD

The absorption of infrared (IR) radiation by matter is a well known process. Measuring the wavelength dependence of the absorption of light in the IR regime is called infrared spectroscopy. In this energy range, the photons have enough energy to excite the vibrations of molecules. The absorption bands in IR spectroscopy correspond to the vibrational frequencies and yield information about the nature of the chemical bonding in the molecule.

In conventional IR spectroscopy, the absorbance, A, is usually obtained by measuring the intensity of the light striking the sample, I_0, and the intensity of light that passes through the sample, I, such that:

$$A = \log(I_0/I) \tag{1.14}$$

The absorbance is proportional to the concentration, C, of the sample and the length of the light through the sample, L. This is expressed by Beer's law:

$$A = \varepsilon CL \tag{1.15}$$

where is ε called the extinction coefficient.

In cases where there is very low number density, such as molecular beams, the intensity of light absorbed is too small to be measured reliably. Different schemes have been implemented in order to combine IR spectroscopy and molecular beam physics. One of them is to measure an "action" produced by the absorption of light rather than the absorption itself.[7,8,48,49] Because the "action" only occurs when light is absorbed, it provides a background-free type of measurement, which is much more sensitive.

In infrared multiple photon dissociation (IRMPD), the dissociation of molecules caused by the sequential absorption of infrared photons is monitored.[50] If an infrared photon is absorbed and excites a given vibrational transition, after a short time the energy is redistributed among the other vibrational levels. This is commonly referred to as intramolecular vibrational redistribution (IVR). Then, a second photon, with the same energy as the first one, can re-excite the same vibrational transition. This sequential absorption of photons can thus "pump" energy into the bath of vibrational levels of a molecule. The term "*multiple photon*" is usually used to describe this type of sequential excitation to differentiate from "*multiphoton*" excitations which refer to the simultaneous absorption of several photons. When the total internal energy reaches a sufficiently high level, it can lead to the dissociation

of the molecule. The background-free appearance of fragments as a function of the IR wavelength can thus be monitored and yields an IRMPD spectrum.

1.2.2 IR selection rules

The most important selection rule in IRMPD is the linear absorption intensity, which is the probability of a single photon to induce a transition between two vibrational levels. This can be derived from Fermi's Golden rule. Considering only the nuclear motion, then:

$$I \propto \langle \psi_v' | M_v | \psi_v'' \rangle^2 \rho \delta(h\upsilon - \Delta E) \tag{1.16}$$

Transitions will only occur if the photon energy corresponds to the energy difference between two vibrational levels. If the internuclear potential (V) as a function of the vibrational coordinate $(r - r_e)$ is approximated to be harmonic:

$$V = \frac{1}{2} k (r - r_e)^2 \tag{1.17}$$

then, the vibrational energy levels are

$$E_v = \left(v + \frac{1}{2}\right) \frac{h}{2\pi} \sqrt{\frac{k}{\mu}} \tag{1.18}$$

and the vibrational wavefunctions are

$$\psi_v = N_v H_v e^{-\sqrt{\mu k}(r - r_e)^2 / 2\hbar} \tag{1.19}$$

where N_v is a normalization constant, H_v is the vth Hermite polynomial, μ is the reduced mass and k is a constant. The electric transition dipole moment, M_v, is defined as:

$$M_v = \vec{\mu} \cdot \vec{E} \tag{1.20}$$

where $\vec{\mu}$ is the molecular dipole moment and $\vec{E}$ is the electric field of the photon. The norm of $\vec{\mu}$ can be expanded in terms of the same $(r - r_e)$ coordinates:

$$|\vec{\mu}| = \mu_{r_e} + \left(\frac{d\mu}{dr}\right)_{r_e} (r - r_e) + \left(\frac{d^2\mu}{dr^2}\right)_{r_e} (r - r_e)^2 + \cdots \tag{1.21}$$

If eq. 1.19 and 1.21 are put back into eq. 1.16, it can easily be shown that the probability of a transition is non-zero only if $\Delta v = 1$. Moreover, the transition probability is proportional to

$(d\mu/dr)_{r_e}$. This means that only vibrational transitions for which the normal coordinate displacements lead to a change in molecular dipole moment are allowed.

For molecules where the IVR is efficient and the number of infrared photons necessary to induced dissociation is small, the IRPMD spectrum can usually be interpreted in terms of linear absorption intensity. However, in cases where the number of photons is large, strong intensity deviations from the linear absorption approximation are often encountered. It is then necessary to perform a complete analysis of the vibrational relaxation and dissociation dynamics in order to understand the IRMPD spectrum intensities.

References:

1) J. H. Kiefer, S. S. Sidhu, R. D. Kern, K. Xie, H. Chen, and L. B. Harding, *Combust. Sci. Technol.* **82** (1-6), 101 (1992).
2) R. Atkinson, *Atmos. Environ.* **34** (12-14), 2063 (2000).
3) L. M. Ziurys, *PNAS* **103** (33), 12274 (2006).
4) K. B. Beckman and B. N. Ames, *Physiological Reviews* **78** (2), 547 (1998).
5) I. Fridovich, *Science* **201** (4359), 875 (1978).
6) P. M. Mayer, C. J. Parkinson, D. M. Smith, and L. Radom, *J. Chem. Phys.* **108** (2), 604 (1998).
7) E. J. Bieske and O. Dopfer, *Chem. Rev.* **100** (11), 3963 (2000).
8) M. A. Duncan, *Int. J. Mass. Spectrom.* **200** (1-3), 545 (2000).
9) B. Brehm, M. A. Gusinow, and J. L. Hall, *Phys. Rev. Lett.* **19** (13), 737 (1967).
10) D. W. Turner, *Molecular Photoelectron Spectroscopy*. (Wiley, London, 1970).
11) M. S. Robinson, M. L. Polak, V. M. Bierbaum, C. H. Depuy, and W. C. Lineberger, *J. Am. Chem. Soc.* **117** (25), 6766 (1995).
12) D. G. Leopold, J. Ho, and W. C. Lineberger, *J. Chem. Phys.* **86** (4), 1715 (1987).
13) X. Li, H. B. Wu, X. B. Wang, and L. S. Wang, *Phys. Rev. Lett.* **81** (9), 1909 (1998).
14) O. Cheshnovsky, S. H. Yang, C. L. Pettiette, M. J. Craycraft, Y. Liu, and R. E. Smalley, *Chem. Phys. Lett.* **138** (2-3), 119 (1987).
15) G. Markovich, S. Pollack, R. Giniger, and O. Cheshnovsky, *J. Chem. Phys.* **101** (11), 9344 (1994).
16) D. E. Manolopoulos, K. Stark, H. J. Werner, D. W. Arnold, S. E. Bradforth, and D. M. Neumark, *Science* **262** (5141), 1852 (1993).
17) J. C. Rienstra-Kiracofe, G. S. Tschumper, H. F. Schaefer, S. Nandi, and G. B. Ellison, *Chem. Rev.* **102** (1), 231 (2002).
18) L. A. Posey, M. J. Deluca, and M. A. Johnson, *Chem. Phys. Lett.* **131** (3), 170 (1986).
19) R. B. Metz, A. Weaver, S. E. Bradforth, T. N. Kitsopoulos, and D. M. Neumark, *J. Phys. Chem.* **94**, 1377 (1990).
20) O. Cheshnovsky, S. H. Yang, C. L. Pettiette, M. J. Craycraft, and R. E. Smalley, *Rev. Sci. Instrum.* **58** (11), 2131 (1987).

21) K. Muller-Dethlefs, M. Sander, and E. W. Schlag, *Chem. Phys. Lett.* **112** (4), 291 (1984).

22) K. Muller-Dethlefs and E. W. Schlag, *Annu. Rev. Phys. Chem.* **42**, 109 (1991).

23) T. N. Kitsopoulos, I. M. Waller, J. G. Loeser, and D. M. Neumark, *Chem. Phys. Lett.* **159** (4), 300 (1989).

24) W. A. Chupka, *J. Chem. Phys.* **98** (6), 4520 (1993).

25) G. Reiser and K. Mullerdethlefs, *J. Phys. Chem.* **96** (1), 9 (1992).

26) C. Bassmann, U. Boesl, D. Yang, G. Drechsler, and E. W. Schlag, *Int. J. Mass. Spectrom.* **159**, 153 (1996).

27) T. Lenzer, I. Yourshaw, M. R. Furlanetto, N. L. Pivonka, and D. M. Neumark, *J. Chem. Phys.* **115** (8), 3578 (2001).

28) T. Lenzer, I. Yourshaw, M. R. Furlanetto, G. Reiser, and D. M. Neumark, *J. Chem. Phys.* **110** (19), 9578 (1999).

29) I. Yourshaw, T. Lenzer, G. Reiser, and D. M. Neumark, *J. Chem. Phys.* **109** (13), 5247 (1998).

30) Y. X. Zhao, I. Yourshaw, G. Reiser, C. C. Arnold, and D. M. Neumark, *J. Chem. Phys.* **101** (8), 6538 (1994).

31) T. N. Kitsopoulos, C. J. Chick, Y. Zhao, and D. M. Neumark, *J. Chem. Phys.* **95** (7), 5479 (1991).

32) C. C. Arnold and D. M. Neumark, *J. Chem. Phys.* **99** (5), 3353 (1993).

33) C. C. Arnold and D. M. Neumark, *Can. J. Phys.* **72** (11-12), 1322 (1994).

34) C. C. Arnold and D. M. Neumark, *J. Chem. Phys.* **100** (3), 1797 (1994).

35) C. C. Arnold, C. S. Xu, G. R. Burton, and D. M. Neumark, *J. Chem. Phys.* **102** (18), 6982 (1995).

36) G. R. Burton, C. S. Xu, C. C. Arnold, and D. M. Neumark, *J. Chem. Phys.* **104** (8), 2757 (1996).

37) D. M. Neumark, *J. Phys. Chem. A* **112** (51), 13287 (2008).

38) A. Osterwalder, M. J. Nee, J. Zhou, and D. M. Neumark, *J. Chem. Phys.* **121** (13), 6317 (2004).

39) A. Eppink and D. H. Parker, *Rev. Sci. Instrum.* **68** (9), 3477 (1997).

40) D. W. Chandler and P. L. Houston, *J. Chem. Phys.* **87** (2), 1445 (1987).

41) A. J. R. Heck and D. W. Chandler, *Annu. Rev. Phys. Chem.* **46**, 335 (1995).

42) B. Baguenard, J. B. Wills, F. Pagliarulo, F. Lepine, B. Climen, M. Barbaire, C. Clavier, M. A. Lebeault, and C. Bordas, *Rev. Sci. Instrum.* **75** (2), 324 (2004).

43) E. Surber, R. Mabbs, and A. Sanov, *J. Phys. Chem. A* **107** (40), 8215 (2003).

44) E. P. Wigner, *Phys. Rev.* **73** (9), 1002 (1948).

45) K. J. Reed, A. H. Zimmerman, H. C. Andersen, and J. I. Brauman, *J. Chem. Phys.* **64** (4), 1368 (1976).

46) J. Cooper and R. N. Zare, *J. Chem. Phys.* **48** (2), 942 (1968).

47) K. L. Reid, *Annu. Rev. Phys. Chem.* **54**, 397 (2003).

48) T. Ebata, A. Fujii, and N. Mikami, *Int. Rev. Phys. Chem.* **17** (3), 331 (1998).

49) W. H. Robertson and M. A. Johnson, *Annu. Rev. Phys. Chem.* **54**, 173 (2003).

50) J. Oomens, B. G. Sartakov, G. Meijer, and G. von Helden, *Int. J. Mass. Spectrom.* **254** (1-2), 1 (2006).

CHAPTER 2

Experimental details

2.1 SEVI experimental setup

2.1.1 Overview

The original SEVI experimental setup[1] was built in the Neumark lab around 2002 by modifying the old ZEKE apparatus.[2,3] Minor variations have been implemented over the years and have been described in details in the Ph.D. thesis of Dr. Matthew J. Nee[4] and Dr. Jia Zhou.[5] The current SEVI apparatus is shown schematically in Figure 2.1. It consists of four connected differentially pumped vacuum chambers, which are shown in alternating shades of grey.

The molecular anion precursor, diluted in a noble gas carrier, is expanded into the source region through a pulsed valve. The anions are formed in the supersonic expansion mainly by dissociative electron attachment. They enter the second differentially pumped region through a skimmer and are extracted into a perpendicular time-of-flight mass spectrometer. They travel through the third differentially pumped region and into the detector region, guided by two sets of electrostatic deflectors and focused by a cylindrical electrostatic Einzel lens. The anions are monitored by a microchannel plate (MCP) assembly in the detector region. In the photoelectron detection mode, the ion detector is retracted and a timing gate applied to the second set of deflectors allows only the anions with the desired mass into the VMI assembly. The anions are photodetached between the first two VMI plates by the focused output of a Nd:YAG pumped dye laser. The photoelectrons are then mapped onto a time-gated imaging MCP coupled with a phosphor screen. The image on the phosphor screen is captured by a CCD camera and sent to a computer for analysis. The following sections describe the important parts of the SEVI apparatus in more detail.

2.1.2 Anion source

The SEVI apparatus uses a high pressure Even-Lavie pulsed solenoid valve.[6] The major advantage of this valve is the very short pulse duration, which allows the use of high stagnation pressure and reduces the load on the pumping system. This is a significant factor in obtaining internally cold anions and well resolved SEVI spectra. Typically, a carrier gas pressure of 300 psi is used and the valve runs with a gas pulse width of 35 μs at a repetition rate of 20 Hz. The carrier gas usually consists of 0.1-1% of a gaseous molecular precursor in a balance of argon. Liquid precursors can also be used if they have sufficient vapor pressure at room temperature.

Two different electron sources are used to produce the anion in the supersonic expansion via dissociative electron attachment. The first one is a circular hot filament ionizer source. It is composed of a thoriated (1%) tungsten filament forming a ~1

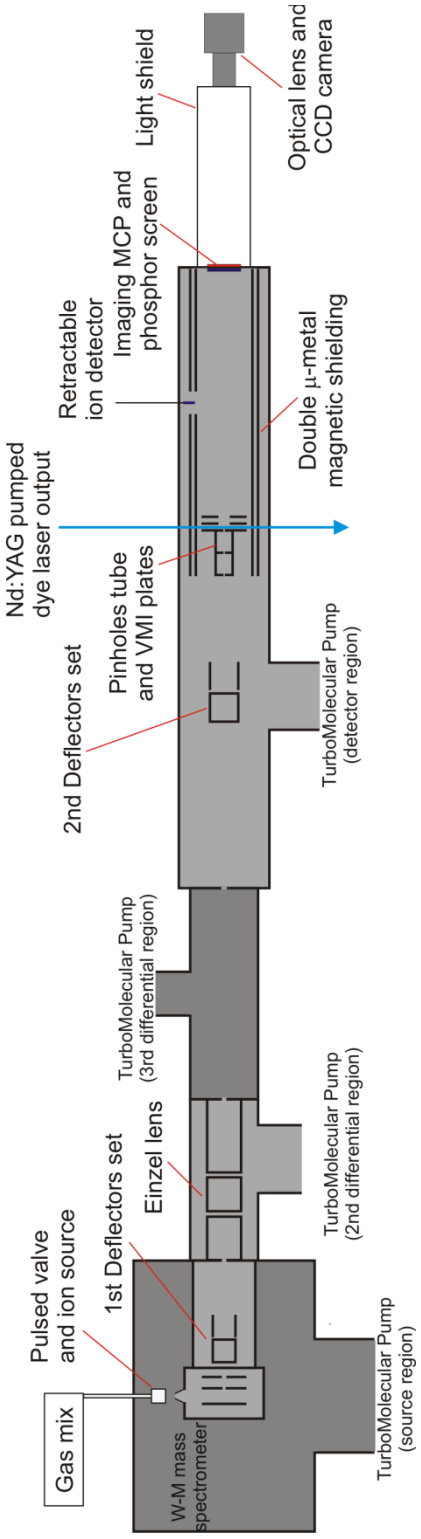

Figure 2.1 Schematic of the current SEVI apparatus, drawn to scale. The various differentially pumped region are shown as alternating shades of gray.

inch diameter ring encircling the gas expansion and placed ~0.25 inch below the valve nozzle. The filament is resistively heated by a 4 A current to stimulate the thermionic emission of electrons. The electrons are accelerated toward a grounded high transmission wire mesh concentric cylindrical grid by applying a negative voltage pulse of 200 V to 800 V to the filament and a surrounding anode. The electrons crossing the grid reach the supersonic gas expansion. The hot filament ionizer is mainly used to produce van der Waals clusters and small anions. Larger molecules requiring more extensive chemistry in the expansion can also be produced but they usually have too much internal energy to yield well-resolved SEVI spectra.

In order to obtain rotationally and vibrationally cold polyatomic anions, a grid discharge source has been designed. This source, shown in Figure 2.2, is an improved version of the plate discharge[7] source commonly used in the production of anions and radicals in supersonic expansion. Here, the gas from the pulsed valve passes through a 2.5 mm x 23 mm channel made from Teflon and aluminum. Two fine grids made of stainless steel wire mesh and separated by 1 mm are placed in the canal about 1mm downstream of the nozzle. These grids are held in place by two steel washers and isolated from each other by Teflon. The first grid is held to +0-15 V while the second is floated to around -100 V to -800 V through a 1kΩ resistor. The passage of the expanding gas through the grids induces a discharge which produces the anions. In contrast to the plate discharge, this source does not require a high-voltage pulse or an external source of electrons for continuous stable operation.

Figure 2.3 shows a comparison of the C_4S^- SEVI spectra obtained with the hot filament ionizer and the grid discharge source. In both cases, a mixture of acetylene (C_2H_2) and carbon disulfide (CS_2) diluted in argon at a stagnation pressure of 300 psi was used. The spectrum obtained with the discharge source exhibits sharper features and a flatter baseline than the one obtained with the hot filament ionizer. Moreover, several peaks due to hot band or sequence band transitions are weaker or disappear completely when the discharge source is used. The intensity ratio of the two peaks at 26615 and 26460 cm^{-1}, which are 0_0^0 transitions originating from the $\Pi_{3/2}$ ground state and $\Pi_{1/2}$ excited spin-orbit state of C_4S^-, respectively, can be used to estimate the internal temperature of the anion. This analysis yields a temperature of 350 K and 100 K for the C_4S^- anions produced by the hot filament ionizer and the grid discharge, respectively.

2.1.3 Mass-selection

The anions formed in the expansion enter the second vacuum region through a 1 mm skimmer and travel between the first two plates of a Wiley-McLaren type time-of-flight mass spectrometer.[8] The anions are perpendicularly extracted by applying a -1750 V pulse to the first plate 250-400 μs after the valve trigger. A -1500 V to -1700 V

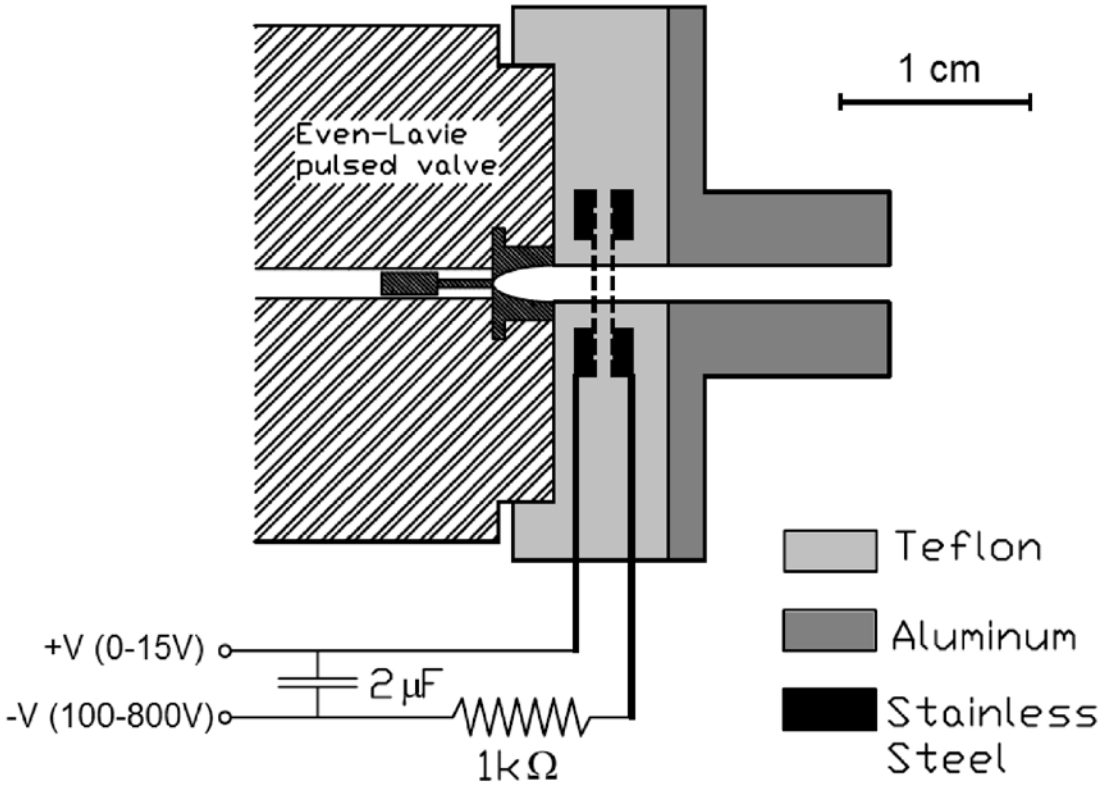

Figure 2.2 Schematic of the grid discharge source

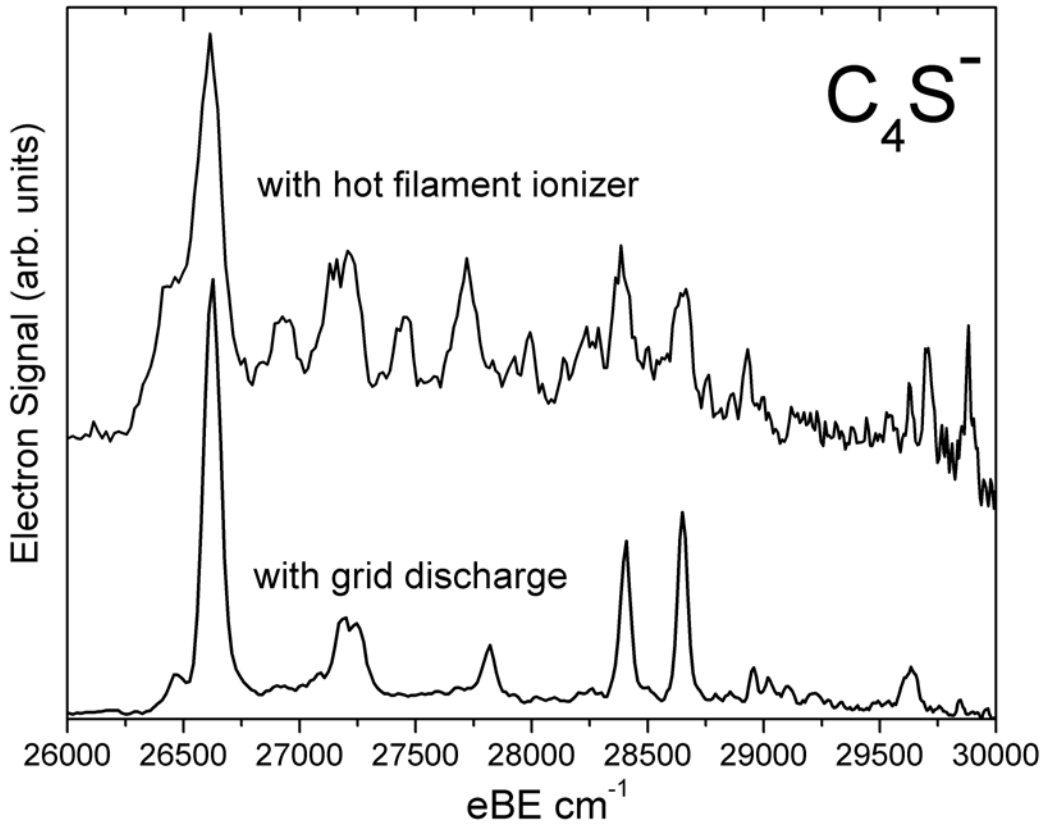

Figure 2.3 Comparison of the C_4S^- SEVI spectrum obtained with the hot filament ionizer (top) and grid discharge (bottom).

pulse is then applied to the second plate 20-50 ns later, while the third plate is kept at ground. The potential and timing of the second plate provides the space and velocity focusing of the anion packet. The anions enter the second differentially pumped region and are steered by a set of perpendicular electrostatic deflectors, which is adjustable from -70 V to +70 V. The anion packet is then focused by a cylindrical electrostatic Einzel lens with the central electrode kept at +3000 V. The anions travel through the third differentially pumped region and enter the detector region guided by a second of set electrostatic deflectors, which is adjustable from -15 V to +15 V but preferentially kept as close as possible to 0 V. Before entering the VMI detector, the anion packets are skimmed by a set of two 3 mm pinholes. The anions are separated according to their mass-to-charge ratio and their arrival time is monitored by a retractable MCP detector located in the detector region. Mass selection is achieved by applying a -50 V potential to one of the deflectors of the 2nd set except when the desired anion mass passes through.

2.1.4 VMI detector

The VMI setup, shown schematically in Figure 2.4, is based on the design of Eppink and Parker[9] and consists of three 10 cm diameter mirror-finished stainless steel plates separated by 15 mm. These plates are placed in the molecular beam axis, in order to minimize the contribution of the anion velocity spread to the ejected photoelectrons. The first plate has a 3 mm pinhole in its center by which the anions enter the VMI assembly and the two other plates have a 25 mm hole in their center. The laser beam intersects the anion packet between the first two plates. The three plate potentials are usually set to -350 V, ~-256 V and 0 V, respectively. The exact value of the second plate potential is finely adjusted during calibration to optimize the energy resolution.

The photoelectrons are accelerated into a 50 cm flight tube that is magnetically isolated by two layers of μ-metal shielding. The electrons are detected by a pair of chevron-mounted 75 mm diameter imaging quality micro-channel plates (MCPs) coupled to a phosphor screen. The front of the first MCP is kept at ground while the back of the second MCP is pulsed from +1 kV to +1.5 kV for 400 ns, starting 100 ns before the laser Q-switch trigger. This gate allows the discrimination between the photoelectrons and the slower co-travelling parent anion and resulting neutral packets. Events on the phosphor screen, which is held at +4.9 kV, are captured by a 1024x1024 pixels CCD camera. The camera operates at a repetition rate of 5 Hz, keeping the shutter open for 200 ms per frame, which corresponds to 4 laser pulses. Each frame is then sent to a computer for analysis.

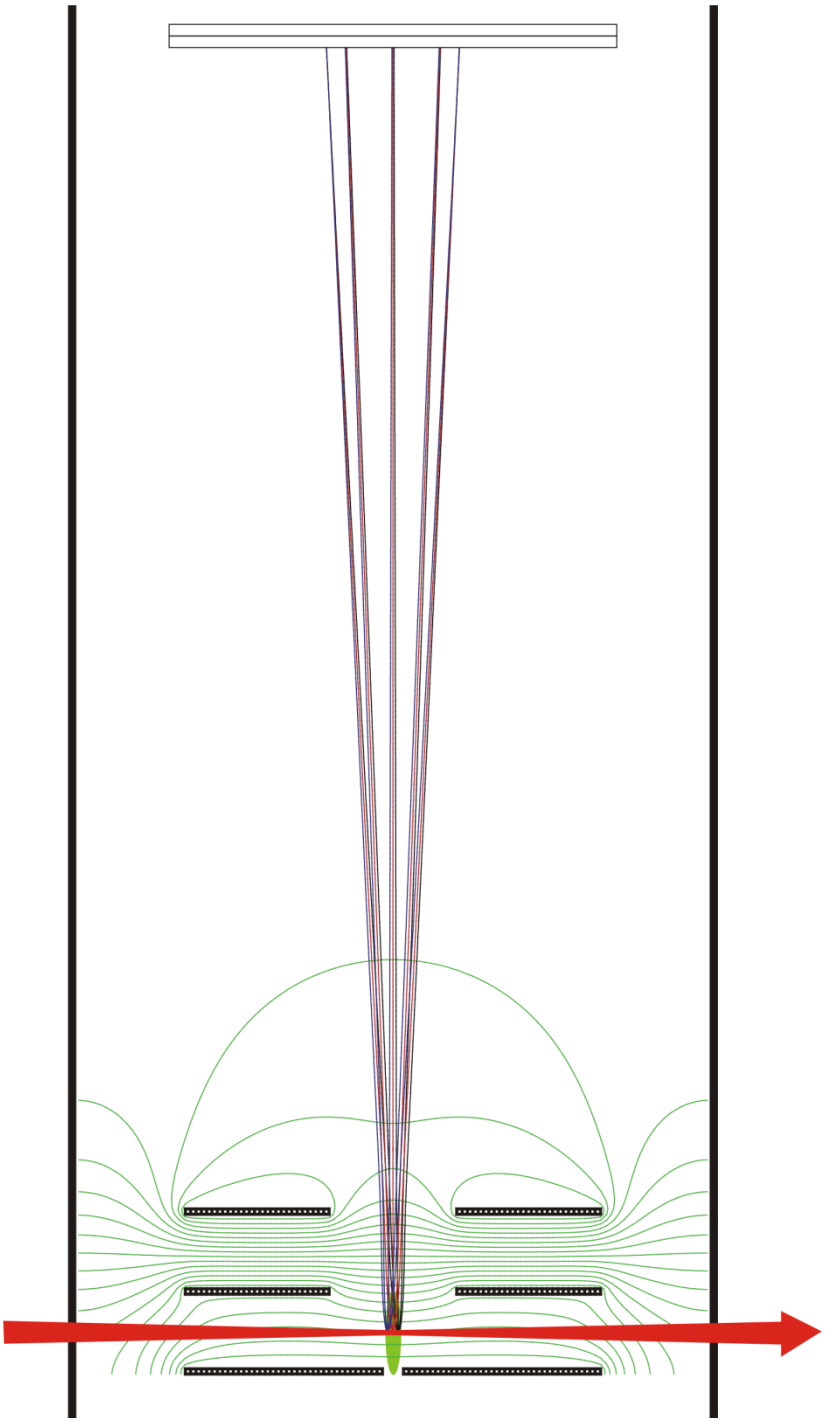

Figure 2.4 Principle of the velocity-map imaging (VMI) detector. The photoelectrons created at the intersection of a laser beam (red) and an anion packet (green) between the first two plates are mapped according to their velocity vector on the position sensitive detector (top)

2.1.5 Laser source

The laser source used in the SEVI experiment is a tunable Nd:YAG pumped dye laser. The laser operates at a repetition rate of 20 Hz and produces ~10 ns light pulses with a bandwidth of around 0.04 cm^{-1}. The output power greatly varies with the dye and wavelength used but usually 100-300 mW of average power is sufficient to obtain good detachment signal. The laser pulse is triggered by the pump laser Q-switch and the timing is set with respect to the pulse on the first plate of the Wiley-McLaren mass spectrometer.

Pumping dyes with the second harmonic of Nd:YAG (532 nm) yields light between 560 nm and 960 nm while the third harmonic (355 nm) yields light between 415 nm and 580 nm. The range can be extended to 280 nm by frequency doubling the output of the dye laser using potassium dihydrogen phosphate (KDP) crystal. The doubled and fundamental laser beams are separated using an arrangement of four dispersion prisms. The laser wavelength ranges are summarized in Table 2.1. The laser beam is directed through the VMI detector region by using a periscope consisting of two or three fused silica 90˚ prisms. The three prism assembly is required when the doubling scheme is not in use in order to have the laser polarization parallel to the detector plane. The laser beam is focused in the plane of the detector by a cylindrical lens with the focal point at the anion packet and enters the vacuum chamber through a fused silica window mounted at the Brewster's angle.

Table 2.1 Photon energy ranges of the Nd:YAG pumped dye laser

Pump	Doubling crystal	Output range		
		wavelength (nm)	energy (eV)	energy (cm^{-1})
532 nm	---	960-560	1.29 -2.21	10420-17860
355 nm	---	580-415	2.14-2.99	17240-24100
532 nm	KDP "D"	322-420	2.95-3.85	23810-31060
532 nm	KDP "R6G"	280-345	3.59-4.43	28990-35710

2.1.6 Data acquisition and analysis

The frames captured by the CCD camera are analysed using the home-made DAQ program[5] which allows the monitoring of real-time and summed images. Each individual frame contains the light intensity due to 10 to several hundred photoelectron events. The camera intensity threshold is set such that a single electron event lights up a single CCD pixel. The images corresponding to 25000 to 50000 laser pulses are summed to create a single image of the photoelectron distribution. This image is then treated using the home-made DEVAL program.[5] First, the image is centered, the intensity is quadrant symmetrized and then smoothed using adjacent averaging algorithm. A slice in the

original 3-D distribution is then obtained by applying an inverse Abel transform algorithm based on the work on Hansen and Law.[10] Other inversion methods using basis set fitting, such as BASEX[11] and pBASEX[12] are also available, however it has been shown previously[5] that the inverse Abel yields the best results for the SEVI images. A velocity spectrum is obtained by angular integration of the intensity for each value of radius R, in pixels. The velocity spectrum is transformed into an electron kinetic energy (eKE, cm^{-1}) spectrum by $eKE=kR^2$, where k is a calibration constant of the VMI (see section 2.1.7). The SEVI spectra are usually presented in terms of electron binding energy (eBE, cm^{-1}), which is obtained by $eBE=h\nu-eKE$.

2.1.7 Calibration and performance

The VMI calibration constant and the optimal potential for the second VMI plates are both highly dependent on the exact position of the laser. It is thus necessary to calibrate every time the laser position changes. This is best done by using atomic ions which produce features with peak widths that are not limited by unresolved rotational envelope and have a well known electron affinity and spin-orbit fine structure. The atomic ions used for SEVI calibration are listed table 2.2.

Table 2.2 Atomic anions used for SEVI calibration

Atomic anion	Anion spin-orbit states (cm^{-1})	Neutral spin-orbit states (cm^{-1})	Electron Affinity (cm^{-1})	Molecular precursor
O^- (^2P)	0.0 ($^2P_{3/2}$)	0.0 ($^3P_2$)	11784.68	N_2O
	177.13 ($^2P_{1/2}$)	158.27 ($^3P_1$)		
		226.98 ($^3P_0$)		
S^- (^2P)	0.0 ($^2P_{3/2}$)	0.0 ($^3P_2$)	16752.98	CS_2
	583.5 ($^2P_{1/2}$)	396.06 ($^3P_1$)		
		573.64 ($^3P_0$)		
I^- (^1S)	---	0.0 ($^2P_{3/2}$)	24672.79	CH_3I
		7603.15 ($^2P_{1/2}$)		
Cl^- (^1S)	---	0.0 ($^2P_{3/2}$)	29145.47	CCl_4
		882.35 ($^2P_{1/2}$)		

The first step of calibration is to finely adjust the potential of the second VMI plate, using an adjustable voltage divider, in order to obtain the narrowest peak width. With the -350 V VMI voltage set, peak widths of ~2-2.5 pixels are routinely obtained for features having a radius of ~100 pixels. Figure 2.5 shows a set of raw Cl^- spectra taken for calibration. The radius (r) and Gaussian peak width (Δr) for each feature is indicated. These values are determined by fitting each peak with a Gaussian function. In this case, the potential of the second VMI plate is adjusted to optimize the width of the Cl($^2P_{1/2}$)

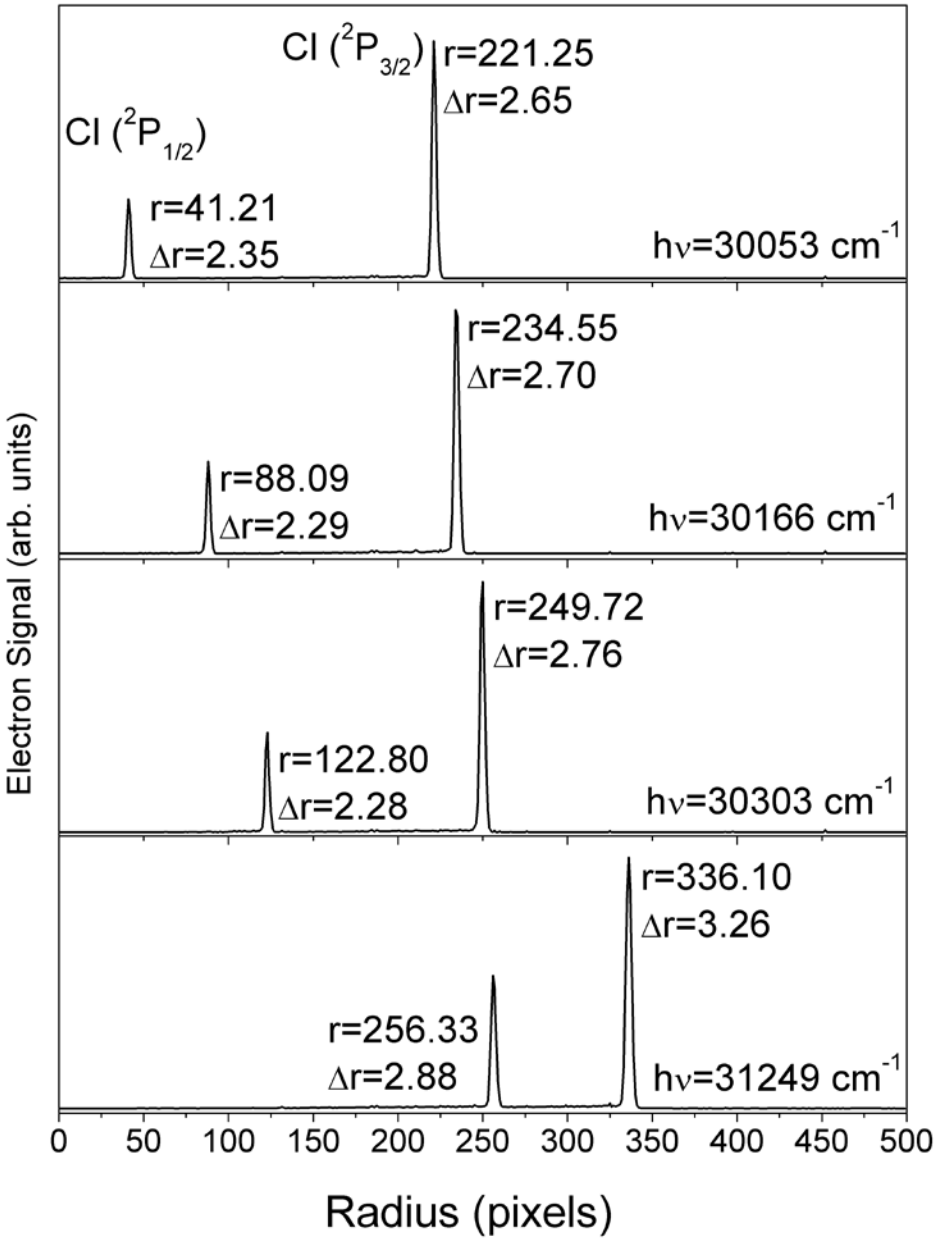

Figure 2.5 Raw Cl^- SEVI spectra taken at different photon energies for calibration

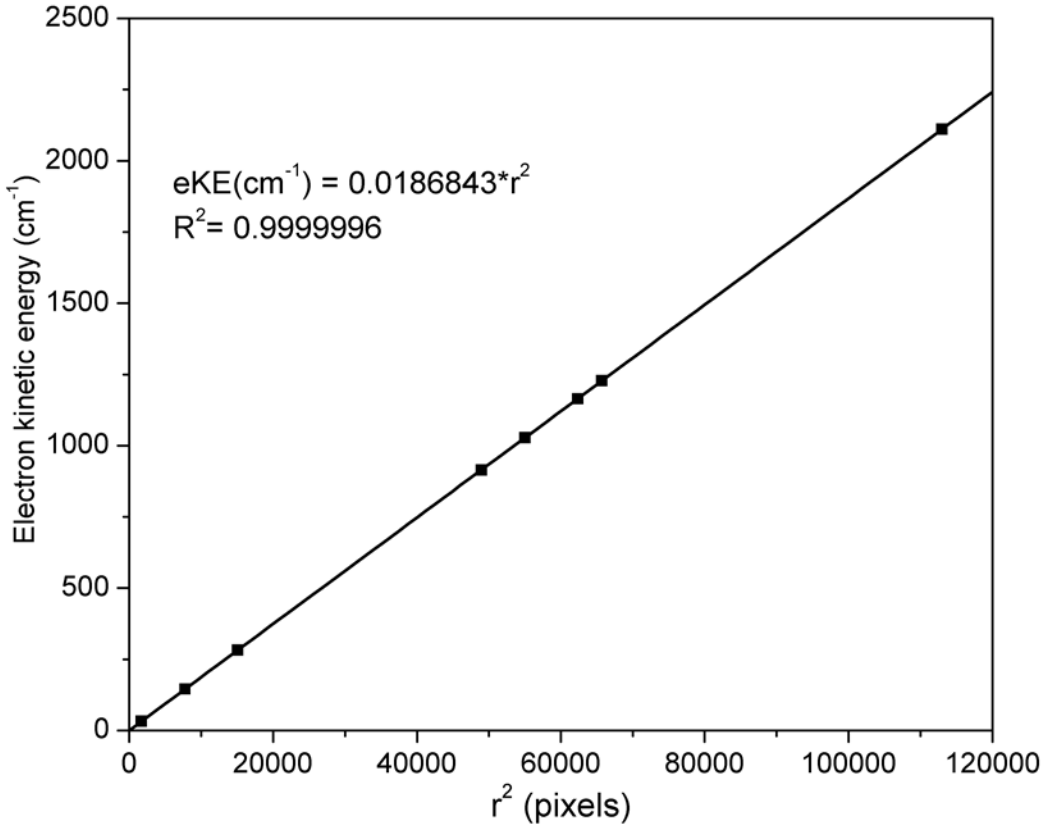

Figure 2.6 Electron kinetic energy as a function of (radius)^2 for the calibration of the SEVI apparatus.

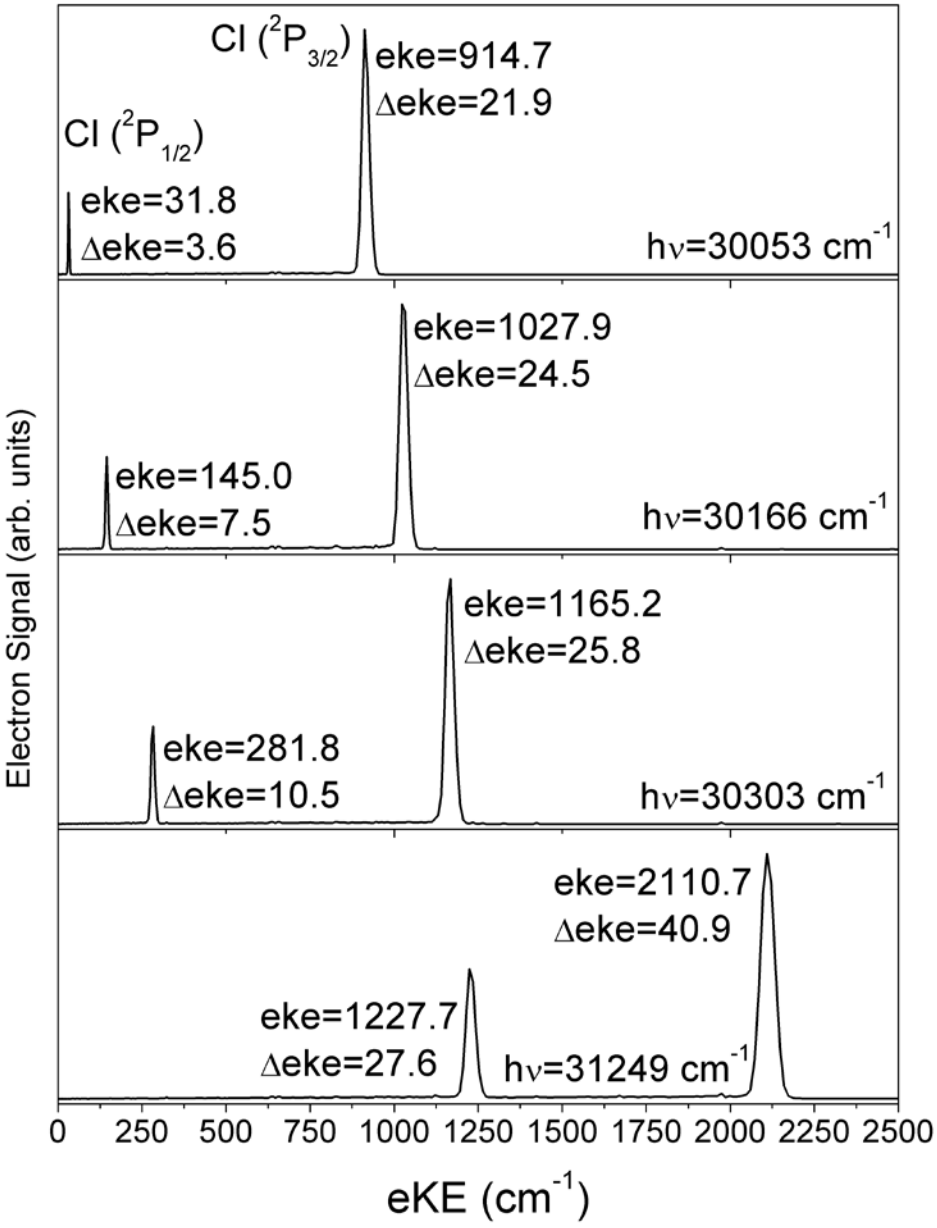

Figure 2.7 Transformed Cl^- SEVI spectra taken at different photon energies for calibration

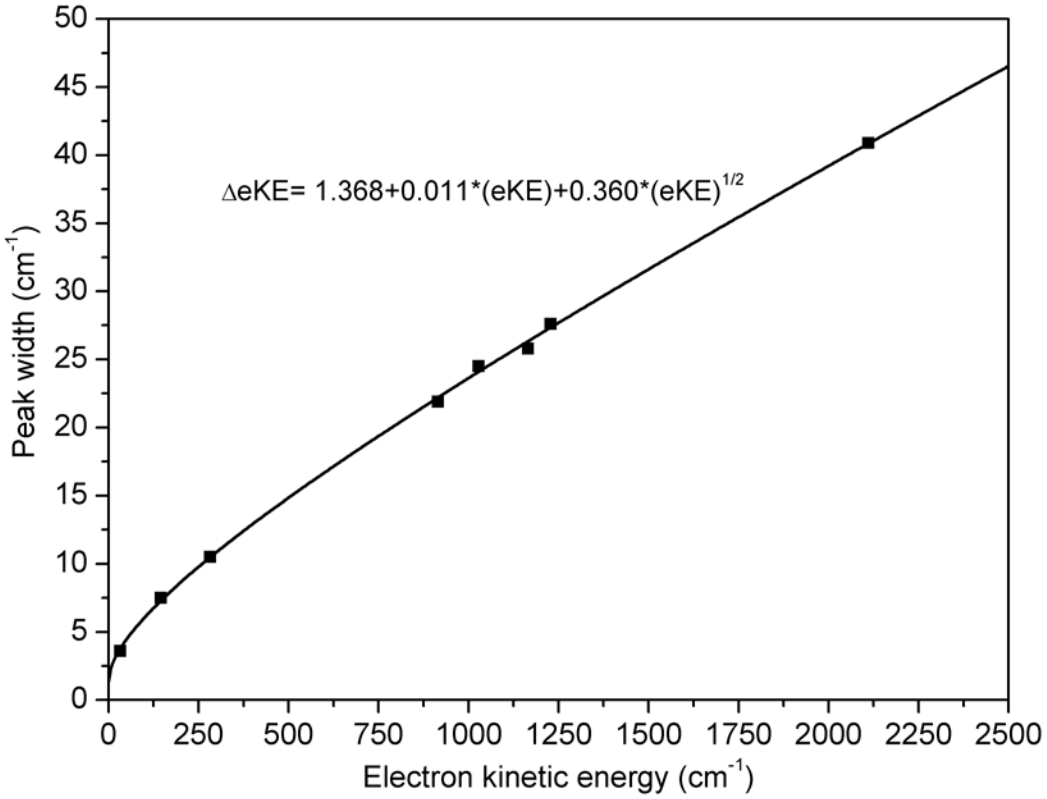

Figure 2.8 SEVI peak widths as a function of electron kinetic energy

feature at photon energy of 30303 cm^{-1} (third panel in Figure 2.5). The peak width slowly increases for features having smaller or greater radius. This is due to a slight dependence of the VMI focus on the electron energies. After several photoelectron images are taken at different laser wavelengths, the k calibration constant is then obtained from the slope of r^2 as a function of the photon energy. Figure 2.6 shows the linear regression of the data presented in Figure 2.5. For the -350 V VMI voltage set, the calibration constant usually has a value in the range of 0.018 to 0.019.

The velocity to energy transformation leads to a peak width that highly depends on the electron kinetic energy. This is illustrated in Figure 2.7 which presents the data of Figure 2.5 transformed into energy space. The peak width as a function of electron kinetic energy is plotted in Figure 2.8. Because of the slight peak width variation in velocity space, the resolution of SEVI in energy space is not well described by a simple $\sqrt{eKE}$ function. For the -350 V VMI voltage set, the SEVI resolution (in cm^{-1}) as a function of eKE is best described by:

$$\Delta eKE = 1.368 + 0.011 * (eKE) + 0.360 * \sqrt{eKE} \qquad (2.1)$$

In the present studies the -350 V VMI voltage set is usually used because it yields a good balance between energy resolution and range of eKE collected in a single image. With this voltage set, the electrons with eKE up to 4600 cm^{-1} (0.57 eV) are collected in an image. For most molecular systems, this is sufficient to get the entire manifold of vibrational transitions associated with a given electronic state within a single image. The unresolved rotational profile also limits the achievable resolution to about 15 cm^{-1} for most molecular system. Therefore, with the -350 V VMI voltage set, the maximum resolution of SEVI of achieved for all the features with less than 500 cm^{-1} of eKE. In theory, lower VMI voltages should yield better resolution. However, because the low voltage renders the photoelectron cloud more sensitive to distortion by stray fields, the gain in resolution is marginal.

2.2 IRMPD experimental setup

2.2.1 Overview

The apparatus used for the IRMPD experiments is an ion trap/tandem mass spectrometer[13] from the group of Dr. Knut Asmis at the Fritz-Haber-Institut der Max-Planck-Gesellschaft in Berlin, Germany. The experimental setup is shown schematically in Figure 2.9. The spectrometer is housed in a vacuum chamber that consists of five differentially pumped regions, which are shown as alternating shades of grey.

The ions are formed in the source region using either a commercial ion-spray source or a conventional laser ablation source. The molecular beam passes through a 3 mm skimmer and is then collimated in a 22 cm long radio-frequency (RF) decapole ion guide operating at 3.9 MHz and filled with helium buffer gas. The ions are mass-selected with a quadrupole mass tri-filter and sent into a linear RF trap by an electrostatic quadrupole deflector. The ions are accumulated in the ion trap and are cooled down by collisions with a 10 K helium buffer gas for 195 ms. The internally cold ions are then extracted from the trap and collimated between the first two plates of a Wiley-McLaren time-of-flight mass spectrometer where they are irradiated with a pulse of an infrared laser. The resulting charged fragments and the remaining ions are then extracted into the 55 cm long time-of-flight mass spectrometer and their arrival time is monitored by a MCP detector. The transient signal is sent to a computer for analysis. The IRMPD spectrum is then constructed by monitoring the fragment signal as the IR wavelength is scanned.

2.2.2 Ion trap

The RF ring electrode trap is based on the design of Gerlich and coworkers.[14] It consists of 24 concentric, Molybdenum ring electrodes with a 10 mm inner diameter. The 1 mm thick electrodes are electrically isolated from each other by a set of interlocking 1 mm thick sapphire disks. Trapping in the radial direction is achieved by the application of a 1.7 MHz RF voltage with maximum amplitude of 350 V and opposite phases applied to adjacent electrodes. Static DC potentials are applied to the entrance and exit lenses of the ion trap for the axial confinement of the ion packet. In addition, six individually adjustable DC potentials superimposed on the RF voltage are applied to each set of four adjacent ring electrodes. This controls the position of the ion cloud inside the ion trap, which is important for the extraction phase.

The ring electrode ion trap is mounted on the cold head of a closed cycle helium cryostat and a heating cartridge installed in-between the cold head and the ion trap

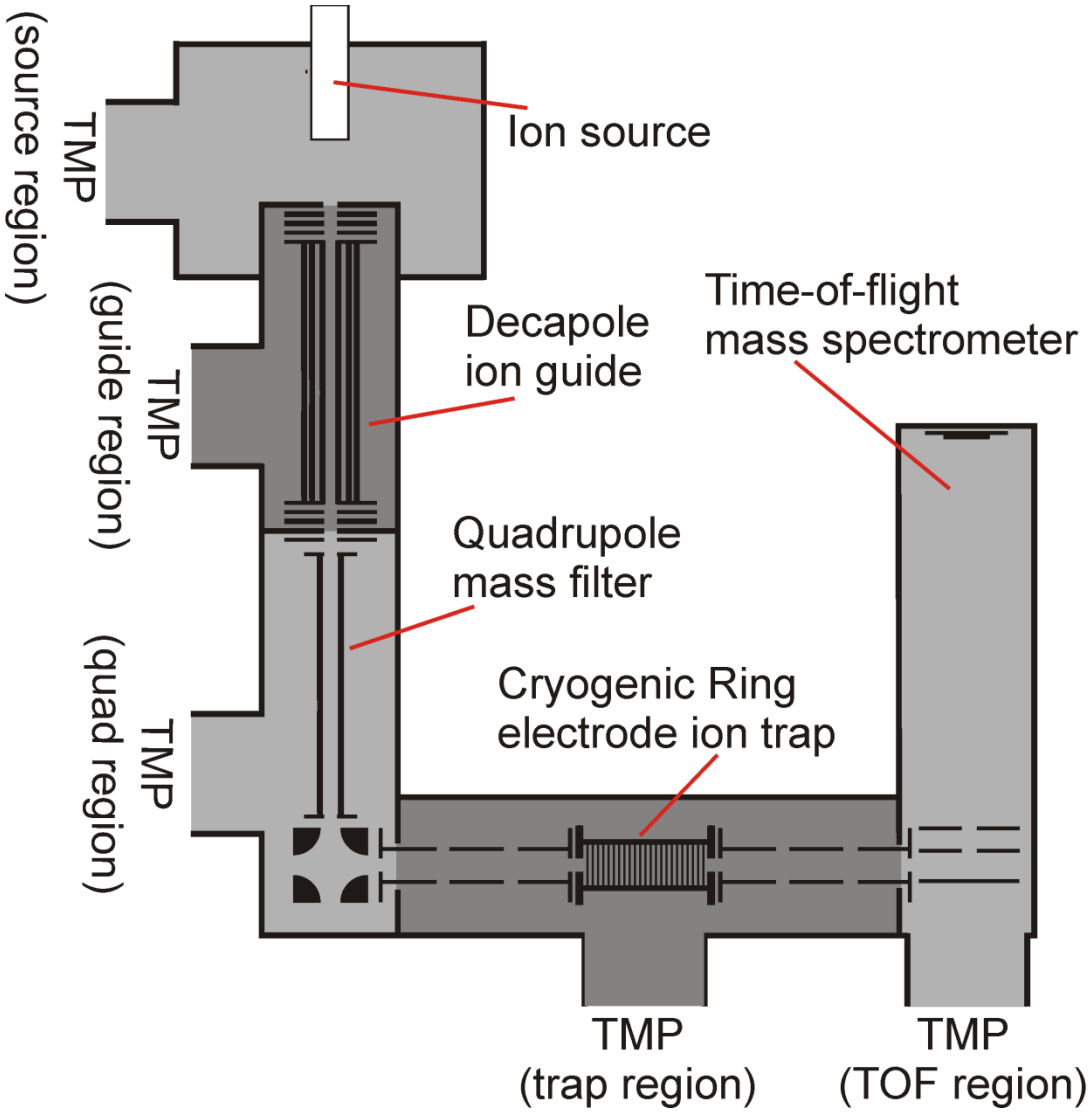

Figure 2.9 Schematic of the ion trap/tandem mass spectrometer apparatus. The various differentially pumped region are shown as alternating shades of gray

allows for continuous temperature control over the range of 10 to 350 K. The trap is continuously filled with helium buffer gas via a hole in one of the center electrodes and the pressure inside the trap is kept at around 10^{-2} mbar. The trapped ions are thus quickly thermalized by collisions with the buffer gas.

A typical measurement cycle is illustrated in Figure 2.4. First, the trap is loaded for 195 ms by setting voltages such that the ions have barely enough kinetic energy to pass the entrance lens. The ions are then reflected by the exit lens potential. They quickly lose kinetic energy by collisions with the buffer gas and cannot pass the entrance lens, becoming confined inside the trap where they are further cooled. The ions are extracted from the trap by lowering the exit lens potential and applying a voltage ramp on the trap electrodes. This ramp and the passage through an Einzel lens focus the ion packet in time and space to the middle of the time-of-flight plates. The laser timing is adjusted so that it interacts with the ions packet only when it reaches that point.

2.2.3 Free electron laser source

The output power of the currently available OPO/OPA based IR lasers is not sufficient to study processes requiring the absorption of more than one or two photons. In order to perform IRMPD experiments, a more powerful laser source, such as a free electron laser (FEL), is needed. In the FEL, coherent laser radiation is obtained from the oscillation of free relativistic electrons injected into a periodical magnetic undulator, which is enclosed in an optical cavity. Tunable photon energy is obtained by changing the period of the undulator and adjusting the energy of the electrons.

One of these lasers operating in the IR range is the Free Electron Laser for Infrared Experiments (FELIX),[15] which is hosted and operated by the FOM Institute for plasma physic Rijnhuizen in Nieuwegein, the Netherland. To conduct the IRMPD experiments described here, the ion trap/tandem mass spectrometer was transported to Nieuwegein and temporarily installed at one of the FELIX external user stations.

FELIX can output light between 3 μm and 250 μm (40 - 3300 cm^{-1}) with a bandwidth of roughly 0.25% rms. The light pulses consist of 5-10 μs macropulses at a repetition rate of 5 Hz. Each macropulse is composed of a train of transform limited 2-20 ps micropulses with repetition rate of 25 MHz and power of 0.5-100 MW. This pulsing scheme is perfect for the processes requiring sequential absorption of photons such as IRMPD. In fact, for most experiments, the FELIX output needs to be attenuated to avoid saturation of the dissociation signal.

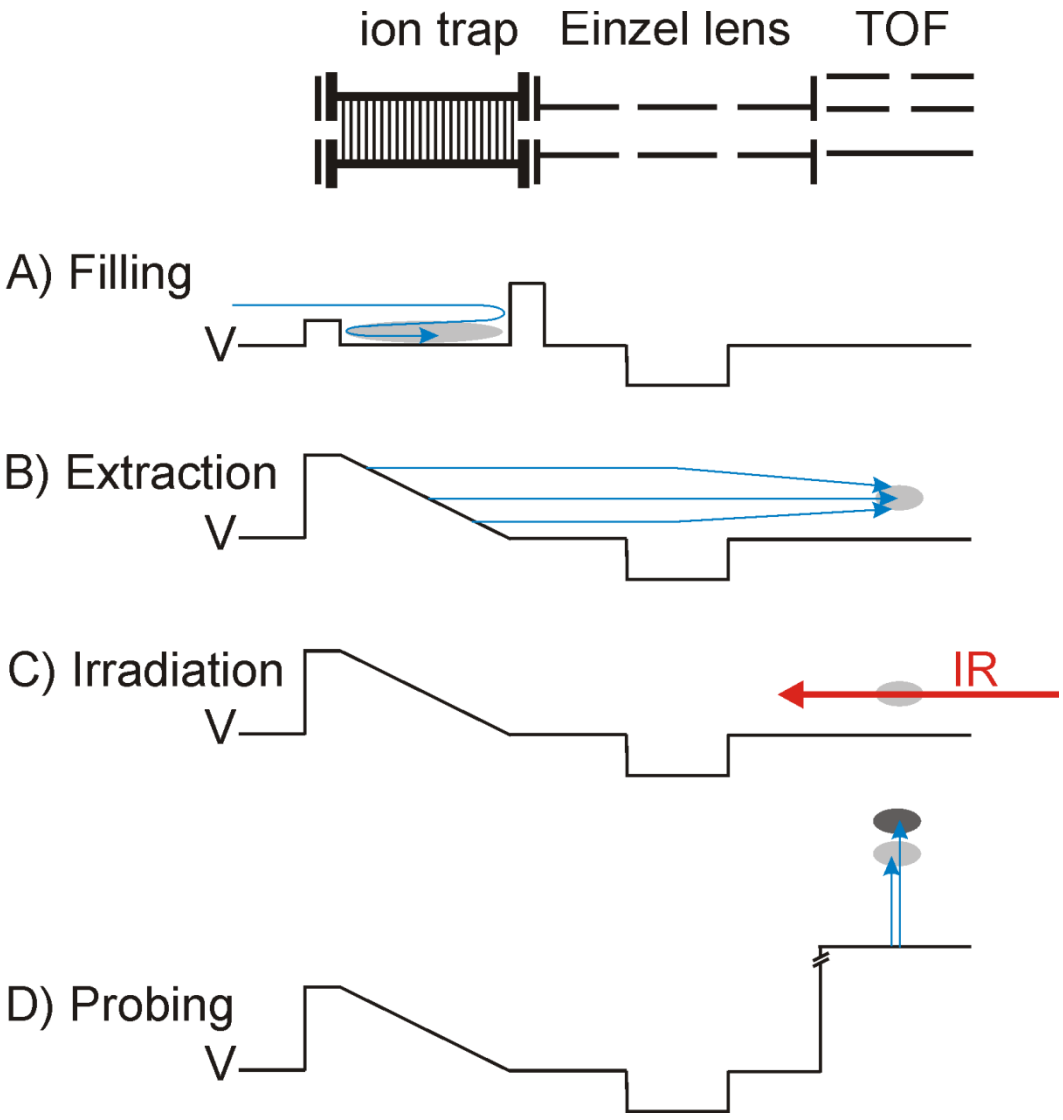

Figure 2.10 Electrostatic potentials and ion trajectories during the typical phases of the IRMPD experiments.

References:

1) A. Osterwalder, M. J. Nee, J. Zhou, and D. M. Neumark, *J. Chem. Phys.* **121** (13), 6317 (2004).
2) T. N. Kitsopolous, Ph. D thesis, University of California, Berkeley, 1989.
3) T. N. Kitsopoulos, I. M. Waller, J. G. Loeser, and D. M. Neumark, *Chem. Phys. Lett.* **159** (4), 300 (1989).
4) M. J. Nee, Ph. D thesis, University of California, Berkeley, 2005.
5) J. Zhou, Ph. D thesis, University of California, Berkeley, 2007.
6) U. Even, J. Jortner, D. Noy, N. Lavie, and C. Cossart-Magos, *J. Chem. Phys.* **112** (18), 8068 (2000).
7) D. L. Osborn, D. J. Leahy, D. R. Cyr, and D. M. Neumark, *J. Chem. Phys.* **104** (13), 5026 (1996).
8) W. C. Wiley and I. H. McLaren, *Rev. Sci. Instrum.* **26** (12), 1150 (1955).
9) A. Eppink and D. H. Parker, *Rev. Sci. Instrum.* **68** (9), 3477 (1997).
10) E. W. Hansen and P. L. Law, *J. Opt. Soc. Am. A* **2** (4), 510 (1985).
11) V. Dribinski, A. Ossadtchi, V. A. Mandelshtam, and H. Reisler, *Rev. Sci. Instrum.* **73** (7), 2634 (2002).
12) G. A. Garcia, L. Nahon, and I. Powis, *Rev. Sci. Instrum.* **75** (11), 4989 (2004).
13) D. Goebbert, T. Wende, R. Bergmann, G. Meijer, and K. R. Asmis, *J. Phys. Chem. A* **113**, 5874 (2009).
14) A. Luca, S. Schlemmer, I. Cermak, and D. Gerlich, *Rev. Sci. Instrum.* **72** (7), 2900 (2001).
15) D. Oepts, A. F. G. van der Meer, and P. W. van Amersfoort, *Infrared Phys. Techn.* **36** (1), 297 (1995).

CHAPTER 3

Slow photoelectron velocity-map imaging of heteroatom doped carbon chains.

3.1 Slow photoelectron velocity-map imaging of C_nH^- (n=5-9) anions

Abstract

High-resolution photoelectron spectra of the C_nH^- anions with n=5-9 are acquired with slow electron velocity-map imaging (SEVI). Spectral features are assigned with the help of electronic structure calculations and Franck-Condon simulations. Well-resolved transitions to the linear $\tilde{X}^2\Pi$ and $\tilde{a}^4\Sigma^-$ neutral states are observed for species with an odd number of carbon atoms. For C_6H^- and C_8H^-, transitions to the $\tilde{X}^2\Pi$ neutral ground state and the low lying $\tilde{A}^2\Sigma^+$ excited state are observed. Precise electron affinities, term energies, fine structure splittings, and gas-phase vibrational frequencies are determined. The C_5H^-, C_7H^- and C_9H^- SEVI spectra are consistent with the anions having $\tilde{X}^3\Sigma^-$ linear triplet ground states.

3.1.1 Introduction

The linear carbon monohydride radical chains, C_nH, are important species in hydrocarbon combustion[1] and in the interstellar medium.[2] In both environments, these radicals serve as precursors for the formation of larger hydrocarbon chains and polycyclic species. The neutral chains with n=2-8 have been observed in the circumstellar envelope of evolved stars,[3] where they can be formed by reactions of C and C_2 with unsaturated, closed-shell hydrocarbons.[3-5] The negatively charged carbon monohydrides C_4H^-, C_6H^-, and C_8H^- were among the first anions to be detected in interstellar and circumstellar media,[6-11] where they are formed by radiative attachment.[12] The chemistry of these species is closely coupled to their spectroscopy, motivating the work described in this chapter, in which we continue the investigation of the carbon monohydride chains via negative ion photodetachment.[13-17] High resolution photoelectron spectra (PE) of the C_nH^- (n=5-9) anions are measured using slow electron velocity-map imaging (SEVI). The SEVI spectra provide a detailed probe of the neutral and anionic states of these species, and yield insights into their geometries, vibronic structure, energetics, and the possibility of structural isomers.

Carbon monohydride radical chains have been the subject of numerous experimental and theoretical studies. Maier and co-workers have measured the UV-visible electronic absorption spectra of several neutral[2,18-23] and anionic[24-27] C_nH^- (n=5-9) species in the gas phase and in rare-gas matrices. Thaddeus and co-workers have used Fourier transformed microwave (FTMW) spectroscopy and millimeter-wavelength absorption spectroscopy to study the neutral $C_{5-9}H$ species[28-36] as well as the C_6H^- and C_8H^- anions.[6,37] PE spectra of C_nH^- (n=5,6,8) have also been reported.[13,16] Reaction kinetics and bond dissociation energies have been measured using flowing afterglow and guided ion beam mass spectrometry.[38,39] Many electronic structure calculations at various levels of sophistication have been carried out on the neutral and anionic carbon monohydrides in the size-range of interest here.[16,40-51]

This body of experimental and theoretical work has revealed significant differences in C_nH neutrals and anions depending on whether n is odd or even. In particular, there is evidence for multiple structural isomers for the odd-n anionic and neutral species. For example, theory and experiment indicate that the cyclic-C_3H isomer lies slightly lower in energy than the linear-C_3H isomer for both the anion and the neutral species.[17,52] Both linear and cyclic isomers of C_5H have been observed in microwave spectroscopy.[28,35] High level ab initio calculations[43,44] have identified the linear isomer of C_5H to be lower in energy. Using these energetics and PE spectroscopy, Sheehan *et al.*[16] recently suggested that a cyclic isomer was the lowest energy structure for the C_5H^- anion. Bowie and co-workers[46,53] have also reported the synthesis of several anionic and neutral isomers of C_5H and C_7H using mass spectrometry techniques and precursors with the proper bond connectivity.

In contrast, it is well-established that the neutral and anionic even-carbon C_nH species are linear. The anions have closed-shell $^1\Sigma^+$ ground states with strong acetylenic character.[48]

The neutral species have low-lying $^2\Pi$ and $^2\Sigma^+$ states whose ordering switches with chain length.[13,40] The C_2H and C_4H radicals have $^2\Sigma^+$ ground-states, while the longer chains have $^2\Pi$ ground-states; the $\tilde{A}^2\Pi - \tilde{X}^2\Sigma^+$ splitting is only 213 cm^{-1} in C_4H.[15] The proximity of these two states in C_2H and C_4H leads to considerable spectral complexity attributed to strong vibronic coupling in both species,[14,15,54,55] while vibronic coupling in the longer chains with $\tilde{X}^2\Pi$ ground states has not been investigated.

In this section, we report high resolution PE spectra of the C_nH^- anions, n=5-9, acquired with SEVI.[56] These spectra are analyzed with the help of electronic structure calculations and Franck-Condon (FC) simulations. For all species, well-resolved vibrational and spin-orbit transitions to the linear $\tilde{X}^2\Pi$ ground state are observed. A second band of peaks is also observed for all species. It is assigned to the $\tilde{a}^4\Sigma^-$ excited state for C_5H, C_7H and C_9H and to the low-lying $\tilde{A}^2\Sigma^+$ state for C_6H and C_8H. Several vibrational frequencies of the neutral species are determined for the first time. This work also demonstrates that the C_5H^-, C_7H^- and C_9H^- anions have $^3\Sigma^-$ linear ground states, in contrast to the bent structures previously reported.[16,46,53]

3.1.2 Experimental details

The SEVI apparatus has been described in detail in chapter 2. In this experiment, C_nH^- anions were produced from of a gas mixture comprising 1% acetylene and 1% propyne in a balance of Ar. The gas mixture, at a stagnation pressure of 300 psi, was expanded into the source vacuum chamber through an Even-Lavie pulsed valve[57] equipped with a grid discharge source. The apparatus was calibrated by acquiring SEVI images of atomic Cl^- and S^- at several different photon energies, using the accurate electron affinities of these species reported previously.[58] With the -350 V VMI repeller voltage used in this study, the full widths at half maximum of the chloride peaks were 7.5 cm^{-1} at 150 cm^{-1} eKE and 18 cm^{-1} at 715 cm^{-1}. Linewidths in the spectra presented here are limited by unresolved rotational structure. Since the origin of an unresolved rotational profile may not be aligned with the observed peak maximum, we report error bars of one Gaussian standard deviation for all energy determinations, typically 8 cm^{-1} for the highest resolution scans performed here.

3.1.3 Experimental Results

SEVI spectra of the odd-carbon anions, C_5H^-, C_7H^- and C_9H^-, are shown in Figures 3.1-3.3, while the SEVI spectra of the two even-carbon species, C_6H^- and C_8H^-, are shown in Figures 3.4 and 3.5. The peak positions, shifts from the band origin, PADs, and assignments (see Analysis section) are summarized in Table 3.1-3.5. Because the anisotropy parameter varies with photon energy,[59] we reported PADs as "p" or "s+d" for features having $\beta>0$ and $\beta<0$, respectively.

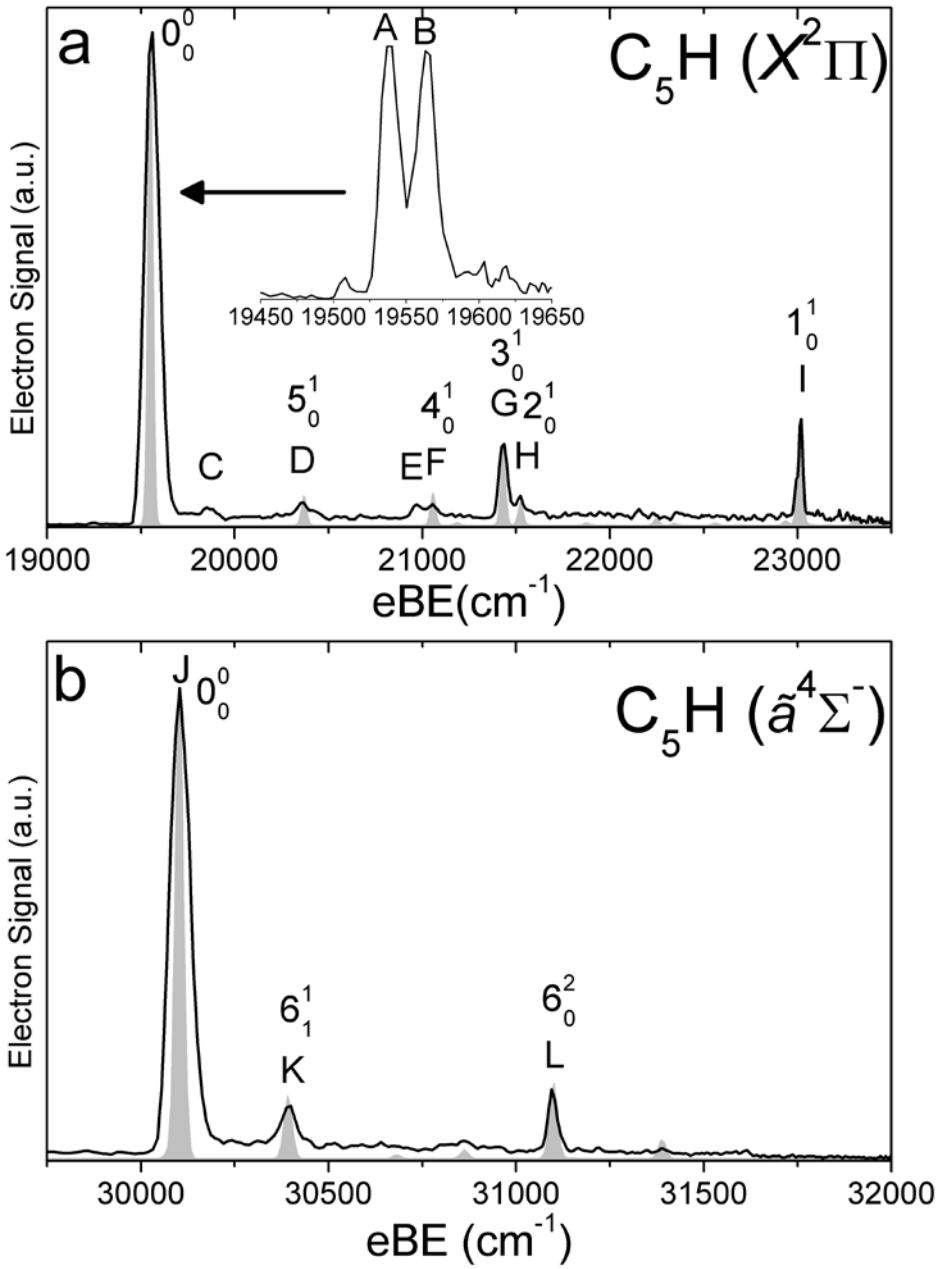

Figure 3.1 SEVI spectra of C_5H^- covering the electron binding energy ranges of 19000 cm^{-1} to 23500 cm^{-1} (panel a) and 29500 to 32000 cm^{-1} (panel b). Franck-Condon simulations show as grey-shaded peaks. Inset shows high-resolution scan of indicated feature.

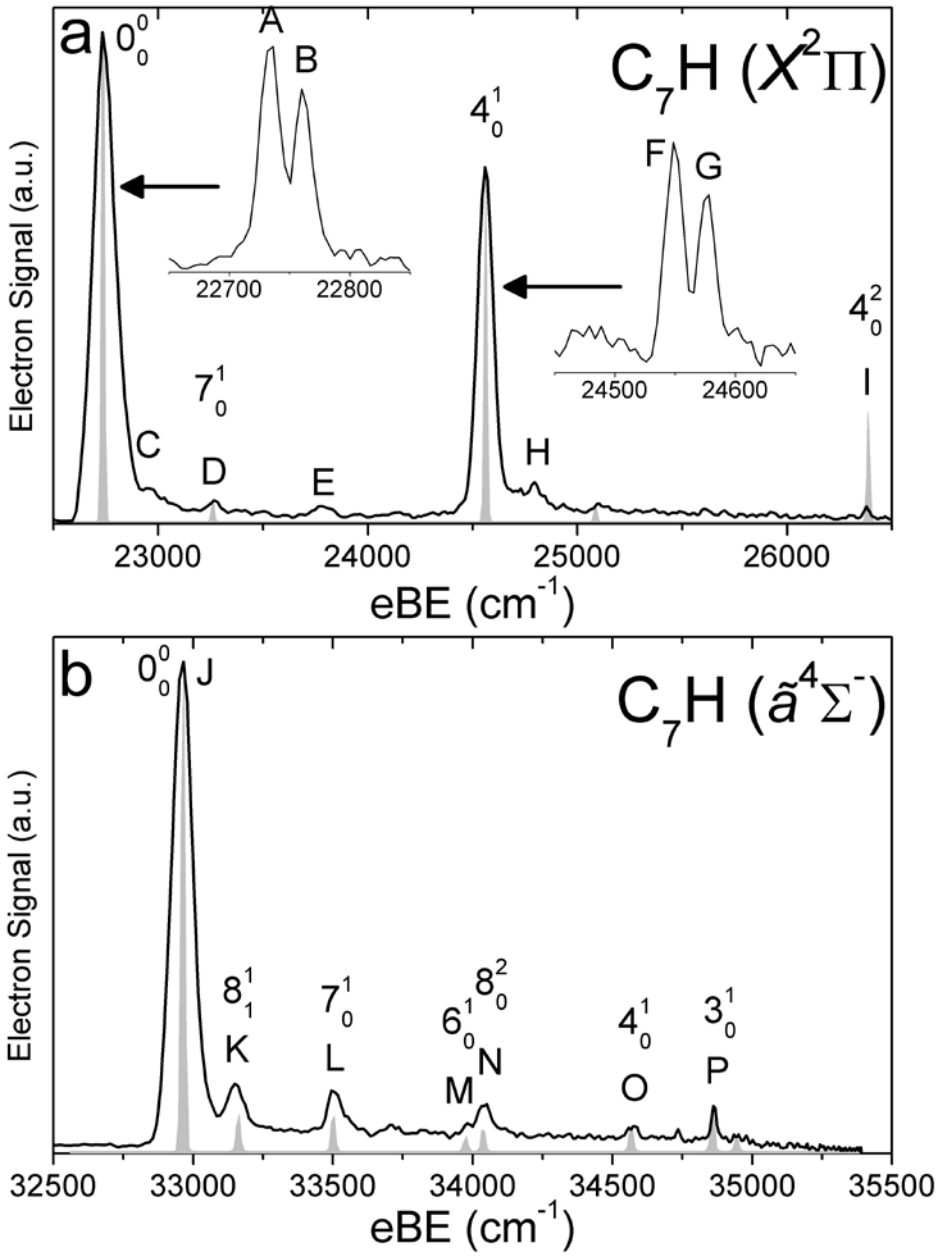

Figure 3.2 SEVI spectra of C_7H^- covering the electron binding energy ranges of 22500 cm^{-1} to 26500 cm^{-1} (panel a) and 32500 to 35500 cm^{-1} (panel b). Franck-Condon simulations show as grey-shaded peaks. Insets show high-resolution scans of indicated features.

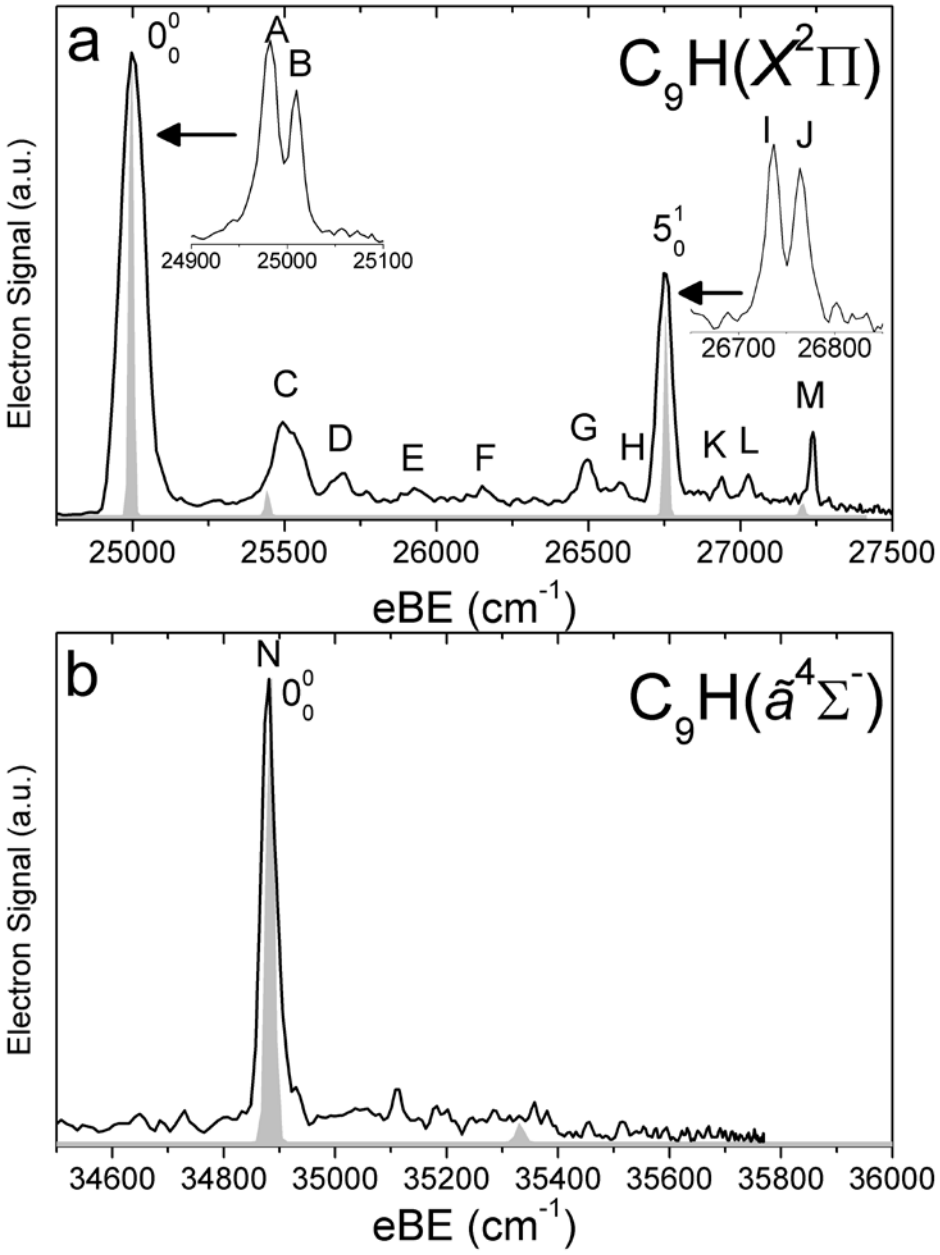

Figure 3.3 SEVI spectra of C_9H^- covering the electron binding energy ranges of 24750 cm^{-1} to 27500 cm^{-1} (panel a) and 34500 to 35800 cm^{-1} (panel b). Franck-Condon simulations show as grey-shaded peaks. Insets show high-resolution scans of indicated features.

Table 3.1 Peak positions, shifts from band origins, angular distributions (PAD), and assignments for the C_5H^- SEVI spectra.

Peak	Position (cm^{-1})	Shift (cm^{-1})	PAD	Assignments (Vibs)	Assignments States
A	19539	0	*s+d*	0_0^0	$\tilde{X}^2\Pi_{1/2} \leftarrow \tilde{X}^3\Sigma^-$
B	19564	25	*s+d*	0_0^0	$\tilde{X}^2\Pi_{3/2} \leftarrow \tilde{X}^3\Sigma^-$
C	19851	312	*s+d*	6_1^1	$\tilde{X}^2\Pi \leftarrow \tilde{X}^3\Sigma^-$
D	20372	833	*s+d*	5_0^1	$\tilde{X}^2\Pi \leftarrow \tilde{X}^3\Sigma^-$
E	20960	1421	*s+d*	6_0^2	$\tilde{X}^2\Pi \leftarrow \tilde{X}^3\Sigma^-$
F	21060	1521	*s+d*	4_0^1	$\tilde{X}^2\Pi \leftarrow \tilde{X}^3\Sigma^-$
G	21434	1895	*s+d*	3_0^1	$\tilde{X}^2\Pi \leftarrow \tilde{X}^3\Sigma^-$
H	21527	1988	*s+d*	2_0^1	$\tilde{X}^2\Pi \leftarrow \tilde{X}^3\Sigma^-$
I	23014	3475	*s+d*	1_0^1	$\tilde{X}^2\Pi \leftarrow \tilde{X}^3\Sigma^-$
J	30101	0	*p*	0_0^0	$\tilde{a}^4\Sigma^- \leftarrow \tilde{X}^3\Sigma^-$
K	30391	290	*p*	6_1^1	$\tilde{a}^4\Sigma^- \leftarrow \tilde{X}^3\Sigma^-$
L	31098	997	*p*	6_0^2	$\tilde{a}^4\Sigma^- \leftarrow \tilde{X}^3\Sigma^-$

Table 3.2 Peak positions, shifts from band origins, angular distributions (PAD), and assignments for the C_7H^- SEVI spectra.

Peak	Position (cm^{-1})	Shift (cm^{-1})	PAD	Assignments (Vibs)	Assignments States
A	22734	0	*s+d*	0_0^0	$\tilde{X}^2\Pi_{1/2} \leftarrow \tilde{X}^3\Sigma^-$
B	22761	27	*s+d*	0_0^0	$\tilde{X}^2\Pi_{3/2} \leftarrow \tilde{X}^3\Sigma^-$
C	22957	223	*s+d*	8_1^1	$\tilde{X}^2\Pi \leftarrow \tilde{X}^3\Sigma^-$
D	23258	524	*s+d*	7_0^1	$\tilde{X}^2\Pi \leftarrow \tilde{X}^3\Sigma^-$
E	23776	1042	*s+d*	8_0^2	$\tilde{X}^2\Pi \leftarrow \tilde{X}^3\Sigma^-$
F	24549	1815	*s+d*	4_0^1	$\tilde{X}^2\Pi_{1/2} \leftarrow \tilde{X}^3\Sigma^-$
G	24576	1842	*s+d*	4_0^1	$\tilde{X}^2\Pi_{3/2} \leftarrow \tilde{X}^3\Sigma^-$
H	24793	2059	*s+d*	$4_0^1 8_1^1$	$\tilde{X}^2\Pi \leftarrow \tilde{X}^3\Sigma^-$
I	26379	3645	*s+d*	4_0^2	$\tilde{X}^2\Pi \leftarrow \tilde{X}^3\Sigma^-$
J	32969	0	*p*	0_0^0	$\tilde{a}^4\Sigma^- \leftarrow \tilde{X}^3\Sigma^-$
K	33149	180	*p*	8_1^1	$\tilde{a}^4\Sigma^- \leftarrow \tilde{X}^3\Sigma^-$
L	33506	537	*p*	7_0^1	$\tilde{a}^4\Sigma^- \leftarrow \tilde{X}^3\Sigma^-$
M	33980	1011	*p*	6_0^1	$\tilde{a}^4\Sigma^- \leftarrow \tilde{X}^3\Sigma^-$
N	34041	1072	*p*	8_0^2	$\tilde{a}^4\Sigma^- \leftarrow \tilde{X}^3\Sigma^-$
O	34572	1603	*p*	4_0^1	$\tilde{a}^4\Sigma^- \leftarrow \tilde{X}^3\Sigma^-$
P	34863	1894	*p*	3_0^1	$\tilde{a}^4\Sigma^- \leftarrow \tilde{X}^3\Sigma^-$

Table 3.3 Peak positions, shifts from band origins, angular distributions (PAD), and assignments for the C_9H^- SEVI spectra.

Peak	Position (cm^{-1})	Shift (cm^{-1})	PAD	Assignments (Vibs)	Assignments States
A	24980	0	*s+d*	0_0^0	$\tilde{X}^2\Pi_{1/2} \leftarrow \tilde{X}^3\Sigma^-$
B	25010	30	*s+d*	0_0^0	$\tilde{X}^2\Pi_{3/2} \leftarrow \tilde{X}^3\Sigma^-$
C	25487	507	*p*		
D	25540	560	*p*		
E	25671	691	*p*		
F	25928	948	*p*		
G	26157	1177	*p*		
H	26495	1515	*p*		
I	26603	1623	*p*		
J	26735	1755	*s+d*	5_0^1	$\tilde{X}^2\Pi_{1/2} \leftarrow \tilde{X}^3\Sigma^-$
K	26766	1786	*s+d*	5_0^1	$\tilde{X}^2\Pi_{3/2} \leftarrow \tilde{X}^3\Sigma^-$
L	26934	1954	*p*		
M	27024	2044	*p*		
N	27236	2256	*p*		
O	34884	9904	*p*	0_0^0	$\tilde{a}^4\Sigma^- \leftarrow \tilde{X}^3\Sigma^-$

For each anion, panels a and b illustrate higher and lower eBE regions, respectively, of the SEVI spectra. Higher resolution SEVI traces taken at photon energies ~100-150 cm^{-1} above the feature at lowest eBE in the upper panels reveals each to be a closely spaced doublet, as shown in the insets in Figures 3.1a-3.5a. These traces show doublet splittings of 25 cm^{-1}, 15 cm^{-1}, 27 cm^{-1}, 21 cm^{-1} and 30 cm^{-1} for C_5H^- to C_9H^-, respectively. Doublets with the same splittings were also resolved for the other intense transition in the first band of C_7H^-(peaks F and G) and C_9H^-(I and J). The same splittings are presumably found on other features in Figures 3.1a-3.5a. However, their weak intensities prevented the acquisition of SEVI spectra sufficiently close to their respective detachment thresholds to observe these small splittings. No doublets were found in high resolution traces of the more intense features in Figures. 3.1b-3.5b

In the C_5H^- , C_6H^-, C_7H^- and C_8H^- spectra, all the features in panel a have "*s+d*" PADs while those in panel b have "*p*" PADs. In the C_9H^- spectra, peaks A, B, I and J in Figures 3.3a have "*s+d*" PADs, while the remaining smaller peaks all have "*p*" PADs. The single peak N in Figure 3.3b also has a "*p*" PAD. In the SEVI spectra of C_5H^-, C_7H^- and C_9H^-, the lowest eBE transitions (peak A) of the first band are found at eBE of 19539 cm^{-1}, 22724 cm^{-1} and 24980 cm^{-1}, respectively, while those of the second band are higher in energy by 10502 cm^{-1}, 10235 cm^{-1} and 9904 cm^{-1}, respectively. The large energy separation and different PADs indicate the features in panel a and b of Figures 3.1-3.3 belong to different

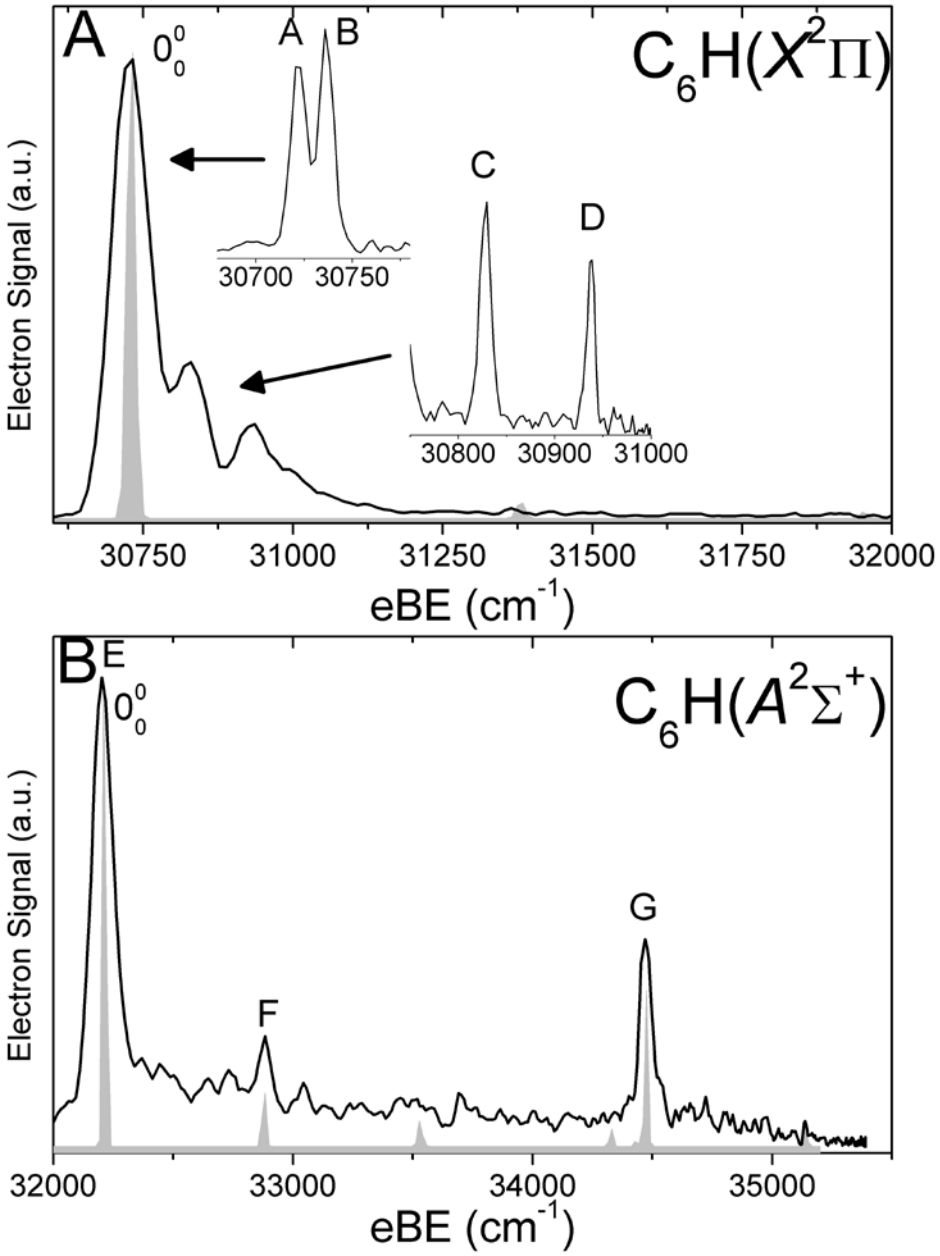

Figure 3.4 SEVI spectra of C_6H^- covering the electron binding energy ranges of 30600 cm^{-1} to 32000 cm^{-1} (panel a) and 32000 to 35500 cm^{-1} (panel b). Franck-Condon simulations show as grey-shaded peaks. Inset shows high-resolution scan of indicated feature.

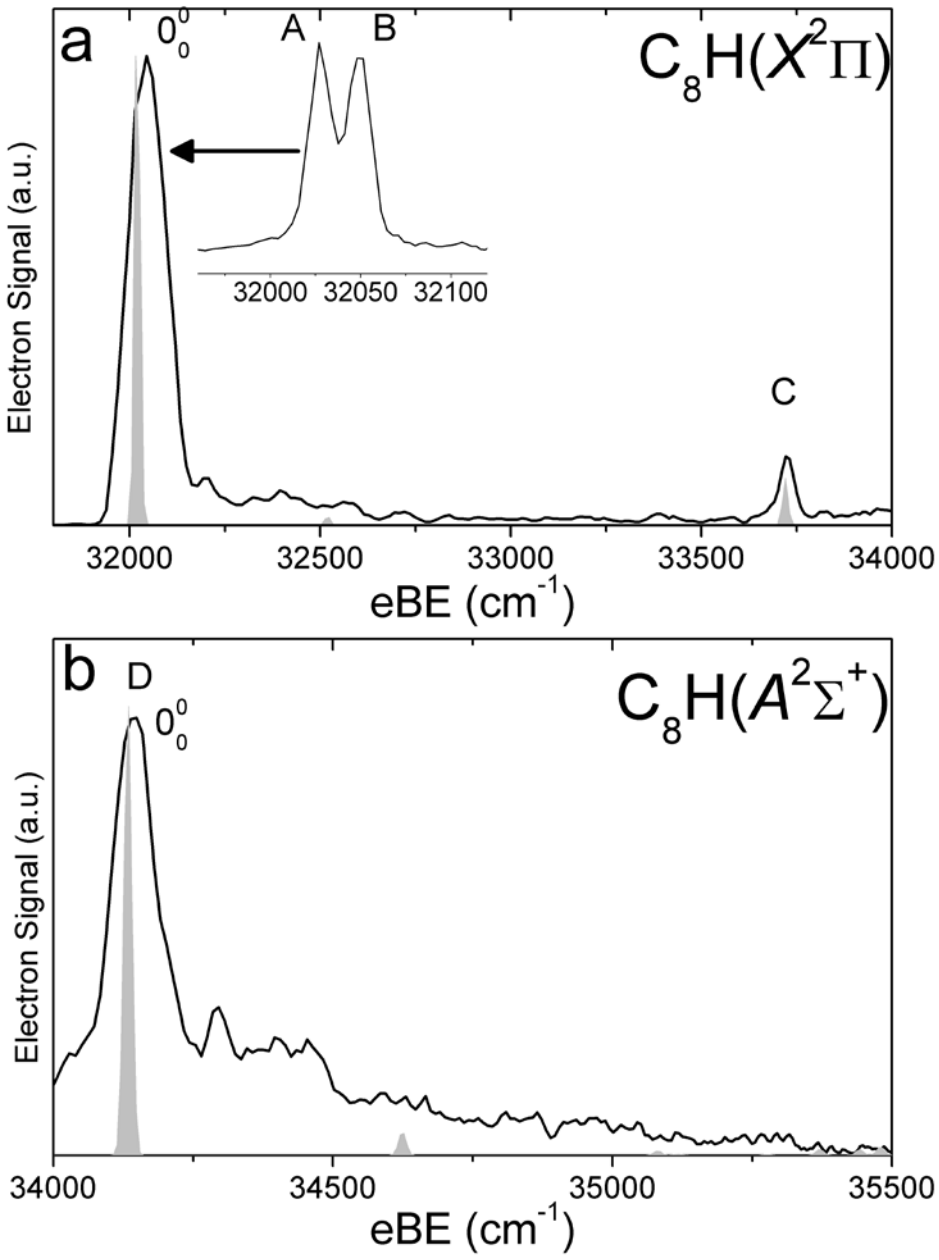

Figure 3.5 SEVI spectra of C_8H^- covering the electron binding energy ranges of 31750 cm^{-1} to 34000 cm^{-1} (panel a) and 34000 to 35500 cm^{-1} (panel b). Franck-Condon simulations show as grey-shaded peaks. Inset shows high-resolution scan of indicated feature.

Table 3.4. Peak positions, shifts from band origins, angular distributions (PAD), and assignments for the C_6H^- SEVI spectra.

Peak	Position (cm^{-1})	Shift (cm^{-1})	PAD	Assignments (Vibs)	Assignments States
A	30722	0	*s*+*d*	0_0^0	$\tilde{X}^2\Pi_{3/2} \leftarrow \tilde{X}^1\Sigma^+$
B	30737	15	*s*+*d*	0_0^0	$\tilde{X}^2\Pi_{1/2} \leftarrow \tilde{X}^1\Sigma^+$
C	30828	106	*s*+*d*		$\tilde{X}^2\Pi \leftarrow \tilde{X}^1\Sigma^+$
D	30937	215	*s*+*d*		$\tilde{X}^2\Pi \leftarrow \tilde{X}^1\Sigma^+$
E	32214	0	*p*	0_0^0	$\tilde{A}^2\Sigma^+ \leftarrow \tilde{X}^1\Sigma^+$
F	32880	651	*p*	6_0^1	$\tilde{A}^2\Sigma^+ \leftarrow \tilde{X}^1\Sigma^+$
G	34474	2260	*p*	2_0^1	$\tilde{A}^2\Sigma^+ \leftarrow \tilde{X}^1\Sigma^+$

Table 3.5. Peak positions, shifts from band origins, angular distributions (PAD), and assignments for the C_8H^- SEVI spectra.

Peak	Position (cm^{-1})	Shift (cm^{-1})	PAD	Assignments (Vibs)	Assignments States
A	32028	0	*s*+*d*	0_0^0	$\tilde{X}^2\Pi_{3/2} \leftarrow \tilde{X}^1\Sigma^+$
B	32049	21	*s*+*d*	0_0^0	$\tilde{X}^2\Pi_{1/2} \leftarrow \tilde{X}^1\Sigma^+$
C	33725	1697	*s*+*d*	5_0^1	$\tilde{X}^2\Pi \leftarrow \tilde{X}^1\Sigma^+$
D	34140	2112	*p*	0_0^0	$\tilde{A}^2\Sigma^+ \leftarrow \tilde{X}^1\Sigma^+$

electronic states. Compared to the odd-carbon species, the SEVI spectra of C_6H^- and C_8H^- show higher electron binding energies for the lower energy band. The lower band origins are found at eBE of 30722 cm^{-1} and 32028 cm^{-1} in the C_6H^- and C_8H^- spectra, respectively, while the first bands in panel b are only 1492 cm^{-1} and 2112 cm^{-1} higher in energy. Although these relatively small energy intervals could represent vibrational frequencies, the different PADs for the features in panel a and b of Figure 3.4 and 3.5 imply that that the spectra in Figs. 3.4b and 3.5b are from transitions to low-lying excited electronic states of C_6H and C_8H, consistent with the assignment of earlier anion photoelectron spectra.[13]

For C_5H^-, C_6H^- and C_8H^-, the observed band structures and positions are consistent with the previously reported anion PE spectra.[13,16] However, the improved resolution of SEVI over conventional PE spectroscopy reveals numerous new features, especially in the lower bands of C_5H^- and C_6H^-. The SEVI spectra of C_7H^- and C_9H^- are the first photodetachment spectra reported for these species.

3.1.4 Electronic structure calculations

Electronic structure calculations were performed on the relevant neutral and anionic states of C_nH. The current calculations serve to produce, at a uniform level of theory, all geometries, normal modes and vibrational frequencies necessary to perform Franck-Condon simulations and interpret the photoelectron spectra. Our calculations were carried out with density functional theory (DFT) using the Becke three- parameter Lee,Yang, and Parr exchange-correlation functional[60,61] (B3LYP) and the augmented correlation consistent polarized valence triple-zeta basis set[62] (AVTZ). All computations were performed using the GAUSSIAN03 program.[63] Franck-Condon simulations were performed with the FCFgaus03 and PESCAL programs[64,65] using the Sharp-Rosenstock-Chen method[66] that treats all the modes as independent harmonic oscillators and relates the normal mode coordinates of the initial and final states via the Duschinsky transformation.[67] The calculated geometries and harmonic vibrational frequencies were used as starting point for the FC simulations. The neutral frequencies were adjusted to the experimental values and the normal mode displacements were adjusted to fit the experimental spectra.

For C_5H^- and C_7H^-, several low-lying isomers with singlet and triplet spin multiplicity have been previously reported.[16,46,53] The carbon backbone of these isomers can be a single chain, a branched chain, or a branched three-membered ring. Consequently, we searched for the lowest energy isomers of C_5H^-, C_7H^- and C_9H^- by performing electronic structure calculations at the B3LYP/6-311+G level of theory on several different initial geometries for both the singlet and triplet surfaces. The lowest energy isomers were then re-optimized at the B3LYP/AVTZ level. We found that the isomer comprising a single carbon chain terminated by one hydrogen was lower in energy than the next-lowest isomer by 0.29 eV, 0.65 eV and 0.84 eV, for n=5, 7, and 9, respectively. These lowest energy isomers were found to have a triplet ground state with the first singlet state lying higher in energy by 0.31 eV, 0.43 eV and 0.47 eV. The next-lowest isomers also consisted of a single carbon chain, but with the hydrogen located on the third carbon for n=5,7 and the fifth carbon for n=9. Hence, only triplet states with H-terminated carbon chains were analyzed in more detail for the odd-carbon anions. For the even-carbon species, only the well-known linear $^1\Sigma^+$ anion state and the accessible low-lying $^2\Pi$ and $^2\Sigma^+$ neutral states were considered.

Calculated geometries and relative energies of the anionic and neutral states of the C_nH species are shown in Table 3.6, while harmonic vibrational frequencies are presented in Table 3.7. Vibrational mode labels for the neutral ground state are used throughout even if the ordering of the frequencies changes. For C_5H^-, the minimum energy structure is a ^{3}A' state with an almost linear carbon backbone and a CCH angle of 164.1°. However, the corresponding linear $^3\Sigma^-$ first-order transition state was found to be only 0.001 eV above the minimum energy structure. With such a small energy difference, the zero-point energy of the CCH bending mode certainly exceeds the barrier to linearity. Thus, the C_5H^- ground state will be considered to be the linear $^3\Sigma^-$ state with the expectation that this state is either

quasilinear or has a very shallow CCH bending potential. This result differs from previous theoretical studies[16,46,68] using the same B3LYP functional with smaller basis sets that yielded strongly bent structures for the triplet ground-state of C_5H^-. This basis set effect might also explain why Blanksby *et al.*[46] did not found the chain isomer to be the lowest in energy by using single-point energy calculations at the RCCSD(T)/AVDZ level on the geometries obtained at the B3LYP/AVDZ level. For C_7H^- and C_9H^-, the truly linear $^3\Sigma^-$ state was found to be the minimum energy structure. This result is again in contrast with previous DFT studies[53,68] using smaller basis sets that found slightly bent structures for the triplet ground states of C_7H^- and C_9H^-.

Table 3.6 Relative energies (eV, including zero-point correction) and geometries (Å, degrees) of the $C_{5\text{-}9}H$ anionic and neutral states calculated at the B3LYP/AVTZ level. The experimental (Ref. 36) or recommended (Ref. 48) bond lengths are shown in parentheses

Specie	State	ΔE	Geometry								
C_5H			**C_1-C_2**	**C_2-C_3**	**C_3-C_4**	**C_4-C_5**	**C_5-H**	**$C_1C_2C_3$**	**$C_2C_3C_4$**	**$C_3C_4C_5$**	**C_4C_5H**
Anion	$\tilde{X}^3A'$	-2.56	1.284	1.302	1.305	1.25	1.061	180.0	179.5	176.9	164.1
	$^3\Sigma^-$	-2.56	1.285	1.301	1.308	1.245	1.058				
Neutral	$\tilde{X}^2\Pi$	0.00	1.304	1.264	1.321	1.221	1.063				
			(1.308)	(1.267)	(1.329)	(1.224)	(1.055)				
	$\tilde{a}^4\Sigma^-$	1.35	1.253	1.287	1.311	1.23	1.061				
C_6H			**C_1-C_2**	**C_2-C_3**	**C_3-C_4**	**C_4-C_5**	**C_5-C_6**	**C_6-H**			
Anion	$\tilde{X}^1\Sigma^+$	-3.64	1.252	1.342	1.231	1.348	1.218	1.059			
			(1.2575)	(1.3518)	(1.2313)	(1.3581)	(1.2189)	(1.0594)			
Neutral	$\tilde{X}^2\Pi$	0.00	1.281	1.312	1.24	1.334	1.215	1.063			
			(1.257)	(1.332)	(1.237)	(1.341)	(1.216)	(1.056)			
	$\tilde{A}^2\Sigma^+$	0.60	1.21	1.355	1.214	1.354	1.207	1.061			
C_7H			**C_1-C_2**	**C_2-C_3**	**C_3-C_4**	**C_4-C_5**	**C_5-C_6**	**C_6-C_7**	**C_7-H**		
Anion	$\tilde{X}^3\Sigma^-$	-2.95	1.275	1.309	1.28	1.271	1.321	1.233	1.059		
Neutral	$\tilde{X}^2\Pi$	0.00	1.295	1.275	1.298	1.243	1.332	1.215	1.062		
			(1.301)	(1.273)	(1.309)	(1.243)	(1.341)	(1.217)	(1.057)		
	$\tilde{a}^4\Sigma^-$	1.31	1.241	1.304	1.281	1.259	1.326	1.221	1.061		
C_8H			**C_1-C_2**	**C_2-C_3**	**C_3-C_4**	**C_4-C_5**	**C_5-C_6**	**C_6-C_7**	**C_7-C_8**	**C_9-H**	
Anion	$\tilde{X}^1\Sigma^+$	-3.79	1.255	1.334	1.236	1.332	1.230	1.347	1.216	1.059	
			(1.2600)	(1.3440)	(1.2360)	(1.3435)	(1.2284)	(1.3592)	(1.2166)	(1.0598)	
Neutral	$\tilde{X}^2\Pi$	0.00	1.281	1.306	1.248	1.315	1.233	1.339	1.212	1.062	
	$\tilde{A}^2\Sigma^+$	0.71	1.212	1.351	1.218	1.343	1.218	1.352	1.208	1.062	
C_9H			**C_1-C_2**	**C_2-C_3**	**C_3-C_4**	**C_4-C_5**	**C_5-C_6**	**C_6-C_7**	**C_7-C_8**	**C_8-C_9**	**C_9-H**
Anion	$\tilde{X}^3\Sigma^-$	-3.25	1.271	1.312	1.268	1.284	1.294	1.256	1.330	1.225	1.059
Neutral	$\tilde{X}^2\Pi$	0.00	1.290	1.280	1.287	1.254	1.311	1.235	1.338	1.212	1.062
	$\tilde{a}^4\Sigma^-$	1.27	1.233	1.315	1.265	1.276	1.298	1.246	1.334	1.217	1.061

Table 3.7 Calculated harmonic vibrational frequencies (cm^{-1}) at the B3LYP/AVTZ level of theory.

State	ν_1	ν_2	ν_3	ν_4	ν_5	ν_6	ν_7	ν_8	ν_9	ν_{10}	ν_{11}	ν_{12}	ν_{13}	ν_{14}	ν_{15}	ν_{16}	ν_{17}
C_5H	**σ**	**σ**	**σ**	**σ**	**σ**	**π**	**π**	**π**	**π**								
$\tilde{X}^3\Sigma^-$	3473	1909	1790	1479	761	130i	456	396	135								
$\tilde{X}^2\Pi$	3449	2054	1952	1461	771	438/756	393/582	289/363	128/133								
$\tilde{a}^4\Sigma^-$	3453	1975	1721	1563	780	502	432	393	139								
C_6H	**σ**	**σ**	**σ**	**σ**	**σ**	**σ**	**π**	**π**	**π**	**π**	**π**						
$\tilde{X}^1\Sigma^+$	3480	2222	2142	1979	1206	641	483	550	494	264	111						
$\tilde{X}^2\Pi$	3451	2101	2132	1898	1224	650	574/701	512/554	393/466	191/245	89/107						
$\tilde{A}^2\Sigma^+$	3466	2285	2220	2114	1212	642	659	530	655	304	118						
C_7H	**σ**	**σ**	**σ**	**σ**	**σ**	**σ**	**σ**	**π**	**π**	**π**	**π**	**π**	**π**				
$\tilde{X}^3\Sigma^-$	3474	2023	1949	1769	1611	1071	564	334	488	470	387	198	81				
$\tilde{X}^2\Pi$	3453	2139	2051	1908	1581	1085	569	531/725	475/612	436/536	312/367	185/191	78/79				
$\tilde{a}^4\Sigma^-$	3455	2056	1999	1677	1628	1093	569	569	503	430	376	203	81				
C_8H	**σ**	**σ**	**σ**	**σ**	**σ**	**σ**	**σ**	**σ**	**π**	**π**	**π**	**π**	**π**	**π**	**π**		
$\tilde{X}^1\Sigma^+$	3478	2231	2200	2096	1982	1354	945	493	515	563	532	467	278	166	65		
$\tilde{X}^2\Pi$	3454	2189	2109	2044	1904	1373	959	499	604/694	543/595	508/528	399/447	248/266	145/162	62/63		
$\tilde{A}^2\Sigma^+$	3463	2279	2241	2174	2109	1346	947	491	654	619	572	493	318	178	66		
C_9H	**σ**	**σ**	**σ**	**σ**	**σ**	**σ**	**σ**	**σ**	**σ**	**π**	**π**	**π**	**π**	**π**	**π**	**π**	**π**
$\tilde{X}^3\Sigma^-$	3473	2072	2055	1945	1735	1658	1245	860	446	434	532	498	464	377	230	133	52
$\tilde{X}^2\Pi$	3454	2180	2130	2021	1850	1638	1255	869	448	583/706	563/663	485/580	438/506	322/364	218/224	126/131	49/50
$\tilde{a}^4\Sigma^-$	3457	2104	2048	2003	1735	1521	1260	869	448	600	588	498	420	348	235	134	51

All the neutral isomers considered here were found to have linear $^2\Pi$ ground-states. The calculated bond lengths in the ground state of C_5H, C_6H and C_7H are very similar to those obtained from microwave spectroscopy[36] and previous high level electronic structure calculations.[40,43] The calculations yield non-degenerate bending modes, as expected for vibrational modes of a $^2\Pi$ state subject to Renner-Teller (RT) coupling. For the neutral odd-carbon species, a linear $^4\Sigma^-$ excited state lying ~1.3 eV above the ground-state was found, similar to previous calculations on C_3H[17] and C_5H.[16] The calculated geometries for these $^4\Sigma^-$ states are similar to those of the $^3\Sigma^-$ anion state but with a shorter C_1-C_2 bond. For C_6H and C_8H, a low-lying $^2\Sigma^+$ excited state was found, in accordance with previous experimental and theoretical work.[13,40,47] The other observed or predicted excited states[18-21,23,44,47] of the linear neutral C_nH species are outside the energy range of the current study and thus were not considered theoretically here.

3.1.5 Analysis

In this section, detailed analyses and assignments of the SEVI spectral features are performed using the electronic structure calculations and FC simulations. Because of their different electronic character, leading to qualitatively different PE spectra, the odd- and even-carbon species will be considered separately. Peak assignments are shown in Table 3.1-3.5,

while experimentally determined electron affinities, term energies and vibrational frequencies are summarized in Table 3.8.

C_5H^-, C_7H^- and C_9H^-

In the C_5H^-, C_7H^- and C_9H^- SEVI spectra shown in Figures 3.1-3.3, the splittings between the bands in the upper and lower panels are very similar to the calculated splittings in Table VI between the neutral $\tilde{X}^2\Pi$ and $\tilde{a}^4\Sigma^-$states. Both states are accessible from the $C_{2n+1}H^-$ (n=2-4) $^3\Sigma^-$ ground states, which have a $[\ldots]\pi^4\pi^4\sigma^2\pi^2$ molecular orbital (MO) configuration. Removal of an electron from the highest occupied π or σ MO produces the neutral $\tilde{X}^2\Pi$ or $\tilde{a}^4\Sigma^-$state, respectively. As shown previously,[14,15,69] photodetachment from π and σ MO's often proceeds via "*s*+*d*" and "*p*" scattering, respectively. We thus assign the lower energy band of peaks to the $\tilde{X}^2\Pi$ neutral ground state and the second band to the $\tilde{a}\ ^4\Sigma^-$ first excited state, with both bands originating from the anion $\tilde{X}^3\Sigma^-$ state.

In the $\tilde{X}^2\Pi$ bands, the splitting of the vibrational origin into two closely spaced peaks, labeled A and B in Figure 3.1a-3.3a, is attributed to spin-orbit coupling in the neutral vibrational ground state, and peaks A and B are assigned as transitions to the $\Pi_{1/2}$ and $\Pi_{3/2}$ spin-orbit components of this state. In C_5H and C_7H, the doublet splittings are 25 cm^{-1} and 27 cm^{-1}, respectively. These values are in good agreement with the spin-orbit splittings of 24.22 cm^{-1} and 26.17 cm^{-1} derived from FTMW and millimeter-wavelength absorption measurements[33,34] as well as the splittings seen in the visible $\tilde{A}^2\Delta \leftarrow \tilde{X}^2\Pi$ bands of C_5H and C_7H.[23] In C_9H, peaks A and B are spaced by 30 cm^{-1}; our spectrum is the first experimental determination of the spin-orbit splitting for this species. From the eBE of peak A, we obtain a refined electron affinity (EA) of C_5H and the first experimental EA of C_7H and C_9H. These values are EA(C_5H)= 2.4225±0.0010 eV, EA(C_7H)= 2.8187±0.0010 eV and EA(C_9H)= 3.0971±0.0010 eV. The calculated EA's at the B3LYP/AVTZ level of theory, including zero-point energy corrections, are 2.56 eV, 2.95 eV and 3.25 eV for C_5H, C_7H and C_9H, respectively, as indicated in Table VI. Thus, the calculations systematically overestimate the EA of these species by around 0.15 eV.

FC simulations of the $\tilde{X}^2\Pi$ bands are shown as grey-shaded peaks in Figure 1a-3a. Only the σ vibrational modes were included in these simulations; inclusion of the bending modes would require incorporating Renner-Teller coupling into the simulations and is beyond the scope of this work. The good agreement between the simulated and experimental spectrum allows us to assign most of the observed features. In C_5H, peaks D, F, G and H are assigned to the 5_0^1, 4_0^1, 3_0^1 and 2_0^1 transitions, respectively. These four modes are all carbon backbone stretching vibrations. Peak I is assigned to the 1_0^1 transition in which the C-H stretching mode is excited. In C_7H, peak D is assigned to the 7_0^1 transition while peaks F and G are assigned to the $\Pi_{1/2}$ and $\Pi_{3/2}$ spin-orbit components of the 4_0^1 transition, respectively. Similarly, in C_9H, peaks I and J are assigned to the $\Pi_{1/2}$ and $\Pi_{3/2}$ spin-orbit components of the

5_0^1 transition, respectively. All of these modes are also carbon backbone stretching vibrations and their vibrational frequencies agree well with the calculated values.

Several smaller peaks are not reproduced by the FC simulations and are thus assigned to transitions involving bending modes. While the definitive assignments of these features would require a fuller understanding of RT coupling in these species, some tentative assignments can be made on the basis of the calculated harmonic bending vibration frequencies shown in Table 3.7. In C_5H and C_7H, the most likely active bending vibrations are the CCH bending modes (ν_6 and ν_8, respectively) because of the large changes in frequency between the anion and the neutral. This change in frequency would give rise to v_0^2 transitions as well as v_1^1 sequence bands located at higher eBE than the origin transition. For C_5H, peaks C and E could arise from the 6_1^1 and 6_0^2 transitions, while peaks C and E in the C_7H^- spectrum could be the 8_1^1 and 8_0^2 transitions, These assignments yield ν_6 frequencies (ignoring anharmonicities and RT effects) of398 and 710 cm^{-1} in C_5H^- and C_5H, respectively, and ν_8 frequencies of 298 and 521 cm^{-1} for anionic and neutral C_7H. While these values are within range of our calculated frequencies in Table VII, evaluation of these assignments and frequencies is difficult because the calculated bend frequencies in the neutral are non-degenerate, the experimental levels have unknown RT splittings, and the calculation for C_5H^- yields an imaginary ν_6 frequency at the linear geometry.

The situation is different in the $\tilde{X}^2\Pi$ band of C_9H, where all the weaker transitions that are not reproduced by the FC simulations have a different PAD than the main spectral features (peaks A, B, I, and J). While these weaker features could originate from a different C_9H isomer, the lowest lying isomers of C_9H^- are calculated to lie more than 0.84 eV above the linear isomer and thus are unlikely to contribute to the spectrum. These features are more likely to be nominally forbidden transitions to the $\tilde{X}^2\Pi$ state, such as bending vibrations with odd $\Delta\nu$, which gain intensity through vibronic coupling. In this case, those vibronically allowed transitions normally have the same PAD as the transitions to the electronic state from which intensity is borrowed.[14,70] The closest electronic state which can couple via bending modes with the $\tilde{X}^2\Pi$ state is the $\tilde{A}\ ^2\Delta$ state. This state is expected to lie 1.88 eV above the ground state based on electronic structure calculations and extrapolations of the corresponding $\tilde{A}^2\Delta \leftarrow \tilde{X}^2\Pi$ transitions in C_5H and C_7H.[23] This term energy is 0.45 eV and 0.21 eV higher in C_5H and C_7H, respectively, providing a possible explanation as to why vibronic coupling effects appear stronger in C_9H than in the shorter chain species.

We next consider the $\tilde{a}^4\Sigma^-$ bands in Figures 3.1b-3.3b. The dominant peak in each panel, labeled J in the C_5H^- and C_7H^- spectra and N in the C_9H^- spectrum, is assigned to the 0_0^0 transition. The term energies of the $\tilde{a}^4\Sigma^-$ states of C_5H, C_7H and C_9H are thus determined to be 1.3095±0.0010 eV, 1.2690±0.0010 eV and 1.2279±0.0010 eV, respectively. These values are in excellent agreement with our calculations that predicted $\tilde{a}^4\Sigma^-$ term energies of 1.35 eV, 1.31 eV and 1.27 eV for these species. FC simulations, shown in shaded gray in

Figure 3.1b-3.3b, result in assignments of all the remaining features in the $\tilde{a}^4\Sigma^-$bands of C_5H and C_7H.

In the C_5H^- spectrum, peaks K and L can be reproduced in the FC simulation by assigning them to the 6_1^1 and 6_0^2 transitions, respectively, by assigning a frequency of 208 cm^{-1} for the corresponding anion bending mode, and by setting the anion vibrational temperature to 150 K. This assignment of peak L yields a value of 499 cm^{-1} for the ν_6 fundamental of the $\tilde{a}^4\Sigma^-$ state, close to our calculated value of 502 cm^{-1} (Table 3.6). The low ν_6 anion frequency implied by this assignment is consistent with the very shallow CCH bending potential of C_5H^- inferred from our calculations. This anion frequency is preferable to that inferred from our assignment of peak C in the $\tilde{X}^2\Pi$ band, given the absence of RT splittings in the $\tilde{a}^4\Sigma^-$ band.

Similar CCH bending activity is found in the SEVI spectrum of C_7H^- where peaks K and N are assigned to the 8_1^1 and 8_0^2 transitions, respectively. These assignments of peak yield 356 cm^{-1} and 572 cm^{-1} for the anion and neutral ν_8 fundamentals (CCH bend), both of which are in reasonable agreement with calculated values in Table 3.7. The remaining peaks in the C_7H^- spectrum, labeled L, M, O and P, are assigned to the 7_0^1, 6_0^1, 4_0^1 and 3_0^1 transitions, respectively. These modes are all stretching vibrations of the carbon backbone and their frequencies are in good agreement with the calculated values.

Table 3.8 Experimentally determined electron affinities (eV), term energies (eV) and vibrational frequencies for the $C_{5\text{-}9}H$ species. Uncertainty is ±0.0010 eV for the energies and ±8 cm^{-1} for the vibrational frequencies.

Specie	State	Energy	ν_1	ν_2	ν_3	ν_4	ν_5	ν_6	ν_7	ν_8
C_5H	$\tilde{X}^3\Sigma^-$							208		
	$\tilde{X}^2\Pi$	EA=2.4225	3462	1975	1882	1508	820			
	$\tilde{a}^4\Sigma^-$	T_0= 1.3095						498		
C_6H	$\tilde{X}^2\Pi$	EA=3.8090								
	$\tilde{A}^2\Sigma^+$	T_0=0.1751		2260				651		
C_7H	$\tilde{X}^3\Sigma^-$									356
	$\tilde{X}^2\Pi$	EA=2.8187				1815			510	
	$\tilde{a}^4\Sigma^-$	T_0= 1.2690			1894	1603		1011	537	536
C_8H	$\tilde{X}^2\Pi$	EA=3.9701								
	$\tilde{A}^2\Sigma^+$	T_0=0.2619					1697			
C_9H	$\tilde{X}^2\Pi$	EA=3.0971					1755			
	$\tilde{a}^4\Sigma^-$	T_0= 1.2279								

C_6H^- and C_8H^-

In the C_6H^- and C_8H^- SEVI spectra shown in Figures 3.4 and 3.5, the lower energy band is assigned to the $\tilde{X}^2\Pi$ neutral ground state and the second band to the $\tilde{A}^2\Sigma^+$ first excited state. Both states are accessible from the C_6H^- and C_8H^- $\tilde{X}^1\Sigma^+$ ground states, which have a $[\ldots]\pi^4\pi^4\sigma^2\pi^4$ MO configuration. Removal of an electron from the highest occupied π or σ MO produces the neutral $\tilde{X}^2\Pi$ or $\tilde{A}^2\Sigma^+$ state, respectively. As discussed earlier, photodetachment from π and σ MO's often proceeds via "*s*+*d*" and "*p*" scattering, respectively, consistent with the observed PADs.

In the $\tilde{X}^2\Pi$ bands, the two closely spaced peaks, labeled A and B in Figure 3.4a-3.5a, are assigned as transitions to the $\Pi_{3/2}$ and $\Pi_{1/2}$ spin-orbit components, respectively, of the vibrational ground state. The splittings between those two peaks are 15 cm^{-1} and 21 cm^{-1}, in good agreement with the spin-orbit splittings of -15.11 cm^{-1} and -19.33 cm^{-1} derived from FTMW and millimeter wavelength absorption measurements[33,34] on C_6H and C_8H, respectively. From the eBE of the peaks labeled A, we obtain refined EA's for these two species: EA(C_6H)= 3.8090±0.0010 eV and EA(C_8H)= 3.9701±0.0010 eV. These values are within the uncertainties of those previously determined by Taylor *et al.*[13] They are also close to the calculated EA's, at the B3LYP/AVTZ level, of 3.64 eV and 3.79 eV for C_6H and C_8H, respectively.

The dominant peaks E and D in Figure 3.4b and 3.5b, respectively, are assigned to the 0_0^0 transitions of the $\tilde{A}^2\Sigma^+$ state. The term energies of the first excited state are thus determined to be 0.1751±0.0010 eV and 0.2619±0.0010 eV, for C_6H and C_8H respectively. These values are within the uncertainties of the term energies reported by Taylor *et al.*[13] They are smaller than our calculated term energies of 0.60 eV and 0.71 eV for these species. However, the C_6H $\tilde{A}^2\Sigma^+$ state experimental term energy is in good agreement with the vertical transition energy of 0.22 eV calculated by Cao and Peyerimhoff.[47]

The C_6H^- and C_8H^- SEVI spectra display little vibrational activity. Some vibrational transitions can be assigned with the FC simulations, the results of which are shown in shaded gray in Figures 3.4 and 3.5. In the $\tilde{A}^2\Sigma^+$ band of C_6H, peaks F and G are assigned to the 6_0^1 and 2_0^1 transitions, respectively. In the $\tilde{X}^2\Pi$ band of C_8H, peak C is assigned to the 5_0^1 transition. Peaks C and D in the $\tilde{X}^2\Pi$ band of C_6H are not reproduced by the FC simulations and are thus assigned to bending vibrational modes. Again, the definitive assignment of these features would require a fuller understanding of the RT coupling in C_6H. Peak C and D are shifted by only 106 cm^{-1} and 215 cm^{-1} from the origin. These positions roughly correspond to the calculated frequencies of the ν_{10} and ν_{11} modes. However, transitions to non-totally symmetric modes with odd $\Delta\nu$ are nominally forbidden, even in the presence of RT coupling. These peaks could be the 11_0^2 and 10_0^2 transitions; such an assignment would imply that the

ν_{11} and ν_{12} frequencies are much smaller than the calculated values or that the RT coupling for these modes is very strong.

Another possibility is that peaks C and D are Δv=1 bending transitions that gain intensity through vibronic coupling with the nearby $\tilde{A}^2\Sigma^+$ state, similar to what was observed in the SEVI spectra[14,15] of C_2H^- and C_4H^-. Usually, we would expect these features to have "*p*" PADs, similar to the features associated with the $\tilde{A}^2\Sigma^+$ state,[14] and not the observed "*s*+*d*" PADs. However, in the SEVI spectrum of C_4H^-, features were assigned to vibronically allowed Δv=1 bending transitions even though the PADs were the same as for nearby, fully allowed transitions.[15]

3.1.6 Discussion

This study addresses the key issue of the structure of C_nH^- anions with an odd number of carbon atoms. Previous DFT studies on C_5H^-, $C_7H^-$and C_9H^- have reported bent geometries for the triplet ground state of the isomer comprising a single carbon chain terminated by a hydrogen.[16,46,53,68] In contrast, the electronic structure calculations presented here predict a quasilinear geometry for C_5H^- and linear geometries for $C_7H^-$and C_9H^-. The FC simulations involving transitions from these calculated linear $^3\Sigma^-$ anion ground electronic states to the $\tilde{X}^2\Pi$ and $\tilde{a}^4\Sigma^-$ neutral states were found to be in excellent agreement with the well-resolved features of the SEVI spectra. The $\tilde{X}^2\Pi$ states of C_5H, C_7H and C_9H, which can be unambiguously identified from the resolved spin-orbit splitting, are known to be linear from FTMW spectroscopy.[33,36] The observed small vibrational activity in the $\tilde{X}^2\Pi$ band is therefore consistent with linear-to-linear transitions. If the anion had a bent geometry, extensive bending progressions would be expected.[71] We thus conclude that the triplet ground states of the C_5H^-, $C_7H^-$and C_9H^- anions are linear, in accordance with our electronic structure calculations.

Another issue addressed here is the energy ordering of the various isomers of the odd-carbon anion species. For C_5H^-, a theoretical study by Blanksby *et al.*[46] found two isomers to be more stable than the single chain with terminal hydrogen (*l*-C_5H^-) discussed here. One isomer has a hydrogen located on the middle of a single carbon chain ($C_2[CH]C_2^-$, $^1A_1$), and the other a branched three-membered ring with the hydrogen located on the ring ([*c*-$C_3H]C_2^-$, $^1A'$); they were found to be 0.15 eV and 0.12 eV below *l*-C_5H^-, respectively. A third isomer, consisting of a branched three-membered ring with the hydrogen located at the end of the branch ([*c*-C_3]C_2H^-, $^1A_1$), was found lie 0.13 eV above *l*-C_5H^-. A recent PE study of C_5H^- invoked the presence of both *l*-C_5H^- and [*c*-C_3]C_2H^- isomers in order to assign all the observed spectral features. Based on their electron affinities and the calculated energetics of the neutral C_5H isomers,[43] the [*c*-C_3]C_2H^- isomer was assigned to lie 0.16 eV below the *l*-C_5H^- isomer.

The electronic structure calculations and the C_5H^- SEVI spectra presented here point toward a somewhat different conclusion. First, the B3LYP/AVTZ calculations predict that *l*-C_5H^- is the most stable isomer by 0.29 eV. Secondly, only the *l*-C_5H^- isomer was necessary to assign the all the observed spectral features in the C_5H^- SEVI spectra. The main difference between the analysis of the current SEVI spectra and the previous PE spectra comes from the linear $^3\Sigma^-$ *l*-C_5H^- anion geometry used in the FC simulations instead of the bent ^{3}A' geometry. The large vibrational activity expected for a bent-to-linear transition was not compatible with some of the observed features in the PE spectrum and these were thus assigned to a cyclic isomer. Since the current study used short chain precursors (acetylene and propyne) that would not have hindered the formation of the various isomers, we conclude that the *l*-C_5H^- ($^3\Sigma^-$) isomer is the lowest energy structure on the C_5H^- potential energy surface. Similar conclusions can be reached for the *l*-C_7H^- ($^3\Sigma^-$) and *l*-C_9H^- ($^3\Sigma^-$) isomers on the same basis of the present DFT calculations and the analysis of the C_7H^- and C_9H^- SEVI spectra.

Our SEVI spectra also probe vibronic coupling in the carbon monohydrides. In C_2H, the small 3600 cm^{-1} spacing between the $\tilde{X}^2\Sigma^+$ and $\tilde{A}^2\Pi$ states results in strong pseudo-Jahn-Teller coupling that is well-documented and understood.[14] For C_4H, the $\tilde{X}^2\Sigma^+$ state lies only 213 cm^{-1} below the $\tilde{A}^2\Pi$ state which presumably yields even larger perturbations of the vibronic levels,[15] but these effects have not been theoretically addressed yet. For the larger even-carbon species studied here, the ordering of the two states is reversed and the splittings are 1492 cm^{-1} and 2112 cm^{-1} for C_6H and C_8H, respectively. While the appearance of peaks C and D in the C_6H^- SEVI spectra might be an indication of vibronic coupling, depending on their assignments, no indication of vibronic coupling is found in the C_8H spectra. This suggests that the amplitude of pseudo-Jahn-Teller coupling between the low-lying $^2\Sigma^+$ and $^2\Pi$ states of the even-carbon is small in C_6H and even smaller in the longer chains. The situation is reversed in the odd-carbon species; evidence of vibronic coupling is found in the SEVI spectra of C_9H^- but not in the spectra of the smaller chain species. If this coupling occurs between the $\tilde{X}^2\Pi$ and the $\tilde{A}^2\Delta$ states, as proposed above, vibronic coupling could be increasingly important for the longer-chain odd-carbon species because the $\tilde{X}^2\Pi - \tilde{A}^2\Delta$ splitting decreases with chain-length.[23]

3.1.7 Conclusions

High-resolution photoelectron spectra of the $C_{5\text{-}9}H^-$ species acquired with SEVI are reported. The spectra of C_5H^-, C_7H^-, and C_9H^- show well resolved transitions to the $\tilde{X}^2\Pi$ and $\tilde{a}^4\Sigma^-$ neutral states. For C_6H^- and C_8H^-, transitions to the $\tilde{X}^2\Pi$ and $\tilde{A}^2\Sigma^+$ neutral states are observed. Most of the observed spectral features are assigned with the help of electronic structure calculations and FC simulations. Precise electron affinities and term energies are determined and several gas-phase vibrational frequencies are determined for the first time. For the odd-carbon species, the observed spectral features and electronic structure

calculations are consistent with linear $\widetilde{X}^3\Sigma^-$ ground states for the anions, with no other isomers contributing to the spectra.

References:

1) J. H. Kiefer, S. S. Sidhu, R. D. Kern, K. Xie, H. Chen, and L. B. Harding, *Combust. Sci. Tech.* **82** (1-6), 101 (1992).
2) E. B. Jochnowitz and J. P. Maier, *Mol. Phys.* **106** (16-18), 2093 (2008).
3) L. M. Ziurys, *PNAS* **103** (33), 12274 (2006).
4) X. B. Gu, Y. Guo, F. T. Zhang, A. M. Mebel, and R. I. Kaiser, *Faraday Disc.* **133**, 245 (2006).
5) R. I. Kaiser, C. Ochsenfeld, D. Stranges, M. Head-Gordon, and Y. T. Lee, *Faraday Disc.* **109**, 183 (1998).
6) M. C. McCarthy, C. A. Gottlieb, H. Gupta, and P. Thaddeus, *Astrophys. J.* **652** (2), L141 (2006).
7) S. Brunken, H. Gupta, C. A. Gottlieb, M. C. McCarthy, and P. Thaddeus, *Astrophys. J.* **664** (1), L43 (2007).
8) J. Cernicharo, M. Guelin, M. Agundez, K. Kawaguchi, M. McCarthy, and P. Thaddeus, *Astron. Astrophys.* **467** (2), L37 (2007).
9) Y. Kasai, E. Kagi, and K. Kawaguchi, *Astrophys. J.* **661** (1), L61 (2007).
10) A. J. Remijan, J. M. Hollis, F. J. Lovas, M. A. Cordiner, T. J. Millar, A. J. Markwick-Kemper, and P. R. Jewell, *Astrophys. J.* **664** (1), L47 (2007).
11) N. Sakai, T. Sakai, Y. Osamura, and S. Yamamoto, *Astrophys. J.* **667** (1), L65 (2007).
12) E. Herbst and Y. Osamura, *Astrophys. J.* **679** (2), 1670 (2008).
13) T. R. Taylor, C. S. Xu, and D. M. Neumark, *J. Chem. Phys.* **108** (24), 10018 (1998).
14) J. Zhou, E. Garand, and D. M. Neumark, *J. Chem. Phys.* **127**, 114313 (2007).
15) J. Zhou, E. Garand, and D. M. Neumark, *J. Chem. Phys.* **127**, 154320 (2007).
16) S. M. Sheehan, B. F. Parsons, T. A. Yen, M. R. Furlanetto, and D. M. Neumark, *J. Chem. Phys.* **128** (17), 174301 (2008).
17) S. M. Sheehan, B. F. Parsons, J. Zhou, E. Garand, T. A. Yen, D. T. Moore, and D. M. Neumark, *J. Chem. Phys.* **128** (3), 034301 (2008).
18) P. Freivogel, J. Fulara, M. Jakobi, D. Forney, and J. P. Maier, *J. Chem. Phys.* **103** (1), 54 (1995).
19) M. Kotterer and J. P. Maier, *Chem. Phys. Lett.* **266** (3-4), 342 (1997).
20) H. Linnartz, T. Motylewski, and J. P. Maier, *J. Chem. Phys.* **109** (10), 3819 (1998).

21) H. Linnartz, T. Motylewski, O. Vaizert, J. P. Maier, A. J. Apponi, M. C. McCarthy, C. A. Gottlieb, and P. Thaddeus, *J. Mol. Spectrosc.* **197** (1), 1 (1999).

22) H. Ding, T. Pino, F. Guthe, and J. P. Maier, *J. Chem. Phys.* **115** (15), 6913 (2001).

23) H. Ding, T. Pino, F. Guthe, and J. P. Maier, *J. Chem. Phys.* **117** (18), 8362 (2002).

24) J. Fulara, D. Lessen, P. Freivogel, and J. P. Maier, *Nature* **366** (6454), 439 (1993).

25) M. Grutter, M. Wyss, and J. P. Maier, *J. Chem. Phys.* **110** (3), 1492 (1999).

26) M. Tulej, F. Guthe, M. Schnaiter, M. V. Pachkov, D. A. Kirkwood, J. P. Maier, and G. Fischer, *J. Phys. Chem. A* **103** (48), 9712 (1999).

27) T. Pino, M. Tulej, F. Guthe, M. Pachkov, and J. P. Maier, *J. Chem. Phys.* **116** (14), 6126 (2002).

28) C. A. Gottlieb, E. W. Gottlieb, and P. Thaddeus, *Astron. Astrophys.* **164** (1), L5 (1986).

29) J. C. Pearson, C. A. Gottlieb, D. R. Woodward, and P. Thaddeus, *Astron. Astrophys.* **189** (1-2), L13 (1988).

30) M. C. McCarthy, M. J. Travers, P. Kalmus, C. A. Gottlieb, and P. Thaddeus, *Astrophys. J.* **467** (2), L125 (1996).

31) M. C. McCarthy, M. J. Travers, A. Kovacs, C. A. Gottlieb, and P. Thaddeus, *Astron. Astrophys.* **309** (2), L31 (1996).

32) M. J. Travers, M. C. McCarthy, C. A. Gottlieb, and P. Thaddeus, *Astrophys. J.* **465** (1), L77 (1996).

33) M. C. McCarthy, M. J. Travers, A. Kovacs, C. A. Gottlieb, and P. Thaddeus, *Astrophysical Journal Supplement Series* **113** (1), 105 (1997).

34) M. C. McCarthy, W. Chen, A. J. Apponi, C. A. Gottlieb, and P. Thaddeus, *Astrophys. J.* **520** (1), 158 (1999).

35) A. J. Apponi, M. E. Sanz, C. A. Gottlieb, M. C. McCarthy, and P. Thaddeus, *Astrophys. J.* **547** (1), L65 (2001).

36) M. C. McCarthy and P. Thaddeus, *J. Chem. Phys.* **122** (17) (2005).

37) H. Gupta, S. Brunken, F. Tamassia, C. A. Gottlieb, M. C. McCarthy, and P. Thaddeus, *Astrophys. J.* **655** (1), L57 (2007).

38) C. Barckholtz, T. P. Snow, and V. M. Bierbaum, *Astrophys. J.* **547** (2), L171 (2001).

39) Y. Shi and K. M. Ervin, *J. Phys. Chem. A* **112** (6), 1261 (2008).

40) D. E. Woon, *Chem. Phys. Lett.* **244** (1-2), 45 (1995).

41) A. L. Sobolewski and L. Adamowicz, *J. Chem. Phys.* **102** (1), 394 (1995).

42) S. Dua, J. C. Sheldon, and J. H. Bowie, *J. Chem. Soc.-Chem. Comm.* (10), 1067 (1995).

43) T. D. Crawford, J. F. Stanton, J. C. Saeh, and H. F. Schaefer, *J. Am. Chem. Soc.* **121** (9), 1902 (1999).

44) J. Haubrich, M. Muhlhauser, and S. D. Peyerimhoff, *J. Phys. Chem. A* **106** (35), 8201 (2002).

45) L. Pan, B. K. Rao, A. K. Gupta, G. P. Das, and P. Ayyub, *J. Chem. Phys.* **119** (15), 7705 (2003).

46) S. J. Blanksby, S. Dua, and J. H. Bowie, *J. Phys. Chem. A* **103** (26), 5161 (1999).

47) Z. X. Cao and S. D. Peyerimhoff, *Phys. Chem. Chem. Phys.* **3** (8), 1403 (2001).

48) P. Botschwina and R. Oswald, *Int. J. Mass. Spectrom.* **277** (1-3), 180 (2008).

49) P. Botschwina, R. Oswald, G. Knizia, and H. J. Werner, *Z. Phys. Chem.* **223** (4-5), 447 (2009).

50) F. Pichierri, *J. Phys. Chem. A* **112** (33), 7717 (2008).

51) M. L. Senent and M. Hochlaf, *Astrophys. J.* **708** (2), 1452 (2010).

52) C. Ochsenfeld, R. I. Kaiser, Y. T. Lee, A. G. Suits, and M. HeadGordon, *J. Chem. Phys.* **106** (10), 4141 (1997).

53) S. Dua, J. H. Bowie, and S. J. Blanksby, *European Mass Spectrometry* **5** (5), 309 (1999).

54) R. F. Curl, P. G. Carrick, and A. J. Merer, *J. Chem. Phys.* **82** (8), 3479 (1985).

55) K. M. Ervin and W. C. Lineberger, *J. Phys. Chem.* **95** (3), 1167 (1991).

56) D. M. Neumark, *J. Phys. Chem. A* **112**, 13287 (2008).

57) U. Even, J. Jortner, D. Noy, N. Lavie, and C. Cossart-Magos, *J. Chem. Phys.* **112** (18), 8068 (2000).

58) J. C. Rienstra-Kiracofe, G. S. Tschumper, H. F. Schaefer, S. Nandi, and G. B. Ellison, *Chem. Rev.* **102** (1), 231 (2002).

59) E. P. Wigner, *Phys. Rev.* **73** (9), 1002 (1948).

60) C. T. Lee, W. T. Yang, and R. G. Parr, *Phys. Rev. B* **37** (2), 785 (1988).

61) A. D. Becke, *J. Chem. Phys.* **98** (2), 1372 (1993).

62) T. H. Dunning, *J. Chem. Phys.* **90** (2), 1007 (1989).

63) M. J. Frisch, G. W. Trucks, H. B. Schlegel*et al.*, Gaussian 03, Revision C.02 (Gaussian, Inc, Wallingford, CT, 2004).

64) K. M. Erwin, FCFgauss03: Gaussian 03 output conversion program (2004).

65) K. M. Erwin, PESCAL, Fortran program (2008).

66) P. Chen, in *Unimolecular and Bimolecular Reaction Dynamics*, edited by T. Baer, C.-Y. Ng, and I. Powis (John Wiley & Sons, Chichester, 1994), pp. 371.

67) F. Duschinsky, *Acta Physiochem. URSS* **7** (4), 551 (1937).

68) S. J. Blanksby, A. M. McAnoy, S. Dua, and J. H. Bowie, *Mon. Not. R. Astron. Soc.* **328** (1), 89 (2001).

69) E. Garand, T. I. Yacovitch, and D. M. Neumark, *J. Chem. Phys.* **130** (6), 064304 (2009).

70) E. Garand, T. I. Yacovitch, and D. M. Neumark, *J. Chem. Phys.* **129** (7), 074312 (2008).

71) E. Garand, T. I. Yacovitch, and D. M. Neumark, *J. Chem. Phys.* **131** (5) (2009).

3.2 Slow photoelectron velocity-map imaging spectroscopy of $C_{2n}N^-$ (n=1-3) anions

Abstract

High-resolution photoelectron spectra of C_2N^-, C_4N^- and C_6N^- anions are reported, obtained using slow electron velocity-map imaging. The spectra show well resolved transitions to the $\tilde{X}\ ^2\Pi$ neutral ground state of all three species and to the $\tilde{a}^4\Sigma^-$ excited state of C_2N and C_4N. This study yields the adiabatic electron affinity of C_2N, C_4N, and C_6N, the spin-orbit splitting in the $\tilde{X}\ ^2\Pi$ state of each radical, and the term energy of the $\tilde{a}^4\Sigma^-$ state in C_2N and C_4N. Relatively little vibrational activity is observed, indicating small geometry changes upon photodetachment. This result, plus the observation of transitions to neutral quartet states, indicates that the $C_{2n}N^-$ (n=1-3) anions all have linear $^3\Sigma^-$ ground states.

3.2.1 Introduction

The nitrogen-doped carbon chains (C_nN) are important interstellar constituents. The three smallest members of the series with odd numbers of carbon atoms, CN, C_3N and C_5N, have been detected[1-4] in the interstellar medium. Recently, the C_3N^- anion has also been detected[5] in the circumstellar envelope of the evolved carbon star IRC + 10216. In contrast, none of the members of the $C_{2n}N$ series have yet been detected in interstellar sources even though these species are predicted to play a role in the interstellar chemistry.[6,7] Their detection by means of radio astronomy is greatly hindered by their small dipole moments.[8] With the exception of C_2N, experimental information on the $C_{2n}N$ species is relatively sparse. In this chapter, high-resolution photoelectron spectra of the C_2N^-, C_4N^- and C_6N^-anions are reported that provide a detailed probe of these anions and the corresponding neutral species.

The C_2N radical has been the subject of numerous experimental and theoretical studies since its first identification by Merer and Travis[9] in 1965, many of which have focused on the strong Renner-Teller (RT) interaction in its $\tilde{X}^2\Pi$ ground state. C_2N has been investigated by UV and IR absorption,[9-15] laser-induced fluorescence (LIF)[16-19], Fourier-transform emission spectroscopy,[20] microwave spectroscopy[21] and laser magnetic resonance spectroscopy.[22] Gabriel *et al.*[23] calculated the RT perturbed rovibronic levels in its $\tilde{X}^2\Pi$ state using variational methods. Excited state molecular orbital configurations, geometries and vibrational frequencies were computed by Chandra[24] at the complete active space SCF (CASSCF) level. The C_4N and C_6N radicals have been studied experimentally by microwave spectroscopy[25] and theoretically using density functional theory (DFT).[26-28]

The only experimental information on $C_{2n}N^-$ anions comes from mass spectrometry studies in which the anions were produced by laser ablation[29,30] or sputtering.[31] Both experiments yielded strong even-odd alternations with the $C_{2n}N^-$ ions being considerably less intense than the $C_{2n+1}N^-$ ions. Second-order Møller-Plesset (MP2) calculations by Zhan and Iwata[32] found singlet ground states for $C_{2n}N^-$ (n=1-3) with C_4N^- and C_6N^- having strongly bent geometries. However, a subsequent DFT study by Pascoli and Lavendy[33] yielded linear triplet ground states and low-lying singlet excited states for these same anions.

Here we report photoelectron (PE) spectra of C_2N^-, C_4N^- and C_6N^-anions obtained with slow electron velocity-map imaging (SEVI). The high resolution afforded by SEVI shows well resolved transitions to the $\tilde{X}^2\Pi$ neutral ground state of all three species and to the $\tilde{a}^4\Sigma^-$ excited state of C_2N and C_4N. These transitions are assigned with the help of electronic structure calculations. We obtain accurate electron affinities for all three radicals and term energies for the $\tilde{a}^4\Sigma^-$ states in C_2N and C_4N. The observation of relatively little vibrational activity and transitions to neutral quartet states indicates that the $C_{2n}N^-$ (n=1-3) anions have linear $^3\Sigma^-$ ground states.

3.2.2 Experimental details

The SEVI technique and apparatus has been described in detail in chapter 2. C_2N^- anions were produced from of a gas mixture comprising 0.005% of acetonitrile (CH_3CN) in argon while C_4N^- and C_6N^- anions were produced from a mixture of 0.05% acetylene and 2% N_2O in a balance of argon. The gas mixture, at a stagnation pressure of 300 psi, was expanded into the source vacuum chamber and anions were formed using the grid discharge source.

The apparatus was calibrated by acquiring SEVI images of atomic S^- and Cl^- at several different photon energies. With the 350V VMI repeller voltage used in this study, the full widths at half maximum of the chloride peaks were 3.3 cm^{-1} at 24 cm^{-1} above threshold.

3.2.3 Experimental results

SEVI spectra of C_2N^-, C_4N^- and C_6N^- are presented in Figures 3.6-3.8. The peak positions, PADs, and assignments are summarized in Table 3.9-3.11. The spectra all display very similar features and are divided into two bands of peaks, separated by about 1 eV, with different PADs. The maximum eBE for each trace corresponds to the photon energy used in collecting the spectrum. Spectra taken at higher photon energy (upper traces in Figures 3.7a and 3.8) probe a wider energy window but yield poorer resolution for the features at lower eBE (i.e. faster electrons).

The traces in Figures 3.6a, 3.7a, and 3.8 are dominated by two peaks, A and B, with spacings varying from 29 cm^{-1} to 38 cm^{-1}. All three spectra show two or three small peaks (a, b, c) at slightly lower eBE than peaks A and B. The C_2N^- spectrum shows a smaller peak C lying at 456 cm^{-1} higher eBE than peaks A and B, while the C_4N^- and C_6N^- spectra show two smaller peaks, C and D, at higher eBE. All peaks in these three panels have "*s+d*" PADs.

Figures 3.6b and 3.7b show transitions to a higher energy band comprising a large peak E and a much smaller peak F. The spacings between peaks A and E are 8413 cm^{-1} for C_2N^- and 9256 cm^{-1} for C_4N^-. All features in Figures 3.6b and 3.7b have "*p*" PADs, suggesting that they arise from photodetachment from a different molecular orbital than the peaks in Figures 3.6a, 3.7a, and 3.8.

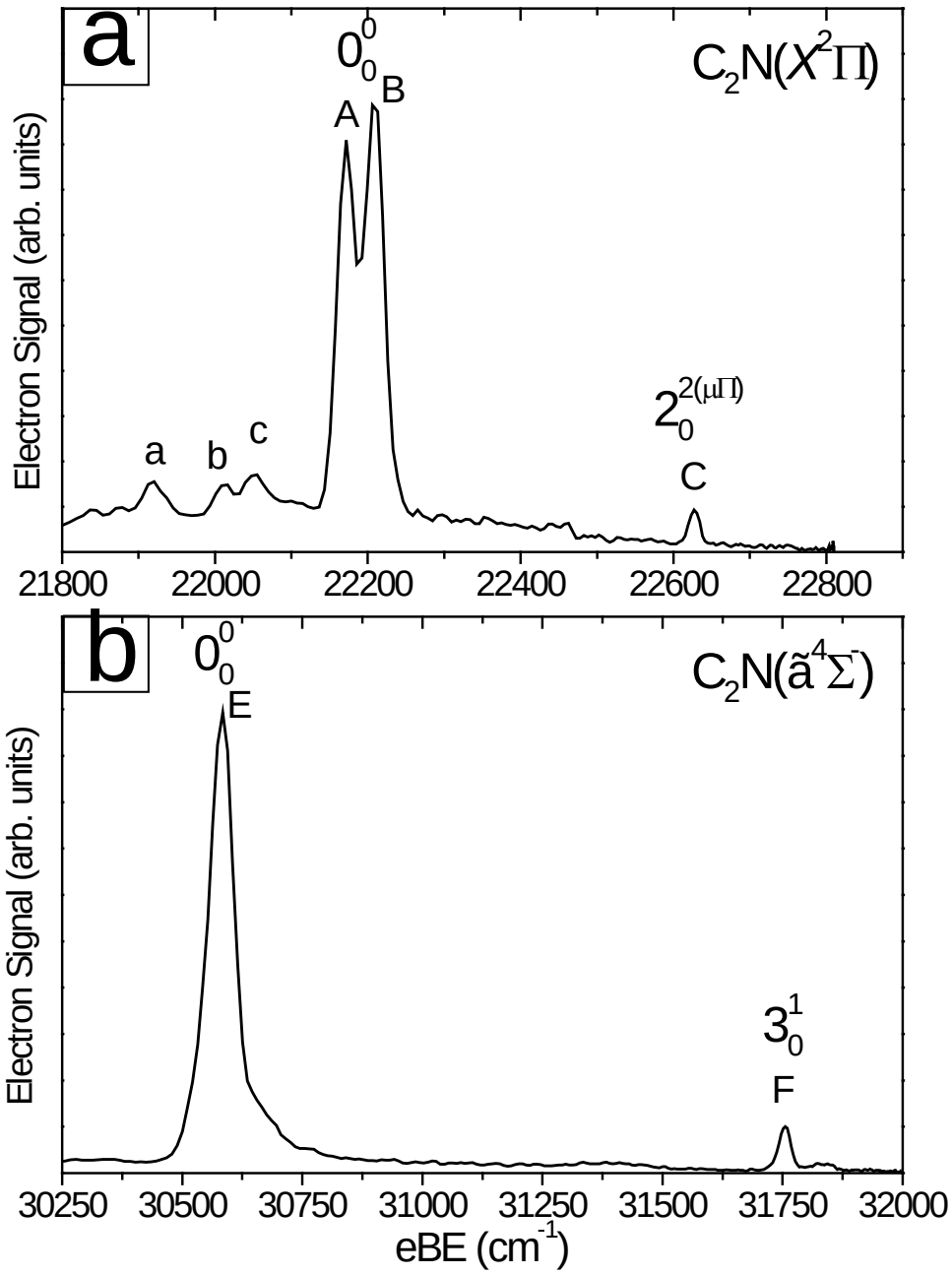

Figure 3.6 SEVI spectra of C_2N^- covering the electron binding energy ranges of 21800 cm^{-1} to 22900 cm^{-1} (panel a) and 30250 to 32000 cm^{-1} (panel b).

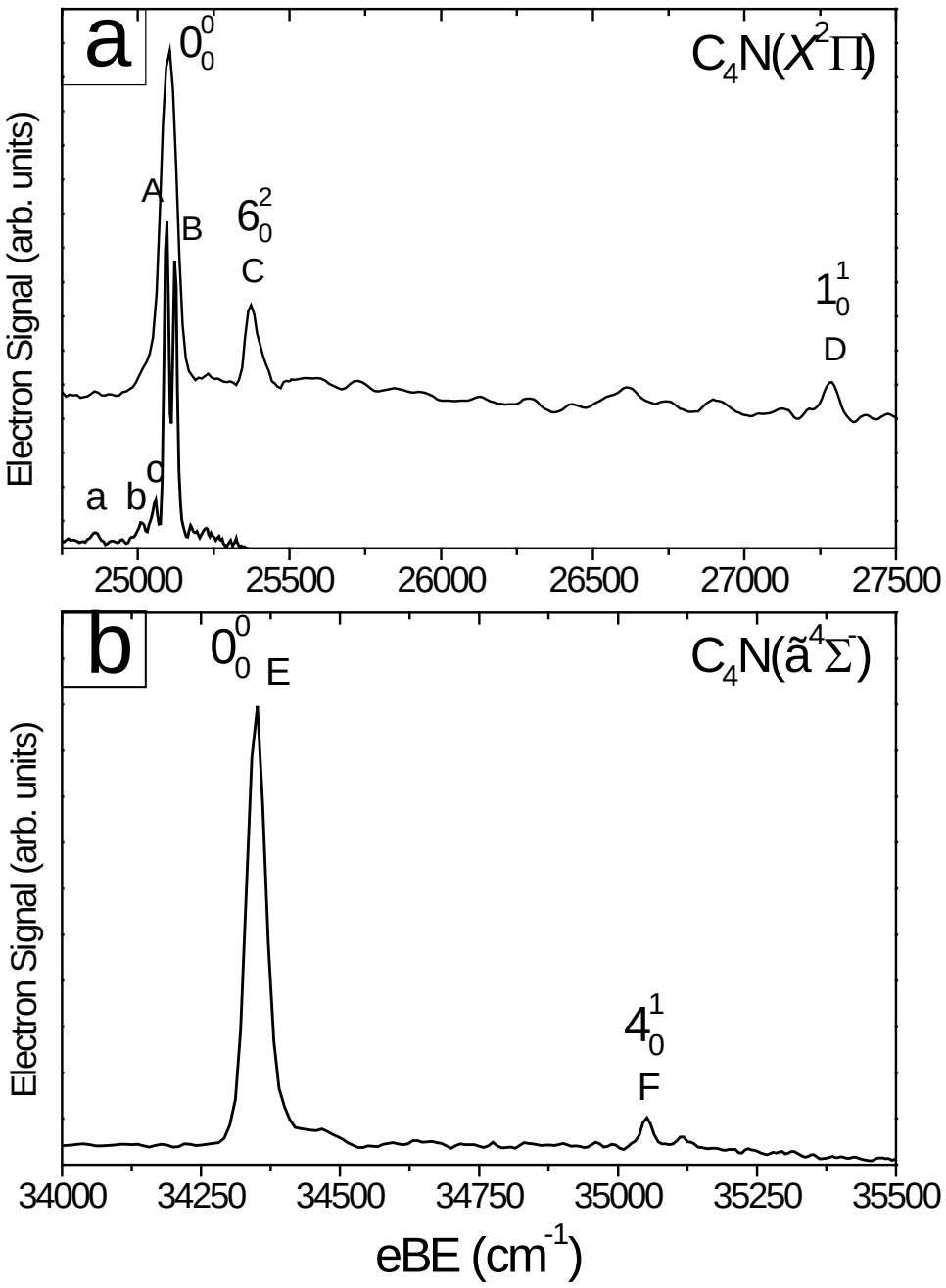

Figure 3.7 SEVI spectra of C_4N^- covering the electron binding energy ranges of 24750 cm^{-1} to 26000 cm^{-1} (panel a) and 34000 to 35500 cm^{-1} (panel b).

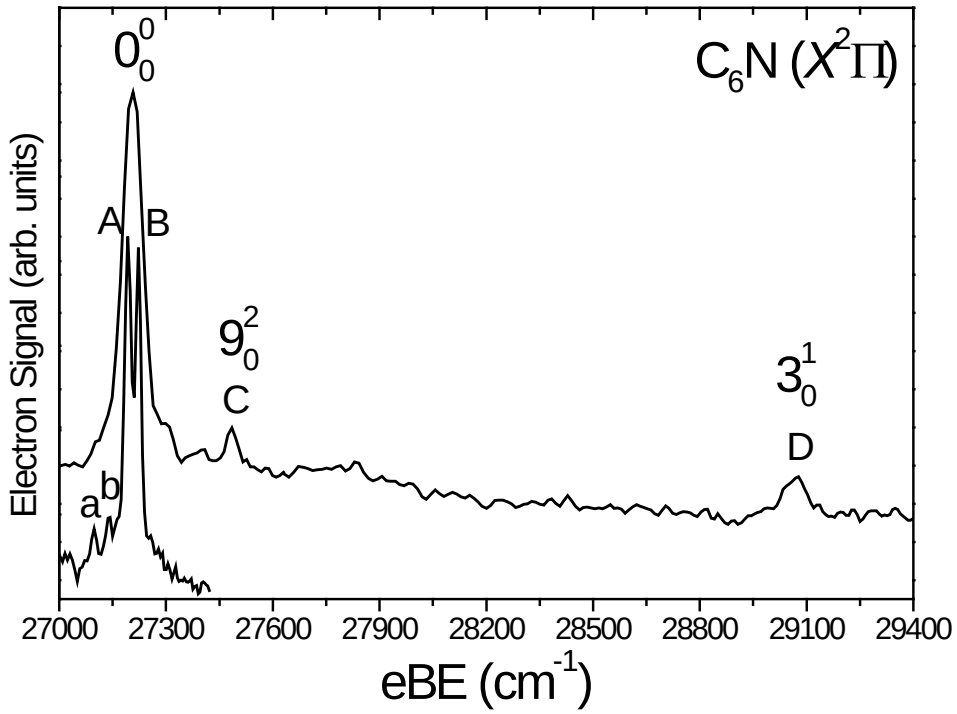

Figure 3.8 SEVI spectra of C_6N^- covering the electron binding energy range of 27000 cm^{-1} to 29400 cm^{-1}.

Table 3.9 Peak positions, angular distributions (PAD) and assignments for the C_2N^- SEVI spectra.

Peak	Position (cm^{-1})	Offset (cm^{-1})	PAD	Assignments (Vibs)	(Electronic States)
a	21920	-232		$2_1^{1(\mu\Sigma)}$	$\tilde{X}^2\Pi \leftarrow \tilde{X}^3\Sigma^-$
b	22015	-137		$2_1^{1(\Delta_{5/2})}$	$\tilde{X}^2\Pi \leftarrow \tilde{X}^3\Sigma^-$
c	21852	-100		$2_1^{1(\Delta_{3/2})}$	$\tilde{X}^2\Pi \leftarrow \tilde{X}^3\Sigma^-$
A	22171	0	*s*+*d*	0_0^0	$\tilde{X}^2\Pi_{1/2} \leftarrow \tilde{X}^3\Sigma^-$
B	22209	38	*s*+*d*	0_0^0	$\tilde{X}^2\Pi_{3/2} \leftarrow \tilde{X}^3\Sigma^-$
C	22627	456	*s*+*d*	$2_0^{2(\mu\Pi_r)}$	$\tilde{X}^2\Pi \leftarrow \tilde{X}^3\Sigma^-$
E	30584	8413	*p*	0_0^0	$\tilde{a}^4\Sigma^- \leftarrow \tilde{X}^3\Sigma^-$
F	31754	9583	*p*	3_0^1	$\tilde{a}^4\Sigma^- \leftarrow \tilde{X}^3\Sigma^-$

Table 3.10 Peak positions, angular distributions (PAD) and assignments for the C_4N^- SEVI spectra.

Peak	Position (cm^{-1})	Offset (cm^{-1})	PAD	Assignments (Vibs)	(Electronic States)
a	24857	-237		6_1^1	$\tilde{X}^2\Pi \leftarrow \tilde{X}^3\Sigma^-$
b	25013	-81		6_1^1	$\tilde{X}^2\Pi \leftarrow \tilde{X}^3\Sigma^-$
c	25056	-38		6_1^1	$\tilde{X}^2\Pi \leftarrow \tilde{X}^3\Sigma^-$
A	25094	0	*s*+*d*	0_0^0	$\tilde{X}^2\Pi_{1/2} \leftarrow \tilde{X}^3\Sigma^-$
B	25123	29	*s*+*d*	0_0^0	$\tilde{X}^2\Pi_{3/2} \leftarrow \tilde{X}^3\Sigma^-$
C	25377	283	*s*+*d*	6_0^2	$\tilde{X}^2\Pi \leftarrow \tilde{X}^3\Sigma^-$
D	27271	2177	*s*+*d*	1_0^1	$\tilde{X}^2\Pi \leftarrow \tilde{X}^3\Sigma^-$
E	34350	9256	*p*	0_0^0	$\tilde{a}^4\Sigma^- \leftarrow \tilde{X}^3\Sigma^-$
F	35051	9957	*p*	4_0^1	$\tilde{a}^4\Sigma^- \leftarrow \tilde{X}^3\Sigma^-$

Table 3.11 Peak positions, angular distributions (PAD) and assignments for the C_6N^- SEVI spectra.

Peak	Position (cm^{-1})	Offset (cm^{-1})	PAD	Assignments (Vibs)	Assignments (Electronic States)
a	27096	-97		9_1^1	$\tilde{X}^2\Pi \leftarrow \tilde{X}^3\Sigma^-$
b	27142	-51		9_1^1	$\tilde{X}^2\Pi \leftarrow \tilde{X}^3\Sigma^-$
A	27193	0	*s*+*d*	0_0^0	$\tilde{X}^2\Pi_{1/2} \leftarrow \tilde{X}^3\Sigma^-$
B	27223	30	*s*+*d*	0_0^0	$\tilde{X}^2\Pi_{3/2} \leftarrow \tilde{X}^3\Sigma^-$
C	27484	291	*s*+*d*	9_0^2	$\tilde{X}^2\Pi \leftarrow \tilde{X}^3\Sigma^-$
D	29067	1874	*s*+*d*	3_0^1	$\tilde{X}^2\Pi \leftarrow \tilde{X}^3\Sigma^-$

Table 3.12 Calculated relative energies and harmonic vibrational frequencies (cm^{-1}) at the B3LYP/aug-cc-pVTZ level of theory.

	State	ΔE (eV)	ν_1	ν_2	ν_3	ν_4	ν_5	ν_6	ν_7	ν_8	ν_9	ν_{10}	ν_{11}
C_2N			σ	π_x/π_y	σ								
Anion	$\tilde{X}^3\Sigma^-$	-2.92	1749	465	1116								
Neutral	$\tilde{X}^2\Pi$	0.00	2216	261/400	1078								
	$\tilde{a}^4\Sigma^-$	1.10	1772	463	1240								
C_4N			σ	σ	σ	σ	π_x/π_y	π_x/π_y	π_x/π_y				
Anion	$\tilde{X}^3\Sigma^-$	-3.29	2009	1830	1473	752	481	394	119				
Neutral	$\tilde{X}^2\Pi$	0.00	2179	1986	1419	752	442/585	355/302	114/132				
	$\tilde{a}^4\Sigma^-$	1.16	2070	1749	1559	765	457	404	128				
C_6N			σ	σ	σ	σ	σ	σ	π_x/π_y	π_x/π_y	π_x/π_y	π_x/π_y	π_x/π_y
Anion	$\tilde{X}^3\Sigma^-$	-3.56	2113	1973	1847	1613	1067	559	495	483	385	186	77
Neutral	$\tilde{X}^2\Pi$	0.00	2242	2091	1953	1558	1068	559	538/612	446/481	321/366	181/182	77/79
	$\tilde{a}^4\Sigma^-$	1.17	2165	2011	1681	1665	1083	562	502	452	392	197	79

3.2.4 Electronic structure calculations

Electronic structure calculations were performed on the relevant neutral and anionic states of $C_{2n}N$, as determined by previous studies.[24,26-28,30,32-34] The current calculations serve to produce, at a uniform level of theory, all the geometries and vibrational frequencies necessary to interpret the photoelectron spectra. Our calculations were carried out with DFT using the Becke three-parameter Lee,Yang, and Parr exchange-correlation functional[35,36] (B3LYP) and the augmented correlation consistent polarized valence triple-zeta basis set[37] (aug-cc-pVTZ). All computations were performed using the GAUSSIAN03 program.[38]

The calculated geometries of the anion $^3\Sigma^-$ state as well as the neutral $\tilde{X}^2\Pi$ and $\tilde{a}^4\Sigma^-$ states are shown in Figure 3.9, while the harmonic vibrational frequencies and relative energies of the different species are presented in Table 3.12. The calculated anion geometries are essentially identical to those reported by Pascoli and Lavendy[33] using the same functional and basis set. The bent singlet states of the anion are not considered here. For the two neutral states of C_2N considered here, the DFT calculations yield shorter CC bond lengths than the CASSCF calculations of Chandra.[24] The C_4N and C_6N ground state bond lengths and frequencies calculated here are similar to previous DFT studies using smaller basis sets.[26-28] All the C_4N and C_6N bending modes in the $\tilde{X}^2\Pi$ state are non-degenerate in the calculations, as expected for vibrational modes subject to RT coupling. Calculated geometries, harmonic frequencies and energetics of the $\tilde{a}^4\Sigma^-$ state of C_4N and C_6N are reported for the first time.

Figure 3.9 emphasizes the geometry changes that occur upon photodetachment. All three species show a lengthening of the C_1-C_2 bond and a contraction of the neighboring bond upon photodetachment to the $\tilde{X}^2\Pi$ state. In C_4N, the four carbon atoms are approximately equally spaced in the anion, with a much more noticeable bond alternation in the neutral characteristic of acetylenic (C-C≡C-C) bonding. In C_6N, the carbon atoms C_1 through C_4 show alternating bond lengths in the anion and neutral, but the phase of the alternation flips upon photodetachment. In all three species, the C-N bond contracts upon detachment to the ground state, but the extent of this contraction decreases with increasing chain length.

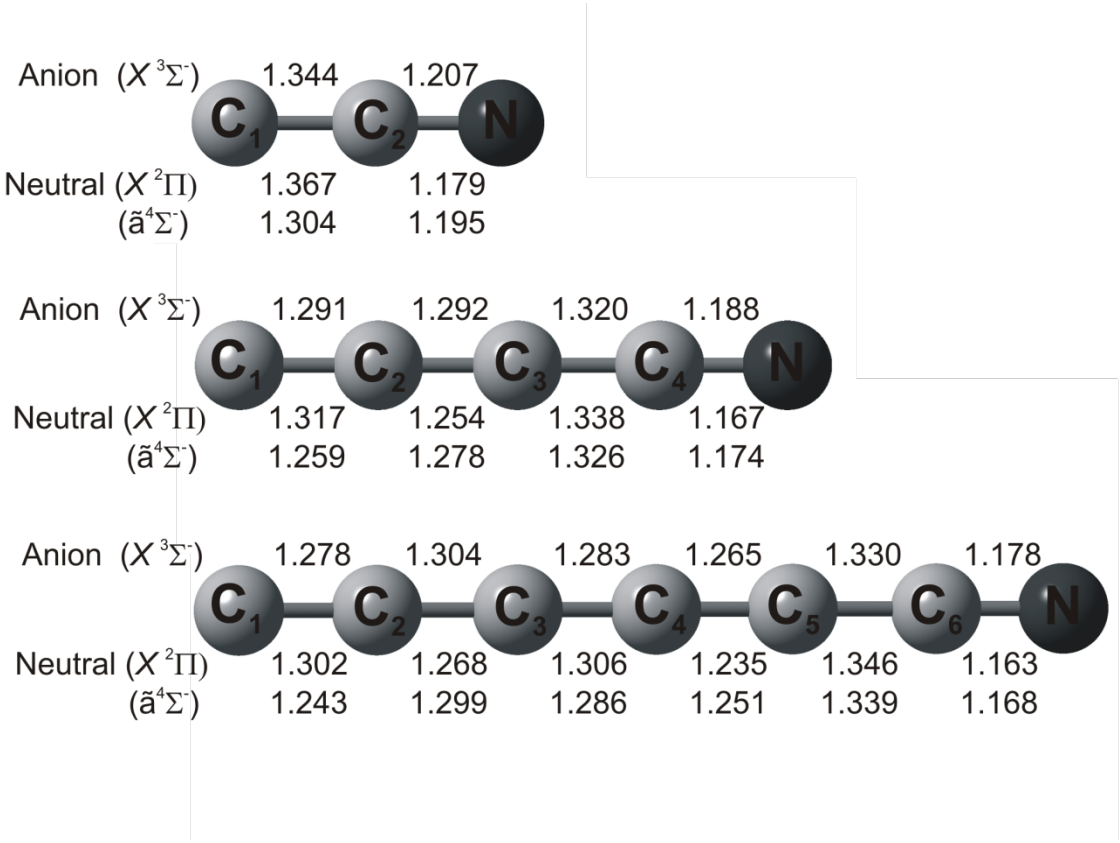

Figure 3.9 Anion and neutral geometries calculated at the B3LYP/aug-cc-pVTZ level.

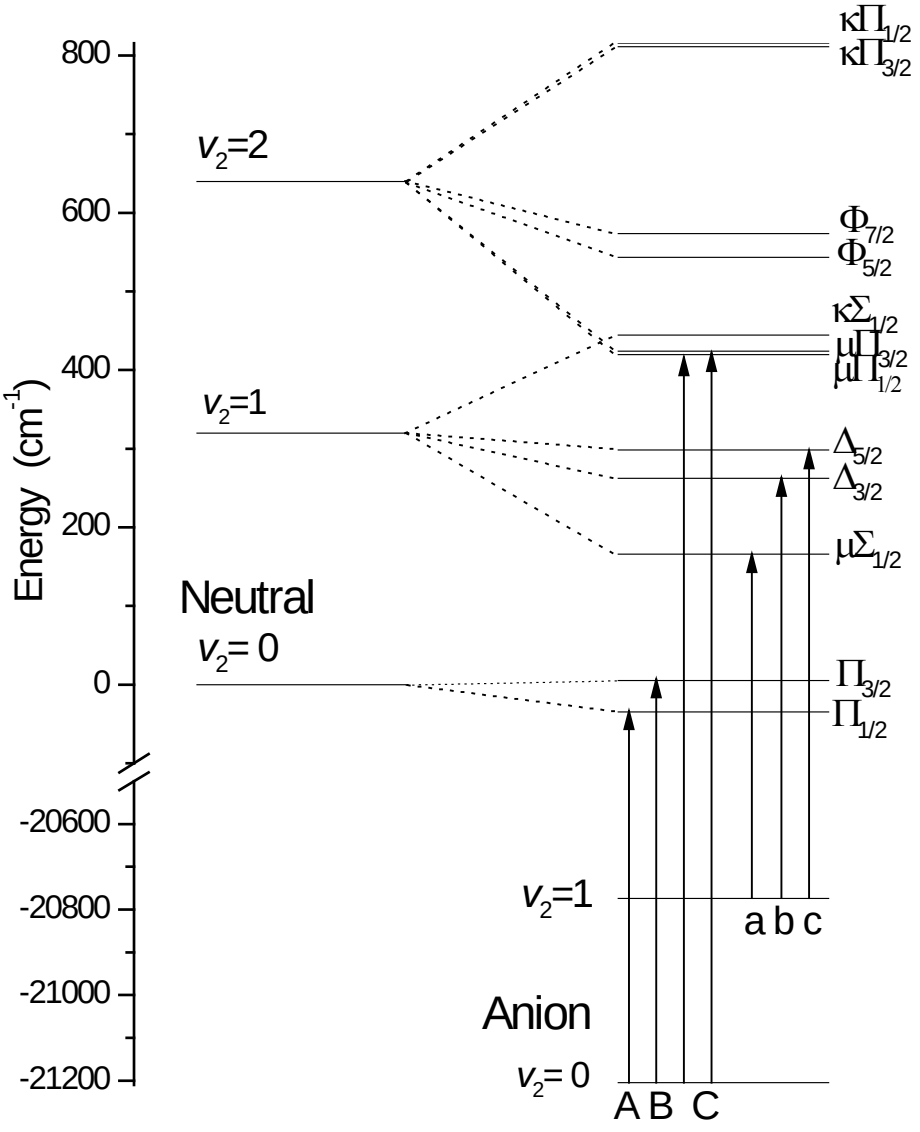

Figure 3.10. The C_2N ($\tilde{X}^2\Pi$) vibronic bending levels for $v_2 \leq 2$ (from Ref. 19) and the observed transitions in the SEVI spectra.

3.2.5 Analysis and discussion

In this section, detailed assignments of the SEVI spectra are presented, starting with the electronic bands in the upper and lower panels of Figures 3.6 and 3.7. The splittings between peaks A and E in those spectra are similar to the calculated splittings in Table IV between the neutral $\tilde{X}^2\Pi$ and $\tilde{a}^4\Sigma^-$ states. Both states are accessible from the $C_{2n}N^-$ $^3\Sigma^-$ states, which have a (core)$\pi^4\sigma^2\pi^2$ molecular orbital (MO) configuration. Removal of an electron from the highest occupied π or σ MO produces the neutral $\tilde{X}^2\Pi$ or $\tilde{a}^4\Sigma^-$ state, respectively. As shown previously,[39,40] photodetachment from π and σ MO's often proceeds via "*s*+*d*" and "*p*" scattering, respectively. We thus assign the lower energy band of peaks to the $\tilde{X}^2\Pi$ neutral ground state and the second band to the $\tilde{a}^4\Sigma^-$ first excited state, with both bands originating from the anion $^3\Sigma^-$ state. This assignment also implies that the $^3\Sigma^-$ state is the anion ground state rather than the bent singlet state found in the calculations of Zhan and Iwata,[32] since the $\tilde{a}^4\Sigma^-$ neutral state cannot be accessed by one-electron detachment from a singlet state of the anion. This point is considered in more detail below.

For each species, the two main peaks of the $\tilde{X}^2\Pi$ bands, A and B, are assigned as transitions to the $\Pi_{1/2}$ and $\Pi_{3/2}$ spin-orbit components, respectively, of the vibrational ground state. In C_2N, the splitting between those two peaks is 38 cm^{-1}, which is in good agreement with the 40.3799 cm^{-1} effective spin-orbit splitting derived from rotationally resolved absorption spectroscopy.[11] In C_4N and C_6N, these peaks are spaced by 29 cm^{-1} and 30 cm^{-1}, respectively, and represent the first experimental determination of the spin-orbit splitting in these species. These spin-orbit splittings are noticeably smaller than the value of 40 cm^{-1} assumed by McCarthy *et al.*[25] in fitting their C_4N and C_6N microwave spectra to a model Hamiltonian; no transitions involving the $\Pi_{3/2}$ component were observed in their study.

From the eBE of the peaks labeled A, we obtain the first experimental electron affinities (EA) of C_2N, C_4N and C_6N. These values are EA(C_2N)= 2.7489±0.0010 eV, EA(C_4N)= 3.1113±0.0010 eV and EA(C_6N)= 3.3715±0.0010 eV. The calculated EA's, including zero-point energy corrections, are 2.92 eV, 3.29 eV and 3.56 eV for C_2N, C_4N and C_6N, respectively. The B3LYP calculations overestimate the EA of these species by around 0.2 eV. Our experimental electron affinities and spin-orbit splittings are listed in Table 3.13.

In the $\tilde{X}^2\Pi$ bands, the small peaks C are too close to the band origin to be any of the stretching modes, according to our calculations, and hence must be from transitions to bend-excited neutral levels. In order to assign these peaks, we have to consider the RT coupling that affects the bending modes in the $\tilde{X}^2\Pi$ states of the $C_{2n}N$ radicals. In C_2N, the vibronic bending levels for $v_2 \leq 2$ obtained using the RT parameters determined by Kohguchi et al.[19] are presented in Figure 3.10. In the absence of additional vibronic coupling, the lowest vibrational bending level accessible by photodetachment from the C_2N^- anion ground state is

the (020)μΠ_r doublet. These levels have never been directly observed experimentally but are calculated to lie 454.4 cm^{-1} and 458.9 cm^{-1} above the origin transition. Peak C in C_2N, which lies 456 cm^{-1} from peak A, is thus assigned to the $2_0^{2(\mu\Pi)}$ transition with the individual doublet components being too close to be resolved in our experiment.

Table 3.13 Experimental electron affinity, ground state spin-orbit splitting, and $\tilde{a}^4\Sigma^-$ state term energy of C_2N, C_4N and C_6N.

	EA (eV) ±0.0010	S-O splitting ($\tilde{X}^2\Pi$) (cm^{-1})	T_0 ($\tilde{a}^4\Sigma^-$) (eV) ±0.0010
C_2N	2.7489	38 (40.3799)[a]	1.0431
C_4N	3.1113	29	1.1476
C_6N	3.3715	30	--

[a] From Reference [11]

By analogy, peak C in each of the C_4N^- and C_6N^- spectra is also likely to involve excitation of neutral bending levels. In C_4N, this feature is shifted by 283 cm^{-1} from peak A and can be either the $6_0^{2(\mu\Pi)}$ or $7_0^{2(\mu\Pi)}$ transition based on the B3LYP frequencies in Table 3.12. Similarly, in C_6N, peak C is spaced 291 cm^{-1} from peak A and could be either the $9_0^{2(\mu\Pi)}$ or the $10_0^{2(\mu\Pi)}$ transition. Based on the calculated frequencies alone, it might seem more reasonable to assign peak C to $7_0^{2(\mu\Pi)}$ in C_4N and $10_0^{2(\mu\Pi)}$ in C_6N. However, the anion and neutral harmonic frequencies for these modes are very similar; this situation generally results in extremely weak $\Delta v \neq 0$ transitions for a nontotally symmetric vibrational mode. Larger calculated changes in frequency are found for the ν_6 and ν_9 modes in C_4N and C_6N, respectively, and the artifactual splitting of the degeneracy is considerably higher, which is generally a signature of stronger RT coupling. This coupling, in turn, can significantly lower the energy of the $6_0^{2(\mu\Pi)}$ and $9_0^{2(\mu\Pi)}$ transitions, in analogy to the situation in C_2N, so assignment of peak C to these transitions may be preferable. More definitive assignments require a fuller understanding of RT coupling in C_4N and C_6N.

In the $\tilde{X}^2\Pi$ band of C_4N^- and C_6N^-, there is also a small peak labeled D. In C_4N, this peak is located 2177 cm^{-1} from the origin and is assigned to the 1_0^1 transition, based on our calculation of 2179 cm^{-1} for the fundamental of the ν_1 mode, the C_3C_4N asymmetric stretch. In C_6N, peak D is shifted 1874 cm^{-1} from the origin. This shift is close to our calculated frequency of 1953 cm^{-1} for the ν_3 mode, primarily a $C_2C_3C_4$ asymmetric stretching motion, so peak D in this case is assigned to the 3_0^1 transition. The assignment of these peaks is also in agreement with Franck-Condon simulations (not shown) which show that ν_1 and ν_3 are the only stretching modes with significant activity in the $\tilde{X}^2\Pi$ bands of C_4N and C_6N, respectively.

In the $\tilde{X}^2\Pi$ bands, there are as many as three small peaks labeled a, b and c below the vibrational origin. These peaks are assigned to transitions originating from excited vibrational states in the anion. Because the main spectral feature is the 0_0^0 transition, one expects the small peaks to be sequence bands with Δv=0. The most likely populated vibrational levels in the anions are the low-frequency bending modes. In C_2N, the (010) mode of the neutral is split into 4 levels by RT coupling (see Figure 3.10); all four are accessible by photodetachment from the anion (010) level. In Figure 3.7a, peaks a and b are split by 95 cm^{-1}, close to the calculated splitting of 96.6 cm^{-1} between the (010)$\mu\Sigma$ and (010)$\Delta_{3/2}$ levels. Similarly, peaks b and c are split by 37 cm^{-1} which is very close to the calculated splitting of 36.2 cm^{-1} between the (010)$\Delta_{3/2}$ and (010)$\Delta_{5/2}$ levels. Peaks a, b and c in the C_2N spectra are thus assigned to the $2_1^{1(\mu\Sigma)}$, $2_1^{1(\Delta_{5/2})}$and $2_1^{1(\Delta_{3/2})}$ transitions respectively. The $2_1^{1(\kappa\Sigma)}$ transition is probably also present but is calculated to be buried under peak B. Using the experimentally known energy of the (010)$\mu\Sigma$ level,[19] this assignment implies that the ν_2 fundamental of the C_2N^- anion is 432 cm^{-1}. This value is in reasonable agreement with the calculated frequency of 465 cm^{-1} in Table 3.12, thereby supporting the proposed assignments.

Again, RT coupling analysis in C_4N and C_6N is required to fully assign the sequence bands in the spectra of these species. The pattern of these peaks in C_4N spectrum is very similar to that in C_2N, suggesting a similar assignment. These peaks are probably the 6_1^1 transitions in C_4N because our calculations suggest a large RT splitting for this mode as well as a significant change in anion vs neutral frequency, both of which are necessary to see multiple, distinct sequence bands. For similar reasons, the sequence bands in the C_6N spectrum are most likely 9_1^1 transitions.

The lower panels of Figures 3.6b and 3.7b display features assigned to the $\tilde{a}^4\Sigma^-$ excited electronic states of C_2N and C_4N, respectively. These spectra represent the first experimental observation of the quartet states. The dominant peak of each quartet band, labeled E, is assigned to the 0_0^0 transition. The term energy of the C_2N $\tilde{a}^4\Sigma^-$ state is thus determined to be 1.0431±0.0010 eV. This value agrees with our calculation which predicted a term energy of 1.10 eV for this state. The 1.03 eV value calculated by Chandra[24] at the higher CASSCF level is also in excellent agreement with experiment. The term energy of the C_4N $\tilde{a}^4\Sigma^-$ state is determined to be 1.1476±0.0010 eV, in excellent agreement with the value of 1.16 eV calculated at the B3LYP level. Note that our calculations indicate that C_6N also has a quartet state lying 1.17 eV above the ground state. However, the detachment photon energy required to access this state is higher than the maximum available with our current laser setup and it could not be observed. The experimental quartet term energies obtained here are listed in Table 3.13.

In the C_2N $\tilde{a}^4\Sigma^-$ band, the smaller peak, labeled F, is assigned to the 3_0^1 transition. This yields a frequency of the ν_3 fundamental of 1170 cm^{-1}, which is slightly smaller than the value of 1240 cm^{-1} calculated in this work and larger than the 1101 cm^{-1} value calculated at

the CASSCF level by Chandra.[24] Similarly, the peak labeled E in the C_4N $\tilde{a}^4\Sigma^-$ band is assigned to the 4_0^1 transition. The ν_4 mode is a symmetric stretch of the carbon chain. This assignment yields a frequency of 701 cm^{-1} for the ν_4 fundamental which is close to our calculated value of 765 cm^{-1}

.

The SEVI spectra presented here address a key issue regarding the electronic structure and geometry of the anion ground states. The $C_{2n}N^-$ anions have close-lying singlet and triplet states with calculated relative energies that depend on the method used.[32,33] Zhan and Iwata[32] used the MP2 method to investigate the structure of the C_nN^- (n=1-13) anions. They found a singlet ground state for all the $C_{2n}N^-$ species with the n>1 chains having strongly bent structures. For C_4N^- and C_6N^-, linear triplet states were found to be 0.368 eV and 0.822 eV above the singlet ground state, respectively. A subsequent study by Pascoli and Lavendy[33] using DFT/B3LYP predicted a linear triplet ground state ($^3\Sigma^-$) for the $C_{2n}N^-$ (n=1-3) anions. A coupled-cluster, single-point energy calculation on the B3LYP optimized geometries located the bent singlet excited state (^{1}A') of C_2N^-, C_4N^- and C_6N^- with term energies of 0.75 eV, 0.25 eV and 0.22 eV respectively. The discrepancy between the two methods was attributed to high spin contamination of the Hartree-Fock reference wavefunction for the linear triplet state in the MP2 calculations.[33]

All SEVI spectra reported here are dominated by the origin (0_0^0) transition and display a small number of transitions to excited vibrational levels. This pattern is consistent with the anion and neutral states having similar geometries. Since it is known from microwave spectroscopy experiments[21,25] that C_2N, C_4N and C_6N all have linear ground states, the anions must also be linear in accordance with the DFT calculations.[33] If the C_4N^- and C_6N^- anions had strongly bent geometries, such as those predicted by MP2 calculations, extended progressions of bending modes would be seen. Moreover, the quartet states of C_2N and C_4N are not accessible by one-electron detachment from an anion singlet state. We thus conclude that the $C_{2n}N^-$ (n=1-3) anions have linear $^3\Sigma^-$ ground states and that the singlet excited state is too high in energy to be significantly populated.

3.2.6 Conclusions

High resolution photoelectron spectra of C_2N^-, C_4N^-, and C_6N^- obtained using slow electron velocity-map imaging (SEVI) are reported. This work provides the first measurement of the adiabatic electron affinities of the three species as well as the term energy of the low-lying $\tilde{a}^4\Sigma^-$ state of C_2N and C_4N. The spin-orbit splitting in the $\tilde{X}^2\Pi$ ground state of C_4N and C_6N is also experimentally determined for the first time. The observation of relatively little vibrational activity and transitions to neutral quartet states in the photoelectron spectra indicates that the $C_{2n}N^-$ (n=1-3) anions all have linear $^3\Sigma^-$ ground states, in agreement with the theoretical study of Pascoli and Lavendy.[33]

References

1) A. McKellar, *Publ. Astron. Soc. Pac.* **52**, 307 (1940).

2) M. Guelin and P. Thaddeus, *Astrophys. J.* **212** (2), L81 (1977).

3) P. Friberg, A. Hjalmarson, W. M. Irvine, and M. Guelin, *Astrophys. J.* **241** (2), L99 (1980).

4) M. Guelin, N. Neininger, and J. Cernicharo, *Astron. Astrophys.* **335** (1), L1 (1998).

5) P. Thaddeus, C. A. Gottlieb, H. Gupta, S. Brunken, M. C. McCarthy, M. Agundez, M. Guelin, and J. Cernicharo, *Astrophys. J.* **677** (2), 1132 (2008).

6) T. I. Hasegawa and E. Herbst, *Mon. Not. Roy. Astron. Soc.* **263** (3), 589 (1993).

7) S. D. Doty and C. M. Leung, *Astrophys. J.* **502** (2), 898 (1998).

8) F. Pauzat, Y. Ellinger, and A. D. McLean, *Astrophys. J.* **369** (1), L13 (1991).

9) A. J. Merer and D. N. Travis, *Can. J. Phys.* **43** (10), 1795 (1965).

10) V. E. Bondybey and J. H. English, *J. Mol. Spectrosc.* **70** (2), 236 (1978).

11) M. Kakimoto and T. Kasuya, *J. Mol. Spectrosc.* **94** (2), 380 (1982).

12) K. Kawaguchi, T. Suzuki, S. Saito, E. Hirota, and T. Kasuya, *J. Mol. Spectrosc.* **106** (2), 320 (1984).

13) M. Feher, C. Salud, J. P. Maier, and A. J. Merer, *J. Mol. Spectrosc.* **150** (1), 280 (1991).

14) M. Feher, C. Salud, and J. P. Maier, *J. Mol. Spectrosc.* **145** (2), 246 (1991).

15) S. A. Beaton, D. A. Gillett, J. M. Brown, M. Feher, and A. Rohrbacher, *J. Mol. Spectrosc.* **209** (1), 60 (2001).

16) K. Hakuta and H. Uehara, *J. Chem. Phys.* **78** (11), 6484 (1983).

17) K. Hakuta, H. Uehara, K. Kawaguchi, T. Suzuki, and T. Kasuya, *J. Chem. Phys.* **79** (2), 1094 (1983).

18) C. R. Brazier, L. C. Obrien, and P. F. Bernath, *J. Chem. Phys.* **86** (6), 3078 (1987).

19) H. Kohguchi, Y. Ohshima, and Y. Endo, *J. Chem. Phys.* **106** (13), 5429 (1997).

20) N. Oliphant, A. Lee, P. F. Bernath, and C. R. Brazier, *J. Chem. Phys.* **92** (4), 2244 (1990).

21) Y. Ohshima and Y. Endo, *J. Mol. Spectrosc.* **172** (1), 225 (1995).

22) M. D. Allen, K. M. Evenson, D. A. Gillett, and J. M. Brown, *J. Mol. Spectrosc.* **201** (1), 18 (2000).

23) W. Gabriel, E. A. Reinsch, and P. Rosmus, *Chem. Phys. Lett.* **231** (1), 13 (1994).

24) R. Pd and P. Chandra, *J. Chem. Phys.* **114** (4), 1589 (2001).

25) M. C. McCarthy, G. W. Fuchs, J. Kucera, G. Winnewisser, and P. Thaddeus, *J. Chem. Phys.* **118** (8), 3549 (2003).

26) J. J. Belbruno, Z. C. Tang, R. Smith, and S. Hobday, *Mol. Phys.* **99** (11), 957 (2001).

27) Y. H. Ding, J. L. Liu, X. R. Huang, Z. S. Li, and C. C. Sun, *J. Chem. Phys.* **114** (12), 5170 (2001).

28) K. Chuchev and J. J. BelBruno, *J. Phys. Chem. A* **106** (16), 4240 (2002).

29) R. B. Huang, C. R. Wang, Z. Y. Liu, L. S. Zheng, F. Qi, L. S. Sheng, S. Q. Yu, and Y. W. Zhang, *Z. Phys. D-Atoms Mol. Clusters* **33** (1), 49 (1995).

30) C. R. Wang, R. B. Huang, Z. Y. Liu, and L. S. Zheng, *Chem. Phys. Lett.* **237** (5-6), 463 (1995).

31) A. K. Gupta and P. Ayyub, *Eur. Phys. J. D* **17** (2), 221 (2001).

32) C. G. Zhan and S. Iwata, *J. Chem. Phys.* **104** (22), 9058 (1996).

33) G. Pascoli and H. Lavendy, *Chem. Phys. Lett.* **312** (2-4), 333 (1999).

34) K. Chuchev and J. J. BelBruno, *J. Phys. Chem. A* **107** (11), 1887 (2003).

35) A. D. Becke, *J. Chem. Phys.* **98** (2), 1372 (1993).

36) C. T. Lee, W. T. Yang, and R. G. Parr, *Phys. Rev. B* **37** (2), 785 (1988).

37) T. H. Dunning, *J. Chem. Phys.* **90** (2), 1007 (1989).

38) M. J. Frisch, G. W. Trucks, H. B. Schlegel*et al.*, Gaussian 03, Revision C.02 (Gaussian, Inc, Wallingford, CT, 2004).

39) J. Zhou, E. Garand, W. Eisfeld, and D. M. Neumark, *J. Chem. Phys.* **127** (3), 034304 (2007).

40) J. Zhou, E. Garand, and D. M. Neumark, *J. Chem. Phys.* **127**, 114313 (2007).

3.3 Slow photoelectron velocity-map imaging spectroscopy of CCO^- and CCS^- anions

Abstract

High-resolution photodetachment spectra of CCO^- and CCS^- using slow photoelectron velocity-map imaging (SEVI) spectroscopy are reported. Well-resolved transitions to the neutral $\tilde{X}^3\Sigma^-$, $\tilde{a}^1\Delta$, $\tilde{b}^1\Sigma^+$ and $\tilde{A}^3\Pi$ states are seen for both species. The electron affinities of CCO and CCS are determined to be 2.3107±0.0006 eV and 2.7475±0.0006 eV, respectively, and precise term energies for the $\tilde{a}^1\Delta$, $\tilde{b}^1\Sigma^+$and $\tilde{A}^3\Pi$ excited states are also determined. The two low-lying singlet states of CCS are observed for the first time, as are several vibronic transitions within the four bands. Analysis of hot bands finds the spin-orbit orbit splitting in the $\tilde{X}^2\Pi$ ground state of CCO^- and CCS^- to be 61 cm^{-1} and 195 cm^{-1}, respectively.

3.3.1 Introduction

The isovalent CCO and CCS radicals are important constituents of the interstellar medium[1,2]. The CCO radical is a key intermediate in hydrocarbon combustion.[3-5] CCS microwave absorption is used a molecular probe of the velocity, density, and age of dark interstellar clouds[6,7]. These species also serve as case studies for the theoretical treatment of spin-rovibronic interaction and vibronic coupling in linear triatomic molecules with triplet states.[8,9] The CCO and CCS radicals are known to have several low-lying singlet and triplet electronic states. While the $\tilde{X}^3\Sigma^-$ ground-state and the first optically accessible electronic state ($\tilde{A}^3\Pi$) of these species have been studied in detail both experimentally and theoretically, less information is available on the singlet states. In this chapter, high resolution photodetachment spectra of the CCO^- and CCS^- anions are reported that provide a detailed probe of the low-lying triplet and singlet states of both neutral radicals.

The CCO radical has been studied by microwave spectroscopy,[10,11] infrared and UV absorption spectroscopy,[12-22] and laser-induced fluorescence (LIF)[23]. Similarly, CCS has been investigated with microwave spectroscopy[2,24,25], infrared and UV absorption spectroscopy[26-28] and LIF [29,30]. These experiments have provided the rotational constants and some vibrational frequencies of the $\tilde{X}^3\Sigma^-$ and $\tilde{A}^3\Pi$ electronic states. Accordingly, most of the theoretical work on the CCO and CCS radical has also focused on the structure of these two states as well as the Renner-Teller coupling in the upper state[8,9,29,31-35]. Some calculations on the energetic and structures of the other low-lying electronic states have also been reported[27,36-38].

The corresponding CCO^- and CCS^- anions have been the subject of a few experimental and theoretical investigations. Maier and co-workers have observed the $\tilde{X}^2\Pi \leftarrow \tilde{A}^2\Sigma^+$ absorption of both ions in a neon matrix[27,39]. Electronic structure calculations of these two states have been reported[27,37] as well as a theoretical investigation of the Renner-Teller effect in the ground state[40,41].

Additional information on the CCO^- anion and CCO neutral is obtained from the anion photoelectron (PE) spectrum.[37,42,43] The PE spectrum yielded an electron affinity of 2.310±0.012 eV[42] and provided the first experimental observation of the neutral singlet states. The anion has a $\ldots(6\sigma)^2(1\pi)^4(7\sigma)^2(2\pi)^3$ molecular orbital configuration. Removal of a 2π electron leads to the $\tilde{X}^3\Sigma^-$, $\tilde{a}^1\Delta$, and $\tilde{b}^1\Sigma^+$ neutral states while removal of a 7σ electron produces the $\tilde{A}^3\Pi$ state. Hence, PE spectroscopy probes all four low-lying neutral states on equal footing, providing not only electronic state energies but also vibrational frequencies for the Franck-Condon active vibrational modes in both the ground and excited states. In addition, the observation of nominally forbidden vibrational excitations provides information on vibronic coupling interactions among these states.

In this section, we report the high-resolution photodetachment spectra of CCO^- and CCS^- using slow photoelectron velocity-map imaging (SEVI) spectroscopy. The SEVI spectra for CCO^- are considerably higher resolution than the previous PE spectra. This work also represents the first photodetachment experiment on CCS^- and the first observation of the low-lying singlet states of CCS. It provides precise electron affinities for CCO and CCS, as well as term energies for the neutral $\tilde{a}^1\Delta$, $\tilde{b}^1\Sigma^+$ and $\tilde{A}^3\Pi$ electronic states of both species. The positions of several previously unobserved vibronic transitions within the four electronic bands are reported and assigned.

3.3.2 Experimental details

The SEVI technique and apparatus has been described in chapter 2. CCO^- anions were produced from of a gas mixture comprising 1% acetylene, 8% O_2, 20% CO_2 in a balance of Ar. Similarly, CCS^- anions were produced from 1% acetylene, 1% CS_2, 30% CO_2 in a balance of argon. The gas mixture, at a stagnation pressure of 300 psi, was expanded into the source vacuum chamber and the anion were formed using the circular ionizer.

The apparatus was calibrated by acquiring SEVI images of atomic chloride and sulfur at several different photon energies. With the 350V VMI repeller voltage used in this study, the full widths at half maximum of the chloride peaks were 3.3 cm^{-1} at 24 cm^{-1} above threshold.

3.3.3 Results and assignments

1) CCO^-

SEVI spectra of CCO^- covering the electron binding energy range from 18000 to 33500 cm^{-1} are shown in Figures 3.11 and 3.12. The spectra comprise 7 SEVI traces taken at different photon energies. The peak positions, photoelectron angular distribution and assignments are summarized in Table 3.14. Our spectra are similar to previously reported PE spectra[37,42] but with much higher resolution.

The SEVI spectra are divided into four bands of peaks, each corresponding to transitions to a different neutral electronic state. Peaks A, D, F and I are assigned to the vibronic origins of the $\tilde{X}^3\Sigma^-$, $\tilde{a}^1\Delta$, $\tilde{b}^1\Sigma^+$ and $\tilde{A}^3\Pi$ states, respectively, based on the calculation of Zengin *et al.*[37] and the previous PE spectra.[37,42] These assignments are supported by the photoelectron angular distributions. All the features at eBE below that of peak I have an *s*+*d* PAD, which is consistent with detachment from the 2π orbital leading to the $\tilde{X}^3\Sigma^-$, $\tilde{a}^1\Delta$, $\tilde{b}^1\Sigma^+$ states. The PAD's for peak I and those at higher eBE have *p*-wave character, consistent with detachment from the 7σ orbital producing the $\tilde{A}^3\Pi$ state.

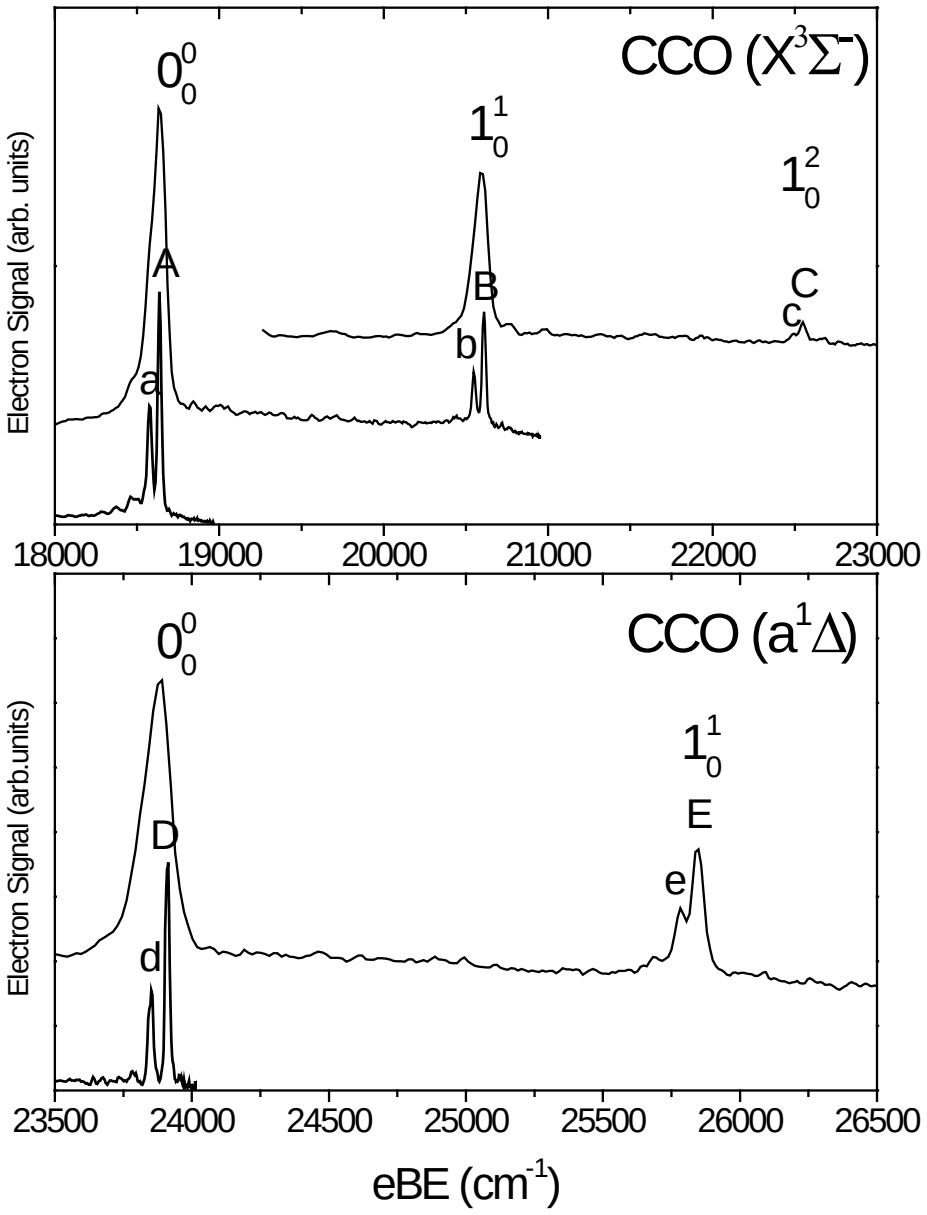

Figure 3.11 SEVI spectra of CCO^- in the 18000 cm^{-1} to 26500 cm^{-1} eBE range. The top panel displays traces taken at photon energy of 24242 cm^{-1}, 21097 cm^{-1} and 19084 cm^{-1} while the lower panel displays traces taken at 27322 cm^{-1} and 24242 cm^{-1}. The traces are vertically offset for clarity.

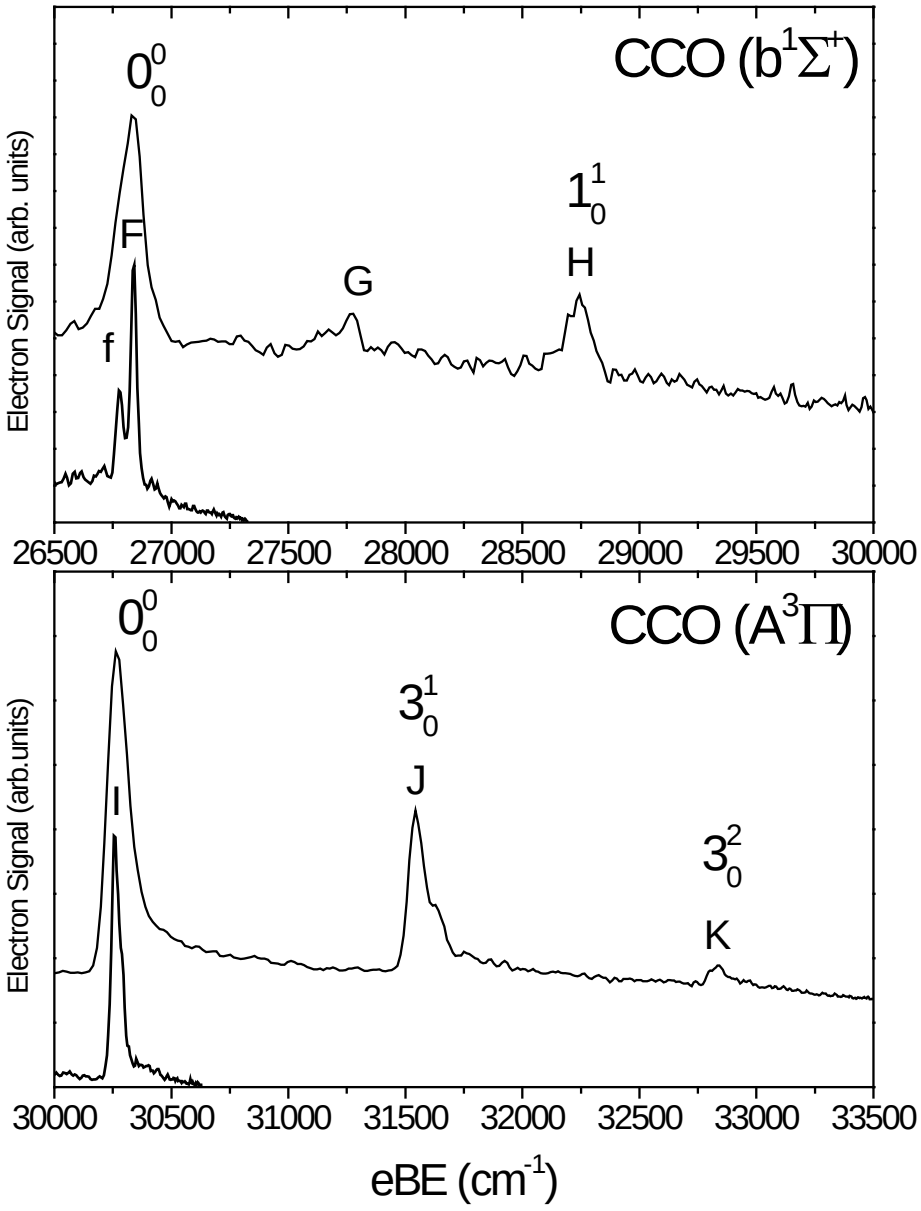

Figure 3.12 SEVI spectra of CCO^- in the 26500 cm^{-1} to 33500 cm^{-1} eBE range. The top panel displays traces taken at photon energy of 30628 cm^{-1} and 27322 cm^{-1} while the lower panel displays traces taken at 33557 cm^{-1} and 30628 cm^{-1}. The traces are vertically offset for clarity.

Table 3.14 Peak positions, photoelectron angular distribution and assignments for the CCO^- SEVI spectra.

Peak	Position (cm^{-1})	Offset (cm^{-1})	PAD	Previous Obs. (cm^{-1})	Calculated (cm^{-1})	Assignment (vib)	Assignment (Electronic states)
a	18576	-61	*s+d*			0_0^0	$\tilde{X}^3\Sigma \leftarrow \tilde{X}^2\Pi_{1/2}$
A	18637	0	*s+d*			0_0^0	$\tilde{X}^3\Sigma \leftarrow \tilde{X}^2\Pi_{3/2}$
b	20549	1912	*s+d*			1_0^1	$\tilde{X}^3\Sigma \leftarrow \tilde{X}^2\Pi_{1/2}$
B	20610	1973	*s+d*	1971[a], 1960[c]	1949[e]	1_0^1	$\tilde{X}^3\Sigma \leftarrow \tilde{X}^2\Pi_{3/2}$
c	22489	3852	*s+d*			1_0^2	$\tilde{X}^3\Sigma \leftarrow \tilde{X}^2\Pi_{1/2}$
C	22550	3913	*s+d*	3976[c]		1_0^2	$\tilde{X}^3\Sigma \leftarrow \tilde{X}^2\Pi_{3/2}$
d	23850	-61	*s+d*			0_0^0	$\tilde{a}^1\Delta \leftarrow \tilde{X}^2\Pi_{1/2}$
D	23911	0	*s+d*			0_0^0	$\tilde{a}^1\Delta \leftarrow \tilde{X}^2\Pi_{3/2}$
e	25784	1873	*s+d*			1_0^1	$\tilde{a}^1\Delta \leftarrow \tilde{X}^2\Pi_{1/2}$
E	25845	1934	*s+d*	1943[b],1944[c]	2005[f]	1_0^1	$\tilde{a}^1\Delta \leftarrow \tilde{X}^2\Pi_{3/2}$
f	26779	-61	*s+d*			0_0^0	$\tilde{b}^1\Sigma^+ \leftarrow \tilde{X}^2\Pi_{1/2}$
F	26840	0	*s+d*			0_0^0	$\tilde{b}^1\Sigma^+ \leftarrow \tilde{X}^2\Pi_{3/2}$
G	27762	3851	*s+d*			1_0^2	$\tilde{a}^1\Delta \leftarrow \tilde{X}^2\Pi_{3/2}$
H	28740	1900	*s+d*	1823[c]	2022[f]	1_0^1	$\tilde{b}^1\Sigma^+ \leftarrow \tilde{X}^2\Pi_{3/2}$
I	30258	0	*p*			0_0^0	$\tilde{A}^3\Pi_2 \leftarrow \tilde{X}^2\Pi_{3/2}$
J	31537	1279	*p*	1282[d], 1266[c]	1271[e]	3_0^1	$\tilde{A}^3\Pi_2 \leftarrow \tilde{X}^2\Pi_{3/2}$
K	32831	2573	*p*	2565[c]		3_0^2	$\tilde{A}^3\Pi_2 \leftarrow \tilde{X}^2\Pi_{3/2}$

a) Ref [20] b) Ref [19] c) Ref [42] d) Ref [12] e) Ref[8] f) Ref[37]

The CCO^- SEVI spectra are dominated by the vibrational origin transitions. In the top panel of Figure 3.11, peaks B and C are assigned to the 1_0^1 and 1_0^2 photodetachment transitions within the $\tilde{X}^3\Sigma^-$ band. This assignment yields a value of 1973 cm^{-1} for the ν_1 fundamental, in excellent agreement with the value of 1971 cm^{-1} found in the infrared diode laser measurement of Moazzen-Ahmadi *et al.*[20] Peaks E and G are assigned to the same 1_0^1 and 1_0^2 transitions within the $a^1\Delta$ band while peak H is assigned to the 1_0^1 transition of the $\tilde{b}^1\Sigma^+$ state. These assignments yield fundamental ν_1 frequencies of 1934 and 1900 cm^{-1}, respectively, for the $\tilde{a}^1\Delta$ and $\tilde{b}^1\Sigma^+$ singlet state. The only other experimental observations of these modes come from the lower resolution PE spectra[37,42]. In Figure 3.11 and in the top panel of Figure 3.12, peaks a-f are found to lie systematically 61 cm^{-1} below a major transition. These peaks are assigned to transitions originating from the excited spin-orbit state ($\tilde{X}^2\Pi_{1/2}$) of the anion. This assignment agrees with calculations by Panten *al.*[40] that predicted a spin-orbit splitting of -57.5 cm^{-1} for CCO^-. Finally, in the lower panel of figure 3.12, peaks J and K are assigned to the 3_0^1 and 3_0^2 transitions within the $\tilde{A}^3\Pi$ band. This state is subject to spin-orbit splitting on the order of 36 cm^{-1}.[8,17] However, the *p*-wave nature of peaks I, J, and K prevent the observation of the individual spin-orbit levels since the photodetachment cross-section is too small at wavelengths sufficiently close to threshold to resolve them[44,45].

2) CCS^-

SEVI spectra of CCS^- covering the electron binding energy range from 21800 to 33500 cm^{-1} are shown in Figures 3.13 and 3.14. The spectra comprise 7 SEVI traces taken at different photon energies. Peak positions, photoelectron angular distributions and assignments for the CCS^- SEVI spectra are summarized in Table 3.15. These are the first photoelectron spectra of CCS^- reported. Peaks A, J, Q and U are the main spectral features and are assigned to the vibronic origins of the $\tilde{X}^3\Sigma^-$, $\tilde{a}^1\Delta$, $\tilde{b}^1\Sigma^+$ and $\tilde{A}^3\Pi$ states, respectively, by analogy to the CCO^- spectra. This assignment is also consistent with the calculated term energies of these states.[27,38] Just as in the CCO^- spectra, all the features at eBE below the $\tilde{A}^3\Pi$ origin (peak U), with the exception of peaks B and E, have a PAD indicative of *s*+*d*-wave detachment, while transitions associated with the $\tilde{A}^3\Pi$ band have *p*-wave character.

The SEVI spectra of CCS^- display more vibrational activity than the CCO^- spectra. In the top panel of Figure 3.13, most of the transitions to the $\tilde{X}^3\Sigma^-$ state can be assigned based on previous observations by LIF[30] and recent calculations by Tarroni *et al.*[9] Peaks B, D and G are assigned to the 2_0^1, 3_0^1 and 1_0^1 transitions within the $\tilde{X}^3\Sigma^-$ band, in agreement with previous observations.[30] Peaks C and I are assigned to the 2_0^2 and 1_0^2 transitions, respectively. Peaks E and F are assigned to the $2_0^1 3_0^1$ and $2_0^2 3_0^1$ combination bands while peak H is the $1_0^1 3_0^1$ combination band. Peaks B and E involve odd Δv transitions in the non-totally symmetric bending mode and are nominally forbidden. They have a *p*-wave PAD and their relative

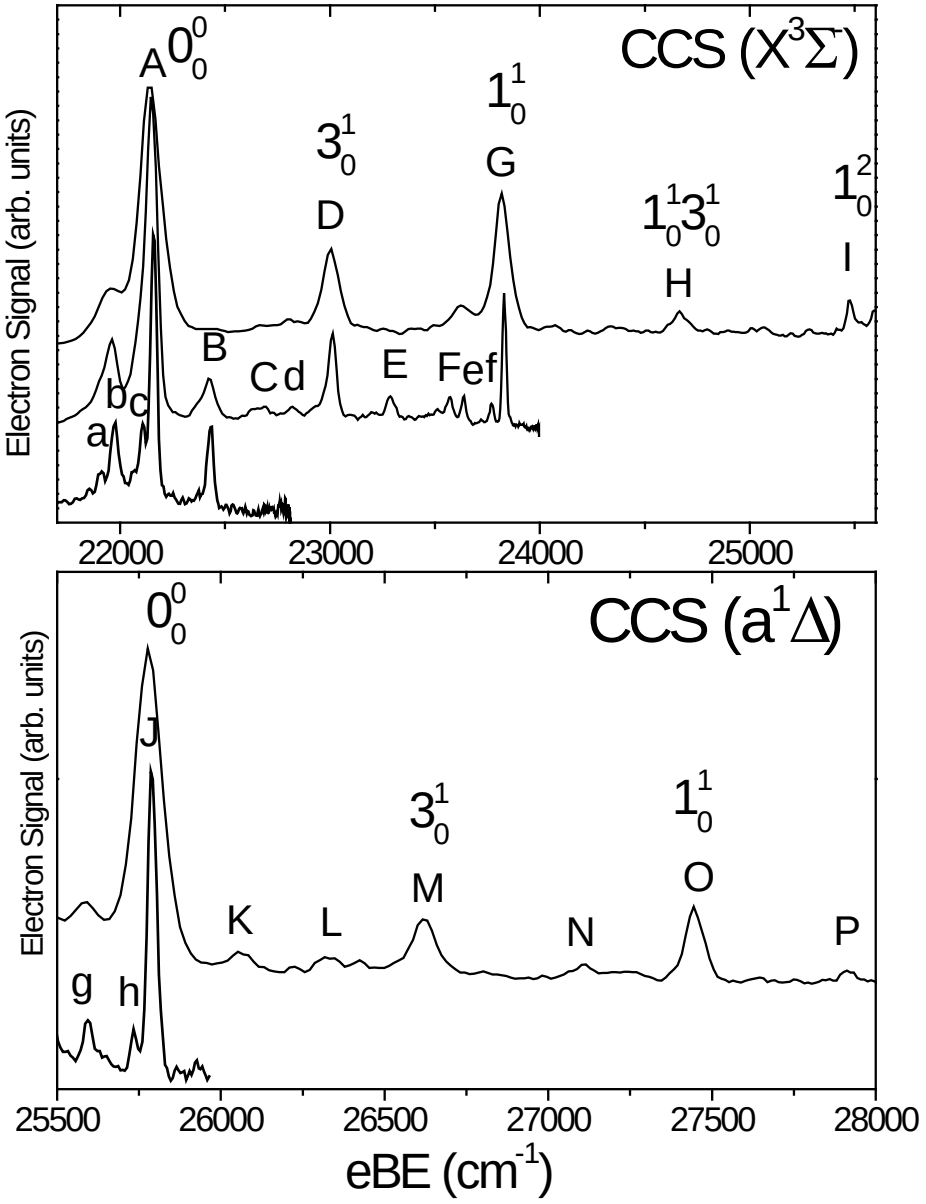

Figure 3.13 SEVI spectra of CCS^- in the 28000 cm^{-1} to 30500 cm^{-1} eBE range. The top panel displays traces taken at photon energy of 31646 cm^{-1} and 29369 cm^{-1} while the lower panel displays traces taken at 33727 cm^{-1} and 31646 cm^{-1}. The traces are vertically offset for clarity.

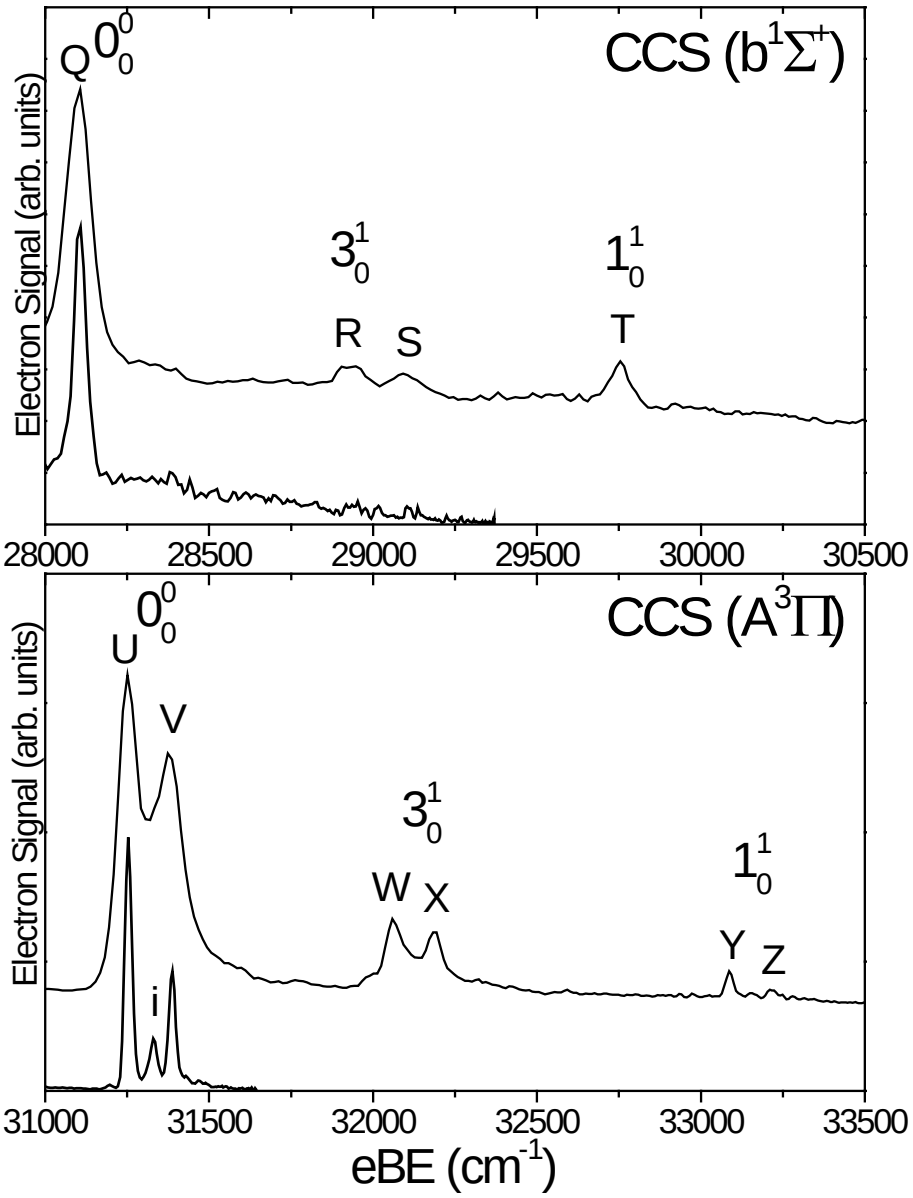

Figure 3.14 SEVI spectra of CCS^- in the 28000 cm^{-1} to 30500 cm^{-1} eBE range. The top panel displays traces taken at photon energy of 31646 cm^{-1} and 29369 cm^{-1} while the lower panel displays traces taken at 33727 cm^{-1} and 31646 cm^{-1}. The traces are vertically offset for clarity.

Table 3.15 Peak positions, photoelectron angular distribution and assignments for the CCS^- SEVI spectra.

Peak	Position (cm^{-1})	Offset (cm^{-1})	PAD	Previous Obs[a] (cm^{-1})	Calculated[c] (cm^{-1})	Assignment (Vib)	Assignment (Electronic States)
a	21910	-250	*s+d*			2_1^1	$\tilde{X}^3\Sigma \leftarrow \tilde{X}^2\Pi\ (\Sigma^-_{1/2}, \Delta_{3/2})$
b	21983	-195	*s+d*			0_0^0	$\tilde{X}^3\Sigma \leftarrow \tilde{X}^2\Pi_{1/2}$
c	22108	-52	*s+d*			2_1^1	$\tilde{X}^3\Sigma \leftarrow \tilde{X}^2\Pi\ (\Sigma^+_{1/2}, \Delta_{5/2})$
A	22160	0	*s+d*			0_0^0	$\tilde{X}^3\Sigma \leftarrow \tilde{X}^2\Pi_{3/2}$
B	22430	270	*p*	266.6	268	2_0^1	$\tilde{X}^3\Sigma \leftarrow \tilde{X}^2\Pi_{3/2}$
C	22685	525	*s+d*	532.8	540	2_0^2	$\tilde{X}^3\Sigma \leftarrow \tilde{X}^2\Pi_{3/2}$
d	22821	661	*s+d*			3_0^1	$\tilde{X}^3\Sigma \leftarrow \tilde{X}^2\Pi_{1/2}$
D	23010	850	*s+d*	857.8	850	3_0^1	$\tilde{X}^3\Sigma \leftarrow \tilde{X}^2\Pi_{3/2}$
E	23288	1128	*p*		1125	$2_0^1 3_0^1$	$\tilde{X}^3\Sigma \leftarrow \tilde{X}^2\Pi_{3/2}$
F	23568	1408	*s+d*		1404	$2_0^2 3_0^1$	$\tilde{X}^3\Sigma \leftarrow \tilde{X}^2\Pi_{3/2}$
e	23636	1476	*s+d*			1_0^1	$\tilde{X}^3\Sigma \leftarrow \tilde{X}^2\Pi_{1/2}$
f	23770	1610	*s+d*			$1_0^1 2_1^1$	$\tilde{X}^3\Sigma \leftarrow \tilde{X}^2\Pi\ (\Sigma^+_{1/2}, \Delta_{5/2})$
G	23831	1671	*s+d*	1670.8	1661	1_0^1	$\tilde{X}^3\Sigma \leftarrow \tilde{X}^2\Pi_{3/2}$
H	24668	2508	*s+d*	2511.6	2494	$1_0^1 3_0^1$	$\tilde{X}^3\Sigma \leftarrow \tilde{X}^2\Pi_{3/2}$
I	25479	3319	*s+d*	3318.4	3298	1_0^2	$\tilde{X}^3\Sigma \leftarrow \tilde{X}^2\Pi_{3/2}$
g	25595	-195	*s+d*			0_0^0	$\tilde{a}^1\Delta \leftarrow \tilde{X}^2\Pi_{1/2}$
h	25735	-55	*s+d*			2_1^1	$\tilde{a}^1\Delta \leftarrow \tilde{X}^2\Pi\ (\Sigma^+_{1/2}, \Delta_{5/2})$
J	25790	0	*s+d*			0_0^0	$\tilde{a}^1\Delta \leftarrow \tilde{X}^2\Pi_{3/2}$
K	26053	263				2_0^1	$\tilde{a}^1\Delta \leftarrow \tilde{X}^2\Pi_{3/2}$
L	26320	530				2_0^2	$\tilde{a}^1\Delta \leftarrow \tilde{X}^2\Pi_{3/2}$
M	26622	832	*s+d*		916[d]	3_0^1	$\tilde{a}^1\Delta \leftarrow \tilde{X}^2\Pi_{3/2}$
N	27115	1325				$2_0^2 3_0^1$	$\tilde{a}^1\Delta \leftarrow \tilde{X}^2\Pi_{3/2}$
O	27450	1660	*s+d*		1796[d]	1_0^1	$\tilde{a}^1\Delta \leftarrow \tilde{X}^2\Pi_{3/2}$
P	27916	2126				$1_0^1 2_0^2$	$\tilde{a}^1\Delta \leftarrow \tilde{X}^2\Pi_{3/2}$
Q	28106	0	*s+d*			0_0^0	$\tilde{b}^1\Sigma^+ \leftarrow \tilde{X}^2\Pi_{3/2}$
R	28931	825	*s+d*			3_0^1	$\tilde{b}^1\Sigma^+ \leftarrow \tilde{X}^2\Pi_{3/2}$
S	29091	3301	*s+d*			1_0^2	$\tilde{a}^1\Delta \leftarrow \tilde{X}^2\Pi_{3/2}$
T	29751	1645	*s+d*			1_0^1	$\tilde{b}^1\Sigma^+ \leftarrow \tilde{X}^2\Pi_{3/2}$
U	31254	0	*p*			0_0^0	$\tilde{A}^3\Pi_2 \leftarrow \tilde{X}^2\Pi_{3/2}$
i	31330	76	*p*			0_0^0	$\tilde{A}^3\Pi_0 \leftarrow \tilde{X}^2\Pi_{1/2}$
V	31387	133	*p*		133	0_0^0	$\tilde{A}^3\Pi_1 \leftarrow \tilde{X}^2\Pi_{3/2}$
W	32061	807	*p*		788	3_0^1	$\tilde{A}^3\Pi_2 \leftarrow \tilde{X}^2\Pi_{3/2}$
X	32190	936	*p*		913	3_0^1	$\tilde{A}^3\Pi_1 \leftarrow \tilde{X}^2\Pi_{3/2}$
Y	33087	1833	*p*	1831[b]	1819	1_0^1	$\tilde{A}^3\Pi_2 \leftarrow \tilde{X}^2\Pi_{3/2}$
Z	33217	1963	*p*	1962[b]	1957	1_0^1	$\tilde{A}^3\Pi_1 \leftarrow \tilde{X}^2\Pi_{3/2}$

a) Ref [30] b) Ref[29] c) Ref[9] d) Ref[36]

intensities increase when the detachment photon energy decreases. These points will be discussed in detail later.

Photodetachment transitions to the two singlet states of CCS are shown in the bottom panel of Figure 3.13 and the top panel of Figure 3.14. There is no experimental information reported for the vibrational levels of the $\tilde{a}^1\Delta$ and $\tilde{b}^1\Sigma^+$ states, but the observed vibrational progressions within these bands have very similar spacings to those of the $\tilde{X}^3\Sigma^-$ band. The features are thus tentatively assigned to similar vibrational levels. Peaks K, M and O in Figure 3.13 are assigned to the 2_0^1, 3_0^1 and 1_0^1 fundamentals of the $\tilde{a}^1\Delta$ state, respectively, yielding vibrational frequencies of 1660 cm^{-1}, 263 cm^{-1} and 832 cm^{-1} for ν_1, ν_2 and ν_3. Using these values, the other transitions can be assigned to overtone and combination bands. Peak L is assigned to the 2_0^2 transition while peaks N and P are assigned to the $2_0^2 3_0^1$ and $1_0^1 2_0^2$ combination bands, respectively. Photodetachment transitions to the $\tilde{b}^1\Sigma^+$ state are displayed in the top panel of Figure 3.14. Peaks R and T are assigned to the 3_0^1 and 1_0^1 transitions, yielding fundamental frequencies of 825 cm^{-1} and 1645 cm^{-1} for these modes in the $\tilde{b}^1\Sigma^+$ state. Peak S does not fit any vibrational levels on the $\tilde{b}^1\Sigma^+$ state and is therefore assigned to the 1_0^2 transition of the $\tilde{a}^1\Delta$ state.

Transitions to the $\tilde{A}^3\Pi$ state are presented in the bottom panel of Figure 3.14. Peaks U and V are separated by 133 cm^{-1} and are assigned to the $^3\Pi_2$ and $^3\Pi_1$ spin-orbit components of the $\tilde{A}^3\Pi$ state origin transition. This splitting is in excellent agreement with calculations by Tarroni *et al.*[9] The $^3\Pi_0$ state is not observed because a photodetachment transition from a $^2\Pi_{3/2}$ anion state to a $^3\Pi_0$ neutral state requires a spin-flip which is nominally forbidden. The two remaining doublets are thus assigned to vibrations belonging to the same two spin-orbit states. Peaks W and X are assigned to the 3_0^1 fundamental while peaks Y and Z are assigned to the 1_0^1 level. This is the first observation of the ν_3 mode in the $\tilde{A}^3\Pi$ state of CCS. The $^3\Pi_2$ and $^3\Pi_1$ components of ν_3 are found to be 807 and 936 cm^{-1} above the $\tilde{A}^3\Pi_2$ ground-state, respectively. These values are slightly lower than the 788 and 913 cm^{-1} calculated by Tarroni *et al.*[9] The position of both ν_1 spin-orbit multiplets are in excellent agreement with previous observations (see Table 3.15).[29]

There are many smaller peaks in Figures 3.13 and 3.14 that appear to be from excited anion levels. Peaks b, e and g each lie 195 cm^{-1} below a major transition. These peaks are assigned to hot bands originating from the excited spin-orbit state ($\tilde{X}^2\Pi_{1/2}$) of the anion. The resulting spin-orbit splitting is slightly larger than the value of -164 cm^{-1} calculated by Riaplov *et al.*[27] Peak i, in Figure 3.14, is assigned to the 0_0^0 transition from the excited spin-orbit state of the anion to the neutral $\tilde{A}^3\Pi_0$ level. This transition does not require a spin-flip and is thus allowed. This assignment places the $^3\Pi_2$ level 271 cm^{-1} above the $^3\Pi_0$ level, approximately twice the splitting between the $^3\Pi_1$ and $^3\Pi_2$ level, as expected.

The remaining small peaks are attributed to transitions from anion excited vibrational states. Because the main spectral features are 0_0^0 transitions and the most likely populated vibrational states are the low-frequency v_2 bending modes, these peaks are assigned to sequence bands from bend-excited levels with $\Delta v_2 = 0$. The resulting energy level pattern is governed by Renner-Teller coupling in the $\tilde{X}^2\Pi$ state of CCS^-. The combination of spin-orbit and Renner-Teller coupling splits the degenerate v_2=1 state into four levels labeled $\Sigma^+_{1/2}$, $\Delta_{5/2}$, $\Delta_{3/2}$ and $\Sigma^+_{1/2}$. Panten *et al.*[41] calculated these levels to lie 310, 318, 480 and 492 cm^{-1} above the $\tilde{X}^2\Pi_{3/2}$ anion ground level, respectively. Using the experimental frequency of v_2 in the neutral $\tilde{X}^3\Sigma^-$ state, the $\Delta v_2 = 0$ sequence bands starting from the anion v_2=1 levels should have binding energies of -43, -51, -213 and -225 cm^{-1}, with respect to transitions originating from the anion v_2=0 level.. Peak c at -52 cm^{-1} is thus assigned to a sequence band with $\Delta v = 0$ transition starting from the $\Sigma^+_{1/2}$ and $\Delta_{5/2}$ anion v_2=1 components while peak a at -250 cm^{-1} originates from the $\Delta_{3/2}$ and $\Sigma^+_{1/2}$ components. Because of the low intensity and small splitting of these transitions, the individual Σ and Δ components could not be resolved in our spectra. Peaks f and h are assigned to a sequence bands from the $\Sigma^+_{1/2}$/ $\Delta_{5/2}$ anion v_2=1 states to the [100] level of the $X^3\Sigma^-$ state and the [000] level of the $a^1\Delta$ state, respectively.

3.3.4 Analysis and discussion

This study determines precise electron affinities of CCO and CCS. The value of EA(CCO) is found to be 2.3107±0.0006 eV, which lies within the uncertainty of the previous experimental value (2.310±0.012) determined by photoelectron spectroscopy[42]. The electron affinity of CCS is 2.7475±0.0006 eV; this is the first reported experimental value for EA(CCS). These values for the electon affinity are slightly larger than those predicted by calculations. Zengin *et al*[37]. calculated an EA of 2.22 eV for CCO while Riaplov *et al.*[27] predicted an EA of 2.68 eV for CCS.

The term energies of the four lowest electronic states of CCO and CCS determined in this study are listed in Table 3.16. For CCO, the singlet term energies are consistent with those previously determined by PE spectroscopy[42] but are more precise. The first two singlet states, $\tilde{a}^1\Delta$ and $\tilde{b}^1\Sigma^+$, are 0.6539±0.0006 eV and 1.0170±0.0006 eV above the ground-state, respectively, while the first excited triplet state lies 1.4408±0.0006 eV above the ground state. The term energy for the $\tilde{A}^3\Pi$ state of CCO found here agrees with previous observations from high-resolution absorption spectroscopy.[16,17] For the CCS radical, this study provides the first observation of the two low-lying singlet states. The $\tilde{a}^1\Delta$ and $\tilde{b}^1\Sigma^+$ states lie 0.4501±0.0006 eV and .7372±0.0006 eV above the ground-state. These values are in good agreement with recent calculations by Zhang *et al.*[38] that predicted term energies of 0.53 eV and 0.77 eV for the two first singlet states. Finally, the $\tilde{A}^3\Pi$ state is found to lie 1.1275±0.0006 eV above the ground state, in accord with previous observations and calculations.[27,29]

The features in the SEVI spectra also comprise unresolved rotational structure. We found that modeling the rotational contours using *s*-wave detachment selection rules[46] yielded corrections smaller than 2 cm^{-1} to the electron affinities and term energies reported here. This insignificant correction reflects the very similar anion and neutral geometries, a situation that places the peak center very close to the band origin for each vibronic transition. An anion rotational temperature of 75K was assumed in order to reproduce the ~20 cm^{-1} peak width observed at detachment close to threshold.

Table 3.16. Experimental and calculated values of the electron affinities and term energies of the four lowest-lying electronic states of CCO and CCS.

State	Current expt. T_0 ±0.0006 (eV)	Previous expt. T_0 (eV)	Calculated T_0 (eV)
CCO ($\tilde{X}^3\Sigma^-$)	0.0	0.0	0.0
($\tilde{a}^1\Delta$)	0.6539	0.653±0.012[a]	0.63[d]
($\tilde{b}^1\Sigma^+$)	1.0170	1.024±0.012[a]	1.00[d]
($\tilde{A}^3\Pi$)	1.4408	1.4401788±0.0000001[b]	1.34[d]
EA(CCO)	2.3107	2.310±0.012[a]	2.22[d]
CCS ($\tilde{X}^3\Sigma^-$)	0.0	0.0	0.0
($\tilde{a}^1\Delta$)	0.4501	--	0.53[e]
($\tilde{b}^1\Sigma^+$)	0.7372	--	0.77[e]
($\tilde{A}^3\Pi$)	1.1275	1.1339±0.002[c]	1.04[c]
EA(CCS)	2.7475	--	2.68[e]

a) Ref [42] b) Ref [17] c) Ref [27] d) Ref [37] e) Ref [38]

The numerous resolved vibrational transitions in the spectra of CCO and CCS allow us to probe the vibronic structure of these radicals. For example, in CCO and CCS, Herzberg-Teller vibronic coupling between the nearby $\tilde{X}^3\Sigma^-$ ground state and $\tilde{A}^3\Pi$ state can be detected by forbidden transitions in the bending mode. The SEVI spectrum of CCO^- displays vibrational activity only in the v_1 and v_3 modes for the four electronic states probed in this study. This is what is expected for a transition between two linear states with $C_{\infty v}$ symmetry, since both modes are totally symmetric. It is also in excellent agreement with Franck-Condon simulations based on the *ab initio* geometry and force constants of the anion and the uncoupled neutral states[37]. Carter *et al*.[8] recently calculated the spin-rovibronic levels of the $\tilde{X}^3\Sigma^-$ and $\tilde{A}^3\Pi$ states of CCO but neglected the vibronic coupling between the two states. Nonetheless, the calculated vibrational frequencies agree well with the experimental values measured here and in previous studies. This points out toward very weak vibronic interactions in the low-lying states of CCO.

However, the situation is different in the CCS^- SEVI spectrum, which exhibits considerably more vibrational activity, in general. All four bands show progressions in the ν_3 mode, whereas no activity in this mode was seen in the CCO^- SEVI spectra. Also, peaks B and E, which are assigned to 2_0^1 and $2_0^1 3_0^1$ transitions, involve odd Δv transitions of non-totally symmetric modes and are thus nominally forbidden in photoelectron spectroscopy. It is thus useful to simulate the spectrum within the Franck-Condon (FC) approximation to determine whether differences with CCO^- arise from simple geometric effects or from vibronic coupling, Duschinsky rotation, or other effects that can arise in PE spectroscopy. We note that FC simulations were carried out by Panten *et al*,[41] using calculated geometries and force constants for the anion and neutral ground states, but these simulations predict more activity in the ν_3 mode than the ν_1 mode. This result does not the experimental spectrum, in which the ν_1 mode is more active.

We have performed two sets of Franck-Condon simulations using the parallel mode approximation that are shown in Figure 3.15 along with the experimental spectra. For the first simulation, shown in the middle panel of Figure 3.15, we used the geometries and frequencies calculated by Panten *et al.*[41] for both the anion and neutral. This simulation yielded a PES spectrum that overestimates the v_3 activity and underestimates the v_1 activity. In the second simulation, shown in the bottom panel of Figure 3.15, we use the known experimental geometry[25] (R_{CC} = 1.2771Å and R_{CS}=1.6477Å) and vibrational frequencies[30] of the $\tilde{X}^3\Sigma^-$ neutral state and the anion bonds length was adjusted to fit the experimental spectra. The best fit was obtained with a CC bond length of 1.268Å and a CS bond length of 1.646Å. These values are close to the bonds length calculated by Panten *et al.*[41] The fact that the intensities of the v_1 and v_3 features could be reproduced with a reasonable anion geometry is consistent with the calculations of Tarroni et al.[9] which found mixing of only 2-3% for the v_1 and v_3 modes. Moreover, the vibrational frequencies calculated by Tarroni *et al*[9]. for these two modes agree well with those found in this study.

The only features not accounted by the FC simulation are the two peaks involving odd quanta of bending excitation. These two nominally forbidden peaks have a different PAD than the other $\tilde{X}^3\Sigma^-$ features, which is reminiscent of the C_2H^- SEVI spectrum[45]. The "p-wave" character of these features is a clear indication that these features are gaining intensity from vibronic coupling between $\tilde{X}^3\Sigma^-$ and $\tilde{A}^3\Pi$ states induced by the bending mode. The "*p*" PAD's of peak B and E also explains why there relative intensities is larger at lower photodetachment energies.

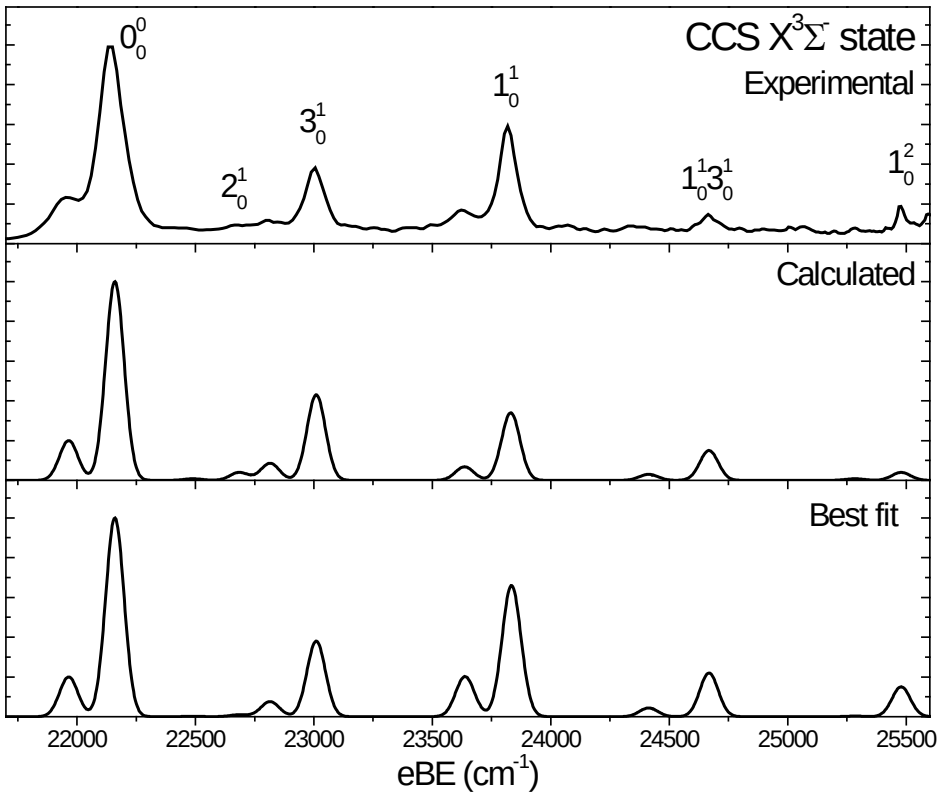

Figure 3.15 Franck-Condon simulation of the CCS $\tilde{X}^3\Sigma^-$ state photodetachment spectrum. The top panel displays the SEVI spectrum taken at photon energy of 26316 cm^{-1}. The middle panel shows the simulated spectra using the geometries and frequencies calculated by Panten *et al.*[41] The lower panel displays the best fit obtained by optimizing the anion geometry. (see text for details)

According the Wigner threshold law[44], the photodetachment cross-section (σ) near threshold is given by

$$\sigma \propto (\Delta E)^{l+½} \qquad (3.1)$$

where ΔE is the difference between the energy of the photo and the detachment threshold and l is the angular momentum of the ejected electron. In the energy range presented in Figure 3.13, the "d" component (l=2) cross-section of the (s+d)-wave drops faster than the cross-section for a p-wave (l=1) detachment when the photon energy is lowered. This leads to increased intensities of peak B and E relative to the others transitions as the photodetachment energy is lowered. Note that this trend in the relative intensities is opposite to what was observed in the C_2H^- SEVI spectrum because the allowed transitions were almost pure s-wave with very small d-wave contribution[45].

3.3.5 Conclusions

The high resolution photoelectron spectra of CCO and CCS using the SEVI technique are reported. This work provides precise electron affinities as well as term energies of the neutral $\tilde{X}^3\Sigma^-$, $\tilde{a}^1\Delta$, $\tilde{b}^1\Sigma^+$ and $\tilde{A}^3\Pi$ electronic states of these two species. Several previously unobserved vibronic transitions on these four states are resolved. The CCS spectrum reveals evidence of small vibronic coupling between the electronic states. The analysis of hot bands allowed the first experimental observation of the spin-orbit orbit splitting on the $\tilde{X}^2\Pi$ ground state of CCO and CCS.

References

1) M. Ohishi, H. Suzuki, S. I. Ishikawa, C. Yamada, H. Kanamori, W. M. Irvine, R. D. Brown, P. D. Godfrey, and N. Kaifu, *Astrophys. J.* **380** (1), L39 (1991).
2) S. Saito, K. Kawaguchi, S. Yamamoto, M. Ohishi, H. Suzuki, and N. Kaifu, *Astrophys. J.* **317** (2), L115 (1987).
3) K. D. Bayes, *J. Chem. Phys.* **52** (3), 1093 (1970).
4) K. H. Becker and K. D. Bayes, *J. Chem. Phys.* **48** (2), 653 (1968).
5) A. Fontijn and S. E. Johnson, *J. Chem. Phys.* **59** (12), 6193 (1973).
6) I. de Gregorio-Monsalvo, J. F. Gomez, O. Suarez, T. B. H. Kuiper, L. F. Rodriguez, and E. Jimenez-Bailon, *Astrophys. J.* **642** (1), 319 (2006).
7) W. D. Langer, T. Velusamy, T. B. H. Kuiper, S. Levin, E. Olsen, and V. Migenes, *Astrophys. J.* **453** (1), 293 (1995).
8) S. Carter, N. C. Handy, and R. Tarroni, *Mol. Phys.* **103** (6-8), 1131 (2005).
9) R. Tarroni, S. Carter, and N. C. Handy, *Mol. Phys.* **105** (9), 1129 (2007).
10) Y. Ohshima, Y. Endo, and T. Ogata, *J. Chem. Phys.* **102** (4), 1493 (1995).
11) C. Yamada, S. Saito, H. Kanamori, and E. Hirota, *Astrophys. J.* **290** (2), L65 (1985).
12) H. Abe, Y. Kawamoto, M. Fujitake, N. Ohashi, T. Momose, and T. Shida, *J. Mol. Spect.* **180** (2), 277 (1996).
13) H. Abe, T. Kikuchi, K. Takahashi, M. Fujitake, and N. Ohashi, *J. Mol. Spect.* **167** (2), 353 (1994).
14) H. Abe, M. Mukai, M. Fujitake, and N. Ohashi, *J. Mol. Spect.* **195** (2), 317 (1999).
15) Z. Abusara, T. S. Sorensen, and N. Moazzen-Ahmadi, *J. Chem. Phys.* **119** (18), 9491 (2003).
16) Deviller.C and D. A. Ramsay, *Can. J. Phys.* **49** (22), 2839 (1971).
17) M. Fujitake, R. Kiryu, and N. Ohashi, *J. Mol. Spect.* **154** (1), 169 (1992).
18) M. E. Jacox, D. E. Milligan, N. G. Moll, and W. E. Thompson, *J. Chem. Phys.* **43** (10P1), 3734 (1965).
19) N. Moazzen-Ahmadi and R. T. Boere, *J. Chem. Phys.* **110** (2), 955 (1999).
20) N. Moazzen-Ahmadi, D. W. D. Sandilands, and R. T. Boere, *Chem. Phys. Lett.* **265** (6), 563 (1997).
21) N. Ohashi, R. Kiryu, S. Okino, and M. Fujitake, *J. Mol. Spect.* **157** (1), 50 (1993).

22) C. Yamada, H. Kanamori, H. Horiguchi, S. Tsuchiya, and E. Hirota, *J. Chem. Phys.* **84** (5), 2573 (1986).

23) W. M. Pitts, V. M. Donnelley, A. P. Baronavski, and J. R. McDonald, *Chem. Phys.* **61** (3), 451 (1981).

24) M. Ikeda, Y. Sekimoto, and S. Yamamoto, *J. Mol. Spect.* **185** (1), 21 (1997).

25) S. Yamamoto, S. Saito, K. Kawaguchi, Y. Chikada, H. Suzuki, N. Kaifu, S. Ishikawa, and M. Ohishi, *Astrophys. J.* **361** (1), 318 (1990).

26) G. Maier, H. P. Reisenauer, and R. Ruppel, *Eur. J. Org. Chem.* (20), 4197 (2004).

27) E. Riaplov, M. Wyss, J. P. Maier, D. Panten, G. Chambaud, P. Rosmus, and J. Fabian, *J. Mol. Spect.* **222** (1), 15 (2003).

28) H. Y. Wang, J. Szczepanski, A. Cooke, P. Brucat, and M. Vala, *Int. J. Quant. Chem.* **102** (5), 806 (2005).

29) M. Nakajima, Y. Sumiyoshi, and Y. Endo, *J. Chem. Phys.* **117** (20), 9327 (2002).

30) A. J. Schoeffler, H. Kohguchi, K. Hoshina, Y. Ohshima, and Y. Endo, *J. Chem. Phys.* **114** (14), 6142 (2001).

31) D. Begue, P. Carbonniere, and C. Pouchan, *J. Phys. Chem. A* **105** (50), 11379 (2001).

32) S. T. Brown, Y. Yamaguchi, and H. F. Schaefer, *J. Phys. Chem. A* **104** (16), 3603 (2000).

33) S. Mishra, W. Domcke, and L. V. Poluyanov, *Chem. Phys. Lett.* **446** (4-6), 256 (2007).

34) I. Perez-Juste, A. M. Grana, L. Carballeira, and R. A. Mosquera, *J. Chem. Phys.* **121** (21), 10447 (2004).

35) Y. M. Xie and H. F. Schaefer, *J. Chem. Phys.* **96** (5), 3714 (1992).

36) Z. L. Cai, X. G. Zhang, and X. Y. Wang, *Chem. Phys. Lett.* **213** (1-2), 168 (1993).

37) V. Zengin, B. J. Persson, K. M. Strong, and R. E. Continetti, *J. Chem. Phys.* **105** (22), 9740 (1996).

38) J. L. Zhang, W. P. Wu, L. B. Wang, and Z. X. Cao, *J. Chem. Phys.* **124** (12) (2006).

39) J. Fulara, M. Grutter, M. Wyss, and J. P. Maier, *J. Phys. Chem. A* **102** (20), 3459 (1998).

40) D. Panten, G. Chambaud, P. Rosmus, and P. J. Knowles, *Chem. Phys. Lett.* **311** (5), 390 (1999).

41) D. Panten, G. Chambaud, P. Rosmus, E. Riaplov, and J. P. Maier, *Z. Phys. Chem.* **217** (3), 231 (2003).

42) H. Choi, D. H. Mordaunt, R. T. Bise, T. R. Taylor, and D. M. Neumark, *J. Chem. Phys.* **108** (10), 4070 (1998).

43) J. M. Oakes, M. E. Jones, V. M. Bierbaum, and G. B. Ellison, *J. Phys. Chem.* **87** (24), 4810 (1983).

44) E. P. Wigner, *Phys. Rev.* **73** (9), 1002 (1948).

45) J. Zhou, E. Garand, W. Eisfeld, and D. M. Neumark, *J. Chem. Phys.* **127** (3) (2007).

46) Y. X. Zhao, I. Yourshaw, G. Reiser, C. C. Arnold, and D. M. Neumark, *J. Chem. Phys.* **101** (8), 6538 (1994).

3.4 Slow photoelectron velocity-map imaging spectroscopy of C_3O^- and C_3S^- anions

Abstract

High-resolution photodetachment spectra of C_3O^- and C_3S^- using slow photoelectron velocity-map imaging (SEVI) spectroscopy are reported. Well-resolved transitions to the neutral $\tilde{X}^1\Sigma^+$ state are seen for both species. The electron affinities of C_3O and C_3S are determined to be EA(C_3O)=1.237±0.003 eV and EA(C_3S)=1.5957±0.0010 eV, respectively. Several vibrational frequencies for gas phase C_3O and C_3S are determined for the first time. The long progression of bending modes observed in the spectra is consistent with electronic structure calculations predicting that the C_3O^- and C_3S^- have bent equilibrium geometries.

3.4.1 Introduction

The heteroatom-doped C_nO and C_nS linear carbon chains are important interstellar species. The first three members (n=1-3) for each species have been identified in interstellar sources by their rotational spectra.[1-8] In this section, we continue our investigation of these two isovalent series of clusters via negative ion photodetachment.[9] The high resolution photoelectron spectra of the C_3O^- and C_3S^- anions are reported, providing a detailed probe of the neutral and anionic ground electronic states of these species.

The C_3O radical has been studied by microwave spectroscopy,[10,11] millimeter-wave spectroscopy,[12] and infrared absorption in rare-gas matrices[13,14] and in the gas-phase.[15] Similarly, C_3S has been studied by microwave spectroscopy[6,16,17] and by infrared absorption in rare-gas matrices[18,19] and in the gas-phase.[20] Several theoretical studies on the equilibrium geometry, electronic structure and vibrational spectra of these two species have been reported.[14,21-31] The combination of high-level *ab initio* calculations and microwave spectroscopy of isotopically substituted species has yielded very accurate bond lengths for the neutral C_3O and C_3S.[25,28]

The corresponding C_3O^- and C_3S^- anions have received considerably less attention. The only experimental data on C_3O^- comes from the photoelectron (PE) spectrum of Oakes and Ellison.[32] This spectrum featured an extended, partially resolved vibrational progression with a frequency of 600±35 cm^{-1}, indicating a large geometry change between the anion and the neutral. The first resolved peak was assigned to the origin transition, yielding an electron affinity (EA) of 1.34±0.15 eV for C_3O. Rienstra-Kiracofe *et al.*[23] subsequently performed electronic structure calculations on C_3O and C_3O^- using the coupled cluster method with single, double and non-iterative triple excitations (CCSD(T)) and found an EA of 0.93±0.1 eV, raising questions about the experimental assignment. No experimental or theoretical studies on the C_3S^- anion have been reported yet.

In this section we present high-resolution photodetachment spectra of C_3O^- and C_3S^- using slow photoelectron velocity-map imaging (SEVI). Well-resolved vibrational transitions to the neutral $\tilde{X}^1\Sigma^+$ state are seen for both species. We obtain a revised EA(C_3O) and the first determination of EA(C_3S). The ν_3, ν_4, and ν_5 frequencies for neutral, gas phase C_3O and C_3S are also determined. Extended progressions of bending modes observed in the spectra are consistent with both anions having bent equilibrium geometries.

3.4.2 Experimental details

The SEVI technique and apparatus has been described in detail in chapter 2. In this experiment, C_3O^- anions were produced from of a gas mixture comprising 1% acetylene and 20% CO_2 in a balance of Ar. Similarly, C_3S^- anions were produced from 1% acetylene and 1% CS_2 in a balance of argon. The gas mixture, at a stagnation pressure of 300 psi, was expanded into the source vacuum chamber through an Even-Lavie pulsed valve[33] equipped with a grid discharge.

The apparatus was calibrated by acquiring SEVI images of atomic oxygen[34] at several different photon energies. With the -350V VMI repeller voltage used in this study, the full widths at half maximum of the oxygen peaks were 7.5 cm^{-1} at 150 cm^{-1} eKE and 18 cm^{-1} at 715 cm^{-1}.

3.4.3 Experimental results

The transformed SEVI images of C_3O^- and C_3S^- taken at photon energies of 14493 cm^{-1} and 15037 cm^{-1}, respectively, are presented in Figure 3.16. Both images display a similar series of closely spaced doublets. However, the two images display features with different PADs, as seen most clearly on the outermost rings. In the C_3O^- image, these rings have more intensity in the direction parallel to the laser electric field, corresponding to $\beta>0$. In contrast, features in the C_3S^- images are more intense in the direction perpendicular to the electric field, indicating $\beta<0$. Figure 3.17 shows the β values for the main features in the SEVI images shown in Figure 1 as a function of their electron kinetic energy (eKE). The highest energy features (outermost ring) have $\beta= 0.6\pm0.1$ and $\beta= -0.8\pm0.1$ for C_3O^- and C_3S^-, respectively. In both images, the rings become more isotropic ($\beta=0$) with decreasing radius, consistent with our expectation that *s*-wave detachment, when allowed, dominates near threshold.[35,36]

Photoelectron spectra obtained from the C_3O^- and C_3S^- SEVI images are shown in Figure 3.18 and 3.19. Each spectrum is composed of several SEVI traces taken at different photon energies and joined together. The C_3O^- spectrum comprises an extended progression of multiplets spread over more than 7000 cm^{-1}. Its most prominent attribute is the progression of peaks labeled A_n, spaced by an average of 603 cm^{-1}. The peak with maximum intensity is A_8, which is located 4801 cm^{-1} above A_0. A second, slightly less intense progression B_n has a similar spacing; each peak B_n lies 111 cm^{-1} above the corresponding A_n peak, on average. The SEVI spectrum shows considerably more structure than the lower resolution PE spectra of Oakes and Ellison,[32] in which only a single, partially-resolved resolved progression of peaks spaced by 600 cm^{-1} was observed, with no evidence for the multiplet structure seen here.

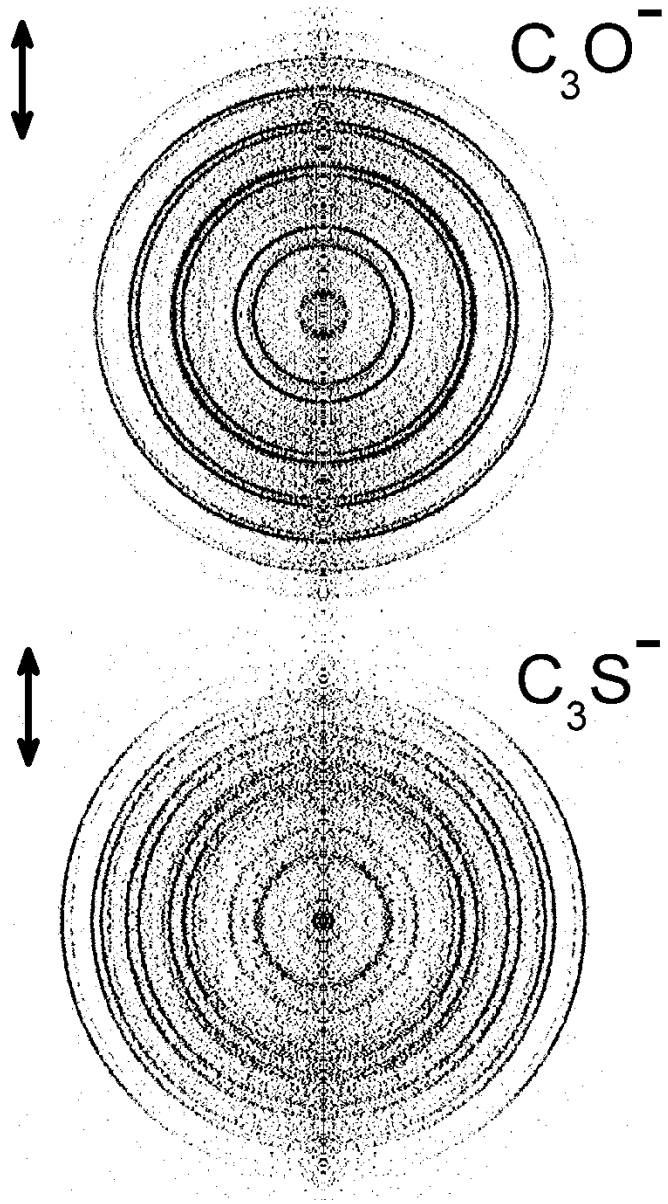

Figure 3.16. Inverse-Abel transformed SEVI images of C_3O^- (top) and C_3S^- (bottom) taken at photon energies of 14493 cm^{-1} and 15037 cm^{-1}, respectively. Arrows indicate the polarization vector of the laser.

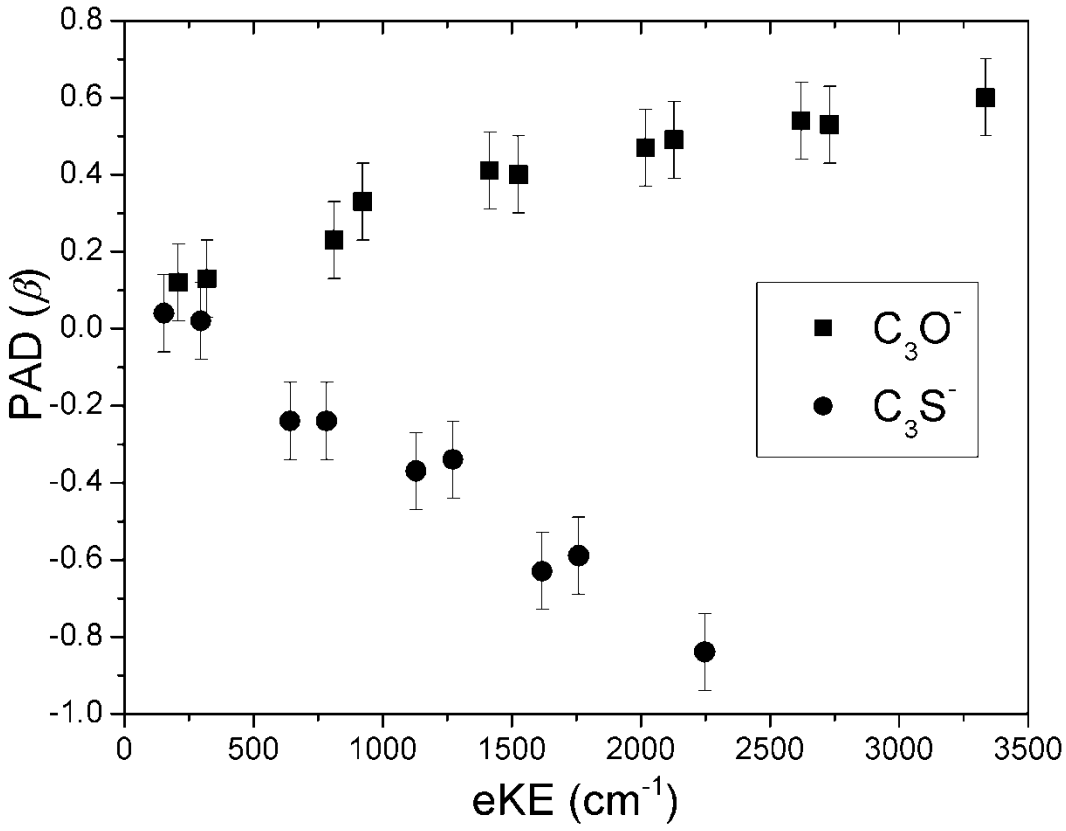

Figure 3.17. Anisotropy parameters β for the main features in the C_3O^- (squares) and C_3S^- (circles) images shown in Figure 3.16 as a function of their electron kinetic energy (eKE).

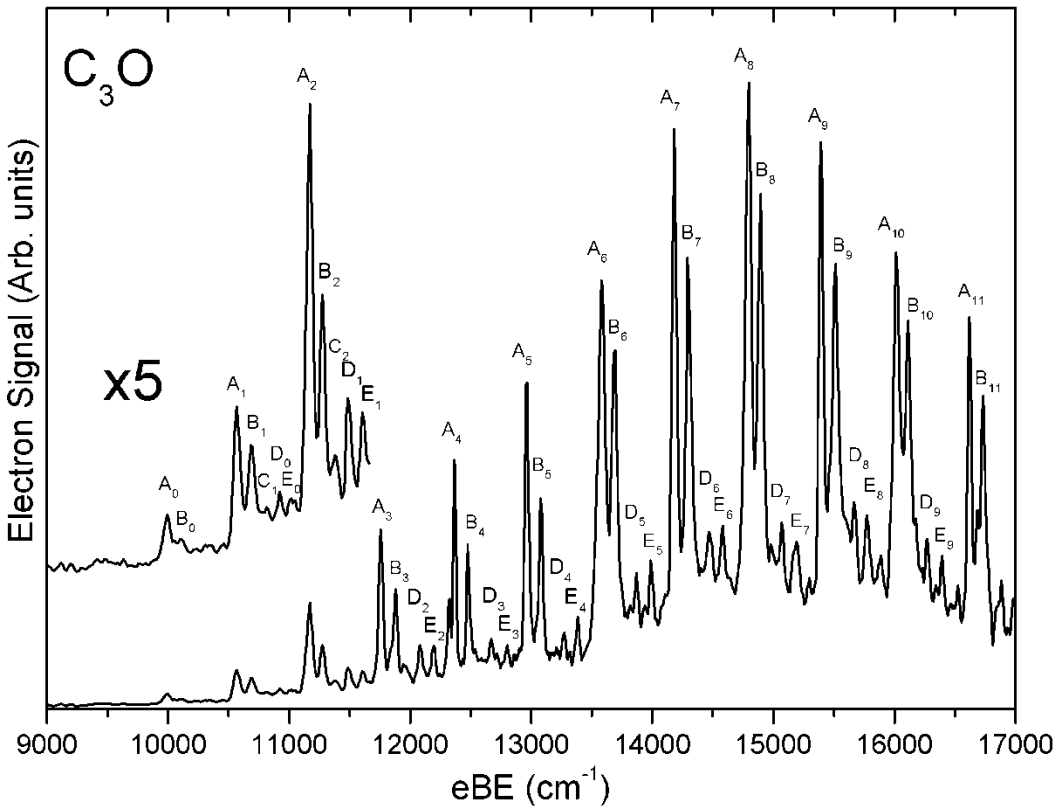

Figure 3.18. SEVI spectra of C_3O^- covering the electron binding energy range of 9000 cm^{-1} to 17000 cm^{-1}.

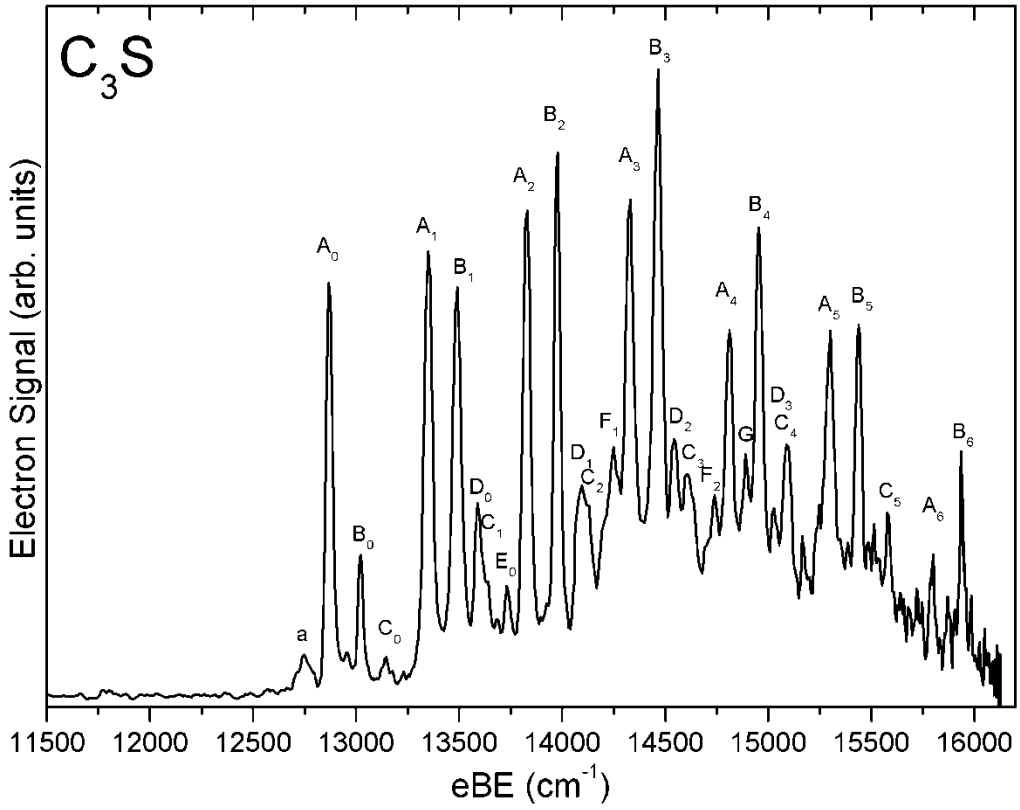

Figure 3.19. SEVI spectra of C_3S^- covering the electron binding energy range of 11500 cm^{-1} to 16250 cm^{-1}.

Table 3.17. Peak positions, shifts from origin and assignments for the C_3O^- SEVI spectra.

Peak Label	Position (cm^{-1})	Shift (cm^{-1})	Assignment	Peak Label	Position (cm^{-1})	Shift (cm^{-1})	Assignment
A_0	9988	0	0_0^0	E_4	13383	3395	$3_0^1 4_0^4 5_0^1$
B_0	10097	109	5_0^1	A_6	13582	3594	4_0^6
A_1	10569	581	4_0^1	B_6	13687	3699	$4_0^6 5_0^1$
B_1	10692	704	$4_0^1 5_0^1$	D_5	13868	3880	$3_0^1 4_0^5$
C_1	10813	825	$4_0^1 5_0^2$	E_5	13991	4003	$3_0^1 4_0^5 5_0^1$
D_0	10923	935	3_0^1	A_7	14183	4195	4_0^7
E_0	11029	1041	$3_0^1 5_0^1$	B_7	14294	4306	$4_0^7 5_0^1$
A_2	11169	1181	4_0^2	D_6	14473	4485	$3_0^1 4_0^6$
B_2	11273	1285	$4_0^2 5_0^1$	E_6	14591	4603	$3_0^1 4_0^2 5_0^1$
C_2	11375	1387	$4_0^2 5_0^2$	A_8	14789	4801	4_0^8
D_1	11495	1507	$3_0^1 4_0^1$	B_8	14898	4910	$4_0^8 5_0^1$
E_1	11612	1624	$3_0^1 4_0^1 5_0^1$	D_7	15068	5080	$3_0^1 4_0^7$
A_3	11758	1770	4_0^3	E_7	15186	5198	$3_0^1 4_0^2 5_0^1$
B_3	11879	1891	$4_0^3 5_0^1$	A_9	15395	5407	4_0^9
D_2	12083	2095	$3_0^1 4_0^2$	B_9	15505	5517	$4_0^9 5_0^1$
E_2	12195	2207	$3_0^1 4_0^2 5_0^1$	D_8	15677	5689	$3_0^1 4_0^8$
A_4	12366	2378	4_0^4	E_8	15780	5792	$3_0^1 4_0^2 5_0^1$
B_4	12475	2487	$4_0^4 5_0^1$	A_{10}	16008	6020	4_0^{10}
D_3	12668	2680	$3_0^1 4_0^3$	B_{10}	16112	6124	$4_0^{10} 5_0^1$
E_3	12802	2814	$3_0^1 4_0^3 5_0^1$	D_9	16280	6292	$3_0^1 4_0^9$
A_5	12962	2974	4_0^5	E_9	16393	6405	$3_0^1 4_0^2 5_0^1$
B_5	13081	3093	$4_0^5 5_0^1$	A_{11}	16621	6633	4_0^{11}
D_4	13270	3282	$3_0^1 4_0^4$	B_{11}	16726	6738	$4_0^{11} 5_0^1$

Table 3.18. Peak positions, shifts from origin and assignments for the C_3S^- SEVI spectra.

Peak Label	Position (cm^{-1})	Shift (cm^{-1})	Assignment	Peak Label	Position (cm^{-1})	Shift (cm^{-1})	Assignment
a	12752	-118	4_1^0	B_3	14453	1583	$4_0^3 5_0^1$
A_0	12870	0	0_0^0	D_2	14532	1662	$3_0^1 4_0^2$
B_0	13021	151	5_0^1	C_3	14599	1729	$4_0^3 5_0^2$
C_0	13142	272	5_0^2	F_1	14740	1870	$3_0^2 4_0^1$
A_1	13348	478	4_0^1	A_4	14811	1941	4_0^4
B_1	13490	621	$4_0^1 5_0^1$	G	14891	2021	$3_0^2 4_0^1 5_0^1$
D_0	13591	721	3_0^1	B_4	14955	2085	$4_0^4 5_0^1$
C_1	13633	763	$4_0^1 5_0^2$	D_3	15026	2156	$3_0^1 4_0^3$
E_0	13735	865	$3_0^1 5_0^1$	C_4	15092	2222	$4_0^4 5_0^2$
A_2	13829	959	4_0^2	A_5	15298	2428	4_0^5
B_2	13976	1106	$4_0^2 5_0^1$	B_5	15438	2568	$4_0^5 5_0^1$
D_1	14073	1203	$3_0^1 4_0^1$	C_5	15581	2712	$4_0^5 5_0^2$
C_2	14116	1246	$4_0^2 5_0^2$	A_6	15797	2927	4_0^6
F_0	14252	1382	3_0^2	B_6	15939	3069	$4_0^6 5_0^1$
A_3	14319	1449	4_0^3				

The C_3S^- spectrum displays a similar pattern. There are two clear progressions, A_n and B_n. The progression A_n has a characteristic spacing of 488 cm^{-1} and each peak B_n appears, on average, 142 cm^{-1} above the corresponding peak A_n The A_n and B_n progressions are less extended than in C_3O^-, and the most intense feature in the C_3S^- spectrum (B_3) is found 1583 cm^{-1} above A_0. In both spectra, lower intensity peaks labeled C_n, D_n and E_n are also resolved between the main transitions. Peak positions in the C_3O^- and C_3S^- SEVI spectra are presented in Tables 3.17 and 3.18.

3.4.4 Electronic structure calculations

Electronic structure calculations were performed on the relevant neutral and anionic states of C_3O and C_3S to produce, at a uniform level of theory, all the geometries and vibrational frequencies necessary to interpret the photoelectron spectra. Our calculations were

carried out with DFT using the Becke three-parameter Lee,Yang, and Parr exchange-correlation functional[37,38] (B3LYP) and the augmented correlation consistent polarized valence triple-zeta basis set[39] (AVTZ). All computations were performed using the GAUSSIAN03 program.[40]

The calculated geometries and relative energies of the different states are shown in Table 3.19, while the harmonic vibrational frequencies are presented in Table 3.20. The bond lengths of the neutral $^1\Sigma^+$ ground state of C_3O and C_3S calculated here are all found to lie within 0.007Å of the recommended values[25,28] for these species. Both neutral species show a short C_1C_2 bond and a longer C_2C_3 bond. For the C_3O^- and C_3S^- anions, we found a bent $^2A'$ ground state. In both species, the $^2\Pi$ linear geometry is found to be a first-order transition state between the two equivalent bent structures. For C_3O^-, the bent minimum is found to be 0.17 eV below the linear geometry. The $^2A'$ state has a C_2C_3O angle of 142.5° and a $C_1C_2C_3$ angle of 167.8°. This geometry is very similar to the higher level CCSD(T)/AVTZ result of Rienstra-Kiracofe *et al.*[23] In C_3S^-, the bent minimum is only 0.02 eV below the linear geometry; the C_2C_3S angle is 171.0° and the $C_1C_2C_3$ angle is 177.7°. For C_3S^-, we found very similar lengths for the two CC bonds and a slightly longer CS bond than in the corresponding neutral. In contrast, for C_3O^- we found a short C_1C_2 bond, a long C_2C_3 bond and a longer CO bond.

Table 3.19. Calculated relative energies and geometries at the B3LYP/AVTZ level of theory. All bond lengths are in Å. The recommended bond length values for the neutral $^1\Sigma^+$ C_3O (Ref 28) and $^1\Sigma^+$ C_3S (Ref 25) are shown in parentheses

	State	ΔE (eV)	R(C_1C_2)	R(C_2C_3)	R(C_3X)	θ($C_1C_2C_3$)	θ(C_2C_3X)	θ($C_1C_2C_3X$)
C_3O								
Anion	$^2A'$	0.0	1.261	1.357	1.210	167.8	142.5	180
	$^2\Pi$ [a)]	0.17	1.296	1.290	1.207	180	180	--
Neutral	$^1\Sigma^+$	1.21	1.266	1.294	1.149	180	180	--
			(1.2728)	(1.2971)	(1.1485)			
C_3S								
Anion	$^2A'$	0.0	1.286	1.296	1.606	177.7	171.0	180
	$^2\Pi$ [a)]	0.02	1.287	1.293	1.605	180	180	--
Neutral	$^1\Sigma^+$	1.73	1.274	1.289	1.542	180	180	--
			(1.2810)	(1.2927)	(1.5374)			

[a)] First-order transition state

Table 3.20. Calculated harmonic frequencies (cm^{-1}) at the B3LYP/AVTZ level of theory.

	State	ν_1 CCC asym str.	ν_2 CCX asym str.	ν_3 CCCX sym str.	ν_4 CCX bend	ν_5 CCC bend
C_3O						
Anion	$^2A'$	1936	1766	915	527	239/226
	$^2\Pi$ [a)]	2084	1622	923	609/324i	285/203
Neutral	$^1\Sigma^+$	2329	1975	966	602	142
C_3S						
Anion	$^2A'$	1840	1440	670	52	360/270
	$^2\Pi$ [a)]	1842	1443	669	511/38i	354/191
Neutral	$^1\Sigma^+$	2136	1566	739	498	161

[a)] First-order transition state

3.4.5 Analysis and discussion

In this section, we present a detailed assignment of the features observed in the SEVI spectra. In addition to the calculations presented here, the neutral C_3O and C_3S vibrational frequencies observed in argon matrix isolation experiments[14,18] and the anharmonic frequency calculations of Hochlaf and co-workers[24,31] are used as guidelines for the assignments. The peak assignments are summarized in Table 3.17 and 3.18.

For both species, the main progression labeled A_n is assigned to 4_0^n transitions involving the C_2C_3X bending vibration. In C_3O, the position of the 4_0^1 transition (peak A_1) yields 581 cm^{-1} for the ν_4 fundamental, in excellent agreement with the value of 580.0 cm^{-1} measured in an argon matrix[14] and the calculated value[24] of 584.4 cm^{-1}. Similarly, the ν_4 fundamental in C_3S is found to be 478 cm^{-1}. Our spectra represent the first experimental observation of this mode in C_3S but its frequency is in excellent agreement with the calculated value[31] of 475.8 cm^{-1}. The peaks labeled B_n are assigned to the $4_0^n 5_0^1$ combination bands. The ν_5 mode corresponds to the low-frequency $C_1C_2C_3$ carbon chain bending mode. The position of peak B_0 yields ν_5 fundamentals of 109 cm^{-1} and 151 cm^{-1} for C_3O and C_3S, respectively; both values are the first direct experimental observation of these modes. Our ν_5 frequency for C_3O is in good agreement with the value of 120 cm^{-1} estimated by Botschwina and Reisenauer[15] from *l*-type doubling and rotational constants. The calculated ν_5 frequencies[24,31] of 114.0 cm^{-1} and 145.0 cm^{-1} for C_3O and C_3S, respectively, are again in excellent agreement with the value found here. The spacing between peaks A_n and C_n peaks is found to be about twice the A_n-B_n splitting and thus the C_n peaks are assigned to the $4_0^n 5_0^2$ transitions.

In the spectra of both species, the spacing in the less intense progression labeled D_n is similar to the ν_4 frequency and the first peak D_0 appears only after peak A_1. The D_n progression is thus assigned to the $3_0^1 4_0^n$ transitions. The ν_3 mode is the symmetric stretch of the three bonds. The position of peak D_0 yields a ν_3 fundamental of 935 cm^{-1} and 721 cm^{-1} for C_3O and C_3S, respectively. This assignment is consistent with the values of 939.1 cm^{-1} and 725.6 cm^{-1} found for C_3O and C_3S, respectively, in argon matrix isolation experiments.[14,18] The D_n-E_n spacing is similar to the ν_5 frequency and thus the E_n peaks are assigned to the $3_0^1 4_0^n 5_0^1$ transitions. A few extra peaks are found in the C_3S^- spectra. The peaks labeled F_n are assigned to the $3_0^2 4_0^n$ transitions while peak G is assigned to the $3_0^1 4_0^1 5_0^1$ transition. The small peak labeled a is found 118 cm^{-1} below the origin transition and is assigned to a hot band transition. The most likely excited vibration in C_3S^- is the ν_4 mode for which the calculated frequency is only 52 cm^{-1}. Peak a is thus assigned to the 4_0^1 transition, yielding a 118 cm^{-1} frequency for this mode in the anion. The difference between the experimental and calculated frequencies reflects the sensitivity of this mode to the height of the small barrier to linearity.

For both species, the position of peak A_0 yields the adiabatic electron affinity. These values are determined as EA(C_3O)= 1.237±0.003 eV and EA(C_3S)= 1.5957±0.0010 eV. The uncertainty on the electron affinity of C_3O is slightly larger than on C_3S because the very weak intensity of the origin peak in C_3O prevented us from acquiring a spectrum at photon energy close to the detachment threshold. The EA of C_3O found here is within the large error bars of the previous value of 1.34±0.15 eV, but the feature assigned as the band origin by Oakes and Ellison[32] corresponds to the A_1/ B_1 doublet of the SEVI spectra. The revised EA(C_3O) is in excellent agreement with the value of 1.21 eV B3LYP/AVTZ calculated here but is still ~0.3 eV larger than the value of 0.93±0.1 eV calculated by Rienstra-Kiracofe *et al.*[23] at the higher CCSD(T)/AVTZ level of theory. The experimental EA of C_3S is reported for the first time and is found to be slightly smaller than the value of 1.73 eV calculated at the B3LYP/AVTZ level. The electron affinities and vibrational frequencies determined in this study are summarized in Table 3.21.

The SEVI spectra of C_3O^- and C_3S^- exhibit substantial bending activity, as expected for photodetachment from bent anions to linear neutral states. The longer ν_4 progression in the C_3O^- spectrum is consistent with our calculations indicating that this anion is considerably more bent than C_3S^-. However, even the relatively small deviation from linearity in the calculated C_3S^- geometry is sufficient to induce substantial bend progressions in the SEVI spectrum.

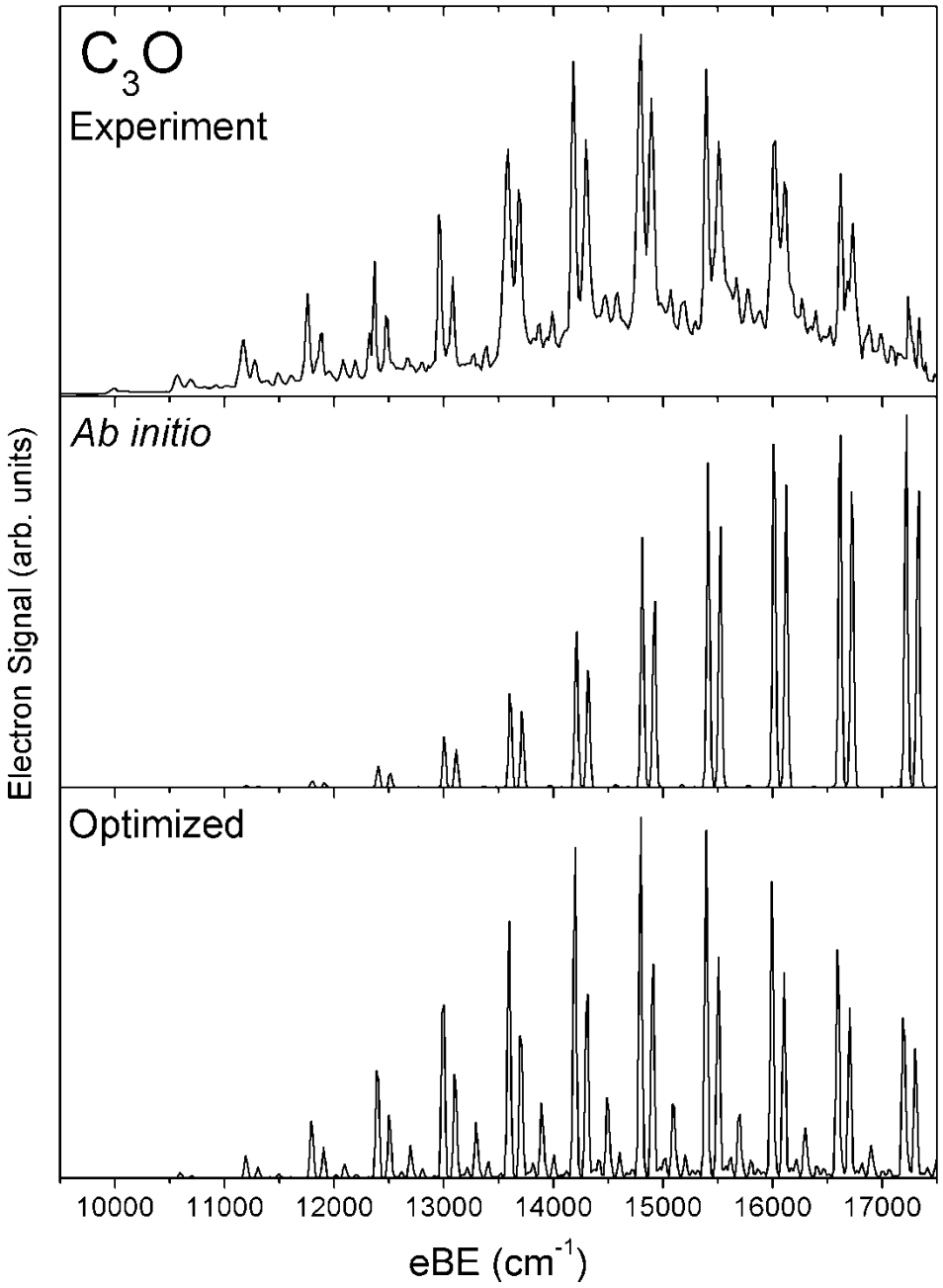

Figure 3.20. Franck-Condon simulation of the C_3O^- SEVI spectra using *ab initio* (center) and optimized (lower panel) parameters. Experimental spectrum is shown in top panel for comparison.

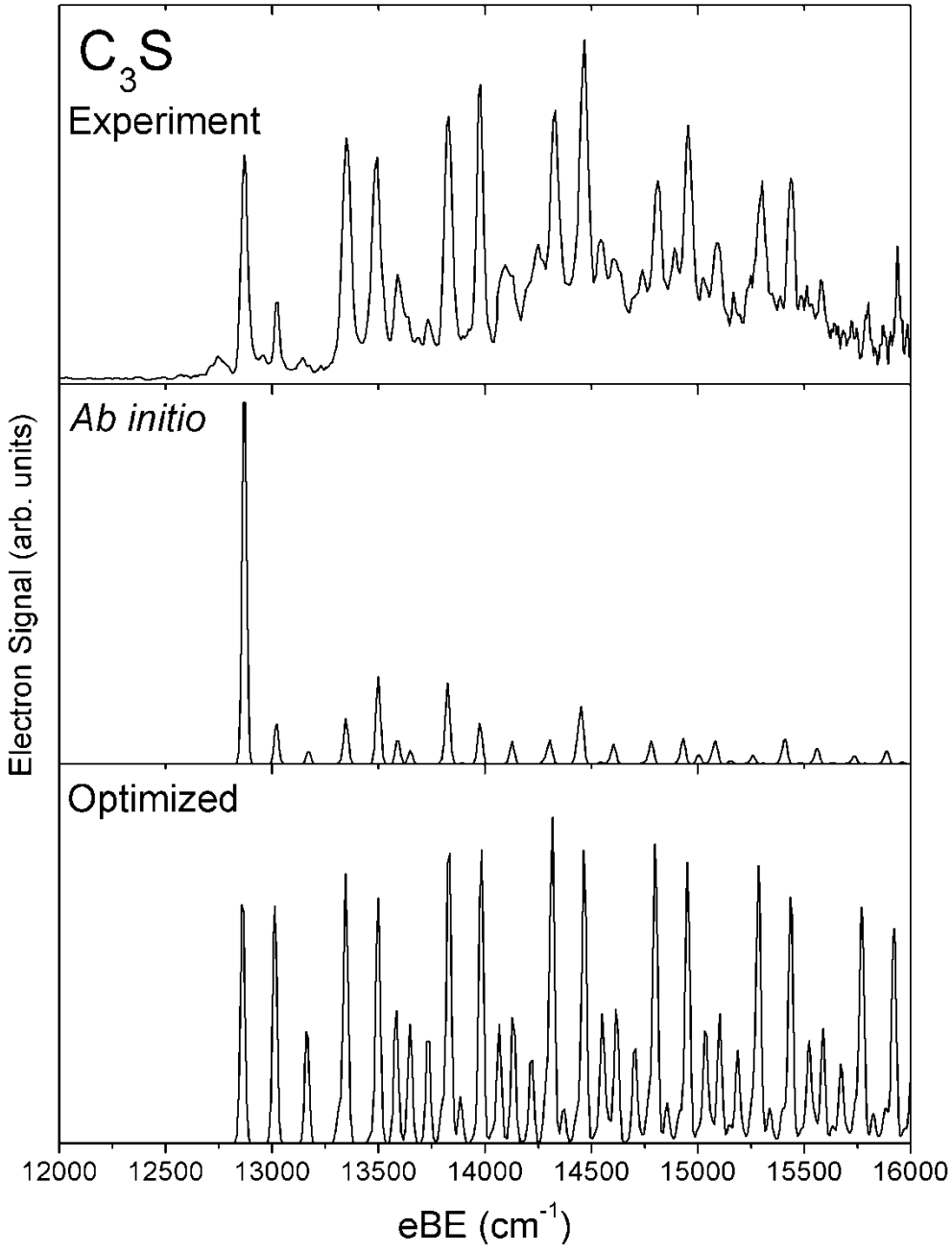

Figure 3.21. Franck-Condon simulation of the C_3S^- SEVI spectra using *ab initio* (center) and optimized (lower panel) parameters. Experimental spectrum is shown in top panel for comparison.

Table 3.21. Experimentally determined adiabatic electron affinities (EA) and fundamental vibrational frequencies for C_3O and C_3S. Error bars on vibrational frequencies are ± 8 cm^{-1}.

	EA (eV)	ν_3 (cm^{-1})	ν_4 (cm^{-1})	ν_5 (cm^{-1})
C_3O	1.237±0.003	935	581	109
C_3S	1.5957±0.0010	721	478	151

In order to understand these effects in more detail, we attempted to simulate the spectra for both species with the usual Franck-Condon and harmonic approximations.[41,42] The C_3O^- and C_3S^- simulated spectra are shown in the middle panels of Figure 3.20 and 3.21, respectively. Neither spectrum could be simulated very well by using the *ab initio* geometries and frequencies. The C_3O simulation displays too much activity in the ν_4 mode and not enough in the ν_3 mode. On the other hand, the C_3S simulation does not display enough activity in the ν_4 and ν_3 modes. In order to get reasonable agreement with the experimental spectra, the normal mode displacements of all the active modes needed to be adjusted with the ν_4 mode requiring the larger adjustments. The results of the simulations with optimized parameters are shown in the bottom panel of Figure 3.20 and 3.21. The optimized parameters correspond to anion structures with $\theta(C_1C_2C_3)$= 172° and $\theta(C_2C_3O)$= 148° for C_3O^- and $\theta(C_1C_2C_3)$= 175° and $\theta(C_2C_3S)$= 160° for C_3S^-. It thus appears that our electronic structure calculations overestimate the distortion from linearity in C_3O^- and underestimate it in C_3S^-. However, we should point out that the analysis used here neglects effects from large-amplitude bending motion and Renner-Teller coupling in the anions, so the optimized geometries are only approximate.

The last point to discuss is the different photoelectron angular distributions in the C_3O^- and C_3S^- SEVI spectra, as shown in Figure 3.17. Close to the detachment threshold, s-wave detachment should dominate for both species,[36] consistent with the nearly isotropic PAD's observed here, and the contributions from higher partial waves should grow with increasing eKE. We indeed see increasingly anisotropic PAD's, but while the features in the C_3O^- spectra exhibit *p*-wave character, those in the C_3S^- spectra show *s*+*d* wave character. In both cases, the electron is ejected from an *a′* orbital with significant amplitude on all four atoms; detachment via s, *p* and *d* partial waves is allowed. However, C_3S^- is nearly linear, and the molecular orbital from which detachment occurs is similar to a π-orbital in a linear molecule. Even though all partial waves are allowed by symmetry from such an orbital, in practice *s*+*d* wave detachment is often dominant.[9,43] In a more strongly bent species like C_3O^-, the propensity rules for detachment are expected to be less strict, so one might expect *p*-wave detachment to become increasingly more important at higher eKE. The C_3O^- and C_3S^- PAD's thus most likely reflect the difference is geometry between the two anions predicted by our DFT calculations.

3.4.6 Conclusions

High resolution photoelectron spectra of C_3O^- and C_3S^- obtained using slow electron velocity-map imaging (SEVI) are reported. These spectra provide a more accurate EA of 1.237±0.003 eV for C_3O and the first measured EA, 1.5957±0.0010 eV, for C_3S. In addition, we determine the gas-phase vibrational frequencies of the ν_3, ν_4 and ν_5 modes for neutral C_3O and C_3S in their $\tilde{X}^1\Sigma^+$ ground states. Since the neutral species are linear, extended progressions of bending modes in the SEVI spectra are consistent with bent equilibrium geometries for both the C_3O^- and C_3S^- anions.

References

1) A. A. Penzias, P. M. Solomon, R. W. Wilson, and K. B. Jefferts, *Astrophys. J.* **168** (2), L53 (1971).

2) A. M. Smith and T. P. Stecher, *Astrophys. J.* **164** (2), L43 (1971).

3) P. Solomon, K. B. Jefferts, A. A. Penzias, and R. W. Wilson, *Astrophys. J.* **163** (2), L53 (1971).

4) H. E. Matthews, W. M. Irvine, P. Friberg, R. D. Brown, and P. D. Godfrey, *Nature* **310** (5973), 125 (1984).

5) R. D. Brown, P. D. Godfrey, D. M. Cragg*et al.*, *Astrophys. J.* **297** (1), 302 (1985).

6) S. Yamamoto, S. Saito, K. Kawaguchi, N. Kaifu, H. Suzuki, and M. Ohishi, *Astrophys. J.* **317** (2), L119 (1987).

7) S. Saito, K. Kawaguchi, S. Yamamoto, M. Ohishi, H. Suzuki, and N. Kaifu, *Astrophys. J.* **317** (2), L115 (1987).

8) M. Ohishi, H. Suzuki, S. I. Ishikawa, C. Yamada, H. Kanamori, W. M. Irvine, R. D. Brown, P. D. Godfrey, and N. Kaifu, *Astrophys. J.* **380** (1), L39 (1991).

9) E. Garand, T. I. Yacovitch, and D. M. Neumark, *J. Chem. Phys.* **129** (7), 074312 (2008).

10) R. D. Brown, P. D. Godfrey, P. S. Elmes, M. Rodler, and L. M. Tack, *J. Am. Chem. Soc.* **107** (14), 4112 (1985).

11) T. B. Tang, H. Inokuchi, S. Saito, C. Yamada, and E. Hirota, *Chem. Phys. Lett.* **116** (1), 83 (1985).

12) W. Klebsch, M. Bester, K. M. T. Yamada, G. Winnewisser, W. Joentgen, H. J. Altenbach, and E. Vogel, *Astronomy and Astrophysics* **152** (1), L12 (1985).

13) R. L. Dekock and W. Weltner, *J. Am. Chem. Soc.* **93** (25), 7106 (1971).

14) P. Botschwina and H. P. Reisenauer, *Chem. Phys. Lett.* **183** (3-4), 217 (1991).

15) D. McNaughton, D. McGilvery, and F. Shanks, *J. Mol. Spectrosc.* **149** (2), 458 (1991).

16) Y. Ohshima and Y. Endo, *J. Mol. Spectrosc.* **153** (1-2), 627 (1992).

17) J. A. Tang and S. Saito, *J. Mol. Spectrosc.* **169** (1), 92 (1995).

18) G. Maier, J. Schrot, H. P. Reisenauer, and R. Janoschek, *Chem. Ber.* **124** (11), 2617 (1991).

19) J. Szczepanski, R. Hodyss, J. Fuller, and M. Vala, *J. Phys. Chem. A* **103** (16), 2975 (1999).

20) S. Takano, J. Tang, and S. Saito, *J. Mol. Spectrosc.* **178** (2), 194 (1996).

21) R. D. Suenram and F. J. Lovas, *Astrophys. J.* **429** (2), L89 (1994).

22) G. Pascoli and H. Lavendy, *Int. J. Mass. Spectrom.* **181**, 11 (1998).

23) J. C. Rienstra-Kiracofe, G. B. Ellison, B. C. Hoffman, and H. F. Schaefer, *J. Phys. Chem. A* **104** (11), 2273 (2000).

24) M. Hochlaf, *J. Mol. Spectrosc.* **210** (2), 284 (2001).

25) P. Botschwina, *Phys. Chem. Chem. Phys.* **5** (16), 3337 (2003).

26) G. L. Li and Z. C. Tang, *J. Phys. Chem. A* **107** (27), 5317 (2003).

27) I. Perez-Juste, A. M. Grana, L. Carballeira, and R. A. Mosquera, *J. Chem. Phys.* **121** (21), 10447 (2004).

28) P. Botschwina, *J. Mol. Struct. (Theochem)* **724** (1-3), 95 (2005).

29) H. Wang, J. Szczepanski, P. Brucat, and M. Vala, *Int. J. Quantum Chem.* **102** (5), 795 (2005).

30) H. Y. Wang, J. Szczepanski, A. Cooke, P. Brucat, and M. Vala, *Int. J. Quantum Chem.* **102** (5), 806 (2005).

31) A. Zaidi, S. Lahmar, Z. Ben Lakhdar, P. Rosmus, and M. Hochlaf, *Theo. Chem. Acc.* **114** (4-5), 341 (2005).

32) J. M. Oakes and G. B. Ellison, *Tetrahedron* **42** (22), 6263 (1986).

33) U. Even, J. Jortner, D. Noy, N. Lavie, and C. Cossart-Magos, *J. Chem. Phys.* **112** (18), 8068 (2000).

34) D. M. Neumark, K. R. Lykke, T. Andersen, and W. C. Lineberger, *Phys. Rev. A* **32** (3), 1890 (1985).

35) M. J. Nee, A. Osterwalder, J. Zhou, and D. M. Neumark, *J. Chem. Phys.* **125**, 014306 (2006).

36) E. P. Wigner, *Phys. Rev.* **73** (9), 1002 (1948).

37) A. D. Becke, *J. Chem. Phys.* **98** (2), 1372 (1993).

38) C. T. Lee, W. T. Yang, and R. G. Parr, *Phys. Rev. B* **37** (2), 785 (1988).

39) T. H. Dunning, *J. Chem. Phys.* **90** (2), 1007 (1989).

40) M. J. Frisch, G. W. Trucks, H. B. Schlegel*et al.*, Gaussian 03, Revision C.02 (Gaussian, Inc, Wallingford, CT, 2004).

41) P. Chen, in *Unimolecular and Bimolecular Reaction Dynamics*, edited by T. Baer, C.-Y. Ng, and I. Powis (John Wiley & Sons, Chichester, 1994), pp. 371.

42) E. H. Kim, S. E. Bradforth, D. W. Arnold, R. B. Metz, and D. M. Neumark, *J. Chem. Phys.* **103** (18), 7801 (1995).

43) T. R. Taylor, C. S. Xu, and D. M. Neumark, *J. Chem. Phys.* **108** (24), 10018 (1998).

3.5 Slow photoelectron velocity-map imaging spectroscopy of HCO_2^- and DCO_2^- anions

Abstract

We report high resolution photoelectron spectra of HCO_2^- and DCO_2^- obtained with slow photoelectron velocity-map imaging. Well-resolved photodetachment transitions to the $^2A_1$ and $^2B_2$ states of the neutral radicals were observed. In addition, vibronic levels of the HCO_2 and DCO_2 radicals with up to 2000 cm^{-1} of internal energy were calculated using a quasidiabatic Hamiltonian approach and high-level *ab initio* calculations. Spectral simulations using the calculated levels were found to be in excellent agreement with the experimental spectra and used to assign many of its features. This study unambiguously determined that the $^2A_1$ state is the ground state of both HCO_2 and DCO_2, in contrast to earlier work, which indicated that the $^2B_2$ state was the ground state for DCO_2. For both isotopologs, the $^2B_2$ state is a very low-lying excited state with term energies of $T_0 = 318\pm8$ cm^{-1} for HCO_2 and $T_0 = 87\pm8$ cm^{-1} for DCO_2. The adiabatic electron affinities are determined to be $EA(HCO_2)= 3.4961\pm0.0010$ eV and $EA(DCO_2) =3.5164\pm0.0010$ eV.

3.5.1 Introduction

The formyloxyl radical (HCO_2) is a reactive intermediate on the potential energy surface for the OH + CO reaction, a reaction of fundamental interest in combustion and atmospheric chemistry.[1-5] It is also a possible intermediate in the thermal decomposition of formic acid.[6,7] Formyloxyl also serves as a prototype for the more complex carboxyl free radicals such as CH_3CO_2, $PhCO_2$, and those derived from amino acids. This species has proven to be very difficult to characterize experimentally because of its metastability with respect to the H + CO_2 dissociation.[8-10] It also presents theoretical challenges owing to its two low-lying excited states which strongly mix and result in a strong pseudo-Jahn-Teller (PJT) coupling that may or may not distort the ground-state equilibrium geometry from C_{2v} symmetry.[11-16] This coupling renders the accurate computation of the geometry and vibronic structure of this species difficult. In this section, we characterize the vibronic structure of the HCO_2 and DCO_2 radicals using slow photoelectron velocity-map imaging (SEVI)[17] in combination with a theoretical treatment using a quasidiabatic Hamiltonian approach parameterized by high-level *ab initio* calculations.

The HCO_2 radical has proved rather elusive. The first reported observations of the formyloxyl radical were made on the basis of emission from vacuum ultraviolet photoexcited formic acid[18,19] and SCF molecular orbital calculations.[20] However, this emission could also have originated from formic acid itself.[21] While Macdonald and Sloan[22] found that the F + DCOOH reaction yielded HF and DF, suggesting that both HOCO and HCO_2 isomers were formed, a subsequent photoionization mass spectrometry study[8] of the same reaction found only HOCO and CO_2 products.

The first definitive observation of the HCO_2 and DCO_2 radicals was reported in 1995 by Kim *et al.*[9] using negative ion photoelectron (PE) spectroscopy of the formate anion, HCO_2^-. The C_{2v} geometry of HCO_2^- is well established,[23-27] so photodetachment of this anion provides a straightforward way to characterize the formyloxyl radical. Moreover, the three lowest neutral states ($^2A_1$, $^2B_2$ and $^2A_2$) can be accessed by one electron photodetachment from the $\ldots(1a_2)^2(4b_2)^2(6a_1)^2$ molecular orbital configuration of the HCO_2^- anion. Analysis of the PE spectra established the $^2A_1$ state as the ground state of HCO_2 with the $^2B_2$ state lying 0.027±0.015 eV (218±121 cm^{-1}) above. For DCO_2, the weak $^2B_2$ origin peak could not be resolved but it was estimated that the $^2B_2$ state was 0.008 eV (65 cm^{-1}) below the $^2A_1$ state.

Kim *et al.*[9] also carried out a vibrational analysis of the PE spectra with Franck-Condon simulations assuming C_{2v} symmetry for the anion and three neutral states. The vibrational modes in this symmetry are shown in Figure 3.22. There are three totally symmetric modes (ν_1- ν_3) with a_1 symmetry, one out-of-plane mode (ν_4) with b_1 symmetry, and two in-plane modes (ν_5, ν_6) with b_2 symmetry. Photodetachment transitions to all three

states were dominated by progressions in the ν_3 mode, owing to the sensitivity of the OCO bend angle to the charge and electronic state of HCO_2, with considerably less activity in the ν_1 and ν_2 modes. The simulations performed reproduced many but not all features in the spectra, and the authors concluded that vibronic (PJT) coupling between the $^2A_1$ and $^2B_2$ states via the two vibrational modes of b_2 symmetry was responsible for additional peaks in the experimental spectrum. However, no quantitative assessment of vibronic coupling effects was performed. Clements and Continetti[10] also used the formate anion as a starting point to probe the formyloxyl radical dissociation dynamics via photoelectron-photofragment coincidence spectroscopy. They found that the three lowest neutral states of HCO_2 predissociate to H + CO_2.

The formyloxyl radical has also been the subject of several theoretical studies,[11-16,23] most of which were aimed at mitigating a tendency for this system to exhibit artifactual symmetry breaking effects and obtaining geometries for and energetics of the three lowest electronic states. However, even in quite sophisticated calculations, the splittings and energy ordering of these states cannot be determined with certainty. Some harmonic vibrational analyses also have been reported.[14-16] While these can be used to characterize the curvature of the various potential energy surfaces, they do not provide an accurate estimate of the vibronic level positions and zero-point energy corrections, owing to strong mixing between the different states.

In this section, we report high resolution SEVI spectra of HCO_2^- and DCO_2^- in the electron binding energy range of the $^2A_1$ and $^2B_2$ neutral states. The increased resolution afforded by SEVI allows the clear separation of the main peaks as well as the observation of several weaker transitions that were not discernible in the previous PE spectrum. Vibronic levels of the HCO_2 and DCO_2 radicals within 2000 cm^{-1} of the ground level are calculated using a quasidiabatic Hamiltonian approach parameterized by high-level *ab initio* calculations. Spectral simulations using the calculated levels are found to be in excellent agreement with the experimental spectra and are used to assign its dominant features. The combined experimental and theoretical analysis yields improved values for the electron affinities of HCO_2 and DCO_2, a revised assignment for the electronic ground state of DCO_2, and new insights into how vibronic coupling effects are manifested in photoelectron spectroscopy.

3.5.2 Experimental details

The SEVI technique and apparatus has been described in detail in chapter 2. In this experiment, HCO_2^- (DCO_2^-) anions were produced from a gas mixture comprising ~0.1% formic acid (formic acid-d_2) and 5% CO_2 in a balance of argon. The gas mixture, at a stagnation pressure of 300 psi, was expanded into the source vacuum chamber through an Even-Lavie pulsed valve[28] equipped with a grid discharge.

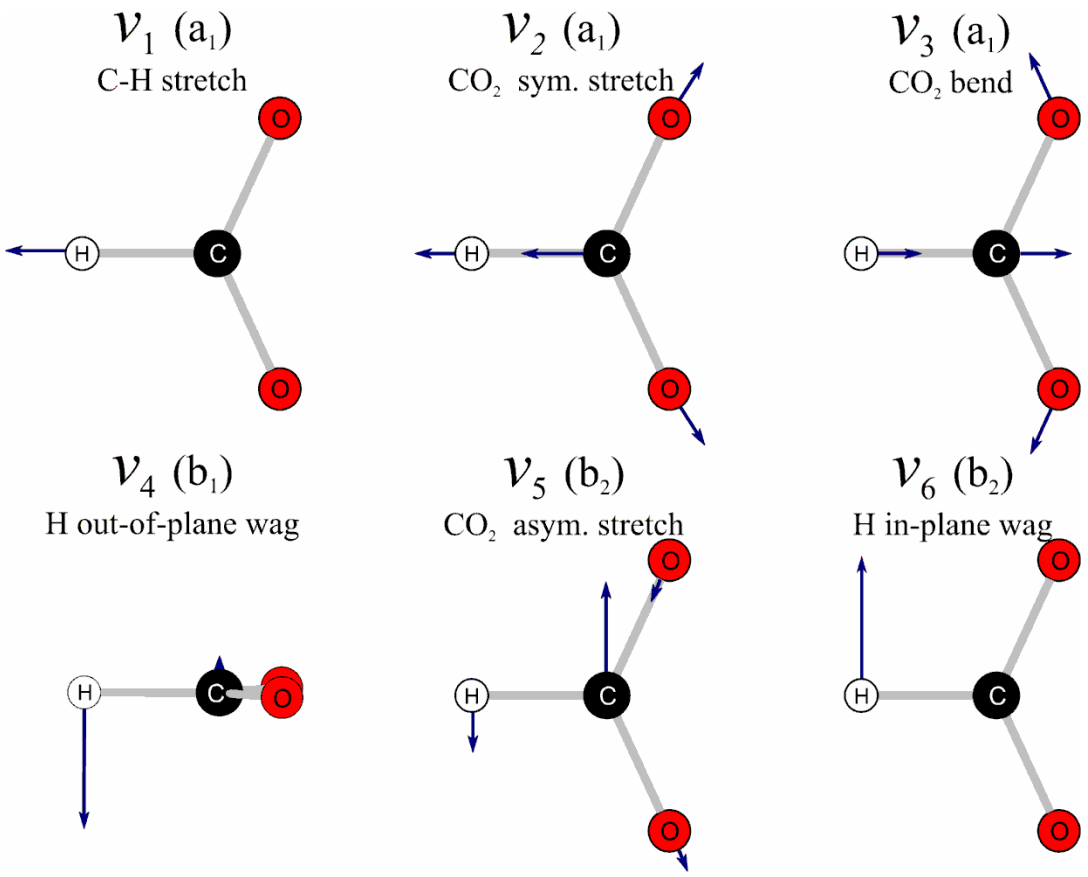

Figure 3.22 Normal coordinates displacement of the HCO_2 vibrational modes.

The apparatus was calibrated by acquiring SEVI images of atomic chloride at several different photon energies. With the 350V VMI repeller voltage used in this study, the Gaussian width (2σ) of the chloride peaks were 4.2 cm^{-1} at 31 cm^{-1} eKE and 28 cm^{-1} at 916 cm^{-1}. Linewidths in the spectra presented here (~15 cm^{-1}) are limited by unresolved rotational structure; since the origin of an unresolved rotational profile may not be aligned with the observed peak maximum, we report error bars of one Gaussian standard deviation (σ) for all energy determinations.

3.5.3 Experimental results

SEVI spectra of HCO_2^- and DCO_2^- in the electron binding energy range of 26500 cm^{-1} to 31500 cm^{-1} are shown in Figure 3.23 and 3.24, respectively. This spectral range includes the features that were assigned to the $^2A_1$ and $^2B_2$ neutral states in the previous PE spectra,[9] although the PE spectra covered a considerably larger range of eBE. Each figure shows three traces corresponding to different photodetachment energies that are vertically offset for clarity. The peak positions, shifts from the origin, and PADs are summarized in Table 3.22. The value of β depends on the detachment energy[29] and thus peaks having $0<\beta<0.3$ are simply labeled as "*s*" while those with $\beta> 1$ are labeled as "*p*".

The SEVI spectra presented here are similar to the previous PE spectra.[9] However the increased resolution afforded by SEVI allows clear separation of the main peaks as well as several weaker transitions that were not discernible in the previous study. In Figures 3.23 and 3.24, the peaks labeled A, which have "p" PAD's and are found at 28198 cm^{-1} and 28362 cm^{-1} for HCO_2^- and DCO_2^-, respectively, correspond to the features that were previously assigned as the origin transitions to the $^2A_1$ state. For HCO_2, the origin transition to the low-lying $^2B_2$ state was assigned to a feature corresponding to the small peak labeled C, with "s" PAD, at 28516 cm^{-1}, and this assignment is confirmed in the work presented here. The SEVI spectra of HCO_2 reveals another weak peak labeled B with the same "s" PAD and located below peak C, at 28239 cm^{-1}; this feature is assigned as a sequence band (see Section V). The DCO_2 spectra show a similar pattern with peaks B and C at 28449 cm^{-1} and 28792 cm^{-1}, respectively. However, our analysis indicates that for this isotopolog, peak B is the origin transition for photodetachment to the $^2B_2$ state. Several weak peaks are also found below peak A in both spectra and are labeled with the lower case letters a-g.

Comparison of the traces in Figures 3.23 and 3.24 shows that the relative intensities of some feature in the SEVI spectra change as the photon energy is varied. This effect reflects the Wigner threshold law,[29,30] which defines the photodetachment cross section (σ) as a function of the energy above threshold (ΔE) and the orbital angular momentum of the ejected electron. Thus, as the photon energy is lowered, the intensity of peaks with "s" PAD's increases with respect to those with "p" PAD's, as seen previously.[31,32]

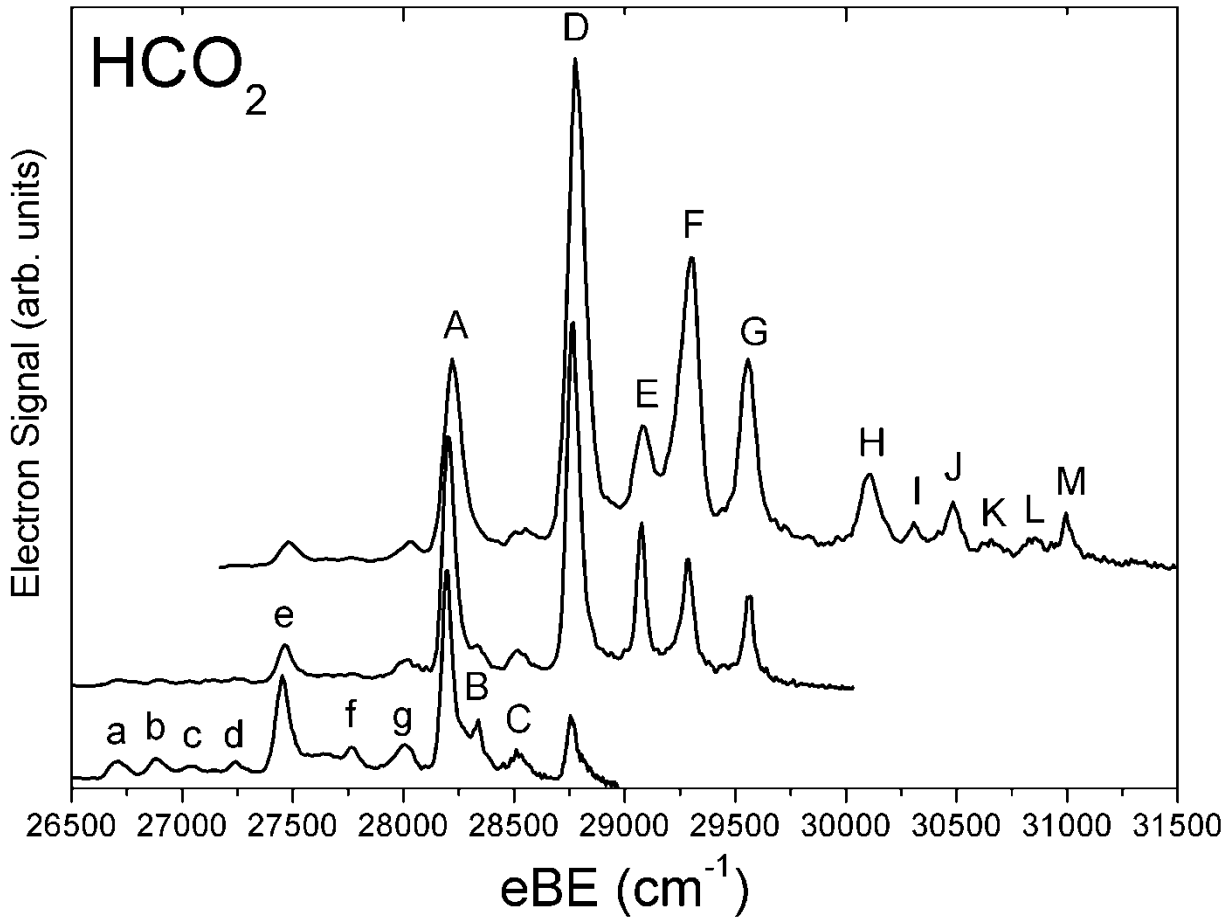

Figure 3.23 SEVI spectra of HCO_2^- between the electron binding energies of 26500 cm^{-1} and 31500 cm^{-1}. The three traces were taken at photon energies of 31745 cm^{-1}, 30030 cm^{-1} and 28986 cm^{-1} and are vertically offset for clarity.

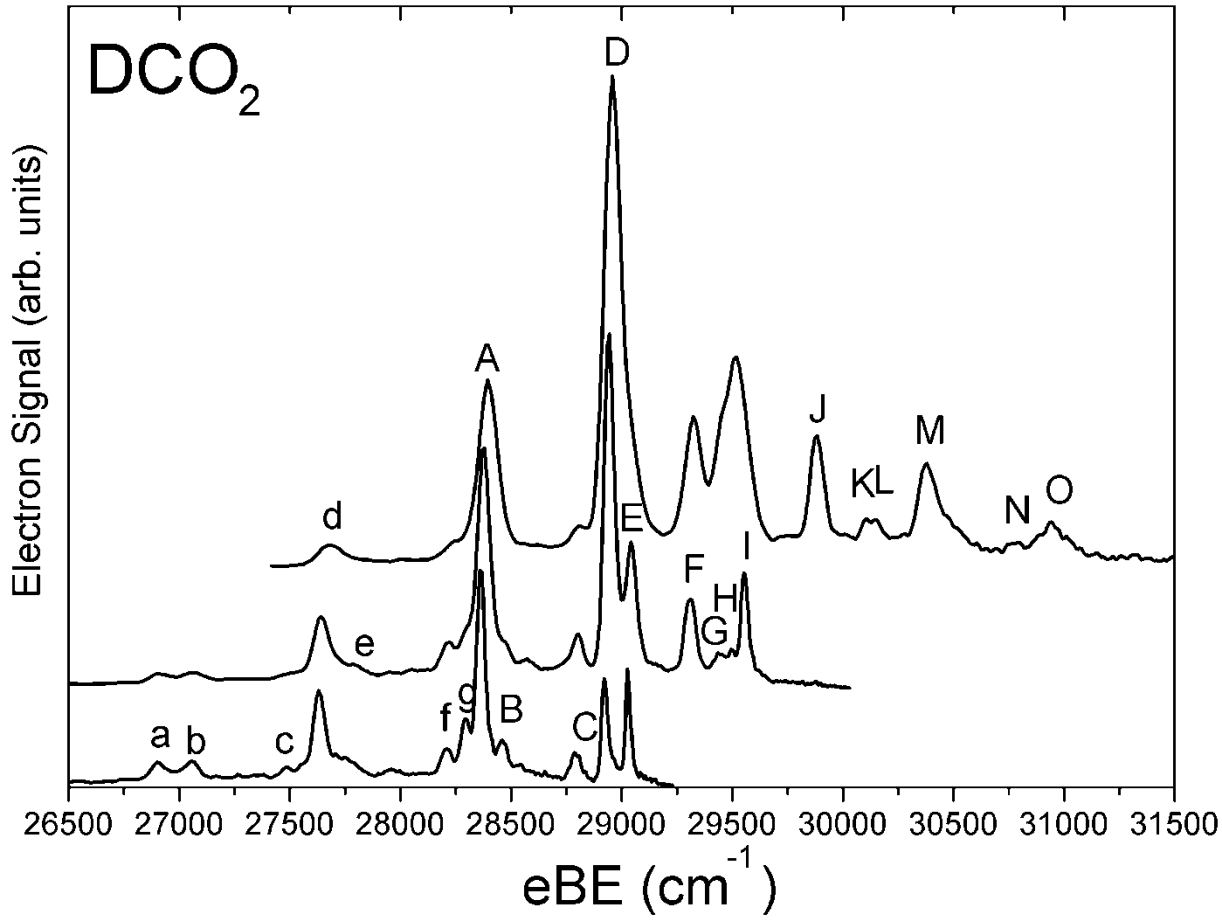

Figure 3.24 SEVI spectra of DCO_2^- between the electron binding energies of 26500 cm^{-1} and 31500 cm^{-1}. The three traces were taken at photon energies of 32023 cm^{-1}, 30052 cm^{-1} and 29240 cm^{-1} and are vertically offset for clarity.

Table 3.22 HCO_2^- SEVI spectra peak positions, shifts from origin and PAD as well as the calculated frequencies and assignments.

Peak	eBE (cm^{-1})	Shift from origin (cm^{-1})	PAD[a]	Calculated position (cm^{-1})	Assignment[b]
a	26713	-1485	*p*	-1504	$3_2^0(^2A_1)$
b	26889	-1309	*p*	-1325	$2_1^0(^2A_1)$
c	27042	-1156	*s*	-1194	$3_2^0(^2B_2)$
d	27240	-958	*p*	-934	$3_2^1(^2A_1)$
e	27455	-743	*p*	-752	$3_1^0(^2A_1)$
f	27763	-435	*s*	-442	$3_1^0(^2B_2)$
g	28002	-196	*p*	-182	$3_1^1(^2A_1)$
A	28198	0	*p*	0.0	$0_0^0(^2A_1)$
B	28329	131	*s*	128	$3_1^1(^2B_2)$
C	28516	318	*s*	310.2	$0_0^0(^2B_2)$
D	28762	564	*p*	569.7 569.9	$3_0^1(^2A_1)$ $6_0^1(^2A_1)$
E	29075	877	*s*	880.1	$3_0^1(^2B_2)$
F	29284	1086	*p*	1058.8 1075.4 1145.4	$3_0^2(^2A_1)$ $3_0^1 6_0^1(^2A_1)$ $2_0^1(^2A_1)$
G	29561	1363	*s*	1337.1 1387.6	$6_0^2(^2A_1) + 6_0^1(^2B_2)$ $3_0^2 6_0^1(^2A_1) + 3_0^2(^2B_2)$
H	30108	1910	*p*	1872.1 1939.8 1968.6	$3_0^1 6_0^2(^2A_1)$ highly mixed highly mixed
I	30307	2109	*p*		
J	30482	2284	*s*		
K	30650	2452	*p*		
L	30855	2657	*p*		
M	30999	2801	*s*		

[a] Peaks with $0<\beta<0.3$ are labeled as "*s*" while those with $\beta> 1$ are labeled as "*p*"

[b] The transitions are labeled according to their best harmonic oscillator and diabatic electronic state representation, whenever possible.

Table 3.23 DCO_2^- SEVI spectra peak positions, shifts from origin and PAD as well as the calculated frequencies and assignments.

Peak	eBE (cm^{-1})	Shift from origin (cm^{-1})	PAD[a]	Calculated position (cm^{-1})	Assignment[b]
a	26903	-1459	*p*	-1489	$3_2^0(^2A_1)$
b	27057	-1305	*p*	-1312	$2_1^0(^2A_1)$
c	27486	-876		-811	$3_2^1(^2B_2)$
d	27630	-732	*p*	-745	$3_1^0(^2A_1)$
e	27720	-642		-645	$3_1^0(^2B_2)$
f	28207	-155	*p*	-180	$3_1^1(^2A_1)$
g	28294	-68	*s*	-67	$3_1^1(^2B_2)$
A	28362	0	*p*	0.0	$0_0^0(^2A_1)$
B	28449	87	*s*	100.5	$0_0^0(^2B_2)$
C	28792	430	*s*	399.8	$6_0^1(^2A_1)$
D	28925	563	*p*	564.8	$3_0^1(^2A_1)$
E	29028	666	*s*	677.8	$3_0^1(^2B_2)$
F	29310	948	*s*	910.0 970.2	$3_0^1 6_0^1(^2A_1)$ $6_0^1(^2B_2)$
G	29446	1084	*p*	1068.3	$3_0^2(^2A_1)$
H	29498	1136	*p*	1138.6	$2_0^1(^2A_1)$
I	29555	1193	*s*	1199.7	$3_0^2(^2B_2)$
J	29882	1520	*p*	1478.1 1492.6	$1_0^1(^2A_1)$ $3_0^1 6_0^2\ (^2A_1)$
K	30105	1743	*s*	1770.0	highly mixed
L	30153	1791	*s*	1835.9	highly mixed
M	30385	2023	*p*	1997.4	highly mixed
N	30780	2418			
O	30945	2583	*p*		

[a] Peaks with $0<\beta<0.3$ are labeled as "*s*" while those with $\beta> 1$ are labeled as "*p*"

[b] The transitions are labeled according to their best harmonic oscillator and diabatic electronic state representation, whenever possible.

3.5.4 Theoretical framework

A) Model Hamiltonian

Calculations of the vibronic level structure of HCO_2 and DCO_2 were made using the quasidiabatic Hamiltonian approach of Köppel, Domcke and Cederbaum (KDC)[33]. The parameterization of the Hamiltonian used in this work is, however, considerably more elaborate than in typical applications of the KDC method. While a full discussion of the theoretical approach taken in the HCO_2 and DCO_2 calculations will be deferred to a subsequent detailed theoretical paper,[34] it is appropriate to give an outline here.

For the present calculations, which are designed to be accurate for states within roughly 0.25 eV (2000 cm^{-1}) of the ground vibronic level, only the $^2A_1$ and $^2B_2$ electronic states of the radical were considered. The $^2A_2$ state, clearly seen in the earlier experiments by Kim *et al.*[9] at *ca*. 0.5 eV, was excluded. More extended calculations of the spectrum, which are ongoing, demonstrate that the effects of coupling to the $^2A_2$ state are negligible in the energy range pertinent to this study. Thus, the quasidiabatic Hamiltonian has the general form

$$H = \begin{pmatrix} T_{AA} & 0 \\ 0 & T_{BB} \end{pmatrix} + \begin{pmatrix} V_{AA} & V_{AB} \\ V_{AB} & V_{BB} \end{pmatrix} \tag{3.2}$$

where the kinetic energy is assumed diagonal and A and B stand for the $^2A_1$ and $^2B_2$ electronic states, respectively. The theoretical foundation for this form of the Hamiltonian is extensively discussed Köppel *et al.*[33] and more recently by Ichino *et al*,[35] where the interested reader is referred for details. The construction of V in this work follows the spirit of the "adiabatic parameterization" approach described by Ichino *et al*,[36] and each block of the potential matrix is expressed as a polynomial in the basis of the dimensionless normal coordinates of the anion, *viz.*

$$V^A = E_0 + \sum_i F_i{}^A q_i + \frac{1}{2}\sum_{ij} F_{ij}{}^A q_i q_j + \ldots \tag{3.3}$$

$$V^B = E_0 + \Delta_0 + \sum_i F_i{}^B q_i + \frac{1}{2}\sum_{ij} F_{ij}{}^B q_i q_j + \ldots \tag{3.4}$$

$$V^{AB} = \sum_i \lambda_i q_i + \ldots \tag{3.5}$$

where E_0 is arbitrary, and Δ_0 is the energy spacing between the two neutral states at the origin of the coordinate system (chosen as the anion geometry).

For HCO_2 and DCO_2, the Taylor expansion of the diagonal blocks of the potential contains terms up to quartic in the totally symmetric modes (ν_1, ν_2 and ν_3), and through quadratic for the coupling modes (ν_5 and ν_6). All anharmonic mixing between the symmetric and coupling modes is assumed to be zero in the quasidiabatic basis. The out-of-plane distortion, ν_4, has b_1 symmetry and does not couple the two states considered here; it is therefore active only through even-quantum transitions from the ground state which, in any event, do not appear to be seen in the range of the spectrum that is relevant to this paper. Its effect is seen only implicitly in terms of the energy gap between the two electronic states, as discussed at the end of this subsection.

As elaborated elsewhere,[36] the quasidiabatic and adiabatic (quantum chemical) potentials are coincident along the totally symmetric coordinates. Consequently, the corresponding potential constants (those that carry indices 1, 2 and 3 only) were obtained from straightforward *ab initio* calculations (see next subsection). In accord with the adiabatic parameterization approach, constants for the $^2B_2$ and $^2A_1$ states were evaluated at the corresponding minimum energy geometries. The coupling constants, which appear only in the off-diagonal block of the potential, were calculated analytically in the framework of the quasidiabatic *ansatz* and formalism of Ichino et al.[35]

The coupling constants in this particular molecular system show a pronounced geometrical dependence, particularly those for ν_6 with regard to the symmetric CO_2 symmetric stretch and bend modes (ν_2 and ν_3). Values of the coupling constants λ_5 and λ_6 at the $^2A_1$ equilibrium geometry for HCO_2 are 2109 and 1341 cm^{-1}, respectively; at the geometry of the $^2B_2$ state, the corresponding values are 2127 and 491 cm^{-1}. The coordinate dependence of λ_6 is so large that efforts to simulate the spectrum with an intermediate constant value were unsuccessful. Thus, the coupling constants were parameterized as follows. At the equilibrium geometries of the $^2A_1$ and $^2B_2$ states, the coupling constants λ_5 and λ_6 were evaluated analytically. It was then assumed that the constants vary linearly with displacement along the symmetric modes, *i.e.*

$$\lambda_i = \lambda_i^0 + \sum_{k=1}^{3} \lambda_{ik} q_k \qquad (3.6)$$

The bilinear terms were first calculated by finite difference of analytic coupling constants around the reference geometry (that of the anion, which is between the two final state equilibrium geometries). The values ultimately used in the parameterization were obtained by scaling these 'vertical' derivatives such that the coupling constants coincide with the analytic values at the final state equilibrium geometries. That is, the first-order variation of the coupling constants is constrained to the proportionality conditions that exist at the reference geometry, but scaled such that the final state coupling constants match the *ab initio* calculations at the final state geometries. Quasidiabatic quadratic force constants (F_{ij}) that

govern the coupling modes (ν_5 and ν_6) were then determined from the corresponding adiabatic force constant (f_{ij}) and coupling parameters *via* the easily derived and well-known second-order perturbation theory relation:[35]

$$F_{ij} = f_{ij} + \frac{2\lambda_i \lambda_j}{E - E'} \tag{3.7}$$

where E is the energy of the state of interest at its equilibrium geometry and E' is the energy of the state to which it is coupled *via* λ_i and λ_j.

The final step in the adiabatic parameterization procedure is to express the potential constants discussed above, in which the expansion points are the minima of the final states, in terms of an expansion about the common reference geometry. This is a straightforward transformation in which force constants of a given order are determined by displacements of the final states relative to the reference state (D_i) and all of the same and higher order force constants (those expressed with respect to the final state geometries).[34] This technically applies to all of the constants, but the diabatic force constants for the coupling modes are, by construction, independent of the origin of the coordinate system since they are not present in the anharmonic part of the *quasidiabatic* potential. All anharmonicity involving ν_5 and ν_6 in the *adiabatic* potentials is carried by the coupling constants. The resulting potential matrix, when diagonalized, gives adiabatic surfaces that satisfy the following criteria:

1) the adiabatic potentials, through quartic terms in the symmetric coordinates and quadratic terms in the non-symmetric (coupling) coordinates, coincide precisely with those given by the ab initio calculations *at the minima of the final states.*

2) the displacements from the reference (anion) geometry to the final state equilibrium geometries are the same as those given by the *ab initio* calculation, while the vertical energy gap is unaffected by the coordinate transformation.

Other features of the *ab initio* adiabatic potentials are not precisely reproduced, namely the vertical distance between the states at the final state equilibrium geometries, the gradient of the final state surfaces at the origin of the coordinate system (the vertical geometry), the adiabatic force fields of the states at the vertical (and other non-equilibrium) geometries, *etc*. The extent to which the latter parameters deviate from the *ab initio* values is related to how faithfully the Taylor expansions of the quasidiabatic potential blocks represent the physics of the problem in the relevant range of displacements. While a detailed discussion of this issue will appear in the forthcoming paper,[34] suffice it to say that with the quartic expansion used here, the representation of the actual adiabatic surfaces is excellent over the entire region of the potential surface that are relevant to the present spectroscopic study.

All parameters used in the calculations are given in Table 3.24 and 3.25. The vertical gap Δ_0 (Eq. 4) of 1337 cm^{-1} obtained in the *ab initio* calculations was shifted by +40 cm^{-1} to approximately reproduce the splitting of the two origin bands in the HCO_2 spectrum, and further adjusted to account for the zero-point energy in the neglected ν_4 mode. The calculated harmonic frequencies for ν_4 are 1017 and 834 cm^{-1} for HCO_2 in the $^2B_2$ and $^2A_1$ states, respectively. Thus, the differential zero point energy (in the harmonic approximation) between the two states is 92 cm^{-1} which, when added to the shifted *ab initio* vertical energy difference of 1377 cm^{-1}, gives the value of Δ_0 found in the leftmost column (top row) of Table 3.25. For DCO_2, the corresponding ab initio harmonic frequencies are 847 and 754 cm^{-1}, for a zero-point differential Δ_0 of 46 cm^{-1}. Thus, the parameterization of the Hamiltonian is 'honest'; apart from the shift of the vertical gap, and essentially purely *ab initio*. No empirical scaling or other fudge factors are used; the only assumption made is that of linear behavior for the coupling constants. The calculations were performed in a direct product harmonic oscillator vibronic basis using 30 functions for the totally symmetric modes, and 15 basis functions for the coupling modes ν_5 and ν_6. The total size of the basis was 12 150 000 functions, and 3000 Lanczos recursions were performed to ensure convergence of the vibronic level positions to *ca.* 2 $cm^{-1.}$ The calculations required only a few hours on a laptop computer and are not computationally demanding. Assignments of the calculated level positions to a diabatic electronic state and vibrational mode were made on the basis of visual inspection of the nodal properties of the corresponding eigenvector. At relatively low energies, this was usually straightforward, but at higher energies the substantial mixing of zeroth-order states was so great that some assignments were not attempted.

Table 3.24 Parameters (in cm^{-1}) appearing in the off-diagonal block of the model Hamiltonian. See text for the definitions. All quantities are in cm^{-1}.

Parameter	HCO_2	DCO_2
λ^0_5	2115	2017
λ_{15}	-13	-24
λ_{25}	1	11
λ_{35}	2	11
λ^0_6	894	896
λ_{16}	16	15
λ_{26}	-163	-144
λ_{36}	-93	-83

Table 3.25 Quasidiabatic force constants (F) at the $^2B_2$ and $^2A_1$ minimum energy geometries in the reduced normal coordinate representation of the anion. Also included are the displacements (D_i) between the final state minima and the equilibrium structure of the anion, and the vertical energy gap Δ_0, as adjusted for the differential zero-point energy of the out-of-plane v_4 mode (see text for details).

	HCO_2		DCO_2			HCO_2		DCO_2	
	$^2B_2$	$^2A_1$	$^2B_2$	$^2A_1$		$^2B_2$	$^2A_1$	$^2B_2$	$^2A_1$
Δ_0	1469	0	1423	0	F_{122}	-21	-92	42	-47
D_1	0.075	-0.245	0.302	-0.420	F_{133}	-11	28	-15	32
D_2	-1.594	0.437	-1.548	0.339	F_{233}	20	-63	17	-57
D_3	-1.998	3.524	-2.034	3.527	F_{123}	-31	-20	-28	-29
F_{11}	3651	2048	2745	1423	F_{1111}	1528	1062	836	582
F_{22}	1631	959	1556	1009	F_{2222}	45	-3	47	3
F_{33}	565	755	562	742	F_{3333}	15	-8	15	-8
F_{12}	-292	250	-215	238	F_{1112}	-113	-80	17	10
F_{13}	-53	55	-37	85	F_{1113}	-35	-23	1	-1
F_{23}	158	-330	154	-318	F_{2223}	-31	-28	-25	-28
F_{55}	1533	1915	1481	1964	F_{1122}	0	3	-7	-4
F_{66}	1234	920	941	628	F_{1133}	0	5	-2	6
F_{56}	239	-308	186	-186	F_{2233}	-19	19	-18	16
F_{111}	-2519	-1894	-1609	-1234	F_{1222}	5	8	-3	8
F_{222}	-338	-107	-330	-134	F_{1333}	-2	-4	42	-47
F_{333}	57	9	56	9	F_{2333}	-6	10	-15	32
F_{112}	192	211	-24	51	F_{1123}	0	3	17	-57
F_{113}	67	48	16	7	F_{1223}	9	-1	-28	-29
F_{223}	47	140	36	133	F_{1233}	2	-9	836	582

B) Quantum chemical calculations

The adiabatic potentials were obtained with the coupled-cluster singles and doubles method[37], as augmented with a perturbative treatment of triple excitations (CCSD(T))[38]. Minima and quadratic force constants were determined and calculated with the aid of analytic first[39-41] and second[42] derivative techniques, and the quartic potential surfaces found in Table IV were determined from numerical fits of a 9x9x9 grid (721 points) of energies evaluated at specific displacements in terms of the normal coordinates of the anion. These calculations used the atomic natural orbital (ANO) basis set of Taylor and Almlöf,[43] truncated to *4s3p2d1f* on C and O, and *4s2p1d* on H. Core electrons were not included in the correlation treatment, and the spherical harmonic representations of the *d* and *f* polarization functions were used.

Quasidiabatic coupling constants were calculated analytically[35] with the equation-of-motion coupled-cluster technique known as EOMIP-CCSD[44] using the double-zeta plus polarization (DZP) basis sets.[45] As the implementation is new, it was necessary to correlate all electrons in these calculations, due to an unresolved issue in how to treat orbital relaxation effects in such calculations when core orbitals are omitted. The variation of coupling constants with geometry was calculated by evaluating the constants analytically at fixed displacements of the nuclei along the three totally symmetric coordinates; derivatives were then obtained by central difference. This is a legitimate procedure in terms of the quasidiabatic *ansatz* of Ref. 35, and is, to our knowledge, the first time that bilinear coupling constants have been calculated in a direct fashion. All *ab initio* calculations used the CFOUR program system.

C) Adiabatic potential energy surfaces

Diagonalization of the quasidiabatic potential (second term in Eq. 3.3) yields the adiabatic potential energy surfaces associated with the two lowest electronic states of formyloxyl. Along the totally symmetric coordinates these are, as mentioned above, identical to the diagonal blocks of V (the off-diagonal matrix element vanishes if the nuclear framework has C_{2v} symmetry) and are not particularly interesting. For HCO_2 and other molecules that exhibit strong pseudo-Jahn-Teller (PJT) effects, the dependence of the adiabatic potential along the coupling modes can be a very sensitive function of the diabatic coupling strength[46] (corresponding to λ_5 and λ_6 for HCO_2). If the coupling exceeds a threshold for a given energy gap Δ between the two states ($|\lambda_i| > [F_{ii}\ \Delta\ /\ 2]^{1/2}$), the adiabatic potential with respect to the coordinate q_i becomes a double minimum with a local maximum at the high symmetry point. Thus, small energy gaps and/or large coupling strengths can act to distort the adiabatic potential surfaces so profoundly that the point group of the equilibrium geometry has a symmetry lower than that of the high-symmetry structure that must always prevail in the absence of coupling.[47]

For HCO_2, a pictorial representation of the lowest adiabatic surface is given in Figure 3.25. Due to the fact that there are five relevant coordinates, the coordinate axes in Figure 3.25 do not correspond to simple isolated normal coordinate displacements. Each point of the potential represented in the figure corresponds to the energy of the lowest adiabatic state at a particular value of the *anion* coordinates q_3 and q_6 (which roughly correspond to the CO_2 bend (a_1) and the H in-plane wag (b_2), with the energy optimized with respect to all other coordinates. The salient feature of the potential, which will be discussed in more detail in Ref. 42, is that the minimum energy C_{2v} geometry associated with the $^2A_1$ electronic state is *not* a minimum on the adiabatic potential energy surface. That is, from the perspective of a quantum chemist, this electronic state of HCO_2 is "not C_{2v}" at the level of theory employed here. However, the magnitude of the barrier (which is less than 20 cm^{-1}) is so small as to be well below the zero-point level -- this little "dimple" in the potential thus has no particular physical relevance. As is amply demonstrated by this work, photodetachment of the anion to

the $^2A_1$ state of formyloxyl can be quite satisfactorily described within a C_{2v} framework; the observation of non-Franck-Condon transitions to levels involving odd number of quanta in the ν_5 and ν_6 coupling modes can be understood only in terms of vibronic coupling, in which the potential energy surface picture of the Born-Oppenheimer approximation is not strictly applicable, anyway.

In contrast to the $^2A_1$ state, the $^2B_2$ electronic state of formyloxyl is much simpler, exhibiting a pronounced minimum at the C_{2v} geometry. In terms of the quasidiabatic model Hamiltonian, the striking difference between the adiabatic potential for $^2A_1$ and $^2B_2$ states is a direct consequence of the coordinate dependence of λ_6 (see Table 3.24); at large values of the OCO angle, the coupling is significantly stronger than at small values of θ_{OCO}. It should be noted that the other possibility – that the vertical gap between the two electronic states is significantly smaller at the $^2A_1$ geometry – is not operative in this example. At the CCSD(T)/ANO1 level, the vertical energy differences between the states is 10866 cm^{-1} at the $^2B_2$ geometry and 10945 cm^{-1} at the $^2A_1$ geometry, a surprisingly small difference that is insignificant in the context of this discussion. Thus, the adiabatic potential of the state with the larger bond angle (144.8^o for the $^2A_1$ state at the CCSD(T)/ANO1 level of theory *vs.* 112.5^o for $^2B_2$) is more profoundly influenced by the coupling. Another experimental finding that can be rationalized in terms of the adiabatic potentials is the significantly smaller value of ν_6 in the $^2A_1$ state of DCO_2 ,430 cm^{-1}, compared to 860 cm^{-1} for the $^2B_2$ state. Finally, it should be pointed out that the rather large difference in state splitting between the normal and deuterated isotopologs is due in part to the fact that CH(D) bond is substantially different in the two diabatic states, with a calculated harmonic frequency of 3106 and 2333 cm^{-1}, respectively for ν_1 in the A_1 and B_2 states of HCO_2. More about the nature of the adiabatic potentials of these two states, as well as the somewhat higher-lying $^2A_2$ state, will be discussed in Ref 42.

3.5.5 Discussion

Simulated spectra of HCO_2^- and DCO_2^- are shown as the lower plots in Figures 3.26 and 3.27, respectively. The present simulations are limited to transitions to neutral states within 2000 cm^{-1} of the ground level. The stick spectra show the calculated positions and intensities of the individual transitions. Transitions to levels with A_1 and B_2 vibronic symmetries are shown in red and blue, respectively. The grey shaded spectra represent the sum of the A_1 and B_2 transitions convoluted with a 20 cm^{-1} full width at half maximum Gaussian function. The top trace in each figure is a composite experimental spectrum made by joining parts of the three SEVI traces shown in Figures 3.23 and 3.24. The composite spectrum is constructed from sections of the three SEVI traces that were not close to either the maximum and minimum electron binding energy. Each section was individually scaled to match the intensity of the SEVI spectrum taken at the highest photon energy and then spliced

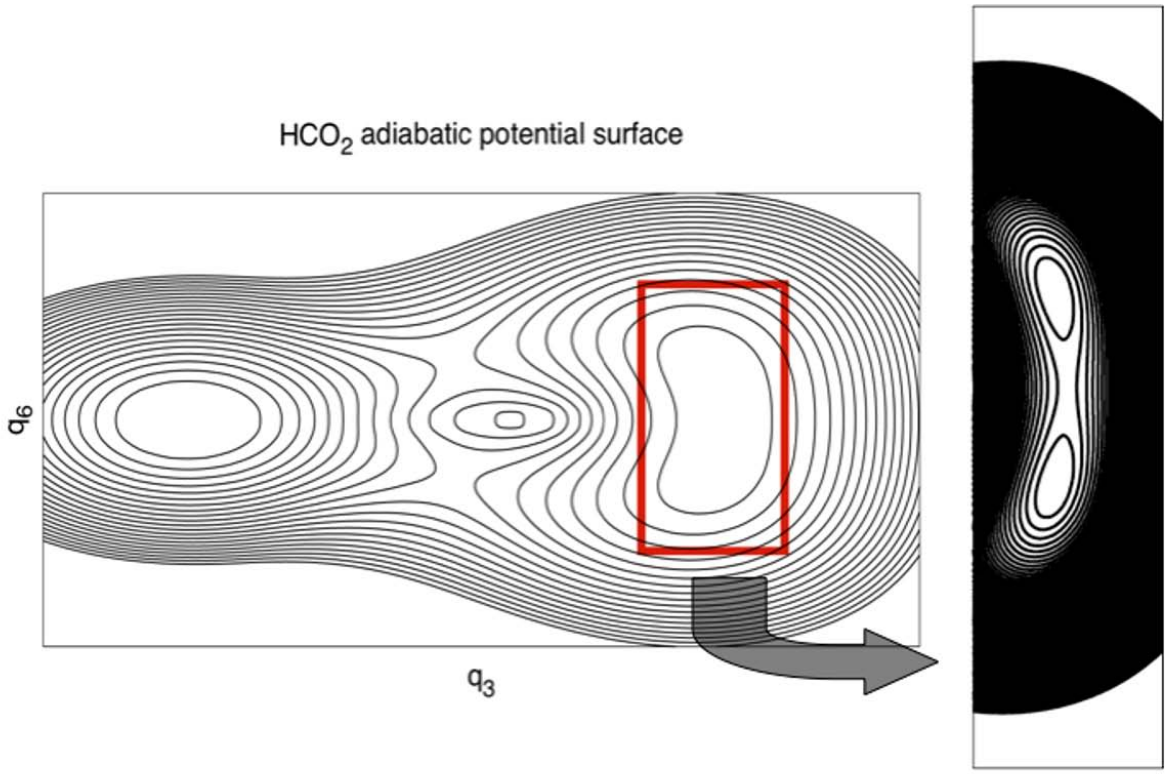

Figure 3.25 Contour representation of the lower adiabatic sheet of the potential energy surface for the formyloxyl radical, obtained by diagonalizing the model potential described in Section IV.i. At each point (q_3,q_6), the adiabatic energy is that obtained when all other coordinates are varied so as to minimize the energy. The $^2B_2$ region of the potential is that at lower values of q_3 (to the left of the conical intersection). The contour level is 100 cm^{-1}, and the region in the immediate vicinity of the $^2A_1$ minimum energy geometry is expanded in the inset to show the nearly negligible double minimum. Points along the line $q_6 = 0$ have C_{2v} symmetry; all other geometries have C_s symmetry with unequal CO bond distances and HCO bond angles. Note that both "electronic states" lay on the same adiabatic sheet of the potential surface and may interconvert by pseudorotation.

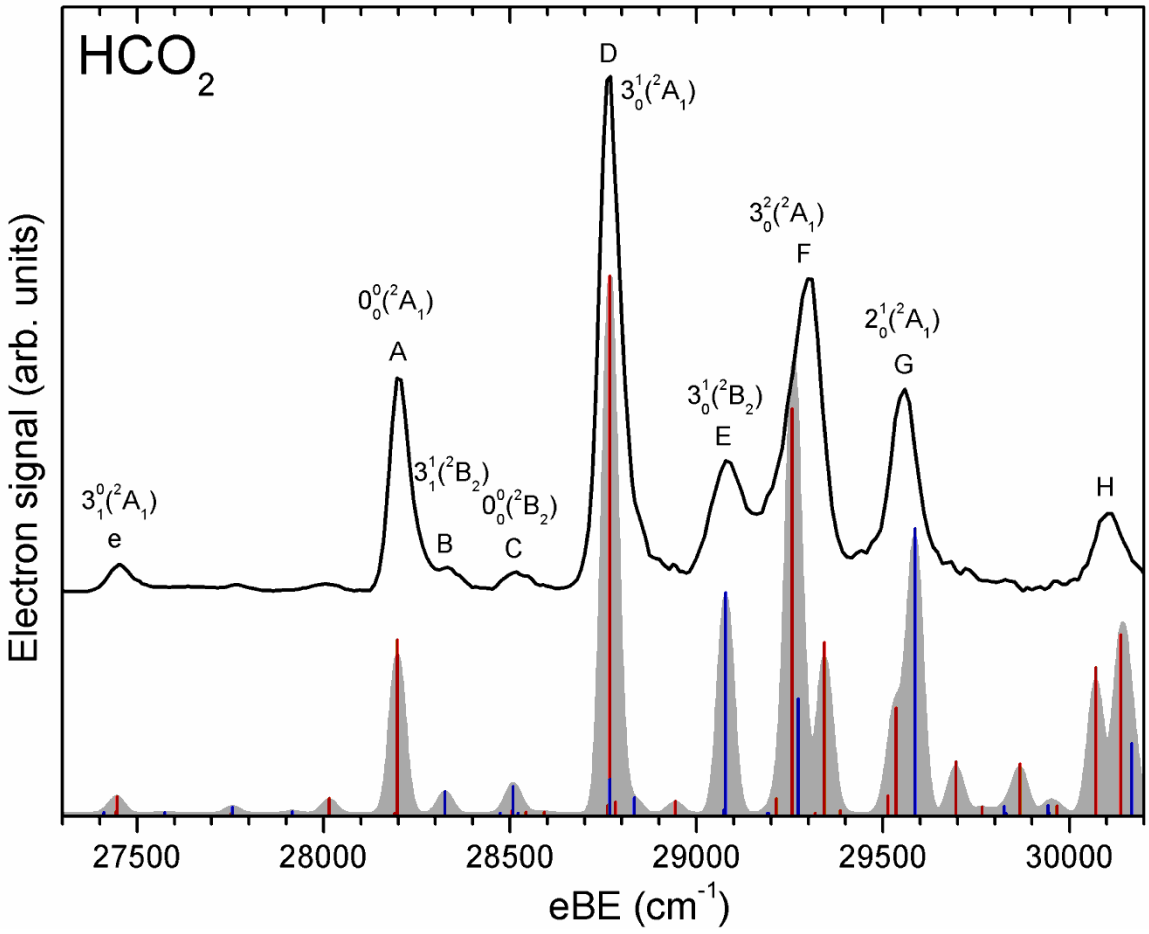

Figure 3.26 Comparison between the HCO_2^- SEVI spectrum and the simulated spectrum. The calculated transitions to levels having A_1 and B_2 vibronic symmetries are shown in red and blue, respectively. The grey shaded spectra represent the sum of the A_1 and B_2 transitions convoluted with a 20 cm^{-1} Gaussian width. The top trace is a composite experimental spectra made by joining parts of the 3 traces shown in Figure 2.

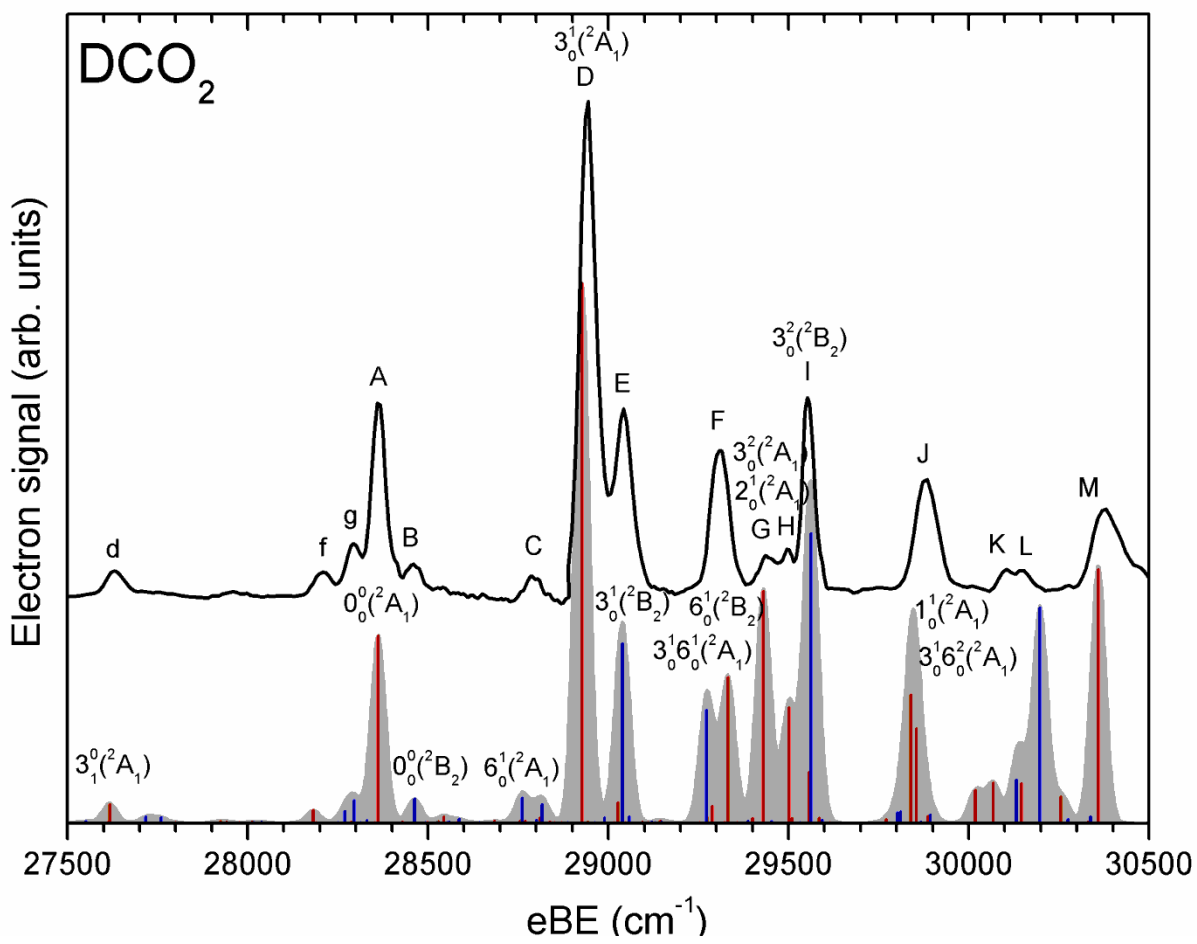

Figure 3.27 Comparison between the DCO_2^- SEVI spectrum and the simulated spectrum. The calculated transitions to levels having A_1 and B_2 vibronic symmetries are shown in red and blue, respectively. The grey shaded spectra represent the sum of the A_1 and B_2 transitions convoluted with a 20 cm^{-1} Gaussian width. The top trace is a composite experimental spectra made by joining parts of the 3 traces shown in Figure 3.

together at points that fall on the baseline. For the simulated HCO_2 and DCO_2 spectra, the calculated origin transition was aligned with the experimental peak labeled "A". The simulated spectra agree well with experiment, allowing straightforward assignment of the dominant features in the HCO_2^- and DCO_2^- SEVI spectra. These assignments are summarized in Table 3.22 and 3.23 along with the calculated positions of the corresponding vibronic levels. In these tables as well as in the following discussion, the transitions are labeled according to their best harmonic oscillator and diabatic electronic state representation, whenever possible.

Peak A in the HCO_2 spectrum is the vibrational origin transition of the $^2A_1$ state. The weak peak labeled C, lying 318 cm^{-1} above peak A, is assigned to the vibrational origin of the $^2B_2$ state. This assignment implies that features having "*p*" and "*s*" PADs correspond to transitions to neutral levels having A_1 and B_2 vibronic symmetry, respectively. Peaks D, F and H in the HCO_2 spectrum, have "*p*" PADs and are thus assigned to A_1 levels. Specifically, peaks D and F are assigned to the 3_0^1 and $3_0^2(^2A_1)$ transitions, respectively, while peak H is assigned to the $3_0^1 6_0^2(^2A_1)$ transition as well as a transition to a highly mixed level of A_1 vibronic symmetry. A transition to another highly mixed state of B_2 symmetry with a calculated position of 1968.6 cm^{-1} might also contribute to peak H.

Peak B, E and G have "*s*" PADs and are thus assigned to transitions to B_2 levels. Peak E, which lies 877 cm^{-1} above the $^2A_1$ origin, is assigned to the $3_0^1(^2B_2)$ transition while peak G is assigned to a transition to a quite mixed level of B_2 symmetry, best described as $3_0^2 6_0^1(^2A_1)$ + $3_0^2(^2B_2)$, with a possible contribution from another transition to a mixed level of A_1 symmetry that is best described as $6_0^2(^2A_1)$ + $6_0^1(^2B_2)$. The small peak B, which lies 131 cm^{-1} above peak A, is apparently not a transition from the anion ground vibrational state. Its assignment is discussed later with the other hot bands.

Similarly, the simulations and the PADs can be used to assign most features in the DCO_2 spectrum. Peaks A, D, G, H, J and M all have "*p*" PAD's and are assigned to transitions to A_1 symmetry levels. Peak A is the vibrational origin transition to the $^2A_1$ state. Peaks D and G, which lie 563 cm^{-1} and 1084 cm^{-1} above the $^2A_1$ origin, are assigned to the $3_0^1(^2A_1)$ and $3_0^2(^2A_1)$ transitions, respectively, while peak H. is assigned to the $2_0^1(^2A_1)$ transition. Peak J is assigned to the overlapped $1_0^1(^2A_1)$ and $3_0^1 6_0^2(^2A_1)$ transitions, while, peak M at 2023 cm^{-1} is assigned to a transition to a highly mixed level with A_1 symmetry.

Peaks B, C, E, F, I, K and L all have "*s*" PADs and are thus assigned to transitions to levels with B_2 vibronic symmetry. The weak peak labeled B, lying only 87 cm^{-1} above the origin is assigned as the vibrational origin transition to the $^2B_2$ electronic state. This assignment is in good agreement with the calculated $^2B_2$ - $^2A_1$ splitting of 100.5 cm^{-1} in DCO_2. This assignment differs from the previous PE spectrum where the weak transition to the $^2B_2$ ground level could not be resolved. In that spectrum, the $^2B_2$ state was tentatively assigned as the DCO_2 ground-state lying ~65 cm^{-1} below the $^2A_1$ state. Peaks E and I are assigned to the

$3_0^1(^2B_2)$ and $3_0^2(^2B_2)$ transitions, respectively. The weak peak C is assigned to the $6_0^1(^2A_1)$ transition, while peak F is assigned to the overlapped $3_0^1 6_0^1(^2A_1)$ and $6_0^1(^2B_2)$ transitions; all three transitions are allowed only by vibronic coupling. Finally, the weak peaks K and L are assigned to highly mixed levels with B_2 vibronic symmetry.

Compared to the HCO_2^- SEVI spectrum, the DCO_2^- spectrum shows more peaks that are unambiguously allowed by vibronic coupling, most notably peaks C and F. This result does not imply stronger vibronic coupling between the DCO_2 states; it reflects the observation that the ν_3 and ν_6 frequencies are nearly the same for the $^2A_1$ state of HCO_2, whereas they differ for the $^2A_1$ state of DCO_2. Hence, in the simulated HCO_2^- spectrum, the weak, vibronically allowed $6_0^1(^2A_1)$ transition occurs at the same energy as the much stronger, fully allowed $3_0^1(^2A_1)$ transition (peak D, Fig. 3.26), so a distinct $6_0^1(^2A_1)$ transition is not observed.

Peaks I-J in the HCO_2^- spectrum as well as peaks N and O in the DCO_2^- spectrum lie more than 2000 cm^{-1} above the origin transition and are thus not included in the present calculations. From the trend observed in both the HCO_2^- and DCO_2^- spectra, these are probably transitions to highly mixed $^2A_1$ and $^2B_2$ levels that cannot readily be described by the usual harmonic oscillator and diabatic electronic state notation. The second excited state ($^2A_2$), which lies ~0.5 eV above the $^2A_1$ ground state, might also contribute to these peaks. More accurate calculations involving all three low-lying states are ongoing.[34]

Several very weak peaks, labeled a-g, are also found in the HCO_2^- and DCO_2^- spectra at lower eBE than the origin transitions. These features are assigned to transitions originating from excited vibrational levels of the respective anions and are well-reproduced by the simulations, assuming an anion vibrational temperature of ~400K. Peak e and a are assigned to the $3_1^0(^2A_1)$ and $3_2^0(^2A_1)$ transitions, respectively. This assignment yields a value of 743 cm^{-1} for the ν_3 fundamental in HCO_2^- which is in excellent agreement with the 744.1 cm^{-1} value measured in Ne matrix.[24] Using this value and the 563 cm^{-1} ν_3 fundamental for the neutral HCO_2 ($^2A_1$) determined previously, we can assign peaks d and g to the $3_2^1(^2A_1)$ and $3_1^1(^2A_1)$ transitions, respectively. Similarly, peaks f and c are assigned to the $3_1^0(^2B_2)$ and $3_2^0(^2B_2)$ transitions, respectively. Peak B, lying 131 cm^{-1} above the origin transition, can be assigned to the $3_1^1(^2B_2)$ transition. The remaining small peak b is assigned to the $2_1^0(^2A_1)$ transition, yielding a 1309 cm^{-1} ν_2 fundamental for HCO_2^-. This value agrees with the frequency of 1323 cm^{-1} measured in a Ne matrix[24] and the *ab initio* value of 1325 cm^{-1} obtained at the CCSD(T)/ANO1 level using second-order vibrational perturbation theory.[34] The same process can be applied to the weak peaks labeled a-g in the DCO_2^- spectrum to assign them to similar hot band transitions involving the ν_2 and ν_3 modes. This analysis yields values of 1305 cm^{-1} and 732 cm^{-1} for the DCO_2^- ν_2 and ν_3 fundamentals, respectively. These are again in excellent agreement with the 1309.1 cm^{-1} and 736.9 cm^{-1} frequencies obtained from Ne matrix isolation experiments[24] and the corresponding *ab initio* fundamentals at 1311 and 745 cm^{-1}.[34]

The present study unambiguously determines that the $^2A_1$ electronic state is the ground state of both HCO_2 and DCO_2, in contrast to the previous assignment for DCO_2.[9] The adiabatic electron affinities are given by the position of the peak labeled "A" in both spectra and are determined to be EA(HCO_2)= 3.4961±0.0010 eV and EA(DCO_2) =3.5164±0.0010 eV. The $^2B_2$ electronic state is found to be a very low-lying excited state with term energies of $T_0(^2B_2)$ = 0.0394±0.0010 eV (318±8 cm^{-1}) for HCO_2 and $T_0(^2B_2)$= 0.0108±0.0010 eV (87±8 cm^{-1}) for DCO_2. Electron affinities, term values, and vibrational fundamentals determined in this work are summarized in Table 3.26.

Table 3.26 Experimental spectroscopic constants determined in this work. All the vibrational frequencies are in cm^{-1}. Error bar on all numbers is ±8 cm^{-1} (±0.0010 eV)

	EA	$T_0(^2B_2)$	Anion (X^1A_1)		Neutral ($^2A_1$)			Neutral ($^2B_2$)
	(eV)	(eV)	ν_2	ν_3	ν_2	ν_3	ν_6	ν_3
HCO_2	3.4961	0.0394	1309	743	-	564	-	559
DCO_2	3.5164	0.0108	1305	732	1136	563	430	579

The calculated term energies for the $^2B_2$ state are within a few wavenumbers of the experimental values which is a very good indication of the accuracy of the *ab initio* method and quasidiabatic Hamiltonian approach used in this study. Moreover, most of the calculated vibronic level positions are found to be within 40 cm^{-1} of the experimental values. There are, however, some notable discrepancies between the simulated spectrum and the experiment with regard to the relative intensity of some of the features. Most of these can be explained in term of the Wigner threshold law which modulates the relative intensity of the "s" and "p" features as a function of detachment photon energy, and is not taken into account in the simulations.

The present work demonstrates how the combination of SEVI and state-of-the-art theory provides a powerful tool to unravel the complex vibronic structure of open-shell species. With respect to conventional PE spectroscopy, the high resolution afforded by SEVI allows the clear observation of close-lying and weak bands which otherwise would be strongly overlapping. A good example of this is the weak $^2B_2$ origin peak in the DCO_2 spectrum which could not be resolved from the stronger $^2A_1$ origin in the previous PE study and led to an erroneous assignment of the DCO_2 ground state. Moreover, in contrast to anion zero electron kinetic energy (ZEKE) spectroscopy,[48] a photodetachment ment technique with comparable resolution, SEVI retains the ability of photoelectron spectroscopy to observe transitions involving photoelectrons ejected with non-zero orbital angular momentum. In the present case, all the transitions to levels with B_2 vibronic symmetry (blue sticks in Figure 3.26 and 3.27), which proceed mainly by *p*-wave detachment, would not have been observed with

ZEKE, thus limiting the amount of spectroscopic information that could be obtained from the spectra.

On the other hand, the results presented here showcase the need for detailed theory to interpret SEVI spectra, especially when the neutral species is subject to strong pseudo-Jahn-Teller coupling. For example, the nominally forbidden $6_0^1(^2A_1)$ and $3_0^1 6_0^1(^2A_1)$ transitions are observed in the DCO_2 spectrum. These transitions have the same "p" PADs as the $^2B_2$ electronic state from which they "borrow" intensity through vibronic coupling, similar to what was observed in CCS[31] and C_2H.[32] In the case of DCO_2, such an assignment is difficult to make *a priori*, because the $^2A_1$ and $^2B_2$ bands overlap one another. Under these circumstances, neither the intensites nor positions of the vibronically allowed transitions can be predicted with simple models. The theoretical treatment presented here thus provides an essential complement to the SEVI spectra by allowing the unambiguous assignment of the observed features.

3.5.6 Conclusions

We report high resolution SEVI photodetachment spectra of HCO_2^- and DCO_2^- in order to probe the $^2A_1$ and $^2B_2$ electronic states of the corresponding radicals. Vibronic levels of the HCO_2 and DCO_2 radicals with up to 2000 cm^{-1} of internal energy are calculated with a quasidiabatic Hamiltonian parameterized by high-level *ab initio* calculations. Spectral simulations using the calculated levels are found to be in good agreement with the experimental spectra and are used to assign most of its features. The combination of the spectral resolution of SEVI and the high-level calculations reported here shows that the $^2A_1$ state is the ground state of both HCO_2 and DCO_2 species. The $^2B_2$ state is found to be a very low-lying excited state with term energies of $T_0 = 318\pm8$ cm^{-1} for HCO_2 and $T_0 = 87\pm8$ cm^{-1} for DCO_2. Several gas-phase vibrational frequencies of the formyloxyl radical and formate anion were also determined for the first time.

References:

1) G. C. Schatz, M. S. Fitzcharles, and L. B. Harding, *Faraday Disc.* **84**, 359 (1987).
2) K. S. Bradley and G. C. Schatz, *J. Chem. Phys.* **106** (20), 8464 (1997).
3) T. V. Duncan and C. E. Miller, *J. Chem. Phys.* **113** (13), 5138 (2000).
4) H. G. Yu, J. T. Muckerman, and T. J. Sears, *Chem. Phys. Lett.* **349** (5-6), 547 (2001).
5) X. L. Song, J. C. Li, H. Hou, and B. S. Wang, *J. Chem. Phys.* **125** (9) (2006).
6) J. S. Francisco, *J. Chem. Phys.* **96** (2), 1167 (1992).
7) J. D. Goddard, Y. Yamaguchi, and H. F. Schaefer, *J. Chem. Phys.* **96** (2), 1158 (1992).
8) B. Ruscic, M. Schwarz, and J. Berkowitz, *J. Chem. Phys.* **91** (11), 6780 (1989).
9) E. H. Kim, S. E. Bradforth, D. W. Arnold, R. B. Metz, and D. M. Neumark, *J. Chem. Phys.* **103** (18), 7801 (1995).
10) T. G. Clements and R. E. Continetti, *J. Chem. Phys.* **115** (12), 5345 (2001).
11) S. D. Peyerimhoff, P. S. Skell, D. D. May, and R. J. Buenker, *J. Am. Chem. Soc.* **104** (17), 4515 (1982).
12) D. Feller, E. S. Huyser, W. T. Borden, and E. R. Davidson, *J. Am. Chem. Soc.* **105** (6), 1459 (1983).
13) A. D. McLean, B. H. Lengsfield, J. Pacansky, and Y. Ellinger, *J. Chem. Phys.* **83**, 3567 (1985).
14) A. Rauk, D. Yu, P. Borowski, and B. Roos, *Chem. Phys.* **197** (1), 73 (1995).
15) J. F. Stanton and N. S. Kadagathur, *J. Mol. Struct.* **376**, 469 (1996).
16) P. Y. Ayala and H. B. Schlegel, *J. Chem. Phys.* **108** (18), 7560 (1998).
17) D. M. Neumark, *J. Phys. Chem. A* **112** (51), 13287 (2008).
18) D. W. G. Style and J. C. Ward, *Trans. Faraday Soc.* **49** (9), 999 (1953).
19) M. Suto, X. Y. Wang, and L. C. Lee, *J. Phys. Chem.* **92** (13), 3764 (1988).
20) T. E. Peacock, D. H. Sleeman, E. S. G. Tuckley, and Riasurra, *Disc. Faraday Soc.* (35), 144 (1963).
21) Y. P. Lee and G. C. Pimentel, *J. Chem. Phys.* **74** (9), 4851 (1981).
22) R. G. Macdonald and J. J. Sloan, *Chem. Phys.* **31** (2), 165 (1978).
23) D. A. Dixon, D. Feller, and J. S. Francisco, *J. Phys. Chem. A* **107** (1), 186 (2003).
24) D. Forney, M. E. Jacox, and W. E. Thompson, *J. Chem. Phys.* **119** (20), 10814 (2003).
25) K. G. Kidd and H. H. Mantsch, *J. Mol. Spectrosc.* **85** (2), 375 (1981).

26) C. Krekeler, M. Mladenovic, and P. Botschwina, *Phys. Chem. Chem. Phys.* **7** (5), 882 (2005).

27) W. H. Zachariasen, *J. Am. Chem. Soc.* **62**, 1011 (1940).

28) U. Even, J. Jortner, D. Noy, N. Lavie, and C. Cossart-Magos, *J. Chem. Phys.* **112** (18), 8068 (2000).

29) E. P. Wigner, *Phys. Rev.* **73** (9), 1002 (1948).

30) K. J. Reed, A. H. Zimmerman, H. C. Andersen, and J. I. Brauman, *J. Chem. Phys.* **64** (4), 1368 (1976).

31) E. Garand, T. I. Yacovitch, and D. M. Neumark, *J. Chem. Phys.* **129** (7), 074312 (2008).

32) J. Zhou, E. Garand, and D. M. Neumark, *J. Chem. Phys.* **127**, 114313 (2007).

33) H. Koppel, W. Domcke, and L. S. Cederbaum, *Adv. Chem. Phys.* **57**, 59 (1984).

34) K. Klein, J. Gauss, E. Garand, D. M. Neumark, and J. F. Stanton, *(in preparation).*

35) T. Ichino, J. Gauss, and J. F. Stanton, *J. Chem. Phys.* **130**, 174105 (2009).

36) T. Ichino, A. J. Gianola, W. C. Lineberger, and J. F. Stanton, *J. Chem. Phys.* **125** (8), 084312 (2006).

37) G. D. Purvis and R. J. Bartlett, *J. Chem. Phys.* **76** (4), 1910 (1982).

38) K. Raghavachari, G. W. Trucks, J. A. Pople, and M. Headgordon, *Chem. Phys. Lett.* **157** (6), 479 (1989).

39) T. J. Lee and A. P. Rendell, *J. Chem. Phys.* **94** (9), 6229 (1991).

40) G. E. Scuseria, *J. Chem. Phys.* **94** (1), 442 (1991).

41) J. D. Watts, J. Gauss, and R. J. Bartlett, *Chem. Phys. Lett.* **200** (1-2), 1 (1992).

42) J. Gauss and J. F. Stanton, *Chem. Phys. Lett.* **276** (1-2), 70 (1997).

43) J. Almlöf and P. R. Taylor, *J. Chem. Phys.* **86** (7), 4070 (1987).

44) J. F. Stanton and J. Gauss, *J. Chem. Phys.* **103** (20), 8931 (1995).

45) L. T. Redmon, G. D. Purvis, and R. J. Bartlett, *J. Am. Chem. Soc.* **101** (11), 2856 (1979).

46) J. F. Stanton, *J. Chem. Phys.* **126** (13), 134309 (2007).

47) I. B. Bersuker, N. B. Balabanov, D. Pekker, and J. E. Boggs, *J. Chem. Phys.* **117** (23), 10478 (2002).

48) T. N. Kitsopoulos, I. M. Waller, J. G. Loeser, and D. M. Neumark, *Chem. Phys. Lett.* **159** (4), 300 (1989).

CHAPTER 4

Slow photoelectron velocity-map imaging of anion van der Waals clusters.

4.1 Slow photoelectron velocity-map imaging spectroscopy of ArO^- anion

Abstract

The high-resolution photoelectron spectrum of ArO^- was obtained using slow electron velocity-map imaging (SEVI). The SEVI spectrum reveals well-resolved vibrational transitions between multiple electronic states of ArO^- and ArO, both of which are open-shell species. These transitions occur within the broad envelope of previous lower resolution photoelectron spectra. Detailed assignments are made by comparison with theoretical simulations based on high level *ab initio* calculations and an atoms-in-molecule model that accounts for spin-orbit coupling in the anion and neutral. The adiabatic electron affinity of ArO is found to be 12481±2 cm^{-1}. Several ArO^- and ArO vibrational frequencies and excited-state term energies are accurately determined from the analysis of the experimental spectra and are found to be in excellent agreement with the calculated values.

4.1.1 Introduction

Photoelectron (PE) spectroscopy of molecular anions is a versatile method for determining electron affinities, excited state term energies, and vibrational frequencies of the corresponding neutral species.[1] A higher resolution variant of this technique, anion zero energy kinetic energy (ZEKE) spectroscopy,[2] has been applied to the study of open-shell van der Waals complexes via photodetachment of the appropriate anion.[3,4] Thus, for example, photodetachment of a rare gas halide such as $ArCl^-$ accesses the ground and low-lying electronic states of the ArCl van der Waals complex.[5] The spectral resolution of ZEKE, 1-3 cm^{-1}, reveals the individual vibrational levels supported by these electronic states that are otherwise difficult to access, and is thus highly complementary to scattering experiments on the same systems.[6] Accurate experimental spectroscopic constants on both the anion and neutral complexes can then be extracted from the spectra which provide a stringent test for the *ab initio* calculated interaction potentials of these species.

Here, we study the related species, ArO^- and ArO, using the recently developed slow electron velocity-map imaging (SEVI) technique, which offers comparable resolution to ZEKE but is considerably easier to implement.[7] The species investigated here are more complex than the rare gas halides, since both the anion and neutral are open shell species with $^2\Sigma^+$ and $^3\Pi$ ground states, respectively. In addition, there are more low-lying neutral electronic states for ArO than for the rare gas-halogen complexes. Hence, the extraction of accurate potential energy curves for the anion and neutral poses a challenge for both experiment and theory.

Early studies on the rare gas oxides were motivated by their possible application in excimer lasers.[8-10] The first experimental data on the interaction potential between Ar and oxygen atom was obtained from the total scattering cross-section experiments of Aquilanti and co-workers.[11-15] Ma *et al.*[16] measured the relative differential cross-section for inelastic intramultiplet transitions for oxygen colliding with Ar. Bowen and co-workers[17,18] have studied ArO^- via PE spectroscopy. The resolution of their apparatus (~200 cm^{-1}) did not allow the observation of individual vibronic transitions. However, a bimodal structure with temperature dependent relative intensity was observed and attributed to transitions originating from the ground state and the two low-lying excited states of the anion.

On the theoretical side, Buchachenko *et al.*[19] have implemented an atoms-in-molecule approach to construct potential energy curves for the anion and neutral electronic states, including spin-orbit coupling, and have simulated the ArO^- PE spectrum using these curves. Unrestricted fourth-order Moller-Plesset perturbation theory (UMP4) *ab initio* calculations were used in combination with this model and the simulated spectra was found to be in good agreement with the experimental measurements. Two subsequent theoretical studies using the restricted version of the coupled cluster method with single, double and non-iterative triple

excitations (RCCSD(T)) have produced more accurate interaction potentials for ArO[20] and ArO^-.[21] Subsequent work simulated the higher resolution ZEKE spectrum of ArO^-,[22] providing motivation for the experimental work described here. Unfortunately, these simulations were affected by a programming error in the intensity calculations. This error, in the symmetry adaptation of the atoms-in-molecule electronic wave functions, led to the absence of many bound-bound transitions in the simulations, a defect that was not apparent by comparison with the broad envelopes of the measured low-resolution PE spectra. The higher resolution experiments presented here have motivated not only a correction of the calculations but also a refined theoretical approach.

In this section, we present high-resolution photoelectron spectra of ArO^- obtained using SEVI. Numerous well-resolved transitions are observed within the broad envelope of the previous lower resolution photoelectron spectra. Accurate theoretical simulations are presented. The new procedure accounts correctly for all the bound-bound transition intensities and, in addition, includes the contribution of bound-free (dissociative photodetachment) transitions. New potentials for ArO^- and ArO are developed based on an advanced RCCSD(T) level of theory. All these improvements allow us to simulate the SEVI spectrum with high accuracy and help to assign most of its resolved features. Several ArO^- and ArO spectroscopic constants accurately determined from analysis of the experimental spectra are found to be in excellent agreement with the calculated values. Previous PE spectra are also reexamined within the improved theoretical approach to confirm the earlier interpretation and establish the connection with the SEVI measurements.

4.1.2 Experimental details

The SEVI technique and apparatus has been described in detail in section 2. ArO^- anions were produced from of a gas mixture comprising 0.1% N_2O and 10% argon in a balance of neon. The gas mixture, at a stagnation pressure of 350 psi, was expanded into the source vacuum chamber through an Even-Lavie pulsed valve[23] equipped with a circular ionizer.

The apparatus was calibrated by acquiring SEVI images of atomic oxygen[24] at several different photon energies. With the 200V VMI repeller voltage used in this study, the full widths at half maximum of the oxygen peaks were 2.2 cm^{-1} at 20 cm^{-1} eKE and 6.8 cm^{-1} at 150 cm^{-1} eKE.

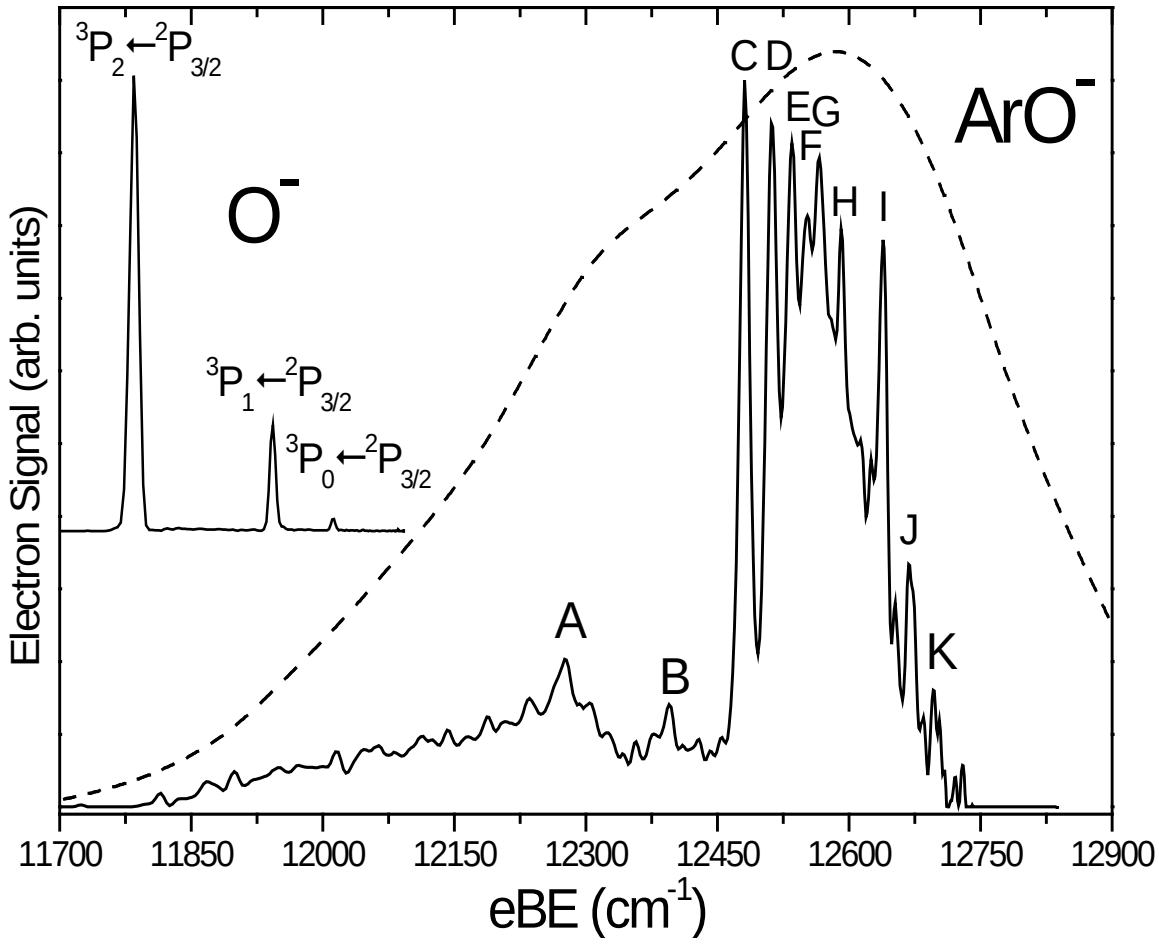

Figure 4.1 ArO^- SEVI spectrum (solid line) and previous PE spectrum from Ref 18 (dashed line) covering the electron binding energy range of 11700 cm^{-1} to 12900 cm^{-1}. The SEVI spectrum of O^- is also shown as an inset.

4.1.3 Experimental results

The ArO^- SEVI spectrum taken at a photon energy of 12838.7 cm^{-1} is shown in Figure 4.1, The spectrum is highly structured, with most transitions occurring between 12450 cm^{-1} and 12700 cm^{-1}. Clearly discernible peaks are labeled A-K and their positions are listed in Table I. The estimated error bars are ±2 cm^{-1}. There are at least two prominent progressions starting with peaks C and I, with characteristic peak spacings of 20-30 cm^{-1}. These progressions appear to lie above a smoothly varying background signal that peaks around 12550 cm^{-1}, but one cannot tell from the spectrum alone if this background results from spectral congestion or transitions to continuum states of the neutral complex. Signal is also seen below the main features, extending below 12000 cm^{-1}. A detailed assignment of the SEVI peaks can be made by comparison with the theoretical results presented in Section 4.1.4.

Figure 4.1 also shows the previous PE spectrum of de Clercq *et al.*[18] taken under source conditions generally characterized as "cold". Comparison of the two spectra illustrates the gain in resolution achieved by SEVI over conventional PE spectroscopy, where only a broad envelope was observed. The region of maximum intensity in the SEVI spectrum approximately coincides with the peak of the envelope in PE spectrum around 12600 cm^{-1}. However, compared to the PE spectrum, the SEVI spectrum displays much less intensity at eBE < 12450 cm^{-1}. De Clercq *et al*. found that intensity in this region was sensitive to ion source conditions and presumably resulted from "hot band" transitions originating from electronically excited anions. Hence, the intensity differences between the SEVI and PE spectra suggest lower anion temperatures in the SEVI experiment.

The SEVI spectrum of O^- taken at 12092 cm^{-1} photon energy and acquired under similar source conditions as the ArO^- spectrum is also shown in Figure 4.1. It comprises three well-resolved transitions from the $^2P_{3/2}$ ground spin-orbit state of O^- to the $^3P_{2,1,0}$ spin-orbit states of the neutral, seen at somewhat higher resolution than in recent photoelectron imaging studies.[25] We observed no transitions from the excited $^2P_{1/2}$ excited spin-orbit state of O^-, which lies 177.13 cm^{-1} above the $^2P_{3/2}$ state,[24] providing additional confirmation of a low anion temperature in our setup. All the features in the O^- and ArO^- spectra in Figure 4.1 have β values of 0.0±0.2, indicating an almost pure *s-wave* detachment behavior.

Table 4.1 Experimental and calculated peaks positions and shift from origin along with transition assignments. All energies in cm^{-1}. Estimated error bars for peaks A-K are $\pm 2\ cm^{-1}$.

Peak	Experimental		Calculated		Difference		Assignments
	eBE	Shift	eBE	Shift	ΔeBE	ΔShift	$n\Omega\ ,\ v \leftarrow n^{-}\ ,\ v^{-}$
A	12276	-205	12279.1	-196.6	-3	8	*II0* , 0 ← *II* , 0
B	12395	-86	12389.3	-86.4	6	1	*X*2 , 0 ← *X* , 1
C	12481	0	12475.7	0	5	0	*X*2 , 0 ← *X* , 0
D	12512	31	12506.3	30.6	6	0	*X*2 , 1 ← *X* , 0
E	12535	54	12527.0	51.3	8	3	*X*2 , 2 ← *X* , 0
F	12553	72	12547.5	71.8	6	0	*II*0 , 0 ← *X* , 1
G	12566	85	12558.8	83.1	7	2	*III*0 , 1 ← *X* , 2
H	12591	110	12578.1	102.4	13	8	*II*0 , 1 ← *X* , 1
I	12639	158	12633.9	158.2	5	0	*II*0 , 0 ← *X* , 0
J	12670	189	12664.6	188.9	5	0	*II*0 , 1 ← *X* , 0
K	12695	214	12685.3	209.6	10	4	*II*0 , 2 ← *X* , 0
a	12235	-246	12237.6	-238.1	-3	-8	*X*2 , 1 ← *I* , 1
b	12305	-176	12310.5	-165.2	-6	-11	*I*0 , 0 ← *X*, 2
c	12330	-151	12331.6	-144.1	-2	-7	*I*1 , 0 ← *X* , 2
d	12410	-71	12410.3	-65.4	0	-6	*I*1 , 0 ← *X* , 1
e	12430	-51	12432.6	-43.1	-3	-8	*I*1 , 1 ← *X* , 1

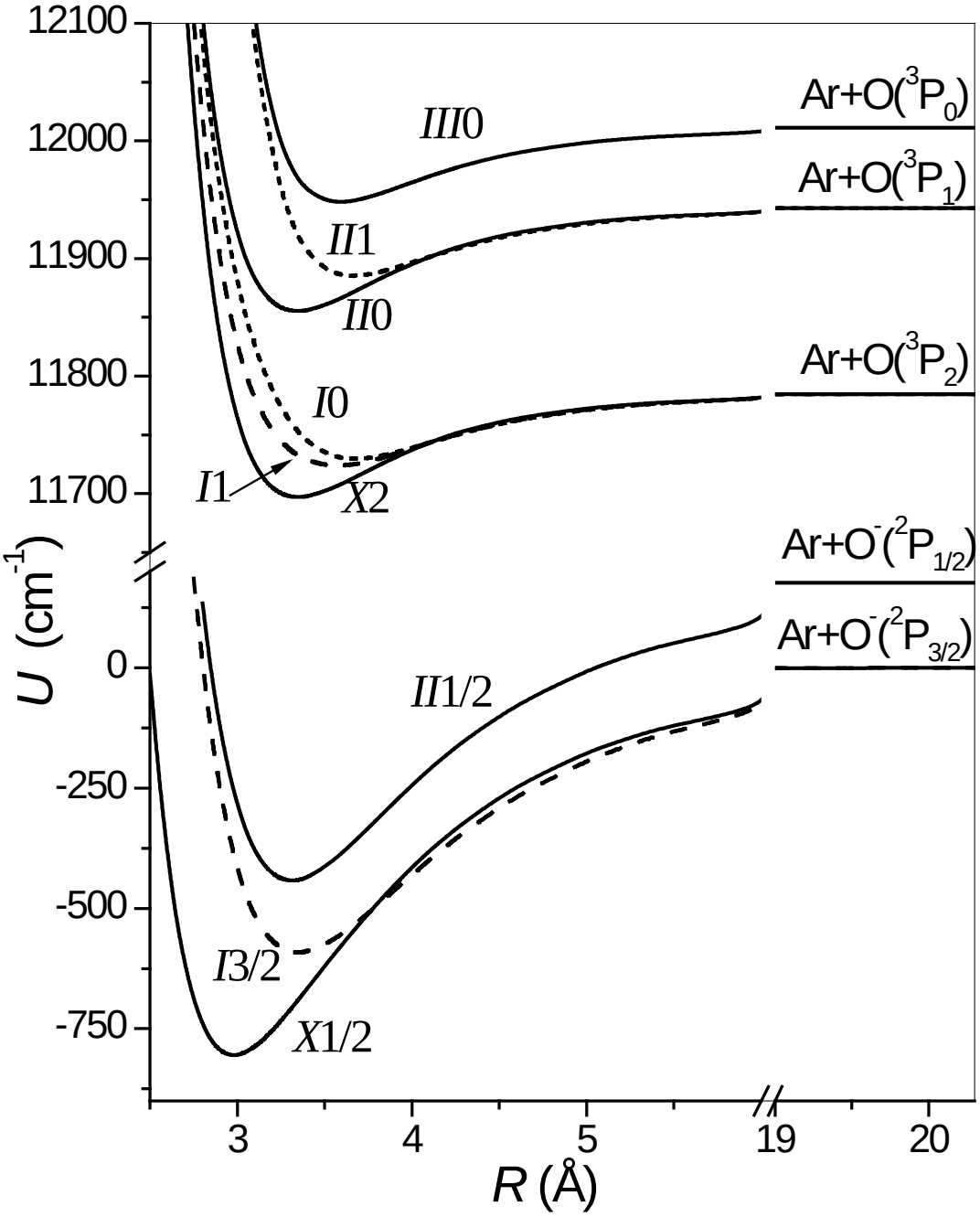

Figure 4.2 Spin-orbit coupled potentials of the ArO anion and neutral calculated using the atoms-in-molecule models from the *ab initio* RCCSD(T) AV6Z/bf33221 non-relativistic potentials.

4.1.4 Theoretical framework

A) Electronic structure and adiabatic potentials

In order to assign the features in the SEVI spectrum, we have performed *ab initio* calculations on the ArO^- anion and ArO neutral and simulated the spectrum. The electronic structure of these species has been described in detail.[19] In brief, under the non-relativistic approximation (or *LS* coupling scheme), the interaction of $Ar(^1S)$ with $O(^3P)$ gives rise to two terms of $^3\Sigma^-$ and $^3\Pi$ symmetry, while the interaction with the $O^-(^2P)$ anion gives two states of $^2\Sigma^+$ and $^2\Pi$ symmetry. The $^3\Pi$ and $^2\Sigma^+$ states are the lower energy states for the anion and neutral, respectively. We denote the corresponding potentials as V_Σ^-, V_Π^-, V_Σ, and V_Π.[19] Spin-orbit (SO) interaction further splits the molecular terms. For the neutral, there are six SO-coupled states designated as $n\Omega(j)$: $X2(2)$, $I1(2)$, $I0(2)$, $II1(1)$, $II0(1)$, and $III0(0)$, where n indexes the states with the same projection of the total electronic angular momentum j on the molecular axis Ω. Note that j is the asymptotically good quantum number with allowed values 0, 1, and 2. The SO-coupled states of the anion classified using similar $n^-\Omega^-(j^-)$ notation are $X1/2(3/2)$, $I3/2(3/2)$ and $II1/2(1/2)$. For clarity, these electronic states will be denoted only as $n\Omega$ ($X2$, $I1$, $I0$, $II1$, $II0$, and $III0$) for the neutral and as n^- (X, I, and II) for the anion. The asymptotic energies of the terms correlating to $Ar + O(^3P_j)$ limits referenced to the lowest $j = 2$ term are Δ_j, $\Delta_1 = 158.27$ and $\Delta_0 = 226.98$ cm^{-1}. [26] The $Ar + O^-(^3P_{1/2})$ limit lies $\Delta^- = 177.13$ cm^{-1} above the ground $Ar + O^-(^3P_{3/2})$ limit.[24] The lowest anion $j^- = 3/2$ and neutral $j = 2$ limits are separated in energy by the electron affinity of oxygen atom,[24] $EA = 11784.7$ cm^{-1}.

Previously,[19] the V_Σ^-, V_Π^-, V_Σ, and V_Π potentials were calculated using the UMP4 method with the augmented correlation consistent aug-cc-pVnZ (AVnZ), n = T basis set[27] and the 3s3p2d set of bond functions (bf332) placed at the midpoint of internuclear distance R. Since then, two refined calculations have been performed. Interaction potentials for RgO (Rg=He-Kr) were computed using the RCCSD(T) method and larger basis set, AVQZ, plus the bf332 augmentation.[20] The calculations of the RgO^- anions for Rg = He-Ar implemented the RCCSD(T) method with AV5Z basis set[21]. To attain consistent and even better description of the non-relativistic interactions for ArO and ArO^- species, we used here the RCCSD(T) method and VnZ and AVnZ bases with n = 5 and 6, sometimes augmented by the 3s3p2d2f1g bond function set (bf33221).[28] We also examined the effect of the second-order Douglas-Kroll (DK) relativistic correction (it was applied in combination with the specially optimized AV5Z-DK basis set) and core correlation correlating explicitly the $2p^6$ shell of Ar [normally, as in the previous calculations, the orbitals of $O(1s^2)$ and $Ar(1s^22s^22p^6)$ shells were treated as the core orbitals]. All the potentials mentioned here were corrected for basis set superposition error using the full counterpoise correction.[29]

Equilibrium distances and interaction energies for various *ab initio* potentials mentioned above are presented in Table 4.2. The new calculations are a significant improvement over the previous UMP4 potentials[19] and agree well with more recent results.[20,21] Saturation of the basis set by the diffuse atomic functions is the most important factor: the V5Z basis unexpectedly gives too deep anion potentials with respect to AV5Z. Further expansion to AV6Z set and addition of the bond functions provides only minor effects. Neither the scalar relativistic correction under the DK approximation, nor the correlation of the Ar $2p^6$ shell are significant. Overall, the results indicate the good convergence of all potentials at the RCCSD(T) AV6Z/bf33221 level of theory, so in what follows we will work with these potentials. For the neutral, they can also be compared to the potentials derived from the beam scattering experiments.[15]

Vectorial SO interaction was introduced using the atoms-in-molecule model that fixes the SO coupling constants at their asymptotic (atomic) values. Explicit expressions for the SO-coupled potentials were given by Eqs.(7) and (10) in Ref.[19] (see also Refs.[15,16,30]). The potentials are depicted in Figure 4.2 and characterized in Table 4.3. Adiabatic transition energies T_0, dissociation energies D_0, and vibrational constants shown therein were obtained by solving the radial Schrödinger equations numerically for zero rotational angular momentum and fitting the lowest vibrational levels to the Dunham expansion. For the deeper anion potentials, the 10 lowest levels were used, while for the neutral, all bound levels supported by the potential (4 or 5) were included.

Table 4.2 *Ab initio* data on equilibrium distances (R_e) and interaction energies (D_e) of the non-relativistic potentials of the ArO anion and neutral.

Method[a]	$ArO^-(^2\Sigma^+)$		$ArO^-(^2\Pi)$		$ArO(^3\Pi)$		$ArO(^3\Sigma^-)$	
	R_e(Å)	D_e(cm^{-1})	R_e(Å)	D_e(cm^{-1})	R_e(Å)	D_e(cm^{-1})	R_e(Å)	D_e(cm^{-1})
V5Z/bf33221	2.945	900	3.346	606	3.355	85.8	3.791	47.1
V5Z-DK/bf33221	2.942	904	3.338	611	3.351	86.1	3.791	47.1
V5Z-DK/bf33221[b]	2.938	907	3.335	614	3.345	86.8	3.786	47.5
AV5Z/bf33221	2.974	851	3.356	591	3.349	87.6	3.785	49.1
AV6Z/bf33221	2.973	852	3.351	592	3.347	87.8	3.781	49.2
AV6Z	2.974	845	3.356	586	3.360	84.8	3.830	47.1
UMP4/AVTZ/bf332[c]	3.013	788	3.408	533	3.384	83.7	3.801	48.2
AVQZ/bf332[d]	-	-	-	-	3.357	85.8	3.799	48.4
AV5Z[e]	2.975	836	3.358	579	-	-	-	-
Exp.[f]	-	-	-	-	3.45 ±0.07	84±8	3.85 ±0.08	41±4

[a] RCCSD(T) unless otherwise stated

[b] With explicit correlation of the Ar($2p^6$) shell

[c] From Ref. 19 [d] From Ref. 20 [e] From Ref. 21 [f] From Ref. 15

Table 4.3 Parameters of the SO-coupled potentials of the ArO anion and neutral calculated using the *ab initio* non-relativistic AV6Z/bf33221 potentials.

State	R_e (Å)	D_e (cm^{-1})	T_0 (cm^{-1})	D_0 (cm^{-1})	ω_e (cm^{-1})	$\omega_e x_e$ (cm^{-1})
ArO^-						
X	2.976	805.9	0	759.7	89.3	2.87
I	3.351	592.2	202.6	557.1	67.6	2.30
II	3.318	620.4	354.9	581.9	76.4	2.66
ArO						
*X*2	3.347	87.8	12475.7	68.6	38.5	4.34
*I*1	3.559	61.3	12496.7	47.6	28.5	3.35
*I*0	3.659	55.6	12502.3	42.0	26.9	3.30
*II*1	3.647	58.2	12659.9	42.7	30.7	4.23
*II*0	3.347	87.8	12634.0	68.6	38.5	4.34
*III*0	3.569	63.9	12724.0	47.3	30.7	3.83

B) Spectral simulations

The positions of spectral features, or electron binding energies eBE, are determined by conservation law:

$$E_i + E_0 = E_f + \text{eKE} = E_i + \text{eKE} + \text{eBE} \tag{4.1}$$

where E_i and E_f are the initial energy of the anion and final energy of the neutral, respectively, and E_0 is the (fixed) photon energy. The transition energy is therefore

$$E = \text{eBE} = E_f - E_i. \tag{4.2}$$

For simplicity and clarity of interpretation, we disregarded rotational structure and considered vibronic bound-bound $n\Omega$, $v \leftarrow n^-$, v^- and bound-free $n\Omega$, $\varepsilon \leftarrow n^-$, v^- transitions, where v^- and v denote the vibrational levels in the particular electronic states of the anion n^- and neutral n, respectively, and ε specifies the kinetic energy of the Ar + O(^3P_j) products above the corresponding dissociation threshold. The theory underlying the spectral envelope simulations is similar to that presented by Buchachenko *et al*,[19] which, in turn, was based on the approach to ZEKE spectral intensities by Zhao *et al*.[3] The starting point for the bound-bound spectral simulation is the Eqs.(13)-(16) in Ref.[19]. For the present case one has

$$I_{if}^{\text{bb}} = I^{\text{bb}}(n\Omega, v \leftarrow n^-, v^-) = \sum_k I_k^{\text{bb}}(n\Omega, v, j_e = 1/2 \leftarrow n^-, v^-), \tag{4.3}$$

where only *s*-wave electron detachment is considered by setting the total angular momentum of the photoelectron j_e to 1/2. The summation index k corresponds to the combined angular momentum of the photon and photoelectron and runs over 1/2 and 3/2.[3] The vibronic line strength factor is

$$I_k^{\mathrm{bb}} = \left| \left\langle v' \left| \mu_k (n \leftarrow \Omega n^-) \right| v^- \right\rangle \right|^2 = (2k+1) \left| \sum_{m,\omega} (-1)^{-\mu-\omega-q} \begin{pmatrix} 1/2 & 1 & k \\ \omega & -\mu & q \end{pmatrix} \left\langle v' \left| T_{n^- n}(1,\mu) \right| v \right\rangle \right|^2 \tag{4.4}$$

Here ω and q are the projections of j_e and k angular momenta to the internuclear axis, respectively, and μ denotes the component of the spherical transition dipole moment operator. The electronic transition dipole matrix element $T_{n^- n}(1,\mu)$ is exactly the same quantity that enters similar Eq.(16) in Ref. [19] and is expressed by Eqs.(17) and (18) therein. The error mentioned in the Introduction was associated to the parity adaptation of the neutral electronic wave functions in the numerical implementation of these equations and does not affect the analytical formulas.

The bound-free component I^{bf} was calculated in the same way by replacing the bound vibrational function $|v\rangle$ in Eq. 4.4 by the continuum function $|\varepsilon\rangle$. The latter was normalized to the semiclassical asymptotic solution to warrant the normalization fully compatible to that of the bound-free component (see, e.g., Ref.[31] and references therein).

The full spectral envelope was synthesized as

$$S(E) \propto \sum_i g_i(T) \int_{-\infty}^{E_0} \left[I_{if}^{\mathrm{bb}}(E') + I_{if}^{\mathrm{bf}}(E') \right] \Theta(E - E' + E_i) dE', \tag{4.5}$$

where $g_i(T)$ is the initial state population taken as the equilibrium Boltzmann factor at the single internal temperature T and Θ is the line shape function taken as Gaussian, of the width (FWHM) Γ, multiplied by the factor $\sqrt{E_0 - E}$ that accounts for the threshold law for *s*-wave electron detachment.[32] Setting $I_{if}^{\mathrm{bb}}(E) = I_{if}^{\mathrm{bb}} \delta(E_f - E_i)$, where δ is the Dirac function, and specifying explicitly electronic and vibrational quantum numbers, one has

$$\begin{aligned} S(E) \propto \sum_{n-v-} \sum g_{n-v-}(T) \sum_{n\Omega} \Bigg[& \sum_v I^{\mathrm{bb}}(n\Omega, v \leftarrow n^- v^-) \Theta(E - E_{n\Omega v} + E_{n-v-}) \\ & + \int_{-\infty}^{E_0} I^{\mathrm{bf}}(n\Omega, E' \leftarrow n^- v^-) \Theta(E - E' + E_{n-v-}) dE' \Bigg]. \end{aligned} \tag{4.6}$$

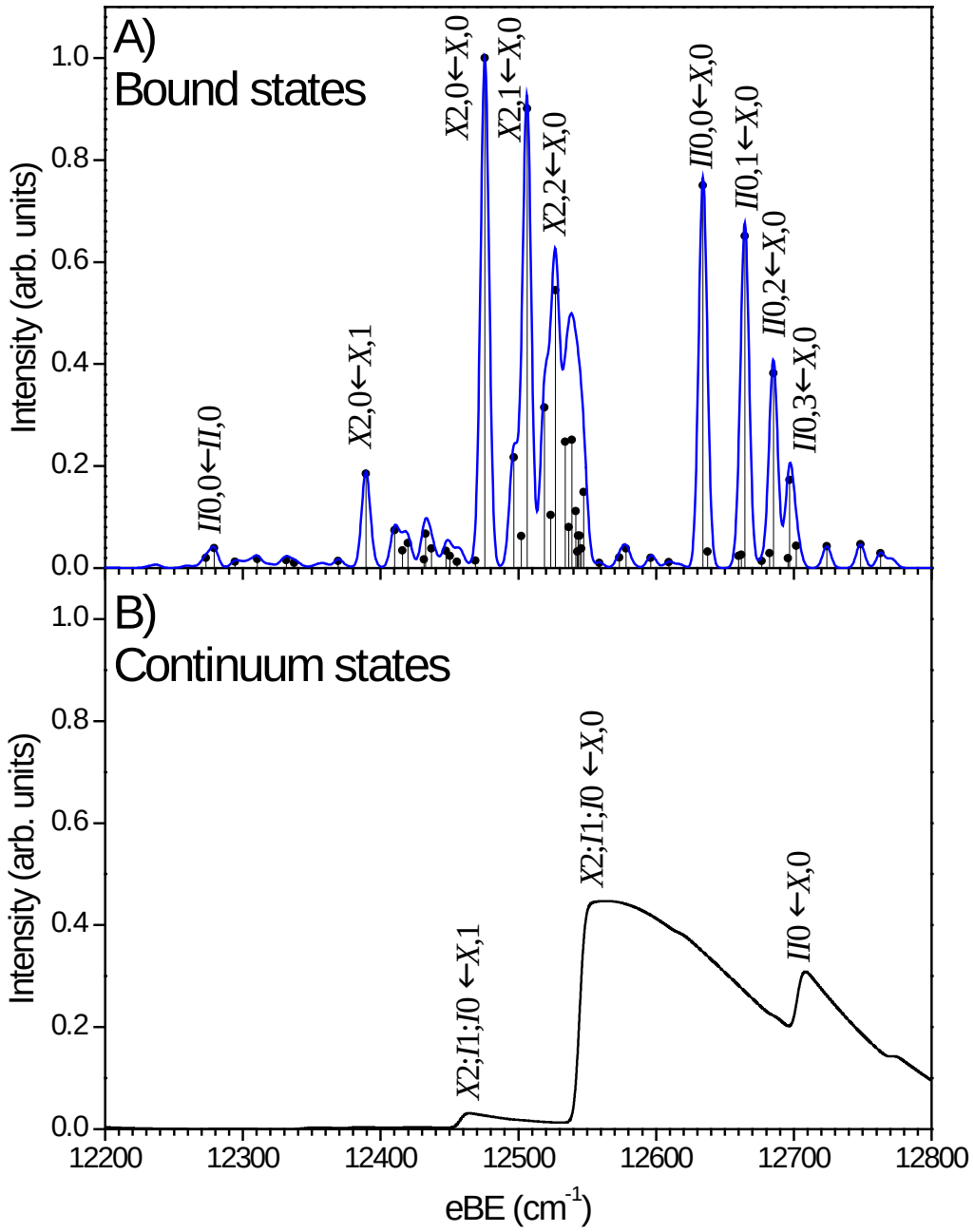

Figure 4.3 Simulated spectrum at T = 50 K and Γ = 5 cm^{-1} showing transitions to bound states (top panel) and continuum states (bottom panel).

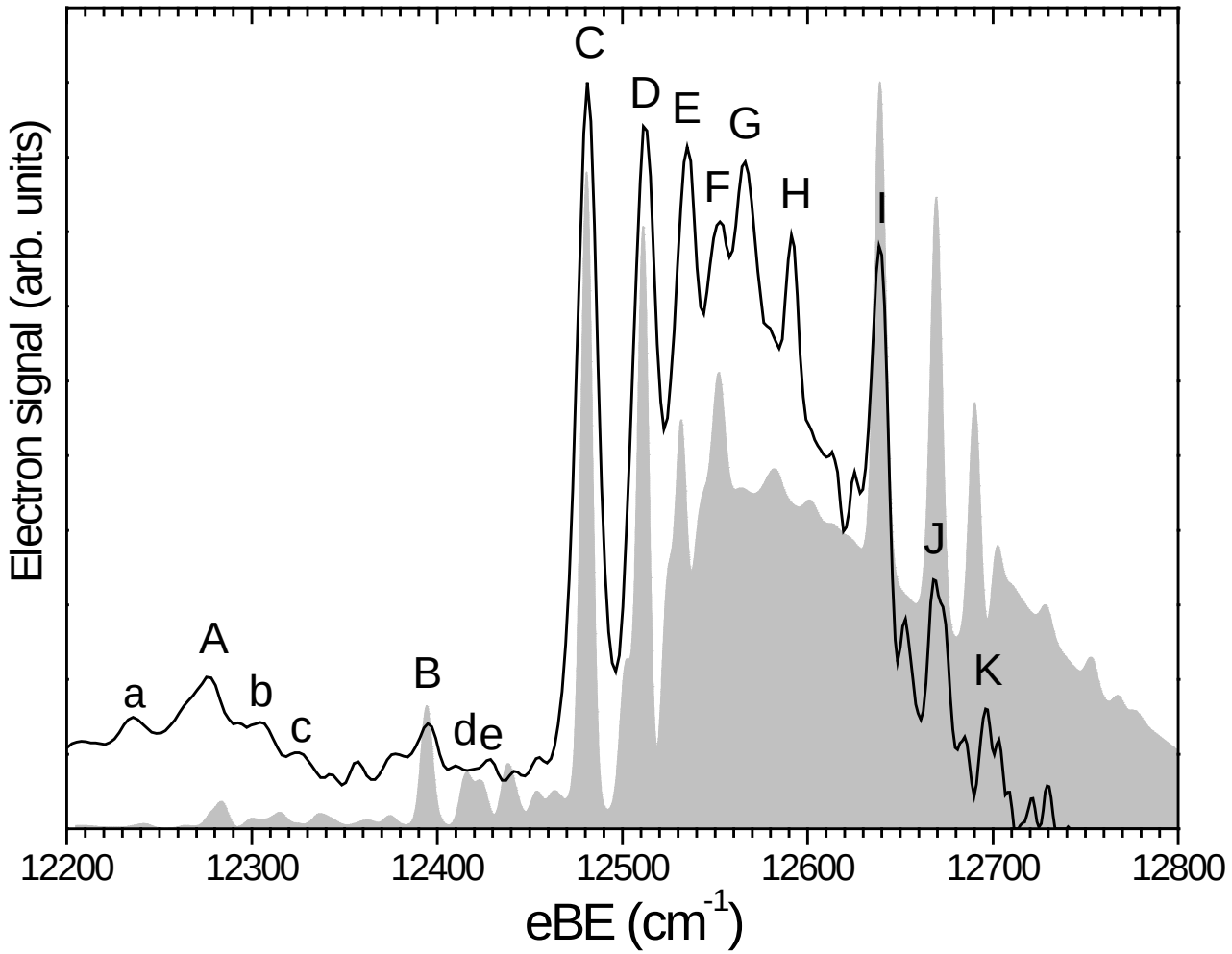

Figure 4.4 Comparison of the experimental (black line) and simulated (shadowed) ArO^- SEVI spectrum in the 12200 cm^{-1} to 12800 cm^{-1} electron binding energy range.

The vibrational wave functions and energies were computed numerically for the adiabatic SO-coupled potentials introduced above. To simulate the bound-bound part of the spectra, transitions to all bound vibronic levels of the neutral from the lowest ten levels of each anion electronic state were taken into account. This set of initial levels ensures the convergence of the anion partition function at the internal temperatures as high as 400 K. In the simulations of the bound-free components, the transitions from the few lowest anion vibronic levels (X, $v^- = 0$-4; I, $v^- = 0$, 1; II, $v^- = 1$) to all adiabatic continua were included. The I^{bf} function was represented on a uniform grid of energies from E_{min} to E_0, where E_{min} corresponds to the energy of the lowest threshold in the set. Integration in Eq. 4.6 was performed using the Simpson one-third rule.

Preliminary adjustment indicated that the values $\Gamma = 5$ cm^{-1} and $T = 50$ K provide good representation for the observed SEVI spectrum. The resulting simulated spectral envelope is shown in Figure 4.3. The bound-bound and bound-free transitions are presented in panels 4.3A and 4.3B, respectively. In Figure 4.3A, the vertical lines represent the positions and intensities of the individual bound-bound vibronic transitions with the more intense being explicitly identified as $n\Omega$, $v \leftarrow n^-$, v^-. Similarly, in Figure 4.3B, the bound-free transitions are denoted as $n\Omega \leftarrow n^-$, v^-. It can be seen from Figure 4.3A that the bound-bound simulated spectrum is dominated by two bands of peaks that are transitions from the anion ground level to the various vibrational levels of the neutral $X2$ and $II0$ states. This result reflects the selectivity of the spin-orbit transitions but also the fact that these two states have an equilibrium geometry more similar to the anion ground state than the equilibrium geometries of the other neutral states (see Figure 4.2 and Table 4.2). The bound vibrational wave functions of the $X2$ and $II0$ states thus have larger Franck-Condon overlap with the anion ground state. The simulated bound-free spectrum is dominated by two main features. The larger feature at 12565 cm^{-1} is composed of transitions from the anion ground level to the $X2$, $I1$, and $I0$ continuum states. Similarly, the second feature at 12712 cm^{-1} is composed of transitions from the anion ground level to the $II0$ continuum.

4.1.5 Analysis and discussion

A. Peak assignments and comparison with theory

Figure 4.4 compares the ArO^- SEVI spectrum and the full simulation, including both panels in Figure 4.3. Overall, the simulated and experimental spectra agree reasonably well, facilitating the assignment of most of the features. The resulting assignments of peaks A-K in the SEVI spectrum are listed in Table 4.1, along with the experimental and calculated position of each peak. Peak C at 12481 cm^{-1} is assigned to the $X2\ ,0 \leftarrow X\ ,0$ origin transition. This value is the electron affinity EA for ArO and is in very good agreement with the calculated value of 12475.7 cm^{-1}. The shifts of all experimental and calculated peaks relative to this transition are given in Table III, as is the difference between the experimental and calculated

shift for each peak, in the "ΔShift" column. These differences are 8 cm^{-1} for the small peaks A and H, and 4 cm^{-1} or less for the remaining peaks.

Peaks D and E are thus assigned to the $X2$, $v \leftarrow X$, 0 transitions with v = 1 and 2, respectively. Peaks I, J and K are assigned to the $II0$, $v \leftarrow X$, 0 progression with v = 0, 1, and 2 , respectively. The positions of the observed levels on these two states are consistent with the atoms-in-molecule model[19] used here. In this model, the potential energy curves of the neutral $X2$ and $II0$ state are only defined by the $^2\Pi$ potential, with the two curves being separated by the 158.27 cm^{-1} $^3P_1$-$^3P_2$ oxygen spin-orbit splitting (Δ_1). In agreement with the calculations, the splitting between peaks C and I in the SEVI spectrum, which is the separation between the vibrational ground state levels of the $X2$ and $II0$ states, is found to be 158 cm^{-1}. We also find an identical fundamental vibrational frequency of 31 cm^{-1} for both states which is in excellent agreement with the calculated value, 30.6 cm^{-1}. However, the experimental frequency of the v = 2 levels in these two states is found to be 3-4 cm^{-1} above the 51.3 cm^{-1} calculated value. This indicates that the calculations slightly overestimate the anharmonicity of the interaction potential for these two particular states.

All the remaining peaks in the SEVI spectrum are assigned to hot band transitions, most of them originating from the first excited vibrational level of the anion ground electronic state. Peaks B and F are assigned to the transitions to $X2,0$ and $II0,0$ neutral levels from the X ,1 level of the anion, respectively. The splitting between peaks F and I is the same that that between peaks B and C and thus yields an experimental fundamental frequency of 86 cm^{-1} for the X anionic ground-state. This is again in excellent agreement with the 86.4 cm^{-1} calculated value.

Peak A at 12276 cm^{-1} is assigned to the $II0$, $0 \leftarrow II$, 0 transition and is the only well resolved feature originating from one of the two low-lying anionic excited states. The separation between peaks A and I thus yields an experimental term energy of 363 cm^{-1} for the II anion state which is slightly larger than the calculated value of 354.9 cm^{-1}. There are several smaller peaks in the vicinity of peaks A and B, labeled a-e in Figure 4 that line up well with smaller features in the simulation from vibrational hot bands. Based on this correspondence, as well as on the results of simulations at higher temperatures in the next subsection, peaks a-e are also assigned in Table 1, but these assignments must be considered as quite tentative owing to the poor signal-to-noise associated with these small features.

Peaks G and H are more difficult to assign. They occur in a spectral region where the simulated bound-bound spectrum is very weak (see Fig. 4.3A) but where detachment to the Ar + O continuum is substantial. Based on calculated peak positions alone (and not intensities), peak G can be tentatively assigned to the $III0,1 \leftarrow X, 2$ transition and peak H to the $II0,1 \leftarrow X,1$ transition. As shown in Table 1, the deviations between calculated and experimental peak positions are quite small, particularly when the "shifted" calculated energies are used. An alternative assignment, however, should also be mentioned. Peaks G

and H are separated by 25 cm^{-1}, which is the same spacing found between peaks D and E (23 cm^{-1}) and J and K (25 cm^{-1}), suggesting that they, like peaks J and K, may represent transitions to the v=1 and 2 levels of the *II0* neutral state (which, as discussed above, has the same vibrational level spacings as the *X2* neutral state). Peaks G and H could originate from the v=0 level of the anion *I*3/2 state, but this assignment would imply a term value T_0=104 cm^{-1} for that state, which considerably lower than the calculated value of 202.6 cm^{-1} in Table 4.3. This, in turn, would require that the dissociation energy of the ArO^- $^2\Pi$ state be increased by around 100 cm^{-1} compared to the calculated value of 592 cm^{-1} in Table 4.2, which seems excessively large. Hence, the assignments in Table I are preferred at present.

It can be seen from the previous discussion and from Table 4.3 that the calculated peak positions and spectroscopic constants are in good overall agreement with the experimental values. This agreement confirms the reliability of the *ab initio* calculations and the spin-orbit treatment used here for the ArO and ArO^- interaction potentials. While the peak positions agree very well, the simulated spectrum displays some noticeable intensity differences from the SEVI spectrum, particularly at high eBE where the continuum contribution appears larger in the simulations than in the experiment. There are many factors that may affect the accuracy of the intensity calculations. Small inaccuracies in the interaction potentials are likely responsible for the too slow fall-off of the continuum at high eBE. Assumption of single-temperature Boltzmann equilibrium, as well as the use of single line width parameter for all transitions including the bound-free ones, are hard to justify *ad hoc*. The theory[19] used for the photodetachment transition dipole matrix elements in Eq. 4.5 does not accurately capture threshold behavior that may affect the intensity not only close to E_0, but also close to the onset of bound-free transitions.

B) Simulations of previous PE spectra

As was already mentioned, conventional photoelectron (PE) spectra of the complexes formed by the O^- anion with Ar, Kr, Xe and N_2 were obtained by de Clercq *et al.*[18] These spectra, recorded at significantly lower resolution (~200 cm^{-1}), have a bimodal structure. Two broad peaks alter their relative intensity depending on the expansion source conditions that correspond to production of "cold", "warm" and "hot" anions, see Figure 4.5. Theoretical analysis of these spectra[19,33] was limited by inaccuracy in the interaction potentials and the error in transition intensity calculation mentioned above that may have led to misinterpretation. Therefore, we performed refined spectral simulations with the same set of transitions as were used for the SEVI simulations, varying only the anion temperature and the Gaussian line width. The spectra simulated with the experimental line width of 200 cm^{-1} always appear as a single broad peak that moves towards lower electron binding energy as the temperature increases. However, the use of a smaller width, Γ = 140 cm^{-1}, provides very reasonable agreement with experiment: as temperature grows from 190 to 310 K, the spectral envelope evolves from higher to lower energy, passing through the bimodal pattern as shown

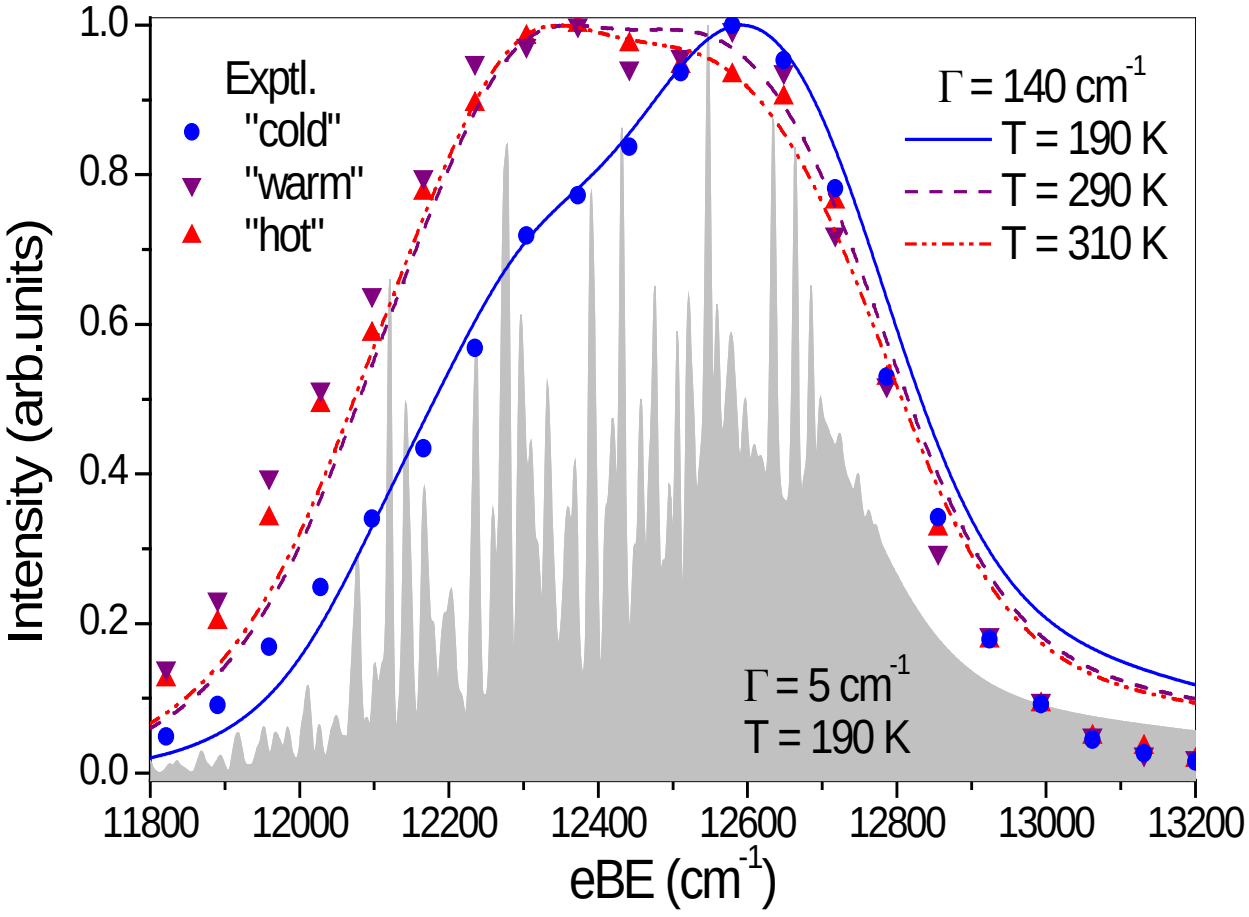

Figure 4.5 Comparison of the experimental[18] and simulated ArO^- PE spectra at three expansion source conditions or temperatures. Shadowed spectrum is simulated at "cold" conditions (190 K) with the SEVI resolution of 5 cm^{-1}.

in Figure 4.5. The positions of both peaks agree very well with the experiment. The reduction of line width can be explained by the "broadening" of simulated spectra due to exaggeration of discrete-continuum contribution, as follows from the analysis of the SEVI spectrum.

To illustrate the connection between the PE and SEVI spectra, we also present in Figure 4.5 the spectrum simulated at "cold" (190 K) temperature and SEVI resolution (Γ = 5 cm^{-1}). Above eBE = 12450 cm^{-1}, this simulation reveals the same transitions as does the true SEVI spectrum. Among them, hot-band transitions forming peaks F, G and H gain intensity with respect to the transitions from the anion ground state represented by peaks C, D and E. The *II*0, 0 ← *X* , 1 transition (peak F) determines the position of the high-energy feature of the PE spectrum. At lower eBE, between 12250 and 12450 cm^{-1}, two of the three most prominent features are also seen in the SEVI spectrum as the weak peaks A, B and d-e. Most of the transitions falling in this region, which determine the low-energy peak in the PE spectra, originate either from the first anion excited state *I*3/2 or from vibrationally-excited levels of the anion ground state *X*. The group of features appearing below peak A (12280 cm^{-1}) corresponds to the transitions from the second excited state *II* with admixtures of transitions from highly excited vibrational levels of the *X* and *I* states. It should be noted that although previous theoretical interpretation of the ArO^- PE spectra by Buchachenko *et al*.[19] was wrong in the detailed assignment of individual transitions, the main conclusion[18] that two peaks generally correspond to two states of the anion, *X* and *I*, remains valid.

4.1.6 Conclusions

The high-resolution photoelectron spectrum of ArO^- obtained using the slow electron velocity-map imaging technique is reported. New high level *ab initio* calculations on the ArO^- and ArO are presented and used in combination with an atom-in-molecule model to simulate the SEVI spectrum. Several ArO^- and ArO vibrational frequencies and excited-state term energies are accurately determined from the analysis of the experimental spectra and are found to be in excellent agreement with the calculated values. The theoretical analysis of the previous PE spectrum of ArO^- has also been revised in the light of the new *ab initio* calculations and spectral simulations.

References:

1) J. C. Rienstra-Kiracofe, G. S. Tschumper, H. F. Schaefer, S. Nandi, and G. B. Ellison, *Chem. Rev.* **102** (1), 231 (2002).
2) T. N. Kitsopoulos, I. M. Waller, J. G. Loeser, and D. M. Neumark, *Chem. Phys. Lett.* **159** (4), 300 (1989).
3) Y. X. Zhao, I. Yourshaw, G. Reiser, C. C. Arnold, and D. M. Neumark, *J. Chem. Phys.* **101** (8), 6538 (1994).
4) I. Yourshaw, T. Lenzer, G. Reiser, and D. M. Neumark, *J. Chem. Phys.* **109** (13), 5247 (1998).
5) T. Lenzer, I. Yourshaw, M. R. Furlanetto, G. Reiser, and D. M. Neumark, *J. Chem. Phys.* **110** (19), 9578 (1999).
6) V. Aquilanti, D. Cappelletti, V. Lorent, E. Luzzatti, and F. Pirani, *J. Phys. Chem.* **97** (10), 2063 (1993).
7) D. M. Neumark, *J. Phys. Chem. A* **112**, 13287 (2008).
8) H. T. Powell, J. R. Murray, and C. K. Rhodes, *Appl. Phys. Lett.* **25** (12), 730 (1974).
9) T. H. Dunning and P. J. Hay, *J. Chem. Phys.* **66** (8), 3767 (1977).
10) S. R. Langhoff, *J. Chem. Phys.* **73** (5), 2379 (1980).
11) V. Aquilanti, G. Liuti, F. Pirani, F. Vecchiocattivi, and G. G. Volpi, *J. Chem. Phys.* **65** (11), 4751 (1976).
12) V. Aquilanti, P. Casavecchia, G. Grossi, and A. Lagana, *J. Chem. Phys.* **73** (3), 1173 (1980).
13) V. Aquilanti and G. Grossi, *J. Chem. Phys.* **73** (3), 1165 (1980).
14) V. Aquilanti, E. Luzzatti, F. Pirani, and G. G. Volpi, *J. Chem. Phys.* **73** (3), 1181 (1980).
15) V. Aquilanti, R. Candori, and F. Pirani, *J. Chem. Phys.* **89** (10), 6157 (1988).
16) Z. Ma, K. Liu, L. B. Harding, M. Komotos, and G. C. Schatz, *J. Chem. Phys.* **100** (11), 8026 (1994).
17) S. T. Arnold, J. H. Hendricks, and K. H. Bowen, *J. Chem. Phys.* **102** (1), 39 (1995).
18) H. L. de Clercq, J. H. Hendricks, and K. H. Bowen, *J. Chem. Phys.* **117** (6), 2619 (2002).

19) A. A. Buchachenko, J. Jakowski, G. Chalasinski, M. M. Szczesniak, and S. M. Cybulski, *J. Chem. Phys.* **112** (13), 5852 (2000).

20) R. V. Krems, A. A. Buchachenko, M. M. Szczesniak, J. Klos, and G. Chalasinski, *J. Chem. Phys.* **116** (4), 1457 (2002).

21) L. A. Viehland, R. Webb, E. P. F. Lee, and T. G. Wright, *J. Chem. Phys.* **122** (11) (2005).

22) A. A. Buchachenko, M. M. Szczesniak, and G. Chalasinski, *Chem. Phys. Lett.* **347** (4-6), 415 (2001).

23) U. Even, J. Jortner, D. Noy, N. Lavie, and C. Cossart-Magos, *J. Chem. Phys.* **112** (18), 8068 (2000).

24) D. M. Neumark, K. R. Lykke, T. Andersen, and W. C. Lineberger, *Phys. Rev. A* **32** (3), 1890 (1985).

25) S. J. Cavanagh, S. T. Gibson, M. N. Gale, C. J. Dedman, E. H. Roberts, and B. R. Lewis, *Phys. Rev. A* **76** (5) (2007).

26) Y. Ralchenko, A. E. Kramida, and J. Reader, (National Institute of Standards and Technology, Gaithersburg, MD., 2008).

27) D. E. Woon and T. H. Dunning, *J. Chem. Phys.* **98** (2), 1358 (1993).

28) S. M. Cybulski and R. R. Toczylowski, *J. Chem. Phys.* **111** (23), 10520 (1999).

29) S. F. Boys and F. Bernardi, *Mol. Phys.* **19** (4), 553 (1970).

30) R. V. Krems and A. A. Buchachenko, *J. Phys. B: At. Mol. Opt. Phys.* **33** (21), 4551 (2000).

31) P. S. Herman and K. M. Sando, *J. Chem. Phys.* **68** (3), 1153 (1978).

32) E. P. Wigner, *Phys. Rev.* **73** (9), 1002 (1948).

33) A. A. Buchachenko, M. M. Szczesniak, J. Klos, and G. Chalasinski, *J. Chem. Phys.* **117** (6), 2629 (2002).

4.2 Slow photoelectron velocity map imaging spectroscopy of KrO^- anion

Abstract

The high-resolution photoelectron spectrum of KrO^- was obtained using slow electron velocity-map imaging (SEVI). The SEVI spectrum reveals numerous vibronic transitions between multiple electronic states of KrO^- and KrO, both of which are open-shell species. Detailed assignments are made by comparison with theoretical simulations based on high level *ab initio* calculations and an atoms-in-molecule model that accounts for spin-orbit coupling in the anion and neutral. Several KrO^- and KrO vibrational frequencies and excited-state term energies are accurately determined from the analysis of the experimental spectra and are found to be in good agreement with the calculated values.

4.2.1 Introduction

Photoelectron (PE) spectroscopy of molecular anions is a versatile method for determining electron affinities, excited state term energies, and vibrational frequencies of the corresponding neutral species.[1] However, its limited energy resolution (5-10 meV) restricts the degree to which low-frequency vibrational modes can be resolved. This deficiency has been addressed using a related higher resolution technique, anion zero energy kinetic energy (ZEKE) spectroscopy,[2] which has been applied to the study of several weakly bound open-shell rare-gas halide complexes via photodetachment of the appropriate anion.[3-6] ZEKE spectroscopy resolves the closely-spaced vibrational levels supported by these electronic states and thus yields spectroscopic information that is highly complementary to scattering experiments on the same systems.[7] Accurate experimental spectroscopic constants for the anion and neutral complexes can be extracted from the spectra and compared to *ab initio* calculated interaction potentials of these species. The recently developed slow electron velocity-map imaging (SEVI) technique, which is a hybrid between ZEKE and conventional PE spectroscopy, has recently been used to study the ClH_2 and ArO van der Waals complexes by photodetachment of ClH_2^- and ArO^-.[8,9] SEVI offers comparable resolution to anion ZEKE (2-3 cm^{-1}) but is considerably easier to implement.[10]

In this section, we continue our investigation of rare-gas oxides using the SEVI technique by studying KrO^- and KrO. These species are both open shell complexes with $^2\Sigma^+$ and $^3\Pi$ ground states, respectively, and have several low-lying electronic states. Hence, the extraction of accurate potential energy curves for the anion and neutral poses a challenge for both experiment and theory.

Early studies on the rare gas oxides were motivated by their possible application in excimer lasers.[11-13] The first experimental data on the interaction potentials between rare-gas and oxygen atoms was obtained from the beam scattering experiments of Aquilanti and co-workers.[14-18] de Clercq *et al*. have studied KrO^- via conventional PE spectroscopy.[19] The resolution of their apparatus (~200 cm^{-1}) did not allow the observation of individual vibronic transitions. However, a bimodal structure with temperature-dependent relative intensity was observed and attributed to transitions originating from the ground state and the two low-lying excited states of the anion.

On the theoretical side, an atoms-in-molecule model in conjunction with *ab initio* calculations has been implemented to construct potential energy curves for the anion and neutral electronic states, including spin-orbit (SO) coupling, and to evaluate the PE transition probabilities.[20] The KrO^- PE spectrum simulated using this approach was found to be in good agreement with the experimental measurements.[21] Unfortunately, as explained in Ref 9, these simulations were affected by a programming error which led to the absence of many bound-

bound transitions in the simulations, a defect that was not apparent by comparison with the broad envelopes of the measured low-resolution PE spectra.

In this section, we present high-resolution photoelectron spectra of KrO^- obtained using SEVI. Numerous transitions are observed within the broad envelope of the previous low- resolution photoelectron spectra. The accompanying theoretical sections rely on the advanced description of the KrO^- and KrO, namely, the calculation of interaction potentials with the coupled cluster method and extended basis set and the *ab initio* analysis of the scalar relativistic effects and vectorial spin-orbit coupling. These curves are incorporated into a simulation procedure[9,20] that accounts correctly for all the bound-bound transition intensities and, in addition, includes the contribution of bound-free (dissociative photodetachment) transitions. Comparison of the simulated and experimental SEVI spectra facilitates assignment of the many resolved features. Several spectroscopic constants for KrO^- and KrO determined from analysis of the experimental spectra are found to agree with the calculated values.

4.2.2 Experimental details

The SEVI technique and apparatus has been described in detail in chapter 2. KrO^- anions were produced from a gas mixture comprising 0.1% N_2O and 10% krypton in a balance of neon. The gas mixture, at a stagnation pressure of 350 psi, was expanded into the source vacuum chamber through an Even-Lavie pulsed valve[22] equipped with a circular ionizer. The apparatus was calibrated by acquiring SEVI images of atomic oxygen[23] at several different photon energies. With the 200V VMI repeller voltage used in this study, the full widths at half maximum (FWHM) Γ of the oxygen peaks were 2.2 cm^{-1} at 20 cm^{-1} eKE and 6.8 cm^{-1} at 150 cm^{-1} eKE. The dependence of Γ upon eKE was found to fit a quadratic expression,

$$\Gamma = 2.0 + 0.031(\text{eKE}) - 1.3\times10^{-5}(\text{eKE})^2 \qquad (4.7)$$

where all units are in wavenumbers.

4.2.3 Experimental results

The SEVI spectrum of KrO^-, taken at a photon energy E_0 = 13334.6 cm^{-1}, is shown in Figure 4.6. The spectrum is quite congested, with most transitions occurring between 12900 cm^{-1} and 13200 cm^{-1}. Clearly discernible peaks are labeled by capital letters A-P and their positions are listed in Table I. The estimated error bars are ±5 cm^{-1}. There are at least two prominent progressions starting with peaks C and K, with characteristic peak spacings of 20-30 cm^{-1}.

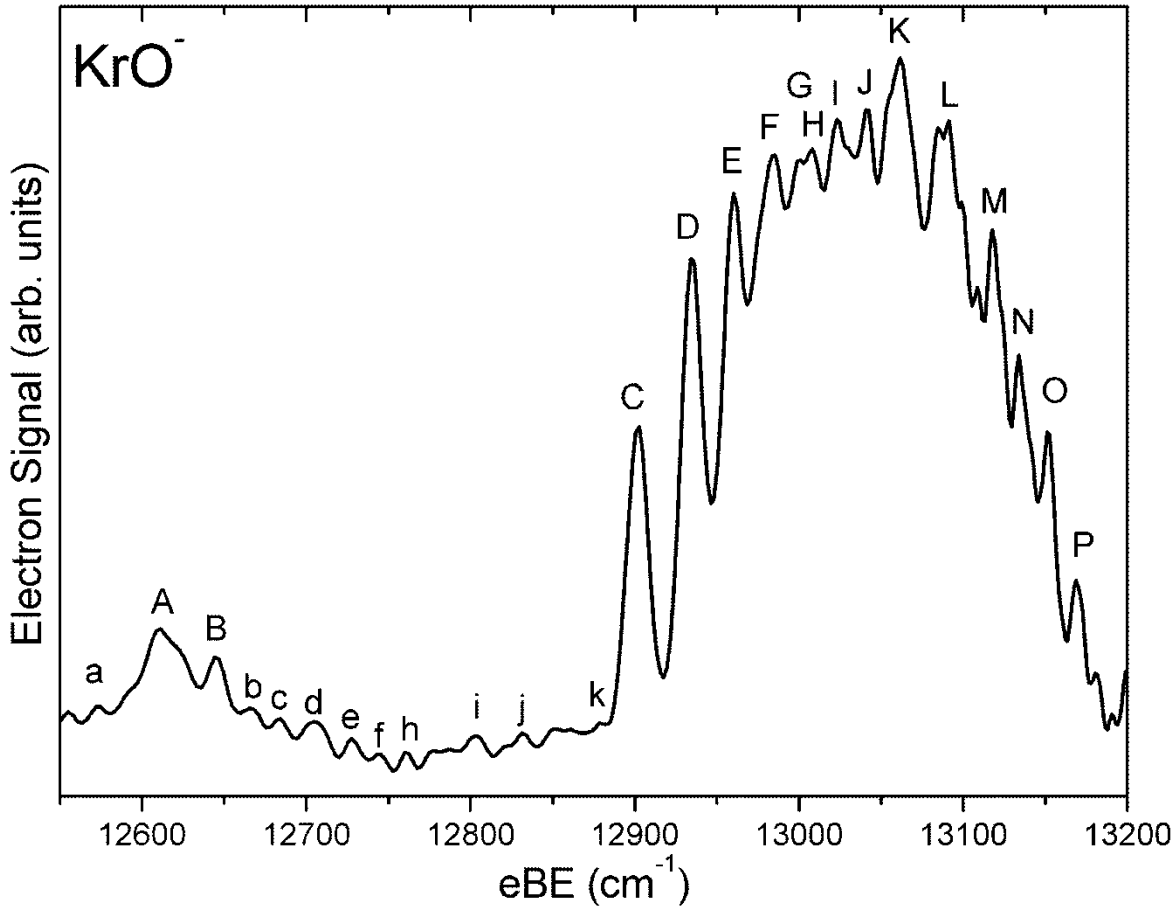

Figure 4.7 SEVI spectrum of KrO^- taken at 13334.6 cm^{-1} photon energy.

Table 4.4 Experimental and calculated peaks positions (cm^{-1}) and shift from origin along with transition assignments. The features labeled a-k and those marked with and asterisks are tentatively assigned.

Peak	Exp eBE (cm^{-1})	shift (cm^{-1})	Theory eBE	Theory shift	Δ(Exp-Theo.) (eBE)	Δ(Exp-Theo.) (shift)	Assignment
a	12572	-330	12577.2	-314.7	-5	15	*II*1, 0 ← *I*, 3
A	12611	-291	12608.5	-283.4	2	8	*X*2, 0 ← *I*, 0
B	12644	-258	12640.3	-251.6	4	6	*X*2, 1 ← *I*, 0
b	12665	-237	12658.3	-233.6	7	3	*I*1, 1 ← *I*, 0
c	12684	-218	12675.8	-216.1	8	2	*I*1, 2 ← *I*, 0
d	12705	-197	12698.1	-193.4	7	4	*X*2, 0 ← *X*, 2
e	12728	-174	12725.0	-166.9	3	7	*I*1, 0 ← *X*, 2
f	12743	-159	12747.9	-144.0	5	15	*I*1, 1 ← *X*, 2
g	12760	-142	12765.3	-126.6	5	15	*I*1, 2 ← *X*, 2
h	12803	-99	12791.8	-100.1	11	-1	*X*2, 0 ← *X*, 1
i	12832	-70	12823.6	-68.3	8	2	*X*2, 1 ← *X*, 1
j	12852	-50	12847.7	-44.2	4	6	*X*2, 2 ← *X*, 1
k	12878	-24	12870.8	-21.1	9	3	*I*1, 3 ← *X*, 1
C	12902	0	12891.9	0	10	0	*X*2, 0 ← *X*, 0
D	12934	32	12923.7	31.8	10	0	*X*2, 1 ← *X*, 0
E	12960	58	12947.8	55.9	12	-2	*X*2, 2 ← *X*, 0
F	12984	82	12964.4	72.5	20	-10	*X*2, 3 ← *X*, 0
G	12999	97	12974.2	82.3	25	-15	*X*2, 4 ← *X*, 0
H*	13008	106	12978.7	86.9	29	-19	*X*2, 5 ← *X*, 0
I*	13023	121	13005.8	113.9	17	-7	*II*0, 2 ← *X*, 1
J*	13041	139	13022.4	130.5	19	-9	*II*0, 3 ← *X*, 1
K	13061	159	13049.9	158.1	11	-1	*II*0, 0 ← *X*, 0
L	13091	189	13081.8	189.9	9	1	*II*0, 1 ← *X*, 0
M	13118	216	13105.9	214.0	12	-2	*II*0, 2 ← *X*, 0
N	13134	232	13122.5	230.6	12	-1	*II*0, 3 ← *X*, 0
O	13151	249	13132.3	240.5	19	-9	*II*0, 4 ← *X*, 0
P*	13169	267	13136.8	245.0	32	-22	*II*0, 5 ← *X*, 0

These progressions appear to lie above a smoothly varying background signal that peaks around 13025 cm^{-1}, but one cannot tell from the spectrum alone if this background results from spectral congestion or transitions to continuum states of the neutral complex. Weak structure is also observed below 12900 cm^{-1}. The most prominent features here are peaks A and B at 12610 cm^{-1} and 12640 cm^{-1}, respectively. Other features are labeled by small letters a-k. A detailed assignment of the SEVI peaks can be made by comparison with the theoretical results presented in Section 4.2.4.

The transitions shown in Figure 4.6 occur within the two broad overlapping envelopes of the PE spectrum reported by de Clercq *et al.*[19] The region of maximum intensity in the SEVI spectrum approximately coincides with the peak of the "X" features in the PE spectrum near 13100 cm^{-1}. However, compared to the PE spectrum, the SEVI spectrum displays much less intensity at eBE < 12900 cm^{-1}. De Clercq *et al*. found that the feature "A" in this region was sensitive to ion source conditions and presumably resulted from "hot band" transitions originating from electronically excited anions. Peak A in the SEVI spectrum coincides with the maximum of the feature "A" near 12600 cm^{-1} in the PE spectrum. Hence, the intensity differences between the SEVI and PE spectra suggest lower anion temperatures in the SEVI experiment, similar to what was observed for ArO^-.[9]

4.2.4 Theoretical framework

A) Electronic structure and adiabatic potentials

1. Ab initio potentials

The electronic structure of the RgO^- anions and RgO neutrals is described in detail elsewhere.[9,20] In brief, under the *LS* coupling scheme [appropriate for both non-relativistic and scalar relativistic (SR) approximations], the interaction of Rg(^{1}S) and O(^{3}P) atoms gives rise to two terms of $^3\Sigma^-$ and $^3\Pi$ symmetry, whereas the interaction between Rg(^{1}S) and the O^-(^{2}P) anion gives two states of $^2\Sigma^+$ and $^2\Pi$ symmetry. Following the notation of the previous studies,[9,20,21] we will denote these potentials as V_{Σ}^{-}, V_{Π}^{-}, V_{Σ} and V_{Π}, respectively.

A set of these potentials was obtained previously[24] for the purpose of interpreting the lower-resolution KrO^- PE spectra.[19,21] The restricted version of the coupled cluster method with single, double and non-iterative triple excitations, RCCSD(T), and the augmented correlation consistent aug-cc-pV*n*Z (AV*n*Z) n = T, Q basis sets[25-27] with the addition of the 3s3p2d set of bond functions (bf332) placed at the midpoint of internuclear distance R was implemented. However, experience with the SEVI spectroscopy of ArO^- [9] indicates that this level may not be high enough to reproduce the high-resolution spectra accurately. Thus, refined *ab initio* calculations have been performed as described below.

All calculations of the interaction energies implemented the RCCSD(T) method to correlate the electrons of the 2s2p shells of the O atom or anion and 4s4p or 3d4s4p shells of the Kr atom. Three types of approaches were used to assess the scalar relativistic effects. In the first approach, no relativistic correction was taken into account. These all-electron calculations were performed using AV5Z basis sets for both Kr and O centers. In the second, scalar relativistic effects were included using the second-order Douglas-Kroll-Hess Hamiltonian (DK) in combination with specially optimized AV5Z-DK basis set for O and AV5Z basis for Kr. Further extension of the basis set denoted as DAV5Z or DAV5Z-DK was achieved by using the doubly augmented V5Z set for O and adding one primitive in each of the spdfgh symmetry types with the exponent continuing the even-tempered sequence of the smallest two exponents of the standard AV5Z basis for Kr. The third approach used the ECP10MDF relativistic effective core potential[28] (ECP) for Kr and supplementary AV5Z-PP and DAV5Z-PP basis sets. In some cases, the 3s3p2d2f1g bond function set (bf)[29] was placed at the midpoint of internuclear distance. Interaction energies were computed over a tight grid in *R* from 1.8 to 25 Å and corrected for basis set superposition error using the full counterpoise correction scheme.[30] All calculations were performed with the MOLPRO program package.[31]

Equilibrium distances and interaction energies for the *ab initio* potentials computed as described above are presented in Table 4.5 along with some previous data. It can be seen that both correlation of Kr(3d) shell and inclusion of the SR effects are important. The former was therefore included in almost all calculations. At the AV5Z level, SR effects in the KrO neutral make both the $^3\Sigma^-$ and $^3\Pi$ interaction potentials deeper, to a very similar extent for DK and ECP calculations. For the KrO^- anion, DK and ECP calculations give qualitatively different results: their effects are opposite for the binding energy of the $^2\Sigma^+$ state and quite different in magnitude for the $^2\Pi$ state. Extension of the basis set to DAV5Z level decreases the equilibrium distance and increases the binding energy for all the potentials to the degree almost identical in both DK and ECP calculations. Inclusion of the bond functions leads to the same effects, again very similar for KrO^-, but significantly larger in the DK than in the ECP calculations for KrO. Overall, bond functions produce stronger effects than inclusion of the extra diffuse primitives to the atomic basis. Unfortunately, all-electron DAV5Z+bf calculations were found to be too demanding.

The results presented in the Table 4.5 indicate good convergence with respect to the basis set extension. As is typical for weakly-bound systems, saturation of the basis set pushes down the binding energy and contracts the bond length. Previous results[21,24] obtained with smaller basis sets are in line with the present calculations. In what follows, we will use the best DAV5Z-PP+bf SR potentials.

Table 4.5 Equilibrium distances R_e (Å) and binding energies D_e (cm^{-1}) calculated for the KrO and KrO^- systems by the RCCSD(T) method using different basis set and scalar relativistic corrections.

Basis set	$KrO(^3\Pi)$		$KrO(^3\Sigma^-)$		$KrO^-(^2\Sigma^+)$		$KrO^-(^2\Pi)$	
	R_e	D_e	R_e	D_e	R_e	D_e	R_e	D_e
AV5Z[a]	3.470	98.3	3.951	53.2	3.007	1189.2	3.356	864.0
AV5Z	3.465	99.1	3.945	53.6	2.967	1267.0	3.324	911.3
AV5Z-DK	3.456	100.0	3.946	54.3	2.964	1264.5	3.315	921.8
AV5Z-PP	3.455	100.1	3.946	54.4	2.959	1278.0	3.306	938.5
DAV5Z-DK	3.448	104.4	3.931	56.9	2.962	1275.9	3.313	931.3
DAV5Z-PP	3.445	104.6	3.933	57.0	2.957	1289.1	3.301	947.8
AV5Z-DK+bf	3.448	109.1	3.913	59.4	2.958	1281.6	3.311	936.7
AV5Z-PP+bf	3.449	106.7	3.925	58.2	2.951	1295.8	3.293	952.7
DAV5Z-PP+bf	3.448	107.0	3.925	58.3	2.951	1296.4	3.293	953.0
AVTZ+bf332[a,b]	3.467	103.5	3.956	55.0	2.963	1277.8	3.322	922.9
Scattering[c]	3.57± 0.07	105.7± 10.6	4.05± 0.08	45.2± 4.5				

[a] Kr(3d) shell is not correlated.

[b] From Refs. 21,24

[c] From Ref.18

To assess the accuracy of the calculations and analyze the long-range (LR) behavior of the potentials, static atomic polarizabilities were computed by the finite-field method using the same level of theory. The dipole polarizability of Kr was estimated as 16.77, 16.67 and 16.78 a_0^3 for DAV5Z-DK and DAV5Z-PP calculations, respectively, in good agreement with the recommended value[32] of 16.76 a_0^3. Quadrupole polarizabilities of 92.9, 91.0 and 95.2 a_0^5 calculated for the same sequence, also agree well with the value 97.1 a_0^5 presented by Koutselos *et al.*[33] Dipole polarizabilities of the oxygen atom are practically independent of the DK correction and were estimated, using the DAV5Z basis set, as 5.83 and 4.94 a_0^3 for the $\Lambda = 0$ and $\Lambda = 1$ components, respectively. The isotropic $\alpha_0 = 5.24$ a_0^3 polarizability agrees well with the measured value[34] of 5.2 ± 0.4 a_0^3 and numerous theoretical estimates.[32,35,36] The anisotropic polarizability $\alpha_2 = -0.30$ a_0^3 is slightly less than the value of -0.36 a_0^3 computed by Medved *et al.*[36] using the second-order complete active space perturbation theory (CASPT2). For O^-, we found 20.63 and 39.98 a_0^3 for the $\Lambda = 0$ and $\Lambda = 1$ components, respectively, or 33.55 and 6.43 a_0^3 for isotropic and anisotropic polarizabilities. Post Hartree-Fock calculations by Mukherjee and co-workers[37] give α_0 ranging from 26.5 to 40.8 and α_2 – from 4.6 to 8.1 a_0^3, in agreement with the more accurate present data. In contrast, Ref. [36]

reports unexpectedly small values of 17.40 and 2.14 a_0^3 for isotropic and anisotropic polarizabilities, respectively.

The most accurate DAV5Z-PP+bf interaction potentials were fitted to an asymptotic LR expansion. For KrO, the dispersion coefficients C_6 and C_8 were found to be 46.8 and 1825 a.u. for the $^3\Sigma^-$ state and 44.1 and 1250 a.u. for the $^3\Pi$ state. Conversion of the lowest-order coefficient to the anisotropic representation[16] gives $C_{6,0}$ = 45.0 a.u. and $C_{6,2}$ = 4.5 a.u. Aquilanti and co-workers[18] used $C_{6,0}$ = 64.8 a.u. as estimated from the average velocity dependence of the scattering cross section. Overestimation is expected in this analysis because no higher-order terms were taken into account. For KrO^-, dispersion coefficients were determined after extraction of the lowest-order induction components proportional to R^{-4} and R^{-6} using the *ab initio* values of the dipole and quadrupole polarizabilities, respectively. The C_6 coefficients for the $^2\Sigma^+$ and $^2\Pi$ states are 29 and 192 a.u., respectively.

Additional hints on the accuracy of the KrO *ab initio* interaction potentials can be obtained by comparison to the beam scattering experiment by Aquilanti and co-workers.[18] The potentials derived from the measured absolute total scattering cross sections Q are characterized in Table 4.5. For the purpose of comparison, we performed the calculations of Q values for both *ab initio* and empirical scattering potentials using the same approach as implemented in Ref. 18. The cross sections were calculated for each adiabatic SO-coupled potential (see next subsection) as functions of collision velocity v and then summed according to the population of each atomic oxygen sublevel in the beam. Experimentally, these populations can be varied using a magnetic selector and Ref. 18 provides the data for zero and high magnetic fields that allow discrimination of the interaction anisotropy.

The results of the quantum calculations converged within 0.5% are plotted in Figure 4.7 using coordinates that emphasize the glory scattering structure. The upper (lower) pair of curves represents the velocity dependence of the cross sections computed with scattering (*ab initio*) potentials at zero and high fields, whereas the symbols with error bars roughly indicate the measured data, as extracted from Figure 4 in Ref. 18. The *ab initio* potentials perfectly reproduce the glory pattern and magnetic field dependence, but systematically underestimate the absolute cross section values by 5.5%. It can be concluded that, at the level of the beam scattering sensitivity, *ab initio* calculations reproduce the shape and anisotropy of the KrO interaction, but underestimate its range. Indeed, Table II reveals a systematic underestimation of the equilibrium distances with respect to scattering potentials (note that within the hard-sphere approximation, the cross section value scales as a square of R_e).

2. SO-coupled potentials

The vectorial spin-orbit interaction splits atomic multiplets. The asymptotic energies Δ_j of the Rg + O(^3P_j) limits counted from the lowest j = 2 term are Δ_1 = 158.27 and Δ_0 = 226.98 cm^{-1}.[38]

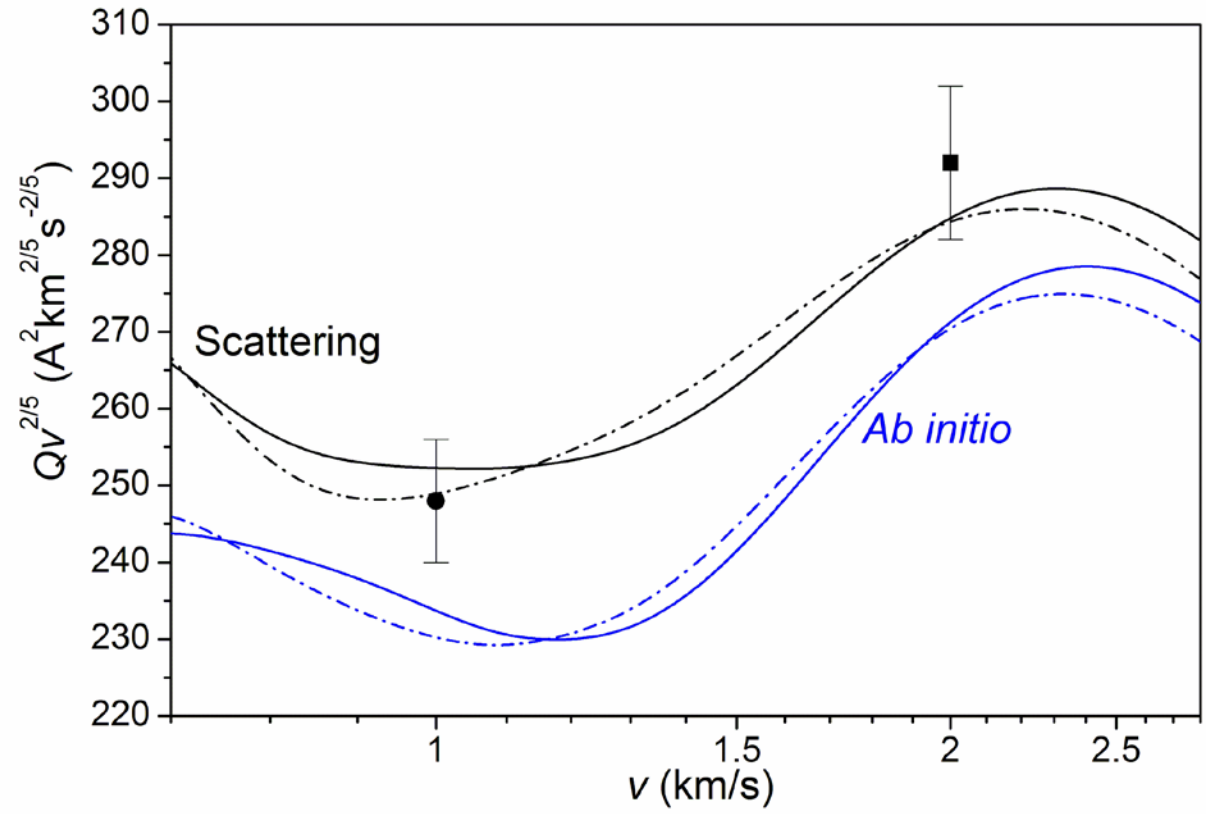

Figure 4.7 Velocity dependence of the absolute total scattering cross sections computed with *ab initio* and scattering potentials at zero (solid lines) and high (dot-dashed lines) magnetic field selection. Dot and square with error bars represent the measurements (from Ref. 18) at zero and high fields, respectively.

At finite distances, there are six SO-coupled states $X2(2)$, $I1(2)$, $I0(2)$, $II1(1)$, $II0(1)$ and $III0(0)$ classified as $n\Omega(j)$, where n indexes the states with the same projection of the total electronic angular momentum j on the molecular axis Ω. The Rg + $O^-(^2P_{1/2})$ limit lies $\Delta^- = 177.14$ cm^{-1} above the ground Rg + $O^-(^2P_{3/2})$ limit.[23] Three states of the anion complex can be classified using similar $n^-\Omega^-(j^-)$ notations as $X1/2(3/2)$, $I3/2(3/2)$ and $II1/2(1/2)$. The lowest anion $j^- = 3/2$ and neutral $j = 2$ limits are separated in energy by the electron affinity of atomic oxygen, $EA = 11784.7$ cm^{-1}.[23]

In previous work,[9,20,21] the vectorial SO interaction that couple Σ and Π states in both neutral and anion oxygen complexes was taken into account within the so-called atoms-in-molecule model in which the coupling matrix elements are approximated by their atomic values. For the specific case of the ^2P or ^3P atoms interacting with rare gases, such models were considered in many studies (see, *e.g.*, Refs. 3,16,39 and references therein). According to this model, the SO-coupled potentials can are expressed analytically through four SR potentials V_Σ^-, V_Π^-, V_Σ and V_Π and three atomic fine-structure energies Δ_1, Δ_0 and Δ^-.

To check the validity of this approximation, *ab initio* calculations of the SO-coupling matrix elements were performed. If the interactions of the states correlating to the ^2P or ^3P atomic multiplets with the higher-lying electronic states are neglected, the only non-zero matrix element of the SO operator V_{SO} in the former case is $<^2\Sigma^+|V_{SO}|^2\Pi> = a^-(R)$, whereas in the latter case two matrix elements do not vanish, $<^3\Sigma^-|V_{SO}|^3\Pi>/\sqrt{2} = <^3\Pi|V_{SO}|^3\Pi> = a(R)$. The asymptotic splittings are related to these matrix elements by $\Delta^- = 3a^-$ and $\Delta_1 = 2a$, $\Delta_0 = 3a$. These relations imply that $\Delta_1/\Delta_0 = 2/3$ for oxygen atom. The experimental ratio[23] of 0.7 indicates that the ground state multiplet of the atom can indeed be considered as isolated.

The above matrix elements were computed using the complete active space multiconfigurational self-consistent field (CASSCF) method followed by state-interacting relativistic configuration interaction calculations with the full Breit-Pauli V_{SO} operator in the CASSCF internal space.[40] Asymptotically, these calculations gave $\Delta^- = 178.4$, $\Delta_1 = 154.8$ and $\Delta_0 = 232.3$ cm^{-1}, energies that agree with the measured term values within 3%. The matrix elements a^- and a weakly depend on internuclear distance. Their deviations from asymptotic values become significant only at distances that correspond to the high-energy repulsive branch of the SR potentials. The analysis of the SO-coupled potentials did not reveal any remarkable effect of these variations so we decided to use the atoms-in-molecule model with the asymptotic atomic parameters.

The SO-coupled potentials based on the most accurate DAV5Z-PP+bf SR potentials are depicted in Figure 4.8 and characterized in Table 4.6. Adiabatic transition energies T_0, dissociation energies D_0, and vibrational constants shown therein were obtained by solving the radial Schrödinger equations by the Numerov method for zero rotational angular momentum and fitting the lowest vibrational levels to the Dunham expansion.

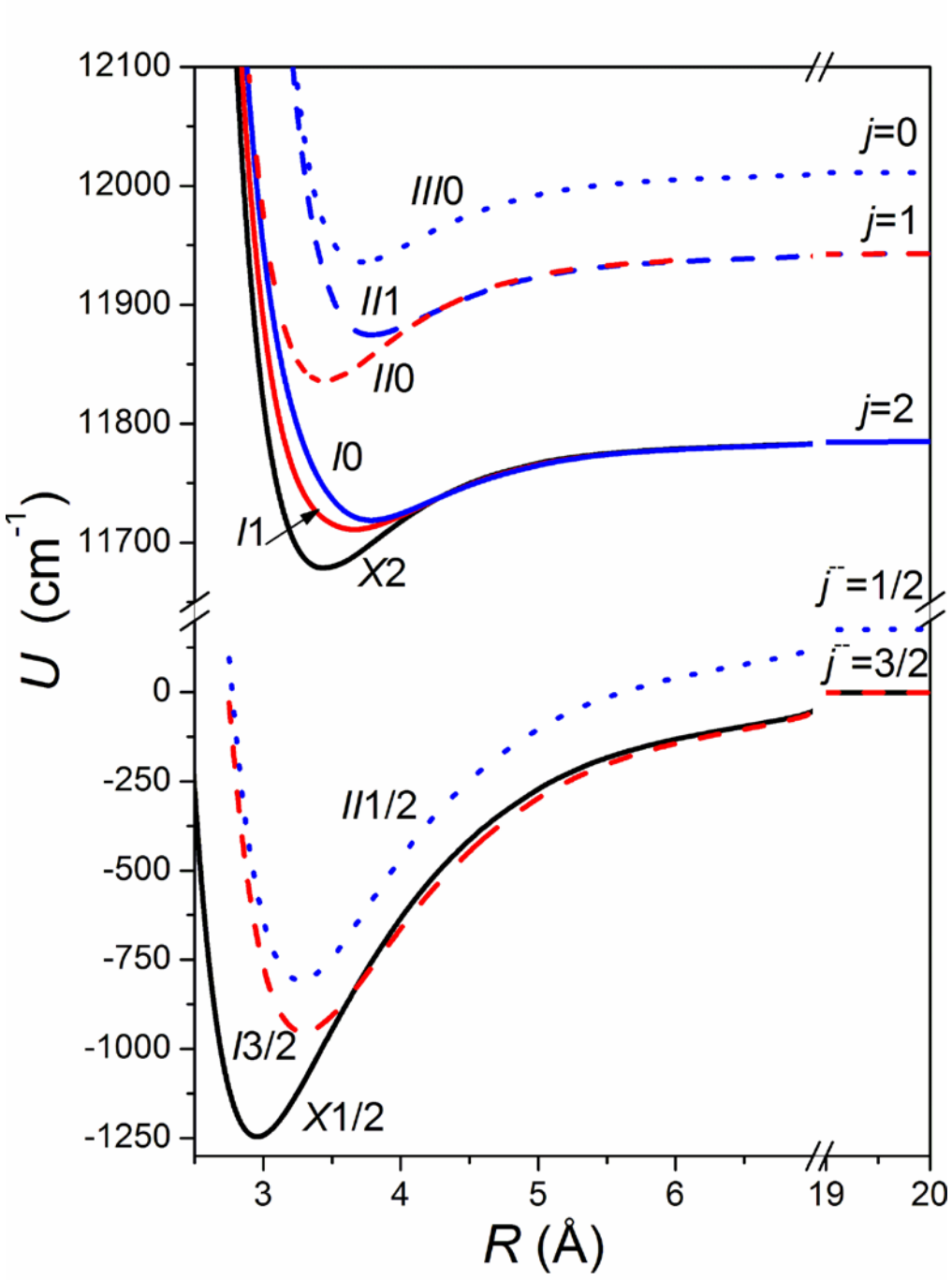

Figure 4.8 SO-coupled potentials of the anion and neutral KrO calculated using the atoms-in-molecule model and *ab initio* RCCSD(T)/ DAV5Z-PP+bf SR potentials.

For the anion potentials, the 10 lowest levels were used, while all bound levels were used for the neutral potentials. T_0 values were calculated with respect to the ground vibronic level of the anion using the measured electron affinity of the oxygen atom.[23]

Table 4.6 Parameters of the SO-coupled potentials of the KrO anion and neutral calculated using the DAV5Z-PP+bf *ab initio* potentials.

State	R_e (Å)	D_e (cm^{-1})	T_0 (cm^{-1})	D_0 (cm^{-1})	ω_e (cm^{-1})	$\omega_e x_e$ (cm^{-1})
KrO^-						
*X*1/2	2.960	1247.8	0	1195.3	103.3	2.61
*I*3/2	3.293	953.0	283.4	911.9	82.5	2.05
*II*1/2	3.274	986.2	430.9	941.5	89.7	2.40
KrO						
*X*2	3.448	107.0	0[a]	88.0	39.0	3.68
*I*1	3.652	74.1	26.9	61.0	28.4	2.76
*I*0	3.773	66.4	34.7	53.3	27.3	2.88
*II*1	3.768	69.1	192.2	53.8	29.8	3.34
*II*0	3.448	107.0	158.3	88.0	39.0	3.68
*III*0	3.699	76.1	254.9	59.7	33.1	3.9

[a] The calculated KrO electron affinity is 12891.9 cm^{-1}

B) Spectral simulations

The SO-coupled potentials based on the RCCSD(T)/DAV5Z-PP+bf calculations were used for the spectral simulations. Details of the underlying theory have been presented elsewhere.[9,20] In brief, the simulations accounted for the bound-bound $n\Omega$, $v \leftarrow n^-$, v^- and bound-free $n\Omega$, $\varepsilon \leftarrow n^-$, v^- transitions, where v^- and v denote the vibrational levels in the particular electronic states of the anion n^- and neutral n, respectively, and ε specifies the kinetic energy of the Kr + O(^3P_j) products above the corresponding dissociation threshold. Rotational structure was not explicitly considered in the simulations. Solution of the radial Schrödinger equation provided anion and neutral vibronic energies $E_{n\text{-}v\text{-}}$, $E_{n\Omega v}$ and the corresponding wave functions that were used to calculate the vibronic line strength factors $I^{bb}(n\Omega, v \leftarrow n^-, v^-)$ and $I^{bf}(n\Omega, \varepsilon \leftarrow n^-, v^-)$ for the bound-bound and bound-free transitions, respectively. Introducing the initial population of the anion levels $g_{n\text{-}v\text{-}}$ and the line shape function Θ, we expressed the full spectral envelope as

$$S(E) \propto \sum_{n-}\sum_{v-} g_{n-v-} \sum_{n\Omega}\left[\sum_{v} I^{\mathrm{bb}}(n\Omega, v \leftarrow n^{-}v^{-})\Theta(E - E_{n\Omega v} + E_{n-v-}) + \int_{-\infty}^{E_0} I^{\mathrm{bf}}(n\Omega, E' \leftarrow n^{-}v^{-})\Theta(E - E' + E_{n-v-})dE'\right]. \quad (4.8)$$

The Θ function was assumed to have the Gaussian form with the width (FWHM) Γ multiplied by the factor $\sqrt{E_0 - E}$ in order to account for the threshold law for *s*-wave electron detachment at the fixed photon energy E_0.

4.2.5 Analysis and discussion

A) Assignment

To assign the measured SEVI spectrum, preliminary simulations were performed with the set of the bound-bound transitions originating from the lowest 14 vibrational levels of anion in each electronic state and terminating at all bound vibronic levels of the neutral. We explored temperatures in the range of T=20-100 K to vary the population of the anion levels and used Γ=5-8 cm^{-1} for the peak widths in Eq. 4.8. The bound-bound simulated stick spectrum calculated at T=100K is shown in Figure 4.9. While these simulations provided only rough agreement with the experimental spectrum envelope, they allowed us to assign many prominent peaks in Figure 4.6 as indicated in Table 4.4. Most peaks at or above the eBE of peak C as well as peaks A and B could be readily assigned based on comparison with these simulations. The assignments of peaks H, I, and J, marked by asterisks in Table 4.4, are more tentative as they occur in the most congested region of the spectrum. Many of the smaller peaks (a-k) could also be assigned through comparison with these simulations or the more complete simulations discussed in the following section. For each peak, Table 4.4 gives the assignment, the absolute electron binding energy eBE, and the shifts with respect to the observed and calculated $X2$, $0 \leftarrow X$, 0 origin transitions. Table 4.4 also shows the differences, ΔeBE and ΔShift, between the observed and computed eBE and shift values, respectively.

Peaks labeled C-H are assigned to the $X2$, $v \leftarrow X$, 0 transitions where v = 0-5, respectively. Similarly, peaks K-P are assigned to the $II0$, $v \leftarrow X$, 0 transitions where v = 0-5. The predominance of transitions from the anion ground state to the various vibrational levels of the $X2$ and $II0$ neutral states is similar to what was observed in the SEVI spectrum of ArO^-.[9] This result reflects the selectivity of the spin-orbit transitions but also the fact that these two states have an equilibrium geometry more similar to the anion ground state than the equilibrium geometries of the other neutral states.

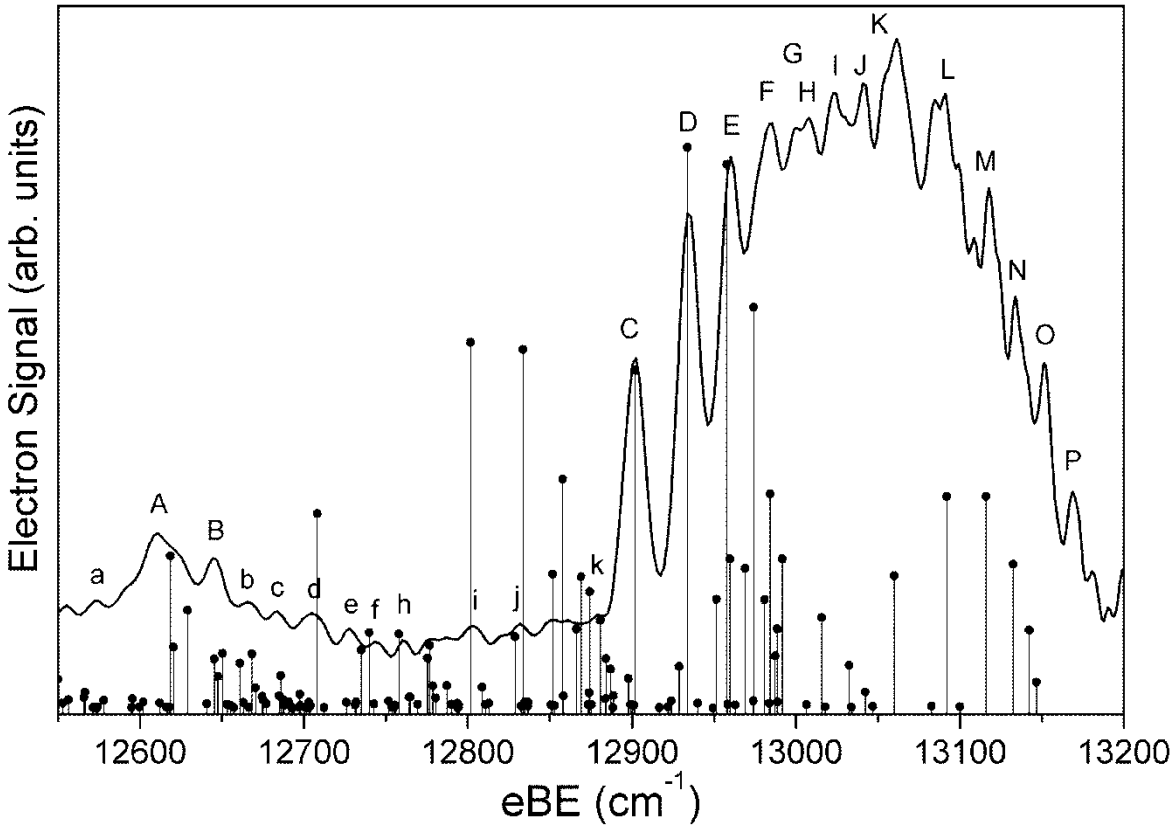

Figure 4.9 Experimental (solid line) and simulated (sticks) KrO^- SEVI spectrum including only the bound-bound transitions and assuming a 100 K equilibrium Boltzmann population of the anion levels. Simulated spectrum is shifted by 10 cm^{-1} toward higher eBE to match the position of the origin (peak C).

The positions of the assigned features allow us to extract several experimental spectroscopic parameters, which can be compared with the calculations presented herein. The position of peak C gives the adiabatic electron affinity of 12902 ± 5 cm^{-1} (1.5996 ±0.0006 eV) for KrO, which is very close to the calculated value of 12891.9 cm^{-1}. The relative positions of peaks C-H yield ω_e = 38.4 ± 1 cm^{-1} and $\omega_e x_e$ = 2.8 ± 0.2 cm^{-1} for the neutral *X*2 state. Similarly, peaks K-P yield ω_e = 35.5 ± 2 cm^{-1} and $\omega_e x_e$ = 2.6 ± 0.5 cm^{-1} for the *II*0 state. These two sets of values agree, within error bars, reflecting the fact that the neutral *X*2 and *II*0 curves should be identical (and the same as the KrO $^3\Pi$ state in Table 4.5). Moreover, the spacing between peaks C and K yields a term energy of 159 ± 5 cm^{-1} for the *II*0 state. This is consistent with the atom-in-molecule model in which the *X*2 and *II*0 curves are separated by the spin-orbit splitting (Δ_1 = 158.27 cm^{-1}) of the oxygen atom.

By assuming that the *X2* and *II0* curves only support the 6 vibrational levels observed in the experimental spectra, the well depths of these two states can be determined to be D_0 = 110 ± 5 and D_0 = 113 ± 5 cm^{-1}. These values suggest that the calculations underestimate the well depth of the *X*2 and *II*0 potential curves by around 20 cm^{-1} and overestimate their anharmonicity. This discrepancy can be directly traced back to the V_Π potential because the *X*2 and *II*0 curves depend only on this potential in the spin-orbit model used here. By using the experimentally determined EA and D_0 of the *X*2 state, we can also determine the well depth of the *X* anion states to be D_0 = 1225 ± 10 cm^{-1}, which is ~30 cm^{-1} deeper than the calculated value.

Most of the other observed peaks can be assigned to "hot band" transitions originating from excited vibrational and/or electronic anion states. The most predominant of these features are peaks A and B which can be unambiguously assigned to the *X*2, 0 ← *I*, 0 and *X*2, 1 ← *I*, 0 transitions, respectively. This assignment allows us to determine the term energy of the anion I state to be T_0=291 ± 5 cm^{-1} which is in good agreement with the 283.4 cm^{-1} calculated value. The remaining weaker peaks a-k and I,J are tentatively assigned to various hot band transitions mainly originating from the first two excited vibrational levels of the *X* anion state, based on the simulation and calculated positions.

B) Simulations

While simulations of the bound-bound transitions allowed us to assign peaks in the SEVI spectrum, they provided only a rough sketch of the measured spectral envelope. In attempt to reach better agreement, a more detailed analysis was undertaken.

A second set of simulations was carried out including the bound-free transitions as described in Section 4.2.3. Also, it was found that the observed SEVI spectrum could not be fit well assuming a single-temperature Boltzmann distribution. We took into account only four low-lying initial states of the anion, namely $n^- = X$, v^- = 0-2 and $n^- = I$, v^- = 0, which,

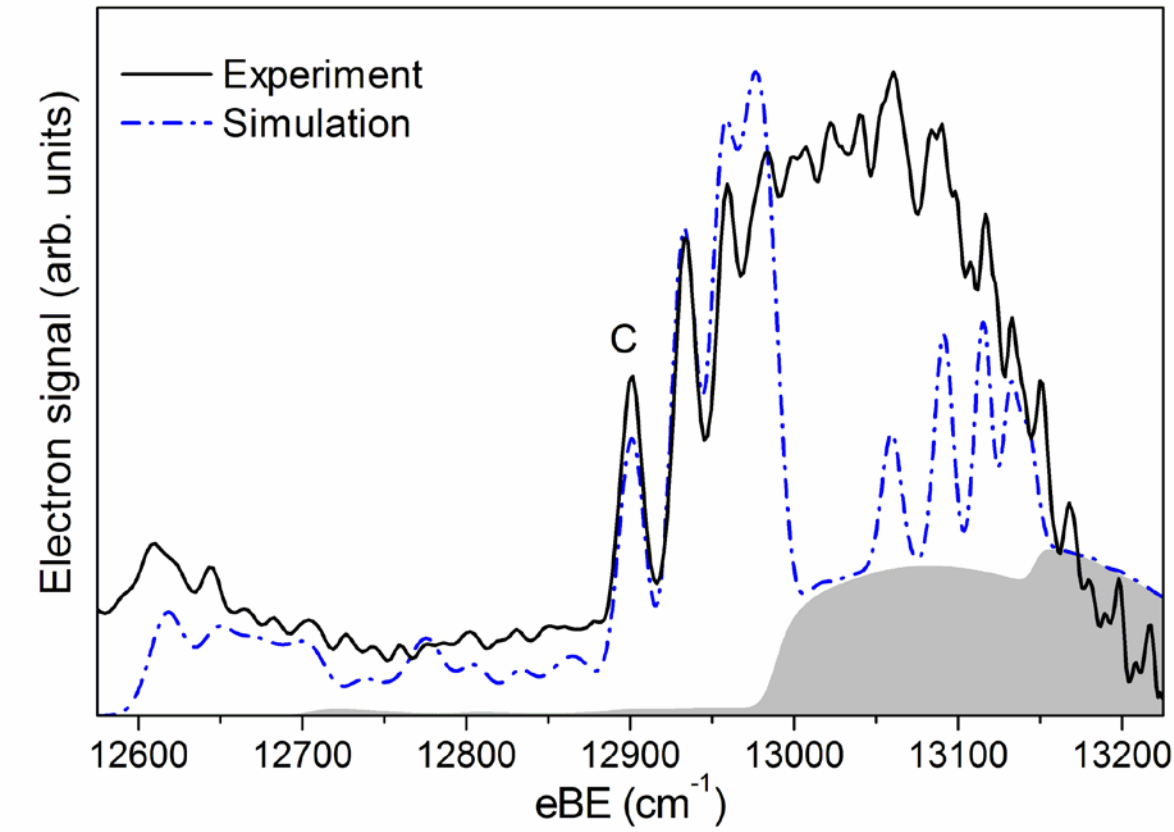

Figure 4.10 Experimental (solid line) and simulated (dashed line) KrSEVI spectrum. Simulated spectrum is shifted by 10 cm^{-1} toward higher eBE to match the position of the origin (peak C). Shadowed region represents the bound-free transition contribution to the simulated envelope.

according to Table 4.4, are responsible for all observed features (except the weak peak a with the smallest eBE). Based on the transition probability ratios for individual transitions, as well as of the bound-bound simulations, the populations of the three excited states were set to 0.02 of the ground state population. All transitions from these states were included in the simulations. In order to remove the uncertainty in the line width parameter, the experimental peak width dependence (eq. 4.7) was used to evaluate line shape function Θ in eq 4.8.

The simulated spectrum is compared with experiment in the Figure 4.10. It reproduces much of the structure below 13000 cm^{-1} associated with $X2$, $v \leftarrow X$, 0 transitions from the vibrational ground state, hot-band transitions at lower eBE, and transitions from the excited anion state at the low energy edge of the spectrum. However, above 13000 cm^{-1} (almost the threshold for dissociative detachment through the $X2 \leftarrow X$, 0 transition), significant disagreement is evident. The simulation does not reproduce the feature due to $X2$, $5 \leftarrow X$, 0 and $II2$, $5 \leftarrow X$, 0 transitions (peak H and P) because the final level is not supported by the too shallow *ab initio* potential. Underestimation of the total intensity and distortion of the pattern associated to the $II0$, $v \leftarrow X$, 0 progression reflects the bound-free contribution shown in Figure 4.10 separately as the shaded region. The bound-free continuous background appears too small and too diffuse. It develops too slowly at the threshold and decays too slowly at higher eBE.

Such behavior was found to be persistent. Neither scaling the depth of *ab initio* interaction potentials and shifting of their equilibrium distances, nor replacing the neutral potentials by the empirical scattering potentials from Ref.18 improves the situation noticeably. Likewise, rotationally resolved simulations that used rotational line strength factors[3,20] failed to produce better agreement with the measurements in the region above 13000 cm^{-1}. These efforts suggest that the discrepancies between the measured and simulated spectra mostly originate from the photodetachment transition probability calculations. The model proposed in Ref. 20 and used here assumes that the rare-gas atom weakly interacts with the O^- anion and that the ejected photoelectron interacts only with the oxygen atom. Indeed, this assumption is less valid for the relatively heavy and strongly polarizable Kr atom. The qualitatively similar discrepancies which appeared to be less pronounced in the ArO^- SEVI spectra[9] tends to support this explanation.

Finally, it is worthwhile to comment on the lower-resolution PE study by Bowen and co-workers.[19] As explained in Ref. 9, previous theoretical calculations[21] were subject to inaccuracies in the interaction potentials and to an error in the transition intensity evaluation. The full set of photodetachment transitions used above to assign the SEVI spectrum provides a good representation of the PE spectrum of KrO^- as well (not shown). In particular, one can reproduce the temperature evolution of the relative intensity of two broad peaks, one at eBE ca. 12600 cm^{-1}, the other at 13100 cm^{-1}. The latter peak corresponds to a feature dominating the SEVI spectrum, but with the structure completely washed out at the resolution of 200 cm^{-1}. The eBE of the peak is close to that of the SEVI peak A and is composed predominantly of

transitions from the electronically-excited *I* state and vibrationally-excited levels of the anion *X*-state. The intensity of the low-eBE peak rises with temperature due to thermal excitations. Therefore, the situation is very close to that discussed for ArO^- anion[9] and corroborates the previous interpretation.[19,21]

4.2.6 Conclusion

(1) The high resolution photoelectron spectrum of the KrO^- anion was obtained using slow electron velocity-map imaging. This technique provides enough resolution to discern rich vibronic structure hidden in the broad maxima of the previous conventional PE spectrum.[19] The SEVI spectrum of KrO^- resembles that of ArO^- reported previously, but is more congested and reveals more structure due to a higher density of states for the neutral product.

(2) Careful *ab initio* studies of KrO^- and KrO were carried out stressing the basis set quality, scalar relativistic and core correlation effects, and vectorial spin-orbit coupling.

(3) The spectral simulations that use the new *ab initio* potentials provide a detailed assignment of the measured spectrum in terms of vibronic transitions. This assignment is used to extract from the measured spectrum transition energies, dissociation energies and vibrational constants for the ground and some low-lying states of the anion and neutral systems.

(4) Comparison with experimental spectroscopic constants, as well as the assessment against the beam scattering data,[18] reveals that the *ab initio* potentials are not as accurate as expected taking into account the high level of the calculations and the depth of their theoretical assessment.

(5) *Ab initio* simulations fit the SEVI spectral envelope quite well, except for the region dominated by dissociative photodetachment.

References:

1) J. C. Rienstra-Kiracofe, G. S. Tschumper, H. F. Schaefer, S. Nandi, and G. B. Ellison, *Chem. Rev.* **102** (1), 231 (2002).
2) T. N. Kitsopoulos, I. M. Waller, J. G. Loeser, and D. M. Neumark, *Chem. Phys. Lett.* **159** (4), 300 (1989).
3) Y. X. Zhao, I. Yourshaw, G. Reiser, C. C. Arnold, and D. M. Neumark, *J. Chem. Phys.* **101** (8), 6538 (1994).
4) I. Yourshaw, T. Lenzer, G. Reiser, and D. M. Neumark, *J. Chem. Phys.* **109** (13), 5247 (1998).
5) T. Lenzer, I. Yourshaw, M. R. Furlanetto, G. Reiser, and D. M. Neumark, *J. Chem. Phys.* **110** (19), 9578 (1999).
6) T. Lenzer, I. Yourshaw, M. R. Furlanetto, N. L. Pivonka, and D. M. Neumark, *J. Chem. Phys.* **116** (10), 4170 (2002).
7) V. Aquilanti, D. Cappelletti, V. Lorent, E. Luzzatti, and F. Pirani, *J. Phys. Chem.* **97** (10), 2063 (1993).
8) E. Garand, J. Zhou, D. E. Manolopoulos, M. H. Alexander, and D. M. Neumark, *Science* **319** (5859), 72 (2008).
9) E. Garand, A. A. Buchachenko, T. I. Yacovitch, M. M. Szczęśniak, G. Chałasiński, and D. M. Neumark, *J. Phys. Chem. A* **113**, 4631 (2009).
10) D. M. Neumark, *J. Phys. Chem. A* **112** (51), 13287 (2008).
11) H. T. Powell, J. R. Murray, and C. K. Rhodes, *Appl. Phys. Lett.* **25** (12), 730 (1974).
12) T. H. Dunning and P. J. Hay, *J. Chem. Phys.* **66** (8), 3767 (1977).
13) S. R. Langhoff, *J. Chem. Phys.* **73** (5), 2379 (1980).
14) V. Aquilanti, G. Liuti, F. Pirani, F. Vecchiocattivi, and G. G. Volpi, *J. Chem. Phys.* **65** (11), 4751 (1976).
15) V. Aquilanti, P. Casavecchia, G. Grossi, and A. Lagana, *J. Chem. Phys.* **73** (3), 1173 (1980).
16) V. Aquilanti and G. Grossi, *J. Chem. Phys.* **73** (3), 1165 (1980).
17) V. Aquilanti, E. Luzzatti, F. Pirani, and G. G. Volpi, *J. Chem. Phys.* **73** (3), 1181 (1980).
18) V. Aquilanti, R. Candori, and F. Pirani, *J. Chem. Phys.* **89** (10), 6157 (1988).

19) H. L. de Clercq, J. H. Hendricks, and K. H. Bowen, *J. Chem. Phys.* **117** (6), 2619 (2002).

20) A. A. Buchachenko, J. Jakowski, G. Chalasinski, M. M. Szczesniak, and S. M. Cybulski, *J. Chem. Phys.* **112** (13), 5852 (2000).

21) A. A. Buchachenko, M. M. Szczesniak, J. Klos, and G. Chalasinski, *J. Chem. Phys.* **117** (6), 2629 (2002).

22) U. Even, J. Jortner, D. Noy, N. Lavie, and C. Cossart-Magos, *J. Chem. Phys.* **112** (18), 8068 (2000).

23) D. M. Neumark, K. R. Lykke, T. Andersen, and W. C. Lineberger, *Phys. Rev. A* **32** (3), 1890 (1985).

24) R. V. Krems, A. A. Buchachenko, M. M. Szczesniak, J. Klos, and G. Chalasinski, *J. Chem. Phys.* **116** (4), 1457 (2002).

25) T. H. Dunning, *J. Chem. Phys.* **90** (2), 1007 (1989).

26) D. E. Woon and T. H. Dunning, *J. Chem. Phys.* **98** (2), 1358 (1993).

27) D. E. Woon and T. H. Dunning, *J. Chem. Phys.* **100** (4), 2975 (1994).

28) K. A. Peterson, D. Figgen, E. Goll, H. Stoll, and M. Dolg, *J. Chem. Phys.* **119** (21), 11113 (2003).

29) S. M. Cybulski and R. R. Toczylowski, *J. Chem. Phys.* **111** (23), 10520 (1999).

30) S. F. Boys and F. Bernardi, *Mol. Phys.* **19** (4), 553 (1970).

31) MOLPRO, version 2006.2, a package of ab initio programs, H.-J. Werner, P. J. Knowles, R. Lindh, F. R. Manby, M. Schütz, and others , see http://www.molpro.net.

32) T. M. Miller, *CRC Handbook of Chemistry and Physics, 83d ed* (CRC Press, 2002).

33) A. D. Koutselos, E. A. Mason, and L. A. Viehland, *J. Chem. Phys.* **93** (10), 7125 (1990).

34) R. A. Alpher and D. R. White, *Physics of Fluids* **2** (2), 153 (1959).

35) H. P. Saha, *Phys. Rev. A* **47** (1), 273 (1993).

36) M. Medved, P. W. Fowler, and J. M. Hutson, *Mol. Phys.* **98** (7), 453 (2000).

37) S. Canuto, M. A. Castro, and P. K. Mukherjee, *Phys. Rev. A* **49** (5), 3515 (1994).

38) Y. Ralchenko, A. E. Kramida, and J. Reader, (National Institute of Standards and Technology, Gaithersburg, MD., 2008).

39) R. V. Krems and A. A. Buchachenko, *J. Phys. B: At. Mol. Opt. Phys.* **33** (21), 4551 (2000).

40) A. Berning, M. Schweizer, H. J. Werner, P. J. Knowles, and P. Palmieri, *Mol. Phys.* **98** (21), 1823 (2000).

4.3 Slow photoelectron velocity-map imaging spectroscopy of ClH_2^- and ClD_2^- anions

Abstract

The degree of electronic and nuclear coupling in the Cl + H_2 reaction has become a vexing problem in chemical dynamics. We report slow photoelectron velocity map imaging (SEVI) spectra of ClH_2^- and ClD_2^-. These spectra probe the reactant valley of neutral reaction potential energy surface, where non-adiabatic transitions responsible for reactivity of the Cl excited spin-orbit state with H_2 would occur. The SEVI spectra reveal progressions in low-frequency Cl·H_2 bending and stretching modes, and are compared to simulations with and without non-adiabatic couplings between the Cl spin-orbit states. Though non-adiabatic effects are small, their inclusion improves agreement with experiment. This comparison validates the theoretical treatment, especially of the non-adiabatic effects, in this critical region of the Cl + H_2 reaction, and suggests strongly that these effects are minor.

4.3.1 Introduction

The $Cl + H_2 \rightarrow HCl + H$ reaction has been studied for over a century, serving as a benchmark for the development of bimolecular reaction rate theory.[1] It has attracted renewed attention over the past decade as fresh theoretical and experimental results have highlighted unanticipated features of the reaction and challenged our fundamental understanding of its dynamics. In particular, a study of the Cl + HD reaction by Skouteris *et al.*[2] provided experimental evidence that the weak van der Waals (vdW) forces in the reactant valley have a significant effect on the branching ratio of the HCl:DCl product as a function of collision energy. These results suggest that spectroscopic study of the pre-reactive $Cl \cdot H_2$ complex would provide new insights into how weak vdW interactions affect chemical reactivity.

Such an experiment would also shed light on an important ongoing controversy concerning the relative reactivities of ground state $Cl(^2P_{3/2})$ and spin-orbit excited $Cl^*(^2P_{1/2})$, lying 882.3 cm^{-1} higher, measured in crossed molecular beam experiments by Liu and coworkers[3,4] For reactions of Cl or F with H_2, only the $X(^2P_{3/2})$ state correlates adiabatically with the HX+H products in their electronic ground state. Experience shows that the Born-Oppenheimer (BO) approximation will govern chemical reactions, so that the electronically adiabatic pathway should always dominate [5,6]. This is confirmed by multi-potential energy surface (PES) reactive scattering calculations on the $F+H_2$ [7] and $Cl+H_2$ [8,9] systems by Alexander *et al*., and, most convincingly, in a very recent comparison with crossed molecular beam experiments by Yang and co-workers[10] on the $F+D_2$ system. In that comparison, the calculations were based on a highly-correlated, scaled set of PES's in which the experimental exoergicity and the presumed experimental barrier height were accurately reproduced. Only at very low collision energies, where the reaction barrier quenches the BO-allowed $F+D_2$ reaction, did the BO-forbidden F^*+D_2 reaction become comparable in relative importance. In contrast, the experiments of Liu and co-workers imply that the exact opposite is true for the Cl/Cl^*+H_2 reaction: at low energy the BO-allowed reaction dominates, but, as the collision energy increases, the BO-forbidden reaction becomes increasingly important. These results can be explained only by postulating that nonadiabaticity in the $Cl+H_2$ reaction is qualitatively different than in the $F+H_2$ reaction, and in the quantum simulations of the $Cl+H_2$ reaction. This difference, and, in particular, the discrepancy between experiment and theory is currently one of the major unresolved problems in chemical reaction dynamics.

With these considerations in mind, we report high-resolution photoelectron imaging spectra of ClH_2^- and ClD_2^-. This experiment spectroscopically probes the pre-reactive complex of the $Cl + H_2$ reaction, offering complementary information to Liu's reactive scattering experiments, in precisely the region where the non-adiabatic transitions responsible for the reactivity of the $Cl^*(^2P_{1/2})$ state are expected to occur. [7-9,11,12] The experimental results are compared with two separate sets of Franck-Condon (FC) simulations in which the non-

adiabatic coupling between the Capecchi-Werner (CW) *ab initio* PES's [13] is first neglected and then retained.

Photoelectron spectroscopy of anionic complexes has previously been used to probe the transition states of bimolecular reactions.[14,15] A notable example of this transition state spectroscopy was a study of the FH_2^- anion, whose ground-state geometry has good FC overlap with the early barrier of the F + H_2 reaction [16,17]. In contrast, the Cl + H_2 reaction has a later barrier and thus the equilibrium geometry of ClH_2^- is much closer to the reactant valley than the transition state, as shown schematically in Figure 4.11. Two of the present authors have previously demonstrated that the ClH_2^- anion wave function has a good FC overlap with the vibrational and hindered rotor states of the neutral $Cl{\cdot}H_2$ van der Waals complex [18]. In addition, they predicted that with an energy resolution of 1 meV, several features associated with bound and resonance states of this pre-reactive complex could be resolved.

Photoelectron spectra of ClH_2^- and ClD_2^- obtained using a conventional negative ion time-of-flight photoelectron spectrometer have been reported previously [19]. They exhibited features associated with the spin-orbit splitting in the $Cl{\cdot}H_2$ complex. However, finer structures associated with vibrations and hindered rotor motions of the complex could not be observed because of the limited resolution, around 8-10 meV. Preliminary SEVI spectra [20] of ClD_2^- resolved more structure than was seen in the photoelectron spectra. However we have significantly improved on the resolution of this earlier study, finding many previously unseen features that allow for rigorous comparison with theory.

4.3.2 Experimental details

The SEVI technique and apparatus has been described in detail in chapter 2. In this experiment, ClH_2^- (ClD_2^-) anions were produced from a gas mixture comprising trace CCl_4 in a 10:1 Ar:H_2(D_2) mix. The gas mixture, at a stagnation pressure of 250 psi, was expanded into the source vacuum chamber through an Even-Lavie pulsed valve[21] equipped with a circular ionizer. The $^{37}ClH_2^-$ isotopologue was chosen to avoid interference from photodetachment of $^{37}Cl^-$, which produces photoelectrons in the same energy range, while the more abundant $^{35}ClD_2^-$ was used.

The apparatus was calibrated by acquiring SEVI images of atomic chloride at several different photon energies. With the -350V VMI repeller voltage used in this study, the Gaussian width (2σ) of the chloride peaks were 4.2 cm^{-1} at 31 cm^{-1} eKE and 28 cm^{-1} at 916 cm^{-1}. Linewidths in the spectra presented here (~10 cm^{-1}) are limited by unresolved rotational structure.

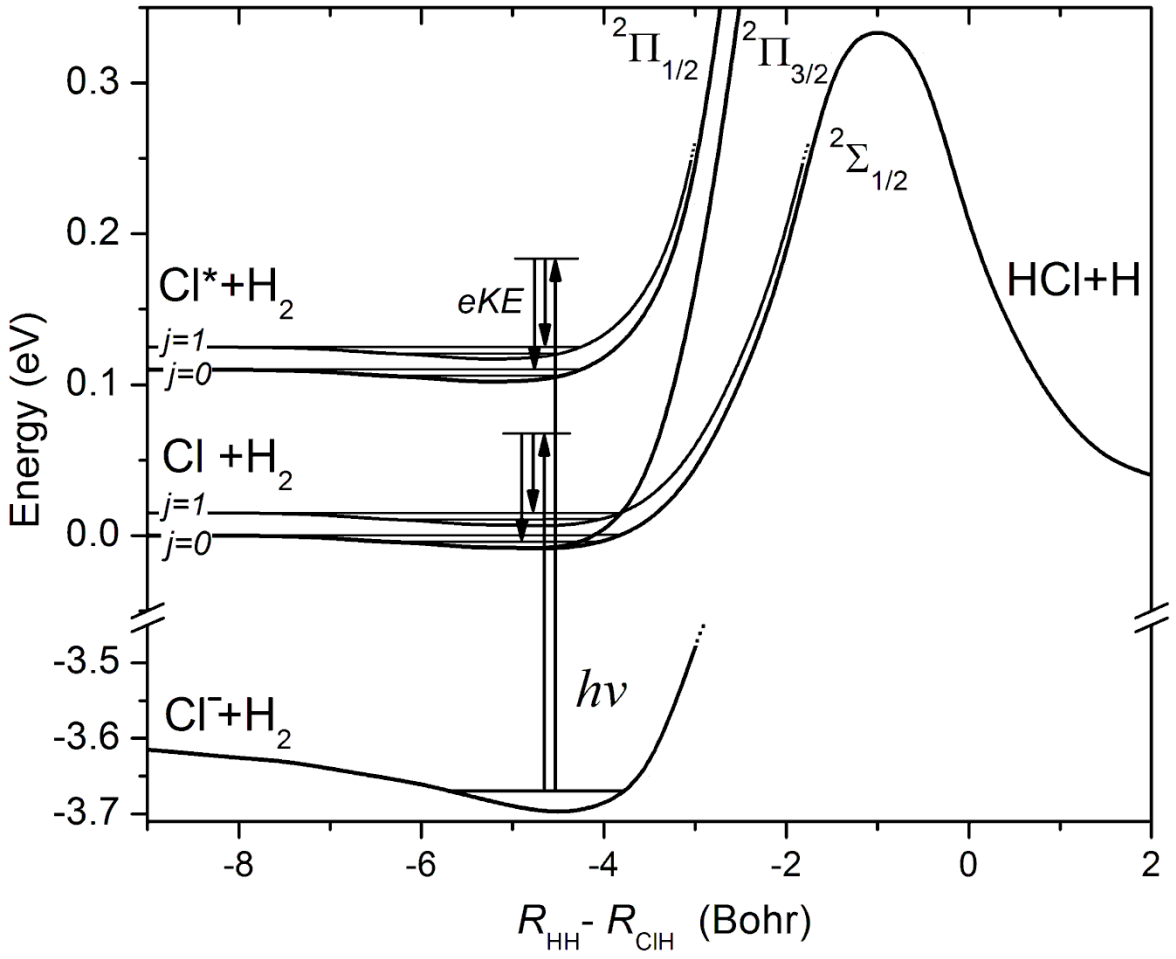

Figure 4.11 Schematic view of the ClH_2 anionic and neutral PES's. Photodetachment of ClH_2^- probes the shallow van der Waals wells in the entrance valley of the Cl + H_2 reaction, where the non-adiabatic transitions responsible for the reactivity of the Cl*($^2P_{1/2}$) state are expected to occur

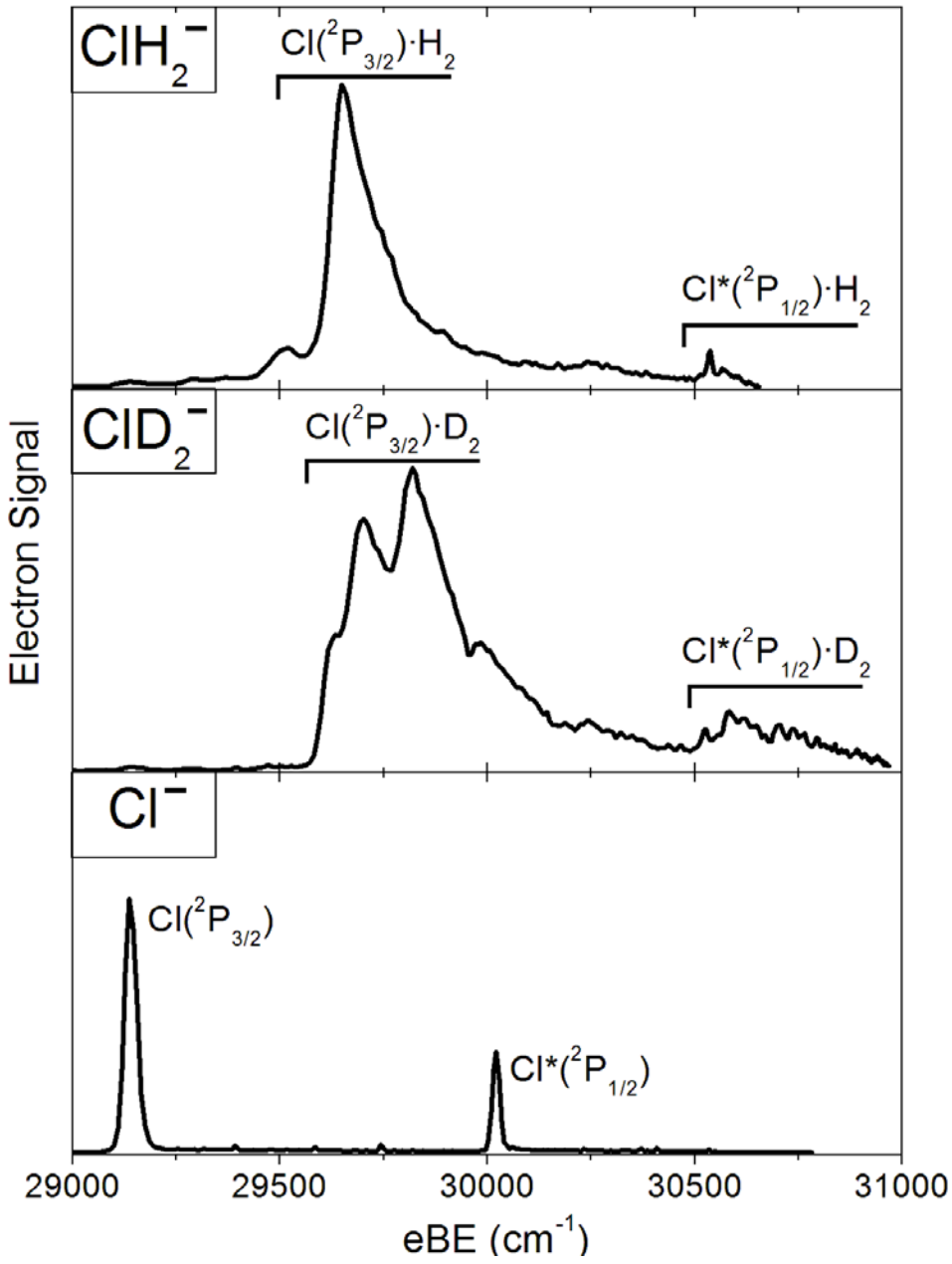

Figure 4.12 Overview SEVI spectra of ClH_2^- (top panel) and ClD_2^- (middle panel) taken at wavelengths of 326.5 nm and 323 nm respectively. The SEVI spectrum of Cl^- (bottom panel) taken at 325 nm is shown for comparison. All spectra show electron signal as a function of electron binding energy (eBE), defined as the difference between the photon energy and the measured electron kinetic energy.

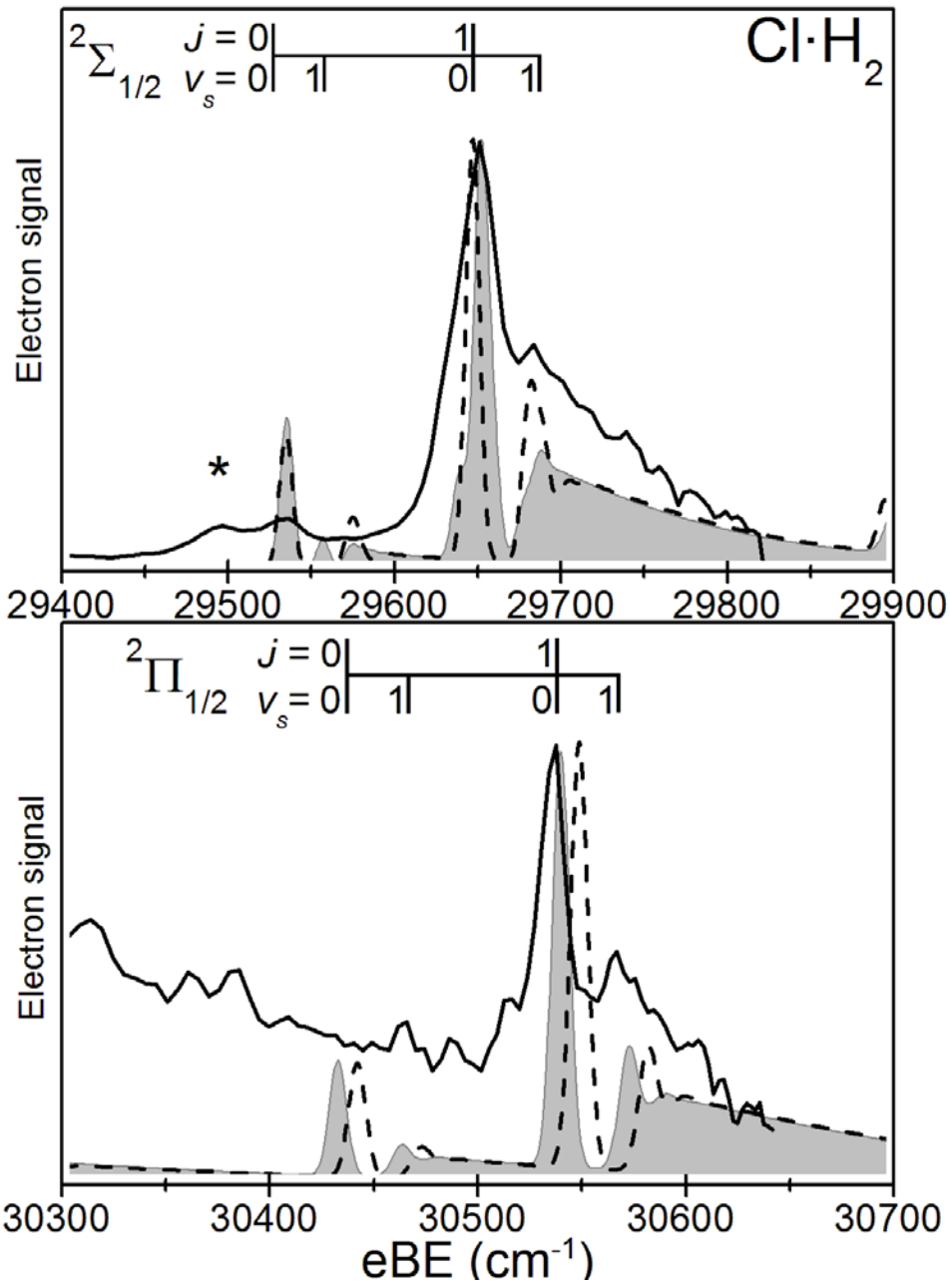

Figure 4.13 The high-resolution SEVI spectrum of ClH_2^- (solid line) is compared with Franck-Condon simulations where the non-adiabatic interactions are neglected (dashed line) and included (grey filled). An average of three spectra taken between 334.5 and 335.5 nm is shown in the upper panel and between 326 and 326.5 nm in the lower.

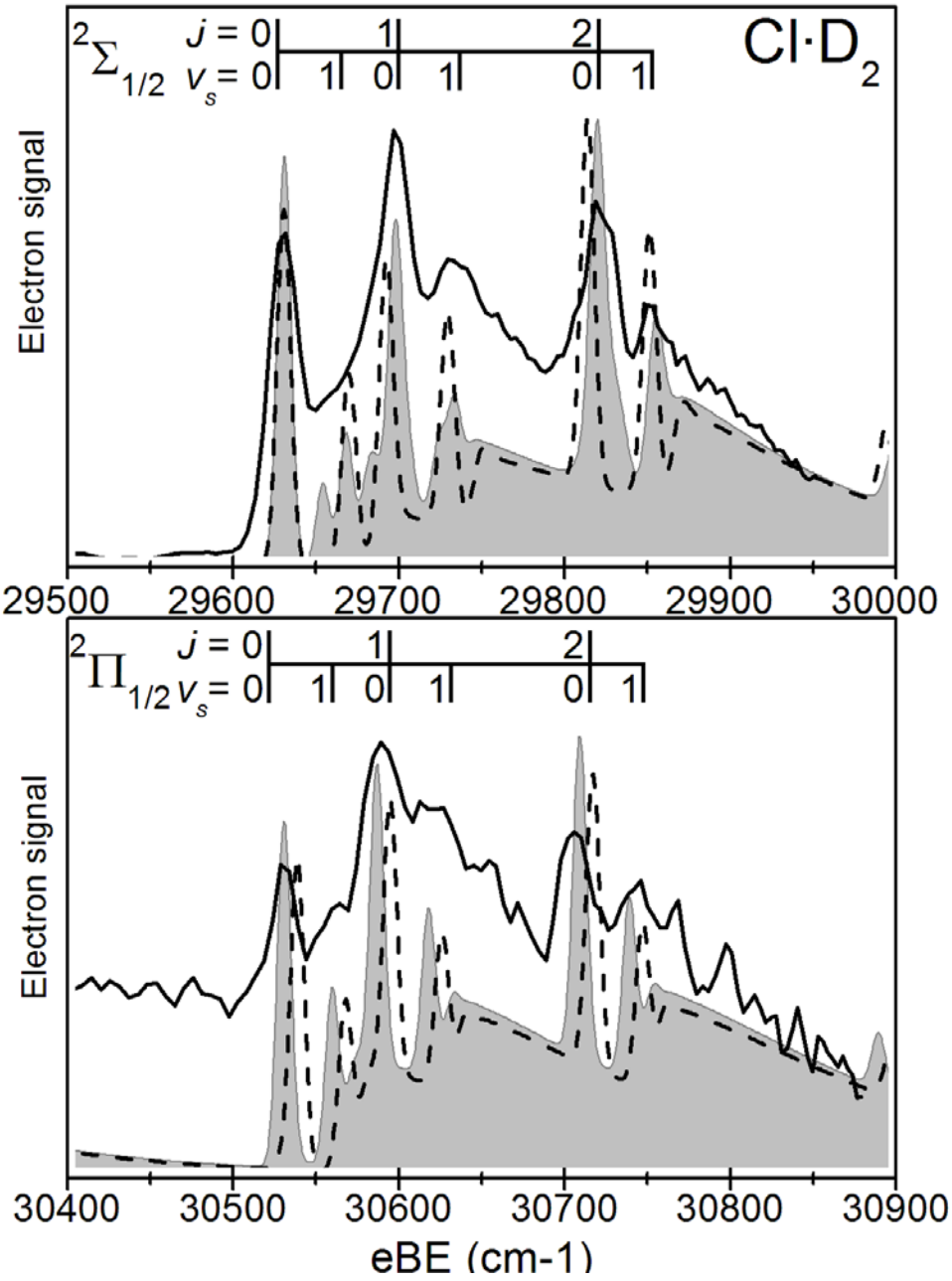

Figure 4.14 The high-resolution SEVI spectrum of ClD_2^- (solid line) is compared with Franck-Condon simulations where the non-adiabatic interactions are neglected (dashed line) and included (grey filled). An average of three spectra between 333 and 334 nm was used in the upper panel and from 323 to 324 nm in the lower panel

4.3.3 Experimental results

Overview SEVI spectra of ClH_2^- and ClD_2^- taken at wavelengths of 326.5 nm and 323.0 nm, respectively, are shown in Figure 4.12. The SEVI spectrum of Cl^- taken at 325 nm, acquired for calibration, is shown in the bottom panel of the figure for comparison. The ClH_2^- and ClD_2^- spectra are dominated by two main features associated with the spin-orbit states of the chlorine atom. Although these features already show more structure than was seen previously, the resolution of the SEVI spectra can be improved further by tuning the detachment laser just above the threshold of the feature of interest.

This procedure yields the spectra of the two spin-orbit features of ClH_2^- and ClD_2^- in Figures 4.13 and 4.14, respectively. These higher resolution spectra reveal several new features. For example, in Figure 4.12, the shoulder and first two peaks in the $Cl(^2P_{3/2})\cdot D_2$ band appear as five features in the top panel of Figure 4.14, with the two peaks each being split into closely spaced doublets.

4.3.4 Analysis and discussion

As shown in Figure 1, the interaction of Cl and Cl* with H_2 ($^1\Sigma_g^+$) gives rise to three adiabatic electronic PES's, labeled $^2\Sigma_{1/2}$, $^2\Pi_{3/2}$ and $^2\Pi_{1/2}$, in linear geometries.[22] In the adiabatic limit, only $Cl(^2P_{3/2})$ atoms that approach H_2 on the $^2\Sigma_{1/2}$ PES react to form ground state products. Figure 4.11 also shows that each electronic state has bend/hindered rotor levels that correlate to various H_2 rotational levels j (only j=0 and 1 are shown) and that each bend level has a shallow vdW well that supports very low frequency $Cl\cdot H_2$ stretching vibrations.

The spectra in Figures 4.13 and 4.14 can be fully assigned on the basis of electronically adiabatic FC simulations of detachment to the three neutral states. The dotted lines in Figures 4.13 and 4.14 show the simulated spectra obtained using the CCSD(T) PES of Alexander [23] for the anion and retaining all three electronically-adiabatic PES's of Capecchi and Werner [13] for the neutral, as described previously [18]. None of the non-adiabatic couplings were included. The simulated spectra assume the usual ortho:para ratio of 3:1 for ClH_2 and 2:1 for ClD_2. (The rotational quantum number j is even for p-H_2 and o-D_2 and odd for o-H_2 and p-D_2.) Since the intensity of the experimental signal is arbitrary, the experimental and calculated intensities have been scaled to give the same maximum peak height in each panel. The theoretical spectra were also shifted slightly to match the position of the origin transition in $Cl\cdot H_2$ (29533 cm^{-1}) and $Cl\cdot D_2$ (29631 cm^{-1}). This shift was the only adjustable parameter used in the simulations.

In the top panel of Figure 4.13, the observed peaks are associated with the hindered H_2(j = 0 and 1) rotor states of the weakly-bound Cl·H_2 complex on the ground $^2\Sigma_{1/2}$ electronic PES. One quantum of excitation in the Cl·H_2 van der Waals stretching vibration (v_s) is also observed at 30 cm^{-1} above the (j=1, v_s=0) level. These quantum numbers can be unambiguously assigned by means of a simple adiabatic-bender analysis [24,25]. Transitions to the van der Waals bound and resonance states associated with the $^2\Pi_{3/2}$ electronic state are predicted to have lower intensities owing to a poorer FC overlap with the anion wave function and are buried beneath these $^2\Sigma_{1/2}$ transitions [18]. The peak marked with a star at 29595 cm^{-1} lies 153 cm^{-1} below the(j=1, v_s=0) peak. Since this shift is close to the measured stretching vibration in the anion,[23]we assign this peak to a hot band originating from the anion v_s=1 state. Finally, the two features in the lower panel of Figure 4.13 are assigned to the (j=1, v_s=0) and (j=1, v_s=1) van der Waals bend-stretch states on the $^2\Pi_{1/2}$ excited electronic state.

The ClD_2^- spectrum exhibits similar features but with a smaller hindered rotor spacing. In the top panel of Figure 4.14, the observed transitions are assigned to hindered D_2 rotor modes (j = 0, 1, 2) on the $^2\Sigma_{1/2}$ ground electronic state, with a 30 cm^{-1} stretching vibration resolved for the j = 1 and 2 levels. Similar transitions are observed on the $^2\Pi_{1/2}$ electronic state and presented in the lower panel of Figure 4.14.

Although the electronically adiabatic simulations in Figures 4.13 and 4.14 allow us to assign most features in the measured spectra, there are some clear differences (on the order of 10 cm^{-1}) between several of predicted peak positions and those observed experimentally. In order to address these discrepancies, we have performed a second set of FC simulations in which the dynamics of the neutral Cl·H_2 complex were described by the same Hamiltonian used by Alexander *et al.* in their multi-PES quantum reactive scattering calculations for Cl + H_2 [8,9]. This treatment includes four quasi-diabatic PES's, as well as the spin-orbit and Coriolis coupling between the electronic-rovibrational states [7].

In modeling the photodetachment process, we assumed as in our adiabatic simulations that the ClH_2^- anion was sufficiently rotationally cold to be modeled by total angular momentum J=0. We also exploited the Wigner threshold law for anion photodetachment[26,27], which implies that the dominant excitation pathway at sufficiently low electron kinetic energies will be the excitation of a Cl 3p electron to a continuum s orbital. Allowing for the angular momenta of the incident photon and the departing photoelectron, these assumptions lead to independent excitation of the J=1/2 and J=3/2 angular momentum states of Cl·H_2, corresponding to the excitation of Cl($^2P_{1/2}$)·H_2 and Cl($^2P_{3/2}$)·H_2 respectively.

The neutral angular momentum states $\Psi^{JM}_{\text{neutral}}$ were constructed by dressing the anion vibrational wave function ψ^{00}_{anion} with appropriate linear combinations of Wigner rotation matrix elements $D^{J*}_{MK}(\Omega)$ (to describe the rotational motion of the triatomic complex) and Cl(^2P) atom electronic states $|JK\rangle$, with equal amplitudes for each of the (2J+1) projections of J on the Cl–H_2 axis, as represented in the following equation:

$$\Psi^{JM}_{\text{neutral}} = \left(\frac{2J+1}{4\pi}\right)^{1/2} \sum_{K=-J}^{J} D^{J*}_{MK}(\Omega) \mid JK > \psi^{00}_{\text{anion}} \ . \qquad (4.9)$$

Here K and M are the projections of J on the body and space frame z axes, and Ω denotes the set of Euler angles used to transform between the two frames.

The FC spectrum, given by Eq. 4.10,

$$P^J(E) = \left\langle \Psi^{JM}_{\text{neutral}} \middle| \delta(E-H) \middle| \Psi^{JM}_{\text{neutral}} \right\rangle \qquad (4.10)$$

was then calculated using the time-dependent wave packet method with absorbing boundary conditions described in [18], but now including electrostatic, spin-orbit, and Coriolis coupling between the diabatic electronic states [7]. The gray filled spectra superimposed in Figures 4.13 and 4.14 are the predicted photoelectron spectra for normal ClH_2^- and ClD_2^- when these non-adiabatic couplings are retained.

Alexander *et al.* [9] have shown previously that the main non-adiabatic effect in the Cl + H_2 reaction is the coupling between the $^2\Sigma_{1/2}$ and $^2\Pi_{1/2}$ electronic states induced by the spin-orbit Hamiltonian. The effect of this coupling will be strongest when the splitting between the $^2\Sigma$ and $^2\Pi$ states, independent of spin-orbit coupling, is comparable to the magnitude of the spin-orbit coupling. The point at which these two are equivalent in magnitude occurs close to the bottom of the pre-reactive van der Waals well probed in this study [9]. In addition, because all of the transitions resolved here correspond to photodetachment to the $^2\Sigma_{1/2}$ and $^2\Pi_{1/2}$ states (recall that transitions to the bend-stretch levels associated with the $^2\Pi_{3/2}$ state have a poorer Franck-Condon overlap with the anion), the effect of this spin-orbit coupling, if large, should be directly observable. However, it can be seen from Figures 4.13 and 4.14 that the inclusion of non-adiabatic effects in the FC simulation induces only subtle changes in the calculated spectra.

The most noticeable difference between the two simulations is the reduction, when the non-adiabatic coupling is retained, of the splitting between the bend-stretch levels associated with the $^2\Sigma_{1/2}$ and $^2\Pi_{1/2}$ states. For example, in the ClH_2 spectra, the splitting between the (j=1, v_s=0) levels associated with these two states is reduced from 902 to 888 cm^{-1}, in excellent agreement with the value of 887 cm^{-1} found experimentally. Similarly, in ClD_2, the spacing between the (j=0, v_s=0) levels is reduced from 908 to 900 cm^{-1} which exactly matches the experimental spectra. These reductions can be explained in terms of small changes in the shapes of the adiabatic-bender potentials induced by the spin-orbit, Coriolis and electrostatic couplings, and the resulting changes in the energies of the bend-stretch van der Waals levels in the two electronic states.

We also observe in the lower panels of Figures 4.13 and 4.14 that the widths of the peaks from the two sets of simulations are comparable. The $^2\Pi_{1/2}$ states can decay by nonadiabatic coupling to the lower $^2\Sigma_{1/2}$ states, but only if nonadiabatic coupling is included. If the magnitude of nonadiabatic were large, the peaks would be significantly broadened in the fully coupled calculation. This is not observed.

The effect of including the non-adiabatic coupling can be seen more clearly in the ClD_2^- spectra, which display a denser vibrational structure owing to the larger mass of the deuterium atom. In the lower $^2\Sigma_{1/2}$ state, the hindered rotor spacing is slightly increased and the v_s=1 level lies closer to the dissociative continuum, when compared with the adiabatic simulation. Overall, the effects of non-adiabatic coupling are small, but their incorporation into the simulations results in a noticeably better match with the high-resolution SEVI spectra.

The comparison between experimental and calculated spectra shown in Figures 4.13 and 4.14 leads to two important conclusions regarding the Cl + H_2 reaction. First, the level of agreement of both sets of simulations with the experimental spectra validates the accuracy of the Capecchi-Werner PES's in the region of the van der Waals well in the reactant valley. This validation is important because the weak interactions that give rise to this well play a decisive role in determining the product branching ratio of the Cl + HD reaction[2]. Second, our results demonstrate for the first time that the effect of non-Born-Oppenheimer couplings in the pre-reactive region have been correctly evaluated in the theoretical simulation, to nearly spectroscopic (1 cm^{-1}) accuracy.

The present treatment of the non-adiabatic electronic-vibrational-rotational motion of the ClH_2 system is based on the same Hamiltonian as was used in the quantum reactive scattering calculations of Alexander *et al.*[8] Hence, the good agreement found here tends to support the prediction of these calculations that the adiabatic Cl + H_2 reaction pathway will dominate as the collision energy increases. In principle, we expect that the sophisticated *ab initio* techniques used by Capecchi and Werner [13] for the determination of the ClH_2 PES's should be as accurate as those used for the FH_2 system, for which theory and experiment agree on the extent of nonadiabaticity.[10] Ultimately, the disagreement between these reactive scattering calculations [8] and earlier experimental work[3,4] may demand a new experimental investigation of this reaction.

4.3.5 Conclusions

We have reported the slow photoelectron velocity map imaging (SEVI) spectra of ClH_2^- and ClD_2^-. These spectra probe the reactant valley of neutral reaction potential energy surface, where non-adiabatic transitions responsible for reactivity of the Cl excited spin-orbit state with H_2 would occur. The SEVI spectra reveal progressions in low-frequency Cl·H_2 bending and stretching modes, and are compared to simulations with and without non-

adiabatic couplings between the Cl spin-orbit states. Though non-adiabatic effects are small, their inclusion improves agreement with experiment. This comparison validates the theoretical treatment, especially of the non-adiabatic effects, in this critical region of the Cl + H_2 reaction, and suggests strongly that these effects are minor.

References:

1) M. Alagia, N. Balucani, L. Cartechini *et al.*, *Science* **273** (5281), 1519 (1996).
2) D. Skouteris, D. E. Manolopoulos, W. S. Bian, H. J. Werner, L. H. Lai, and K. P. Liu, *Science* **286** (5445), 1713 (1999).
3) F. Dong, S. H. Lee, and K. Liu, *J. Chem. Phys.* **115** (3), 1197 (2001).
4) S. H. Lee and K. P. Liu, *J. Chem. Phys.* **111** (14), 6253 (1999).
5) P. J. Dagdigian and M. L. Campbell, *Chem. Rev.* **87** (1), 1 (1987).
6) R. J. Donovan, *Chem. Rev.* **70** (4), 489 (1970).
7) M. H. Alexander, D. E. Manolopoulos, and H. J. Werner, *J. Chem. Phys.* **113** (24), 11084 (2000).
8) M. H. Alexander, G. Capecchi, and H. J. Werner, *Science* **296** (5568), 715 (2002).
9) M. H. Alexander, G. Capecchi, and H. J. Werner, *Faraday Disc.* **127**, 59 (2004).
10) L. Che, Z. Ren, X. Wang*et al.*, *Science* **317**, 1061 (2007).
11) E. E. Nikitin, *Theory of elementary atomic and molecular processes in gases*. (Clarendon Press, Oxford, UK, 1974).
12) V. Aquilanti and G. Grossi, *J. Chem. Phys.* **73**, 1165 (1980).
13) G. Capeccehi and H. J. Werner, *Phys. Chem. Chem. Phys.* **6** (21), 4975 (2004).
14) D. M. Neumark, *Phys. Chem. Chem. Phys.* **7**, 433 (2005).
15) D. M. Neumark, *J. Chem. Phys.* **125** (13) (2006).
16) S. E. Bradforth, D. W. Arnold, D. M. Neumark, and D. E. Manolopoulos, *J. Chem. Phys.* **99** (9), 6345 (1993).
17) D. E. Manolopoulos, K. Stark, H. J. Werner, D. W. Arnold, S. E. Bradforth, and D. M. Neumark, *Science* **262** (5141), 1852 (1993).
18) D. E. Manolopoulos and M. H. Alexander, *Phys. Chem. Chem. Phys.* **6** (21), 4984 (2004).
19) M. J. Ferguson, G. Meloni, H. Gomez, and D. M. Neumark, *J. Chem. Phys.* **117** (18), 8181 (2002).
20) A. Osterwalder, M. J. Nee, J. Zhou, and D. M. Neumark, *J. Chem. Phys.* **121** (13), 6317 (2004).
21) U. Even, J. Jortner, D. Noy, N. Lavie, and C. Cossart-Magos, *J. Chem. Phys.* **112** (18), 8068 (2000).

22) V. Aquilanti, S. Cavalli, F. Pirani, A. Volpi, and D. Cappelletti, *J. Phys. Chem. A* **105** (11), 2401 (2001).

23) M. H. Alexander, *J. Chem. Phys.* **118** (21), 9637 (2003).

24) S. L. Holmgren, M. Waldman, and W. Klemperer, *J. Chem. Phys.* **67** (10), 4414 (1977).

25) M. H. Alexander, S. Gregurick, and P. J. Dagdigian, *J. Chem. Phys.* **101** (4), 2887 (1994).

26) R. C. Bilodeau, M. Scheer, and H. K. Haugen, *Phys. Rev. Lett.* **8714** (14) (2001).

27) E. P. Wigner, *Phys. Rev.* **73** (9), 1002 (1948).

CHAPTER 5

Infrared multiple photon dissociation spectroscopy of ionic clusters

5.1 Infrared multiple photon dissociation spectroscopy of $HCO_3^-\cdot(H_2O)_{1\text{-}10}$ clusters

Abstract

Infrared multiple photon dissociation spectra are reported for hydrated bicarbonate anion ($HCO_3^-(H_2O)_{1\text{-}10}$) clusters in the spectral range of 600-1800 cm^{-1}. In addition, electronic structure calculations at the MP2/6-311+G(d,p) level have been performed on the n=1-8 clusters to identify the structure of the low-lying isomers and to assign the observed spectral features. General trends in the stepwise solvation motifs of the bicarbonate anion can be deduced from the overall agreement between the calculated and experimental spectra. The most important of these is the strong preference of the water molecules to bind to the negatively charged CO_2 moiety of the HCO_3^- anion. However, a maximum of four water molecules interact directly with this site. The binding motif in the most stable isomer of the n=4 cluster, a four-membered ring with each water forming a single H-bond with the CO_2 moiety, is retained in all the lowest-energy isomers of the larger clusters. Starting at n=6, additional solvent molecules are found to form a second hydration layer, resulting in a water-water network bound to the CO_2 moiety of the bicarbonate anion. Binding of a water to the hydroxyl group of HCO_3^- is particularly disfavored and apparently does not occur in any of the clusters investigated here. Similarities and differences with the infrared spectrum of aqueous bicarbonate are discussed in light of these trends.

5.1.1 Introduction

The bicarbonate anion, HCO_3^-, is a ubiquitous species in aqueous chemistry. Because bicarbonate is a weak base, it plays a central role in the acid-base equilibrium formed when CO_2 is dissolved in water:

$$CO_2 + H_2O \leftrightarrow H_2CO_3 \leftrightarrow HCO_3^- + H^+ \leftrightarrow CO_3^{2-} + 2H^+ \quad (5.1)$$

This species is thus important in processes such as pH homeostasis in oceans,[1] the formation of external skeletons by calcifying organisms,[2] the transport of CO_2 between the metabolizing tissues and the lungs,[3] and the regulation of blood pH. The nucleophilic attack of the hydroxide anion on CO_2,

$$OH^- + CO_2 \rightarrow HCO_3^- \quad (5.2)$$

is a benchmark for the study of solvation effects on chemical reaction dynamics.[4-9] While this reaction is predicted to proceed without a reaction barrier in the gas-phase[4,6,10], a substantial enthalpic barrier of 13.0±0.6 kcal/mol has been reported in aqueous solution.[11,12] Solvent interactions with the reactants, products, and complex along the reaction coordinate are thus important in understanding the thermodynamics and kinetics of this reaction in the aqueous phase. In this paper, we report gas-phase infrared spectra of the $HCO_3^-\cdot(H_2O)_{1-10}$ clusters. These spectra, in combination with the accompanying electronic structure calculations, provide a detailed probe of bicarbonate anion microsolvation.

The gas-phase thermochemical properties of the bare bicarbonate anion have been studied via collision-induced dissociation and proton transfer reactions.[13] The HCO_3^- anion has been studied by Raman and infrared spectroscopy in aqueous solution[14-18] and in the crystalline phase.[17,19,20] Analysis of these spectra is complicated by possible counter-ion interactions and formation of bicarbonate dimers. Rudolph and coworkers have studied the infrared and Raman spectra of very dilute solutions of $KHCO_3$ and $KDCO_3$ and concluded that the hydrated HCO_3^- anion possess a C_1 symmetry, in contrast to the C_s (planar) symmetry expected in the gas-phase.[17,18] They also reported density functional theory (DFT) calculations on the $HCO_3^-\cdot(H_2O)_{1-3}$ clusters.[17] While these bulk studies probe the structure of the HCO_3^- in solution, they do not provide detailed information on the microscopic structure of the solvation shells or the specific interactions between the solvent molecules and the anion. On the other hand, infrared spectroscopy of size-selected ion clusters has emerged in recent years as a very powerful technique for probing microscopic ion hydration.

Here, we use vibrational action spectroscopy of gas phase clusters to probe the microhydration of the HCO_3^- anion by studying the effect of stepwise hydration on its spectroscopy, structure, and energetics. We measure infrared multiple photon dissociation

spectra of mass-selected $HCO_3^-\cdot(H_2O)_n$ clusters at low temperature and in the absence of a counter-ion. The spectra are acquired in the spectral region spanning 550 cm^{-1} to 1800 cm^{-1}, which includes five of the characteristic vibrational modes of the anion as well as the libration and bending modes of the solvent molecules. The spectra are analyzed with the help of simulated linear absorption spectra from electronic structure calculations. This combination of experiment and theory has proved very useful in recent studies[21,22] on the microhydration of the SO_4^{2-} and NO_3^- anions.

5.1.2 Experimental details

Infrared multiple photon photodissociation (IRMPD) experiments[23,24] were carried out on the ring electrode trap/tandem mass spectrometer,[25] which was temporarily installed at the "Free Electron Laser for Infrared eXperiments" (FELIX) user facility[26] in the FOM Institute Rijnhuizen (The Netherlands). $HCO_3^-(H_2O)_n$ ions were produced by electrospray of a 5 mM solution of sodium bicarbonate ($NaHCO_3$) in a 1:1 mixture of water and acetonitrile using a modified Waters z-spray source. The negative ions were transferred into a high vacuum system, sampled by a 3 mm diameter skimmer, and focused into a radio frequency (RF) linear ion guide. Ions of interest were then mass-selected in a quadrupole mass tri-filter, deflected by 90° using an electrostatic quadrupole ion deflector, and focused into a linear, ring electrode RF ion trap. The ion trap was filled with He buffer gas and cooled to 12 K by means of a closed cycle He cryostat in order to cool the ions by collisions. The ions were accumulated and cooled in the trap for 195 ms. They were then brought into the extraction region of a time-of-flight (TOF) mass spectrometer and irradiated with the pulsed radiation from FELIX prior to the application of high voltage pulses to the TOF plates. FELIX macropulses were used at a repetition rate of 5 Hz, a pulse length of 5 μs, a laser wavelength bandwidth of ca. 0.25% RMS over the range from 550 – 1800 cm^{-1}, and typical pulse energies of up to 50 mJ.

5.1.3 Experimental results

IRMPD spectra of $HCO_3^-\cdot(H_2O)_n$ clusters, with n = 1-10 are shown in Figure 5.1. These spectra were generated by summing the yield of the various fragment ions as a function of the photodissociation laser wavelength and reflect the absorption spectrum of the parent ion. This signal was nearly background-free, in contrast to monitoring depletion of the parent ion signal. The only fragmentation pathways observed involved loss of one or more water molecules. The loss of more than one water molecule might have been due in part to fragment absorption as the different cluster sizes have similar infrared absorption bands. No fragmentation was observed for the bare HCO_3^- anion.

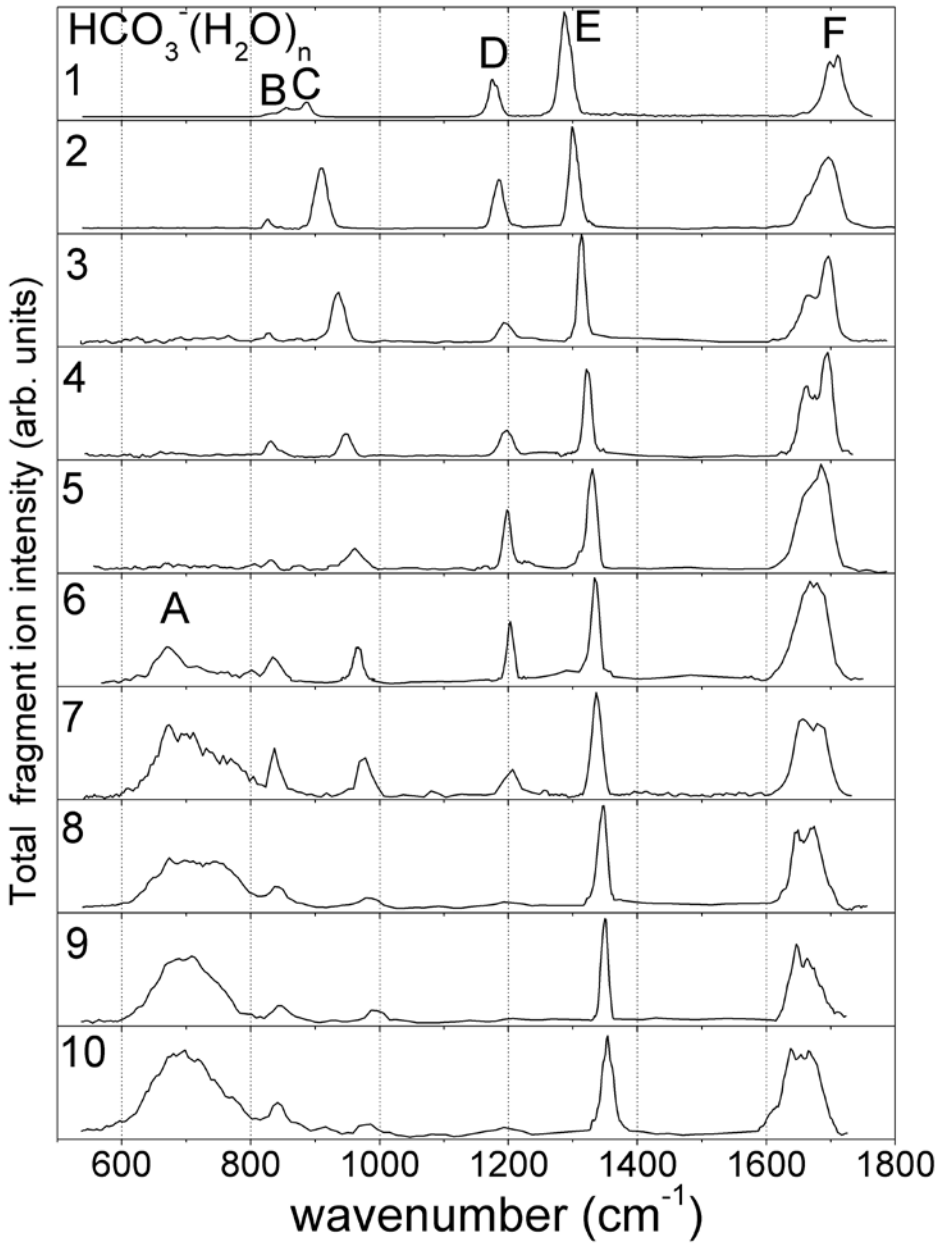

Figure 5.1 Experimental IRMPD spectra of $HCO_3^-\cdot(H_2O)_n$ ions with n = 1 – 10. The total fragment ion yield is plotted as a function of irradiation wavenumber (cm^{-1})

The experimental IRMPD spectra comprise six bands labeled A-F in Figure 5.1. Peak B, which appears as a small shoulder for the n=1 cluster, red-shifts from 860 cm^{-1} to 825 cm^{-1} upon addition of the second water. This peak subsequently blue-shifts by only 16 cm^{-1} from n=3-10. Peak C blue-shifts from 887 cm^{-1} to 986 cm^{-1} as the number of waters increases. Peak D moves from 1177 cm^{-1} to 1205 cm^{-1} between $HCO_3^-\cdot(H_2O)_1$ and $HCO_3^-\cdot(H_2O)_7$ and is not observed for larger clusters. Peak E, which is the most intense feature in most of the spectra, blue-shifts from 1288 to 1353 cm^{-1} as the cluster size increases. Peak F is a broader feature whose individual components are partially resolved only for a few cluster sizes. In contrast to the other bands, it generally red-shifts as the number of water molecules increases. Finally, the peak labeled A is a broad, unresolved feature between 600 cm^{-1} and 800 cm^{-1} that only appears in the spectra of $HCO_3^-\cdot(H_2O)_6$ and larger clusters. Experimental frequencies for $HCO_3^-\cdot(H_2O)_{1\text{-}10}$ are summarized in Table 5.1.

Table 5.1 Peak positions (in cm^{-1}) in the $HCO_3^-\cdot(H_2O)_{1\text{-}10}$ experimental IR spectra. Band assignments are referenced to HCO_3^- vibrational modes in Figure 5.2.

$HCO_3^-\cdot(H_2O)_n$	Band A	Band B (ν_8)	Band C (ν_5)	Band D (ν_4)	Band E (ν_3)	Band F (ν_2, water bend)
1	-	859	887	1177	1288	1706
2	-	826	909	1185	1301	1666, 1697
3	-	827	936	1196	1313	1666, 1696
4	-	832	948	1197	1323	1663, 1694
5	-	831	961	1198	1330	1663, 1691
6	675	837	966	1203	1334	~1670
7	~700	837	976	1205	1337	1656, 1686
8	~710	841	983	-	1346	1646, 1672
9	~700	841	986	-	1349	1646, 1665
10	~700	841	986	-	1353	~1653
$HCO_3^-{}_{(aq)}$ [a]	675	843	1014	1320	1364	1634
$HCO_3^-{}_{(aq)}$ [b]	-	844	1009	-	1359	1617
$H_2O_{(liq)}$ [c]	~690					~1640

a) From Ref. [17]
b) From Ref. [16]
c) From Ref. [27]

5.1.4 Electronic structure calculations

Electronic structure calculations were performed using the Gaussian 03 program[28] in order to assign the various experimental spectra to particular solvation motifs of the HCO_3^-

anion. Because of computational limitations, only the n=1-8 clusters were studied. Geometry optimizations were performed for a large number of initial structures of $HCO_3^-\cdot(H_2O)_n$ clusters using density functional theory, employing the B3LYP hybrid exchange-correlation functional[29,30] and the 6-311+G(d,p) basis set. Vibrational analysis was performed on all the optimized geometries to ensure that the structures corresponded to local minima. The lowest energy isomers were then re-optimized with the second order Moller-Plesset (MP2) method using the same 6-311+G(d,p) basis set. The MP2 structures were found to be very similar to those obtained with DFT but the energetic ordering of the various isomers often changed for the clusters with n≥3. In some instances, small differences in structures between isomers were observed, for instance an H-atom pointing up or down, in which case the lowest energy form was used, but for the purposes of our study these were not considered to be distinct isomers. Simulated infrared spectra were derived from the MP2/6-311+G(d,p) scaled harmonic frequencies (scaling factor: 0.970)[31] and linear absorption intensities. For comparison with experimental results, stick spectra from the simulations were convoluted using a Gaussian line shape function with a 15 cm^{-1} full width at half-maximum (FWHM). All the energetics presented herein were derived from the MP2/6-311+G(d,p) values and include the scaled zero-point energy correction.

5.1.5 Analysis

The six bands observed in the IRPMD spectra can be readily assigned based on previous infrared studies of HCO_3^- in bulk water[17] and calculated vibrational frequencies of the bare and solvated anion. The normal modes of HCO_3^- are shown in Figure 5.2, along with their calculated and scaled gas-phase frequencies at the MP2/6-311+G(d,p) level of theory. The small peaks B and C are assigned to the CO_3 out-of-plane mode (ν_8) and C-OH stretching mode (ν_5), respectively. Peak D is assigned to the COH bending mode (ν_4) while the more intense peak E is assigned to the CO_2 symmetric stretch (ν_3). Peak F is assigned to the CO_2 asymmetric stretch (ν_2) of the anion core as well as the various water bending modes.[27] These assignments are summarized in Table 5.1. Finally, peak A is located in the region where the CO_2 bending mode (ν_6) is expected. However, this mode has very weak infrared absorption[17] and thus band A is instead assigned to the various water librational modes.[27]

The following sections summarize the theoretical and experimental results for each individual cluster. For each cluster up to n=8, the structures, energetics, and simulated linear absorption spectra of the three lowest lying isomers are shown together with the corresponding experimental IRMPD spectra in Figures 5.3-5.10. The atom and position labeling used in this section and in Section 5.1.6 is shown at the bottom of Figure 5.2.

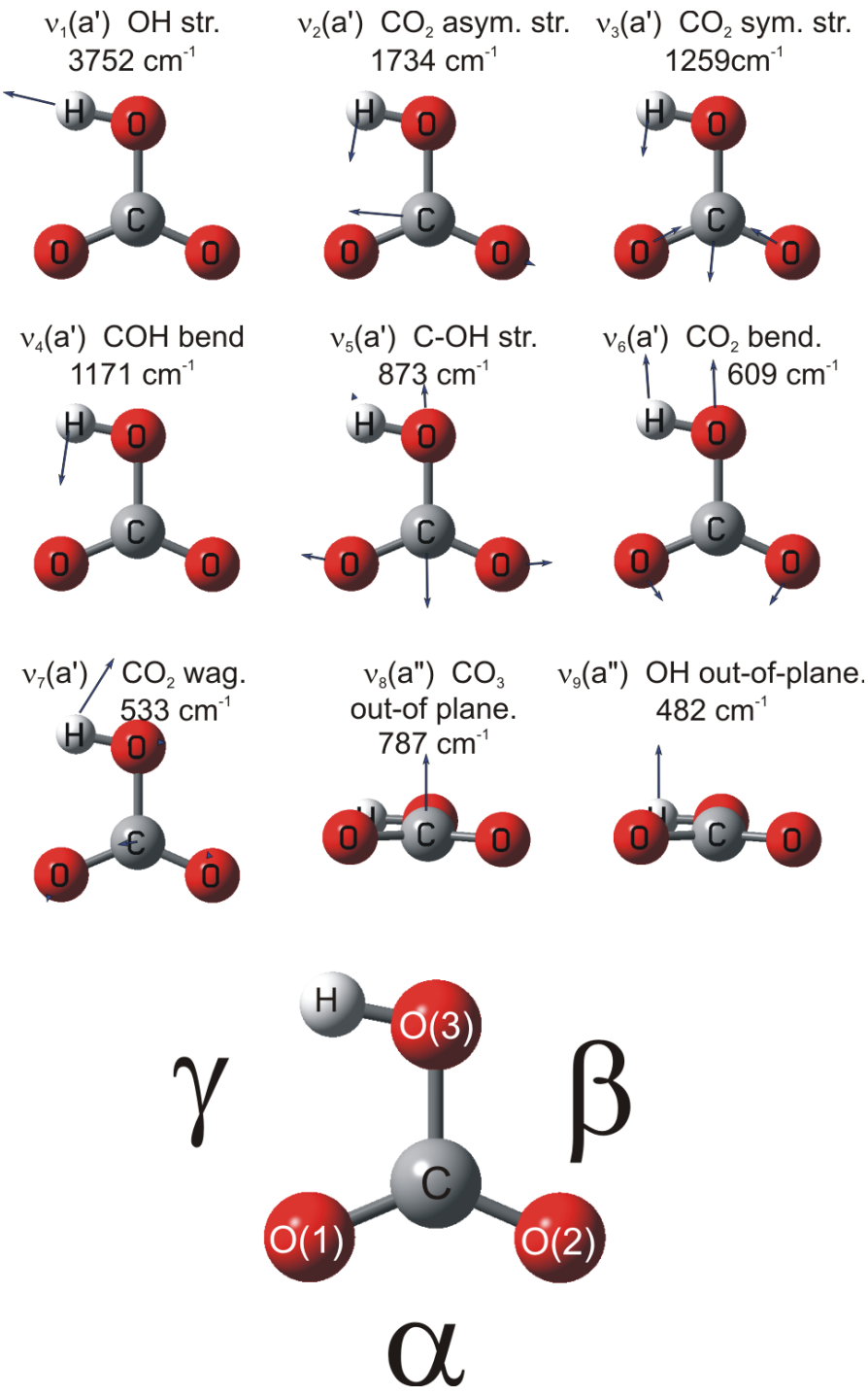

Figure 5.2 HCO_3^- normal modes and calculated gas-phase frequencies at the MP2/6-311+G(d,p) level as well as the atom and position labeling used in the analysis and discussion section.

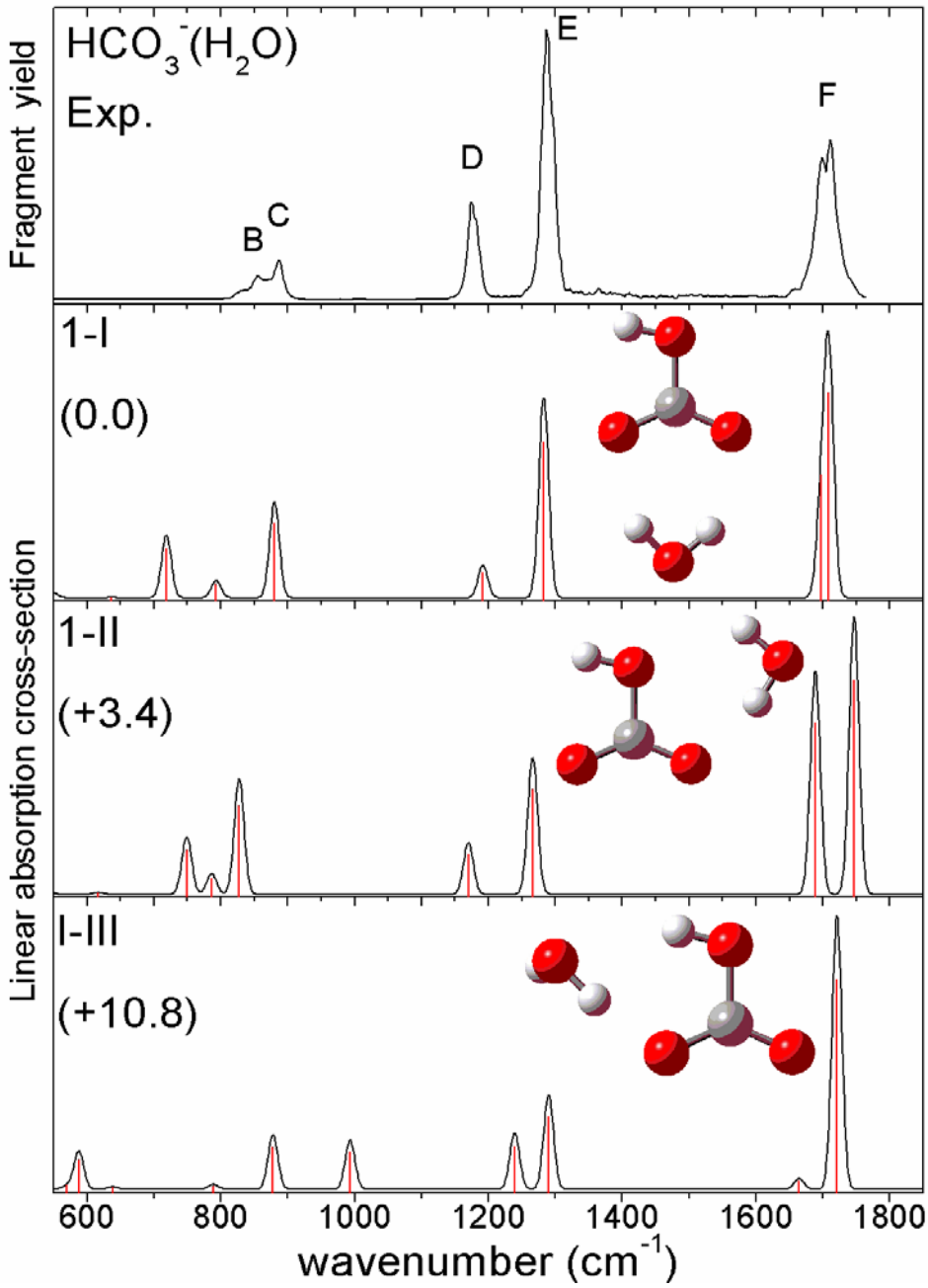

Figure 5.3 Experimental IRMPD spectrum of $HCO_3^-\cdot(H_2O)$ (top panel), with the simulated linear absorption spectra, structures and relative energies (kJ/mol) of the three lowest energy isomers.

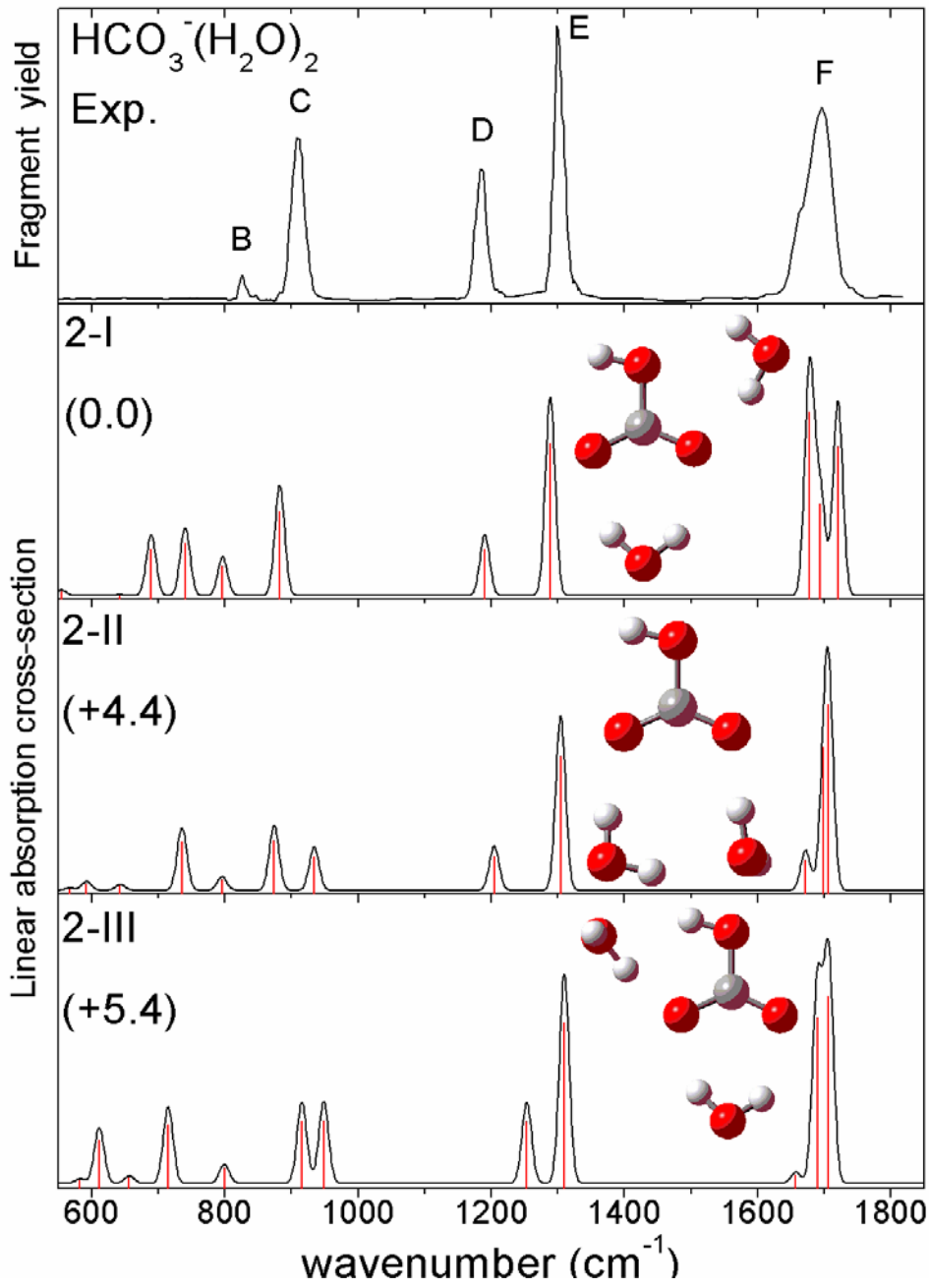

Figure 5.4 Experimental IRMPD spectrum of $HCO_3^-\cdot(H_2O)_2$ (top panel), with the simulated linear absorption spectra, structures and relative energies (kJ/mol) of the three lowest energy isomers.

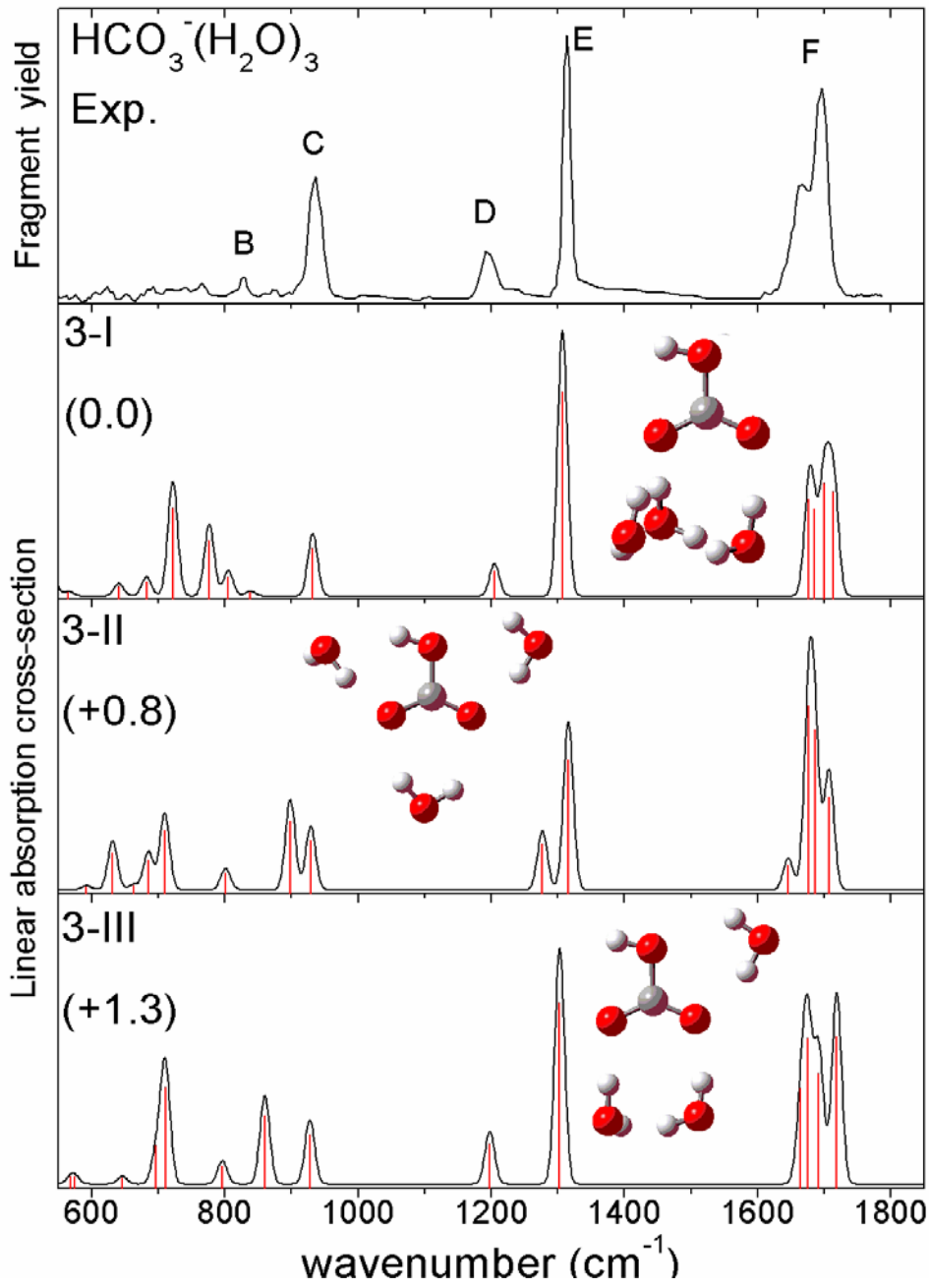

Figure 5.5 Experimental IRMPD spectrum of $HCO_3^-\cdot(H_2O)_3$ (top panel), with the simulated linear absorption spectra, structures and relative energies (kJ/mol) of the three lowest energy isomers.

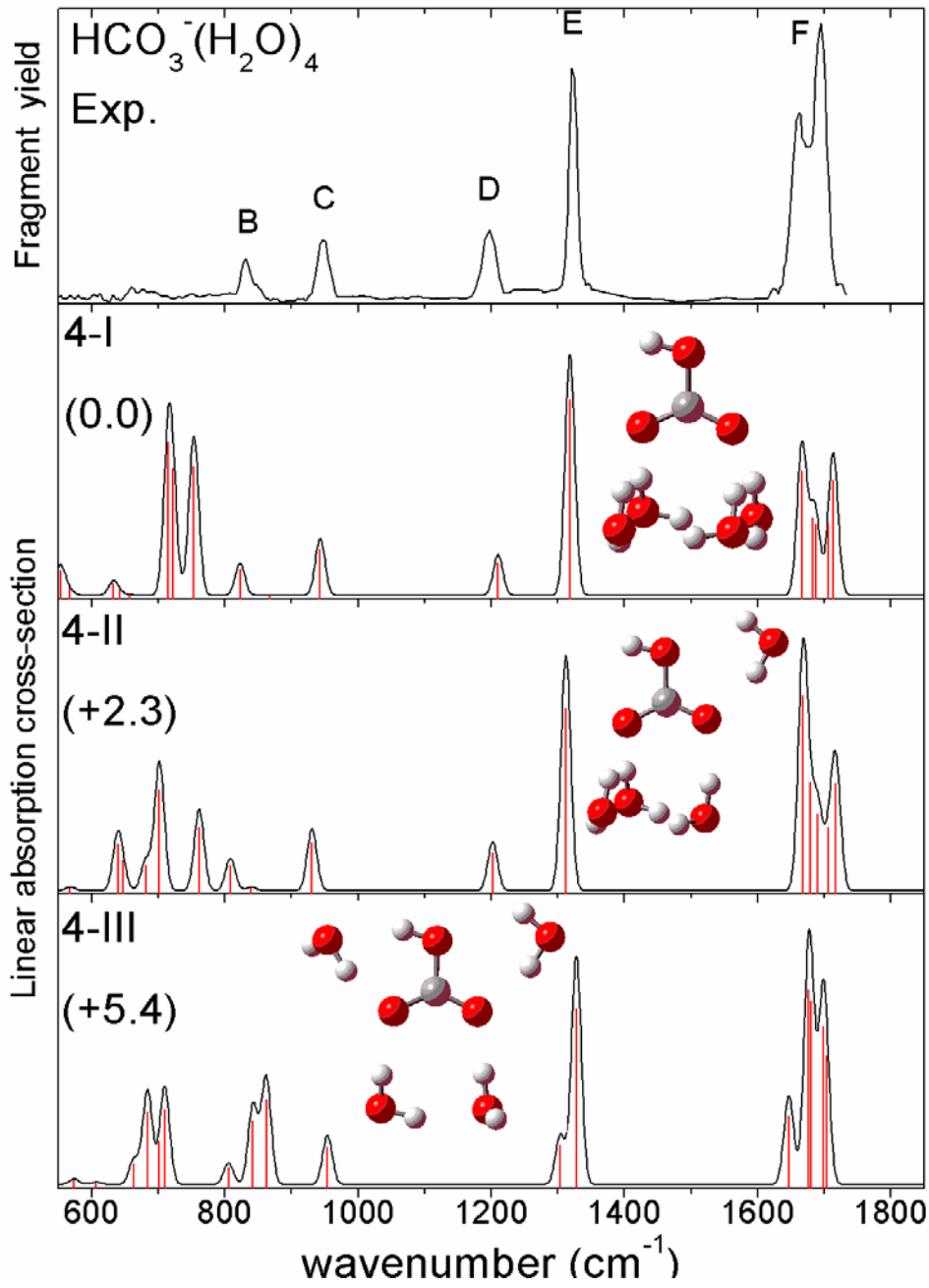

Figure 5.6 Experimental IRMPD spectrum of $HCO_3^-\cdot(H_2O)_4$ (top panel), with the simulated linear absorption spectra, structures and relative energies (kJ/mol) of the three lowest energy isomers.

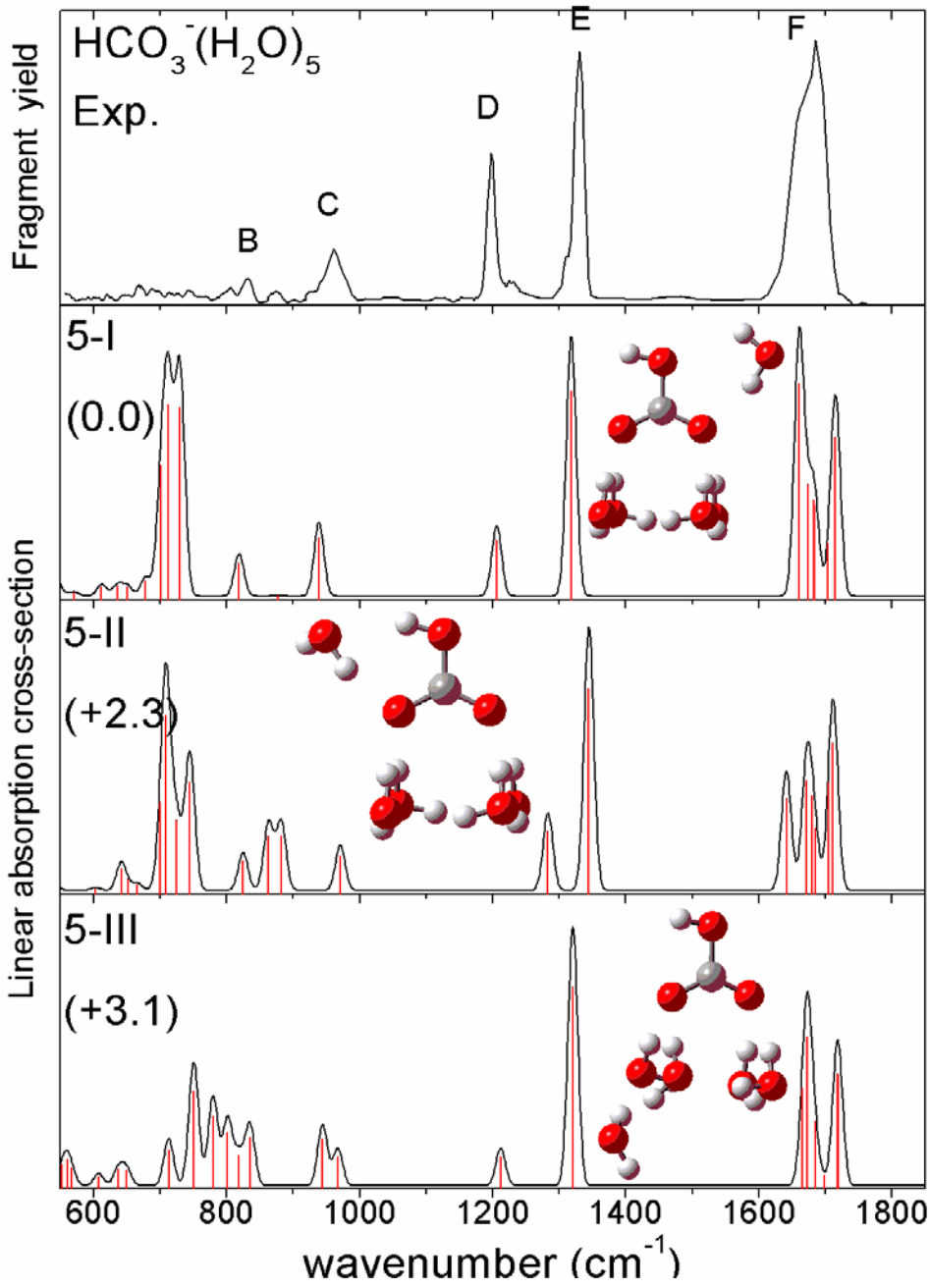

Figure 7: Experimental IRMPD spectrum of $HCO_3^-\cdot(H_2O)_5$ (top panel), with the simulated linear absorption spectra, structures and relative energies (kJ/mol) of the three lowest energy isomers.

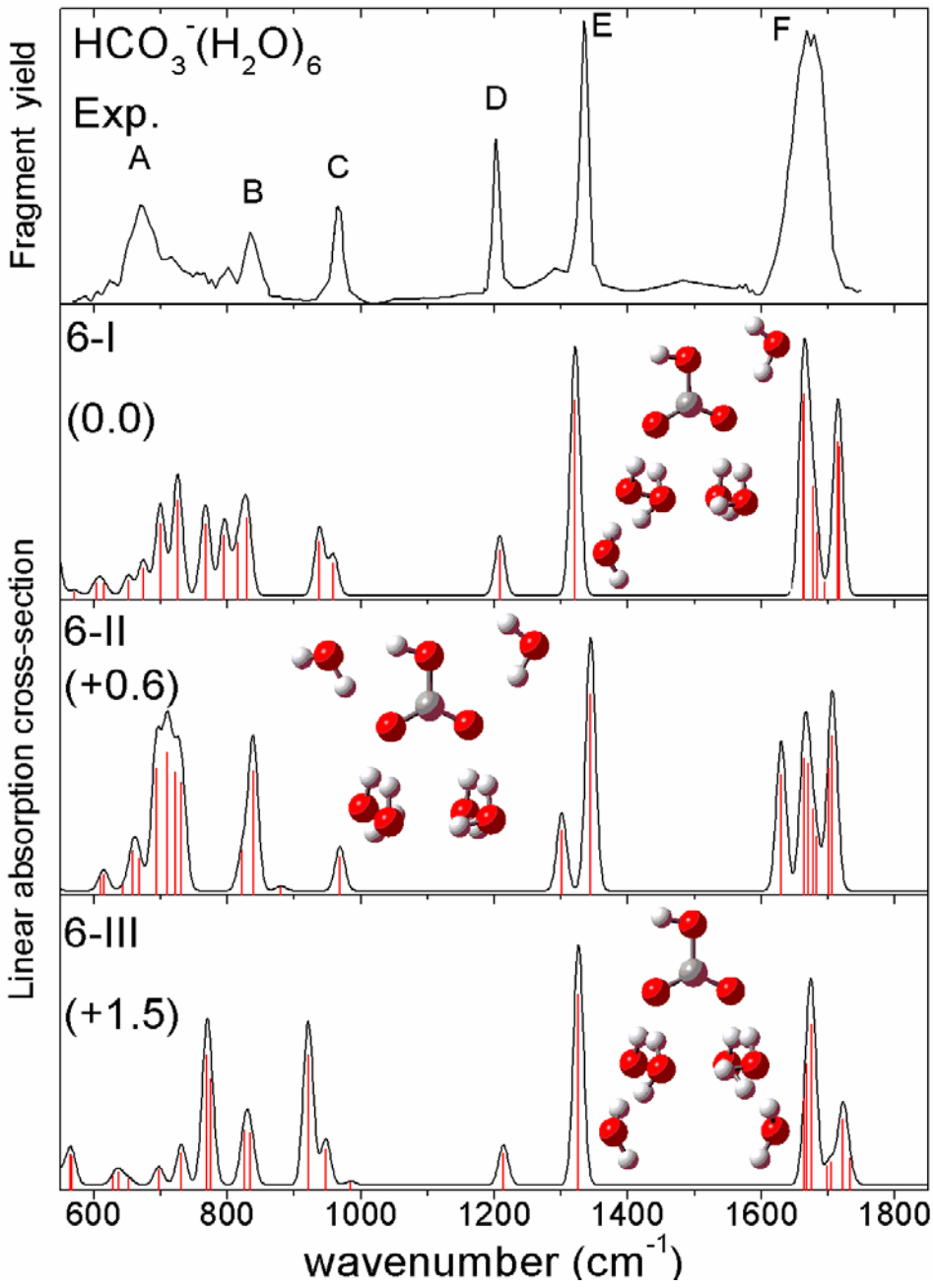

Figure 5.8 Experimental IRMPD spectrum of $HCO_3^-\cdot(H_2O)_6$ (top panel), with the simulated linear absorption spectra, structures and relative energies (kJ/mol) of the three lowest energy isomers.

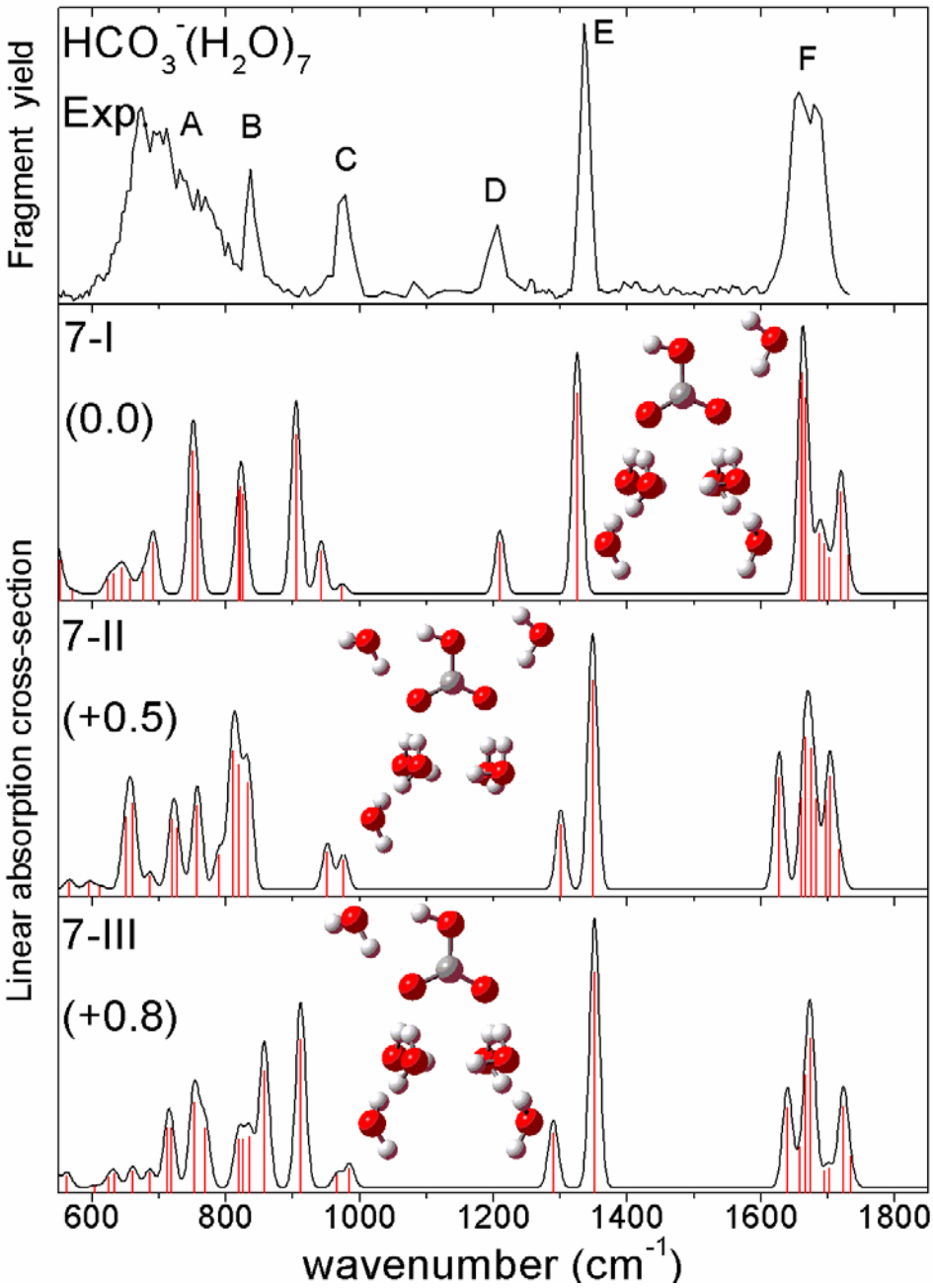

Figure 5.9 Experimental IRMPD spectrum of $HCO_3^-\cdot(H_2O)_7$ (top panel), with the simulated linear absorption spectra, structures and relative energies (kJ/mol) of the three lowest energy isomers.

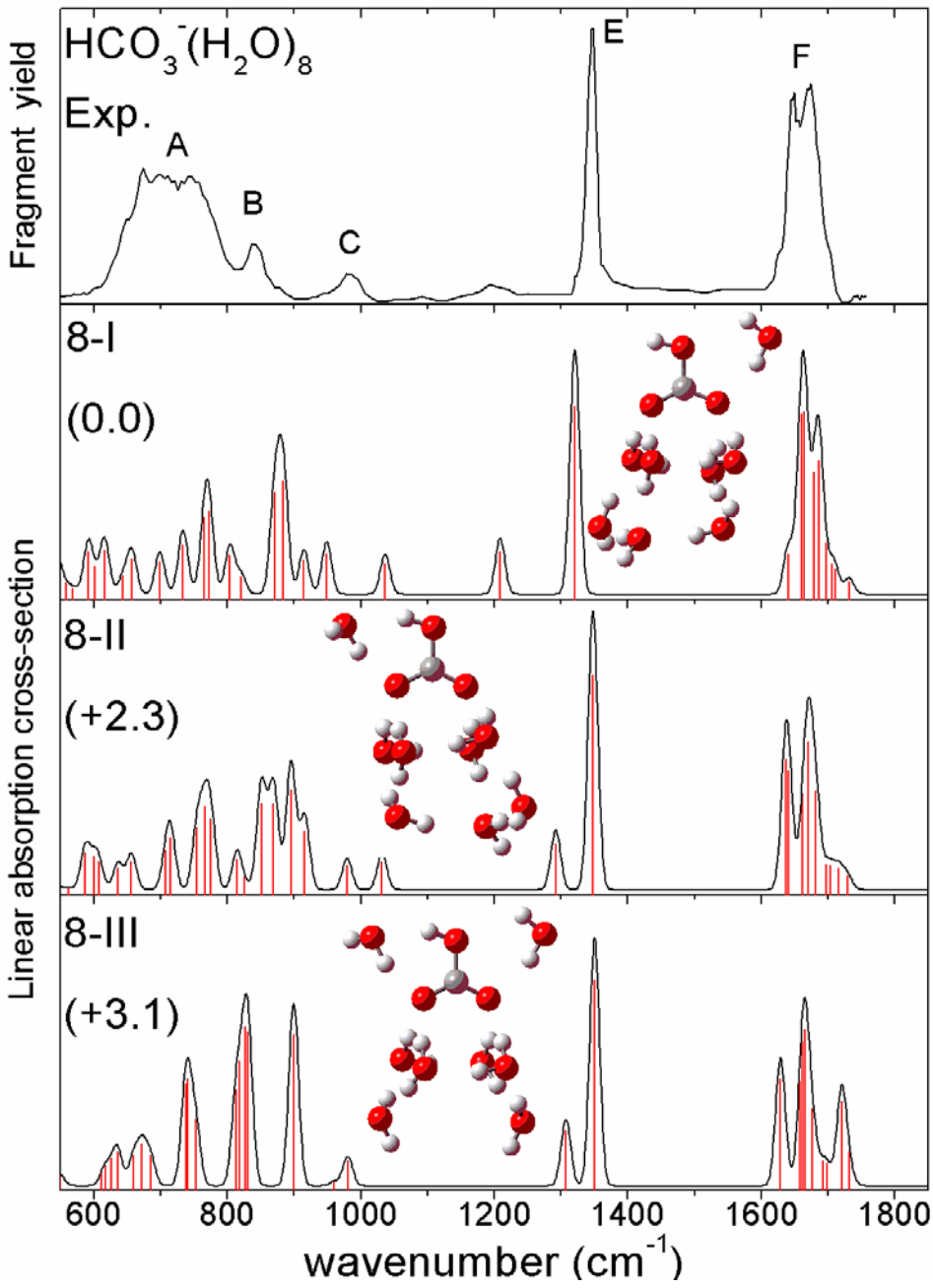

Figure 5.10 Experimental IRMPD spectrum of $HCO_3^-\cdot(H_2O)_8$ (top panel), with the simulated linear absorption spectra, structures and relative energies (kJ/mol) of the three lowest energy isomers.

1) $HCO_3^-\cdot(H_2O)$

In Figure 5.3, the lowest energy isomer, labeled 1-I, is a C_s structure in which the water forms two H-bonds with the negatively charged CO_2 moiety of the HCO_3^- anion. The 1-II isomer lies 3.4 kJ/mol higher and consists of a doubly H-bonded water in which the hydroxyl group oxygen of the OH and one oxygen of the CO_2 act as acceptors. In this isomer, the water molecule is located slightly out of the HCO_3 plane. In the third isomer, 1-III, the water forms one H-bond with the CO_2 moiety and acts as an acceptor for a second H-bond with the OH group. This isomer lies 10.8 kJ/mol above 1-I. No minima were found for isomers with a singly H-bonded water at either the B3LYP/6-311+G(d,p) or MP2/6-311+G(d,p) level of theory.

The simulated infrared spectra of 1-I agrees best with experiment. This isomer yields calculated position of peaks C-F which are in excellent agreement with the experimental values. However, the simulated spectrum of 1-I includes a peak at 719 cm^{-1} corresponding to the water libration mode that is not observed experimentally. The absence of features in the 550-800 cm^{-1} region of the IRMPD spectra of the small $HCO_3^-\cdot(H_2O)_{1-5}$ clusters is a general feature that will be discussed in Section VI. The presence of isomer 1-II can be eliminated on the basis of feature F. In the simulated spectra of 1-II, the water bending (1692 cm^{-1}) and asymmetric CO_2 stretching (1746 cm^{-1}) modes form two distinct features, while only a single peak is observed in the IRMPD spectra. For isomer 1-III, peak D occurs at higher energy than in the experimental spectrum and an extra water vibrational feature at 993 cm^{-1} is predicted which is not seen experimentally. With reference to Figure 5.2, the position of the water in isomers 1-I to 1-III corresponds to the α, β and γ sites, respectively, and this labeling scheme will be used to describe solvation motifs in the larger clusters.

2) $HCO_3^-\cdot(H_2O)_2$

Figure 5.4 shows that in the lowest energy isomer of the n=2 cluster, 2-I, the waters are at the α and β sites and each forms two H-bonds with the HCO_3^- anion. The 2-II isomer lies higher in energy by 4.4 kJ/mol and consists of two waters in the α position connected by a water-water H-bond, each of which is singly-bonded to the HCO_3^-. The 2-III isomer, which lies 5.4 kJ/mol above 2-I, consists of a doubly H-bonded water in the α position and another in the γ position. No minima were found for isomers with two doubly H-bonded waters at the same site.

The simulated spectrum of 2-I agrees best with experiment. The main discrepancy is the splitting of peak F which is smaller and not resolved in the experimental spectra. In the simulated spectra of 2-II and 2-III, peak C is split into two distinct features, which is not observed experimentally. These two modes can be described as the linear combination of the C-OH stretching motion and the libration of the singly H-bonded water. Also, in 2-III (as in

1-III), the water at the γ position induces a blue shift of peak D with respect to the experimental frequency.

3) $HCO_3^-\cdot(H_2O)_3$

In the lowest energy isomer for the n=3 cluster, 3-I, the three waters are in the α position, as shown in Figure 5.5. Each forms one H-bond with the HCO_3^- anion and another with an adjacent water, resulting in a three-membered water ring. The second isomer, 3-II, lies only 0.8 kJ/mol above 3-I and has one water molecule at each of the three sites. The 3-III isomer has two waters in the α position and one in the β position. Note that isomer 3-II was found to be the global minimum at the B3LYP level, in accordance with the previous study of Rudolph *et al.*[17] Once again, the simulated spectrum of the lowest energy isomer offers the best agreement with the experiment. The simulated spectra of 3-II and 3-III exhibit a splitting of peak C that is not observed experimentally. Just as in isomers 2-II and 2-III, this splitting arises from two linear combinations of the C-OH stretch and libration of the singly H-bonded water. However, since the intensities of the liberation bands are uncertain (see Section 5.1.6.), the presence of isomer 3-III cannot be ruled out. In 3-II, the calculated position of peak D at 1277 cm^{-1} is noticeably higher than the experimental frequency, 1196 cm^{-1}. It thus appears that isomer 3-II does not contribute to the experimental spectrum.

4) $HCO_3^-\cdot(H_2O)_4$

Figure 5.6 shows results for the n=4 cluster. In the lowest energy isomer, 4-I, all four waters are at the α site. Each forms one H-bond with the HCO_3^- anion and another with an adjacent water, resulting in a four-membered ring. Isomer 4-II, lying 2.3 kJ/mol above 4-I, has a three-membered ring in the α position, similar to 3-I, and the fourth water in the β position. Isomer 4-III has two singly H-bonded waters in the α position while the two remaining waters are at the β and γ sites. This isomer lies 5.4 kJ/mol above 4-I.

The simulated spectra of 4-I and 4-II are very similar and in good agreement with experiment. The position and intensity of peak F is in slightly better agreement with the simulated spectrum of 4-I but the presence of 4-II cannot be ruled out. For isomer 4-III, the calculated position of peak D is blue-shifted with respected to the experimental value to such an extent that it appears as a shoulder on peak E in the simulation. Isomer 4-III was found to be the minimum energy structure at the B3LYP level which is again not consistent with the experimental observations.

5) $HCO_3^-\cdot(H_2O)_5$

For the n=5 cluster, shown in Figure 5.7, the three lowest energy structures each have four waters in the α position forming a single H-bond with the HCO_3^-, similar to the ring arrangement in 4-I. In the lowest energy isomer, labeled 5-I, the fifth water molecule is in the

β position while it is at the γ site in the 5-II isomer. In the 5-III isomer, the fifth solvent molecule does not bind directly to the HCO_3^- anion but rather to two other water molecules, thus forming a five-membered hydrogen bonded network in the α position. Isomers 5-II and 5-III are 2.3 kJ/mol and 3.1 kJ/mol above the 5-I structure, respectively.

The simulated spectra of 5-I and 5-III are in reasonable agreement with the experiment but both overestimate the splitting of peak F. The spectrum of 5-I reproduces the experimental spectrum better around peaks B and C. Isomer 5-II can be ruled out on the basis of the doublet between peaks B and C that is not observed experimentally, and the predicted position of peak D which is blue-shifted with respected to the experimental value.

6) $HCO_3^-\cdot(H_2O)_{6-8}$

Experimental and simulated spectra from the three calculated lowest-lying isomers of $HCO_3^-\cdot(H_2O)_{6-8}$ are shown in Figure 5.8-5.10. For each of these three clusters, the calculated lowest energy structure is based on 5-I; the additional water molecules extend the water-water network at the α site and form a second solvation layer. Most of the other low-lying isomers in this range have one water binding in the γ position. For the n=6 and n=7 clusters, we can rule out these isomers as the major contributors to the experimental spectra on the basis of the position of band D, just like in the smaller clusters. However, for n=6, we observe a weak absorption at ~1290 cm^{-1} which might indicate a small amount of 6-II. In the n=8 experimental spectrum, band D is not clearly observed but there is a weak feature at ~1200 cm^{-1} which corresponds to the calculated position of band D in isomer 8-I. The calculated shape of band F for 8-I is also in better agreement with the experimental spectrum than the other isomers. Thus, we conclude that 8-I is probably the main isomer present in the experiment.

5.1.6 Discussion

For some clusters, comparing the experimental and calculated spectra does not always identify a single isomer as being responsible for the spectrum. It is particularly difficult to distinguish between the isomers with water binding in the α or β position, because they typically have very similar spectra in the energy range studied here. However, the overall good agreement between the calculated spectra and the experiment indicates that our binding motifs are reasonable. Clear trends emerge from the calculated stepwise solvation motifs presented here. The most striking of these is the strong preference of the water molecules for the α position. This trend is consistent with the classical picture of the bicarbonate anion in which the negative charge is shared by the O(1) and O(2) oxygen atoms. However, we find that four waters at most can directly interact with the HCO_3 anion in the α position. The binding motif in isomer 4-I, in which each of the 4 waters in the α position forms a single H-bond with the CO_2 moiety, is retained in all the most stable isomers of the larger clusters.

Our calculations found a maximum of one water molecule outside the α position in the most stable isomers. It is preferentially located at the β site, forming H-bonds with both the O(2) and O(3) oxygen atoms of the bicarbonate anion. The isomers having water molecules in the γ position were systematically found to be higher in energy. Moreover, these isomers always yielded a frequency for peak D, the ν_4 COH bend, that was blue-shifted relative to the experimental spectra.

For clusters with n>5, five water molecules at most were found to interact directly with the bicarbonate anion. Starting at n=6, the additional solvent molecules formed a second hydration shell, extending the water-water network located at the α site. Finally, in all the isomers presented here, the water molecules were located within or close to the plane of the bicarbonate anion. Isomers with water located on top of the HCO_3^- core were significantly higher in energy. This result differs from the microsolvation motifs found for the similarly planar NO_3^- anion. For $NO_3^-(H_2O)_n$ cluster with n=4-6, the most stable isomers comprised a four-membered water ring located above the NO_3^- molecular plane.[21]

The monotonic frequency shifts observed in the IRMPD spectra as a function of cluster size are well-reproduced by the calculations. In order to understand these solvation-induced frequency shifts, we have to examine the effect of hydration on the HCO_3^- anion geometry. In the bare anion, the C-O(1), C-O(2) and C-O(3) bond lengths are calculated to be 1.254Å, 1.238Å and 1.452Å, respectively, at the MP2/6-311+G(d,p) level. These bond lengths are consistent with the C-O(3) having single bond character while the C-O(1), C-O(2) have ~1.5 bond character owing to sharing of the negative charge. The slightly longer C-O(1) bond, with respect to C-O(2), indicates that the interaction between the hydrogen and O(1) stabilizes the resonance structure in which the negative charge is on the O(1) atom. Upon the addition of a water in the α position, (isomer 1-I) the C-O(3) bond length is reduced to 1.424Å. On the other hand, the C-O(1) and C-O(2) bonds are slightly elongated to 1.259Å and 1.242Å, respectively. These changes are consistent with the water molecule shifting the negative charge onto the O(1) and O(2) atoms. Thus, the interaction of water at the α position increases the strength of the C-O(3) bond while weakening the C-O(1) and C-O(2) bonds. These trends continue as more water molecules are added at the α position. For example, in isomer 8-I, the C-O(1), C-O(2) and C-O(3) bond lengths are calculated to be 1.258Å, 1.251Å and 1.393Å, respectively.

In the experimental spectra, bands C and E display the largest frequency shifts upon sequential addition of water molecules. They are blue-shifted by 99 cm^{-1} and 65 cm^{-1}, respectively, as the cluster size increases from 1 to 10 water molecules. These two bands are assigned to the ν_5 and ν_3 modes, which primarily consist of C-O(3) stretching motion. The large blue-shift observed for these bands is thus consistent with strengthening of the C-O(3) bond induced by the water interactions in the α position. The frequency of the ν_2 mode, which mainly involves C-O(1) and C-O(2) stretching motion, cannot be directly derived from

our spectra because of the overlap with the bending mode of the water in band F. However, from the overall shifts of band F, we estimate that the frequency of this mode is red-shifted by about 50 cm^{-1} as the cluster size increases from 1 to 10 water molecules. This trend is again consistent with the water interactions in the α position which elongate the C-O(1) and C-O(2) bonds. The frequency of the ν_4 mode (band D), the CO(3)H bending motion, is blue-shifted by only 30 cm^{-1} with increasing cluster size. This is consistent with our calculations which show that no water molecule directly interacts with the H of the HCO_3^- core in the cluster size range studied here. The small blue-shift of band D might be from shortening of the C-O(3) bond and increased charge on the CO_2 moiety which would perturb the interaction between the H and O(1) atoms.

The only band which does not show a monotonic frequency shift upon solvation is peak B, assigned to the CO_3 out-of-plane mode. It red-shifts from 860 cm^{-1} to 825 cm^{-1} upon addition of the second water and subsequently blue-shifts by only 16 cm^{-1} from n=3-10. The calculation does not reproduce this non-monotonic behavior of peak B in the smaller clusters. It is possible that this discrepancy is due to anharmonic effects because in the solvated clusters, the CO_3 out-of-plane mode of the bicarbonate anion also involves water libration motions. It is also possible that peak B in the $HCO_3^-\cdot(H_2O)$ experimental spectrum, where it appears as a small shoulder, does not correspond to the CO_3 out-of-plane mode of isomer 1-I, but rather the C-OH stretching mode (feature C) of another isomer such as 1-II.

Some of the calculated absorption bands are not observed in the experimental spectra, most notably the absorption bands in the 600-800 cm^{-1} spectral region for clusters with n<6 (labeled as peak A in the larger clusters). These bands are from various water librational modes. Their absence in the experimental spectra is similar to what was observed for the $NO_3^-(H_2O)_n$ clusters[21] and can originate from several effects. First, the number of photons required to reach the dissociation continuum is three times larger at 600 cm^{-1} than at 1800 cm^{-1}. This renders the low frequency modes considerably more difficult to observe in our IRMPD spectra than those at higher frequencies. However, peaks B and C appear in our spectra with intensities close to their calculated linear absorptions, so frequency alone cannot explain the absence of peak A in small cluster sizes.

Structural changes that accompany IR multiphoton absorption offer a more likely origin for the absence of low-frequency librational bands. For example, in the 1-I isomer, the absorption of a few photons at the water librational mode frequency is not sufficient to break both H-bonds, but can break a single H-bond. However, the resulting singly-bonded water cannot absorb any additional photons, because the absorption frequency of its librational mode has changed and is now out of resonance with the irradiation wavelength. This interpretation is supported by our experimental spectra in which the water libration band (band A) appears only for clusters with six or more water molecules, since $HCO_3^-(H_2O)_6$ is the smallest cluster in which the lowest lying isomer (isomer 6-I) contains a singly-bonded water molecule. These clusters are thus more likely to dissociate rather than isomerize upon

absorption of infrared photons. Moreover, the intensity of band A doubles in $HCO_3^-(H_2O)_7$, for which the lowest energy isomer (7-I) contains two singly-bonded water molecules.

In the cluster size range studied here, the frequencies of all the observed absorption bands monotonically shift toward their aqueous values as the number of water molecule is increased. With the exception of band D, all the absorption bands are within 30 cm^{-1} of their position in aqueous solution by the n=10 cluster. In the smaller clusters, band D is found to be more red-shifted than the other bands with respect to the aqueous frequencies. In the n=7 cluster, the largest cluster in which this band is clearly observed, band D is still 115 cm^{-1} below its aqueous frequency of 1320 cm^{-1}. This difference can be easily understood from the calculated vibrational spectra of the various isomers. Our calculations found that cluster isomers with a water at the γ site were systematically higher in energy. However, it can be seen from the calculated spectra of those isomers that a water molecule at the γ position induces a ~100 cm^{-1} blue-shift of band D. In aqueous solution, at least one water molecule is certainly found in this position. It would be of interest to determine how large a cluster has to be before the lowest energy structure has a water at the γ site.

Finally, it is worthwhile to comment on the insights that the present study may yield on the structure of the fully hydrated bicarbonate anion. Careful examination of the polarization of the Raman modes in very dilute solutions of $KHCO_3$ and $KDCO_3$ led Rudolph and co-coworkers to conclude that the hydrated HCO_3^- anion has a C_1 symmetry in contrast to the C_s symmetry expected in the gas-phase.[17,18] In the clusters considered here, the calculated lowest lying isomers all have a HCO_3^- anion with C_s (planar) symmetry. However, the isomers having a water in γ position (such as 8-III) have a HCO_3^- core with a C_1 symmetry, with a O(1)CO(3)H dihedral angle of about 2°. Thus, the HCO_3^- core may well adopt a geometry with C_1 symmetry in larger clusters and bulk water where the ion is fully solvated.

5.1.7 Conclusion

Infrared spectra are reported for the $HCO_3^-(H_2O)_n$, n=1-10 clusters in the 600-1800 cm^{-1} spectral range. Electronic structure calculations using DFT and MP2 have been performed on the n=1-8 species to determine the structure of the lowest-lying isomers. Comparison of the experimental and calculated spectra does not always enable unambiguous identification of a single isomer for each cluster. Nonetheless, the overall good agreement between the calculated spectra and experiment allows us to determine general trends in the stepwise solvation motifs of the bicarbonate anion. The most important of these is the strong preference of water molecules to bind to the negatively charged CO_2 moiety (the α site) of the HCO_3^- anion. However, a maximum of four waters can directly interact with the anion at this position. The binding motif in the most stable isomer of n=4, which consists of a four-membered ring with each water forming a single H-bond with the CO_2 moiety, is retained in

all the most stable isomers of the larger clusters. Starting at n=6, the additional solvent molecules are found to form a second hydration shell, extending the water-water network located at the α site of the bicarbonate anion. We also find that binding at the hydroxyl group of HCO_3^- is disfavored for all clusters studied here; this result accounts for the largest discrepancy between the cluster spectra and the IR spectrum of aqueous bicarbonate.

References:

1) K. Caldeira and M. E. Wickett, *Nature* **425** (6956), 365 (2003).
2) J. C. Orr, V. J. Fabry, O. Aumont*et al.*, *Nature* **437** (7059), 681 (2005).
3) D. N. Silverman and S. Lindskog, *Acc. Chem. Res.* **21** (1), 30 (1988).
4) Z. Peng and K. M. Merz, *J. Am. Chem. Soc.* **115** (21), 9640 (1993).
5) M. M. Davidson, I. H. Hillier, R. J. Hall, and N. A. Burton, *Mol. Phys.* **83** (2), 327 (1994).
6) A. V. Nemukhin, I. A. Topol, B. L. Grigorenko, and S. K. Burt, *J. Phys. Chem. B* **106** (7), 1734 (2002).
7) K. Iida, D. Yokogawa, H. Sato, and S. Sakaki, *Chem. Phys. Lett.* **443** (4-6), 264 (2007).
8) K. Leung, I. M. B. Nielsen, and I. Kurtz, *J. Phys. Chem. B* **111** (17), 4453 (2007).
9) P. P. Kumar, A. G. Kalinichev, and R. J. Kirkpatrick, *J. Phys. Chem. B* **113** (3), 794 (2009).
10) B. Jonsson, G. Karlstrom, and H. Wennerstrom, *J. Am. Chem. Soc.* **100** (6), 1658 (1978).
11) B. R. W. Pinsent, L. Pearson, and F. J. W. Roughton, *Trans. Faraday Soc.* **52** (11), 1512 (1956).
12) D. A. Palmer and R. Vaneldik, *Chem. Rev.* **83** (6), 651 (1983).
13) R. R. Squires, *Int. J. Mass Spec. Ion Processes* **117** (1-3), 565 (1992).
14) A. R. Davis and B. G. Oliver, *J. Solution Chem.* **1** (4), 329 (1972).
15) B. G. Oliver and A. R. Davis, *Can. J. Chem.* **51** (5), 698 (1973).
16) K. D. Dobson and A. J. McQuillan, *Langmuir* **13** (13), 3392 (1997).
17) W. W. Rudolph, D. Fischer, and G. Irmer, *App. Spect.* **60** (2), 130 (2006).
18) W. W. Rudolph, G. Irmer, and E. Konigsberger, *Dalton Trans.* (7), 900 (2008).
19) D. L. Bernitt, K. O. Hartman, and I. C. Hisatsun, *J. Chem. Phys.* **42** (10), 3553 (1965).
20) K. Nakamoto, Y. A. Sarma, and H. Ogoshi, *J. Chem. Phys.* **43** (4), 1177 (1965).
21) D. J. Goebbert, E. Garand, T. Wende, R. Bergmann, G. Meijer, K. R. Asmis, and D. M. Neumark, *J. Phys. Chem. A* **113**, 7584 (2009).
22) J. Zhou, G. Santambrogio, M. Brummer, D. T. Moore, G. Meijer, D. M. Neumark, and K. R. Asmis, *J. Chem. Phys.* **125** (11) (2006).

23) J. Oomens, B. G. Sartakov, G. Meijer, and G. von Helden, *Int. J. Mass. Spectrom.* **254** (1-2), 1 (2006).

24) K. R. Asmis, A. Fielicke, G. von Helden, and G. Meijer, in *The Chemical Physics of Solid Surfaces. Atomic Clusters: From Gas Phase to Deposited*, edited by D. P. Woodruff (Elsevier, Amsterdam, 2007), Vol. 12, pp. 327.

25) D. Goebbert, T. Wende, R. Bergmann, G. Meijer, and K. R. Asmis, *J. Phys. Chem. A* **113**, 5874 (2009).

26) D. Oepts, A. F. G. van der Meer, and P. W. van Amersfoort, *Infrared Phys Techn* **36** (1), 297 (1995).

27) NIST Mass Spec Data Center, S. E. Stein, and director, in *NIST Chemistry WebBook, NIST Standard Reference Database Number 69* (Eds. P.J. Linstrom and W.G. Mallard, National Institute of Standards and Technology, Gaithersburg MD, 20899, http://webbook.nist.gov, (retrieved November 2, 2009).).

28) M. J. Frisch, G. W. Trucks, H. B. Schlegel*et al.*, Gaussian 03, Revision C.02 (Gaussian, Inc., Wallingford CT, 2004).

29) C. Lee, W. Yang, and R. G. Parr, *Phys. Rev. B* **37** (2), 785 (1988).

30) A. D. Becke, *J. Chem. Phys.* **98** (7), 5648 (1993).

31) A. P. Scott and L. Radom, *J. Phys. Chem.* **100** (41), 16502 (1996).

5.2 Infrared multiple photon dissociation spectroscopy of $(SiO)_{3\text{-}5}^{+}$ clusters

Abstract

The first gas-phase infrared spectra of silicon monoxide cations $(SiO)_n^+$, n = 3-5, using multiple photon dissociation in the 550-1250 cm^{-1} frequency range, are reported. All clusters studied here fragment via loss of a neutral SiO unit. The experimental spectra are compared to simulated linear absorption spectra from calculated low energy isomers for each cluster. This analysis indicates that a "ring" isomer is the primary contributor to the $(SiO)_3^+$ spectrum, that the $(SiO)_4^+$ spectrum results from two close-lying bicyclic ring isomers, and that the $(SiO)_5^+$ spectrum is from a bicyclic ring with a central, fourfold-coordinated Si atom. Experiment and theory indicate that the energies and energetic orderings of $(SiO)_n^+$ isomers differ from those for neutral $(SiO)_n$ clusters.

5.2.1 Introduction

Silicon-oxide nanoparticles are important constituents of the interstellar medium, since they act as catalysts for chemical reactions[1] and nucleation centers for planetesimal formation[2]. Silicon particles or silicon-oxide clusters containing Si-Si bonds are also candidates for the source of the intense extended red emission (500-800 cm^{-1}) and UV-VIS extinction observed in the interstellar medium.[3,4] Because SiO is the most abundant oxygen-bearing species in interstellar clouds, it has been proposed that formation of small silicon monoxide clusters, $(SiO)_n$, is the first step toward the formation of silicon-containing structures.[5,6] However, the subsequent steps toward silicon $(Si)_n$ and silicates $(SiO_2)_n$ are not well understood. Recently, silicon monoxide clusters have drawn attention in the field of nanotechnology as they play a crucial role in the growth of silicon nanowires[7-9]. High yields of silicon nanowires surrounded by SiO_2 sheaths were obtained from evaporation or laser vaporization of mixed Si/SiO_2 powder and of pure SiO. The highest yield was obtained with targets containing equal amount of silicon and oxygen, highlighting the importance of small $(SiO)_n$ clusters in the early steps of the process.[7] Several theoretical studies on $(SiO)_n$ have shown that for $n \geq 5$, formation of isomers containing a Si core (i.e. at least one Si-Si bond) surrounded by a SiO_2 layer is energetically favored.[10-12] Such segregation of silicon and oxygen in $(SiO)_n$ and subsequent fragmentation[10,13] of these clusters could therefore account for the formation of both silicates and silicon structures.

Here we report the first gas-phase infrared (IR) spectra of silicon monoxide cluster cations, $(SiO)_n^+$ with n=3-5, using multiple photon dissociation spectroscopy. Although silicon monoxide clusters have been the subject of several theoretical studies,[10-16] only limited experimental information is available. Neutral $(SiO)_n$ clusters with $n \leq 3$ have been studied with IR and Raman spectroscopy in rare-gas matrices by Ogden and co-workers.[17-19] Analysis of these spectra indicated a planar, D_{3h} ring structure for $(SiO)_3$, a result borne out by the more recent calculations. Photoelectron spectra of the anion clusters $(SiO)_n^-$, n=3-5 measured by Wang *et al.*[20] showed electronic bands that were interpreted in terms of ring structures for all three anion clusters as well as for the neutrals created by photodetachment. The experiments and supporting theory reported here, however, indicate more complex structures for the cations, particularly for the n=4 and 5 clusters, where the lowest energy isomers appear to be bicyclic rings.

5.2.2 Experimental details

Experiments were performed on a tandem mass spectrometer-ion trap system using radiation from the broadly tunable Free Electron Laser for Infrared eXperiments (FELIX)[21]. Silicon monoxide cations, $(SiO)_n^+$, were produced by laser vaporization of a pure silicon target in the throat of a 0.1% O_2/He gas supersonic expansion at 10 Hz. The ion beam was

then collimated in a He-filled ion guide and mass-selected in a quadrupole mass filter. Mass-selected clusters were guided into a cryogenically cooled radio frequency ring electrode trap filled with continuously flowing He. Through many collisions with the He buffer gas, the ions were decelerated, trapped and cooled. With the present setup, internal (rotational) cluster temperatures of ~70 K are typically reached, determined by analysis of the rovibrational band contour of the ν_3 mode of $NH_2^+ \cdot Ar$. $(SiO)_n^+$ clusters were trapped and allowed to cool for at least 10 ms prior to irradiation with a single 5 μs FELIX macropulse. The macropulses were produced at 5 Hz with typical energies of 10-40 mJ and a bandwidth of ~0.6 full width at half maximum (FWHM) of the central wavelength. Resonant absorption of the IR radiation resulted in multiple photon dissociation (IRMPD) of the parent ion[22] and was detected by extracting the irradiated ions into a time-of-flight mass spectrometer and measuring the extent of fragmentation. IR spectra were measured from 8-20 μm (1250-500 cm^{-1}).

5.2.3 Electronic structure salculations

To aid in the interpretation of the spectral features, electronic structure calculations at the B3LYP/cc-pVTZ level of theory were performed with the GAUSSIAN 03 package.[23] For each cluster size, 10-15 different isomers were optimized. Harmonic frequencies and linear IR intensities for the lowest energy structures were then calculated. Initial geometries were based on the extensive study of neutral structures by Lu *et al.*,[10] who performed both MP2 and B3LYP calculations with a 6-31G(d) basis set, and on our knowledge of chemical bonding in silicon oxide clusters. Lu *et al*. found that MP2 and B3LYP calculations gave nearly the same energetics for several clusters, thus justifying the use of B3LYP for optimizing the large number of structures explored in their study. We have assumed that a similar situation applies to cationic silicon oxide clusters. We used a larger basis set than Lu *et al.*, but found only small differences in cation structures, energetics, and spectra using the smaller 6-311G* basis set. As an additional check, we calculated the B3LYP/cc-pVTZ harmonic frequencies and IR intensities of neutral $(SiO)_3$ and found very good agreement with the available experimental spectra.[17,19]

5.2.4 Results and analysis

Experimental IRMPD spectra of $(SiO)_3^+$, $(SiO)_4^+$ and $(SiO)_5^+$ are presented in the top panel of Figures 1-3. For all the clusters studied here, the only observed fragmentation channel upon absorption of IR radiation is the loss of one SiO unit from the parent ion:

$$(SiO)_n^+ + m \cdot h\nu \rightarrow SiO + (SiO)_{n-1}^+. \qquad (5.3)$$

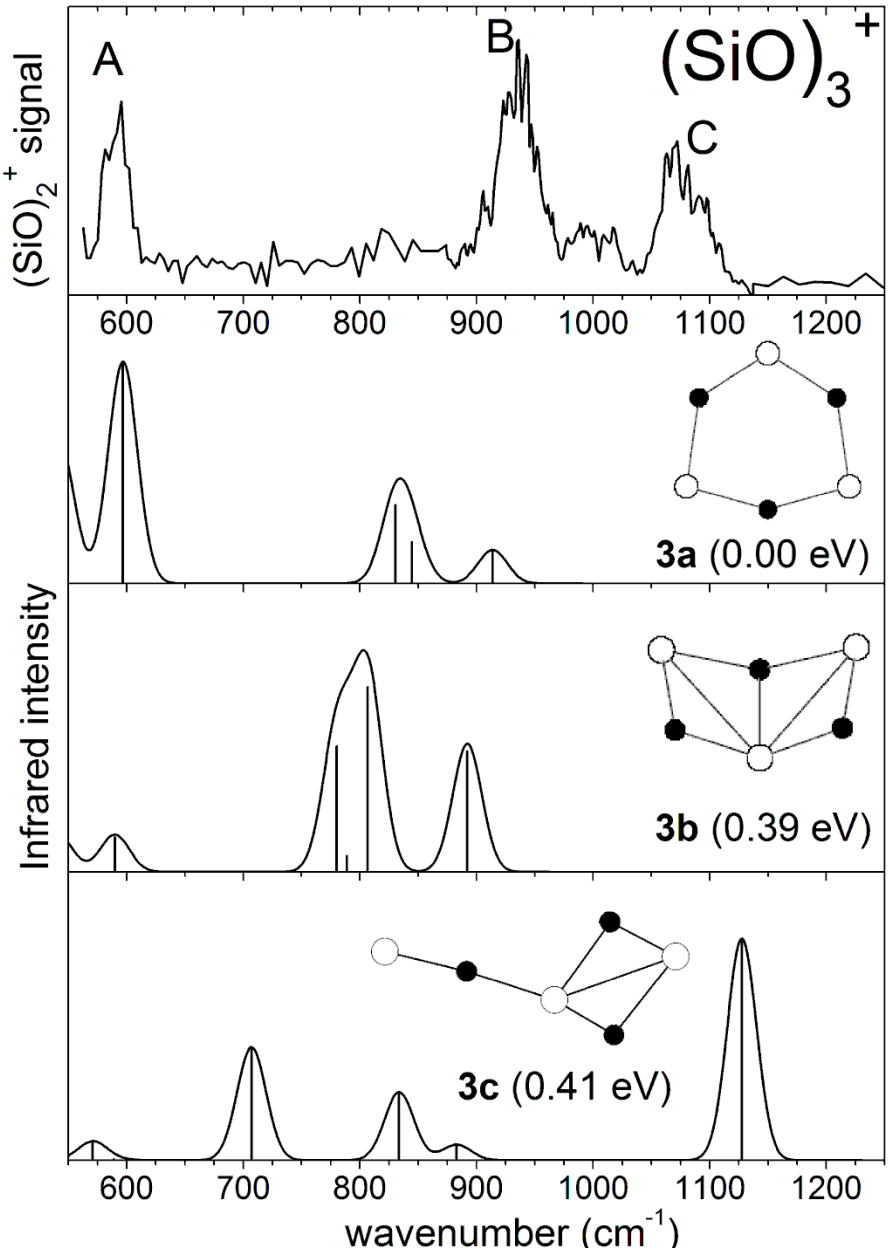

Figure 5.11 Experimental and calculated spectra for the $(SiO)_3^+$ cluster. The experimental IRMPD spectrum (top panel) was recorded by measuring the intensity of the $(SiO)_2^+$ fragment. Calculated (B3LYP) structure and linear absorption spectra for the three lowest energy isomers are shown in lower panels. Black and white circles represent oxygen and silicon atoms respectively. The calculated stick spectra were convoluted with a Gaussian line function (25 cm^{-1} FWHM).

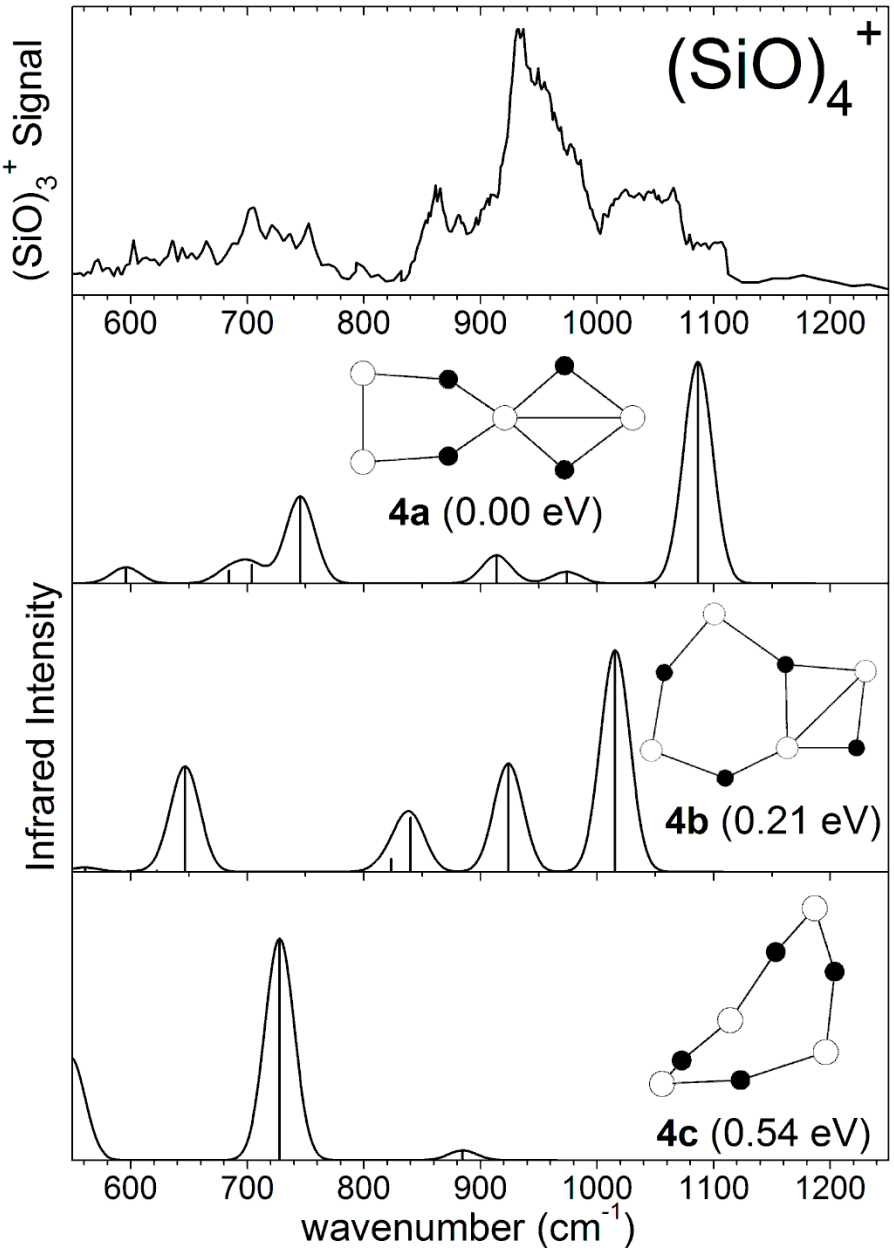

Figure 5.12 Experimental and calculated spectra for the $(SiO)_3^+$ cluster. The experimental IRMPD spectrum (top panel) was recorded by measuring the intensity of the $(SiO)_2^+$ fragment. Calculated (B3LYP) structure and linear absorption spectra for the three lowest energy isomers are shown in lower panels. Black and white circles represent oxygen and silicon atoms respectively. The calculated stick spectra were convoluted with a Gaussian line function (25 cm^{-1} FWHM).

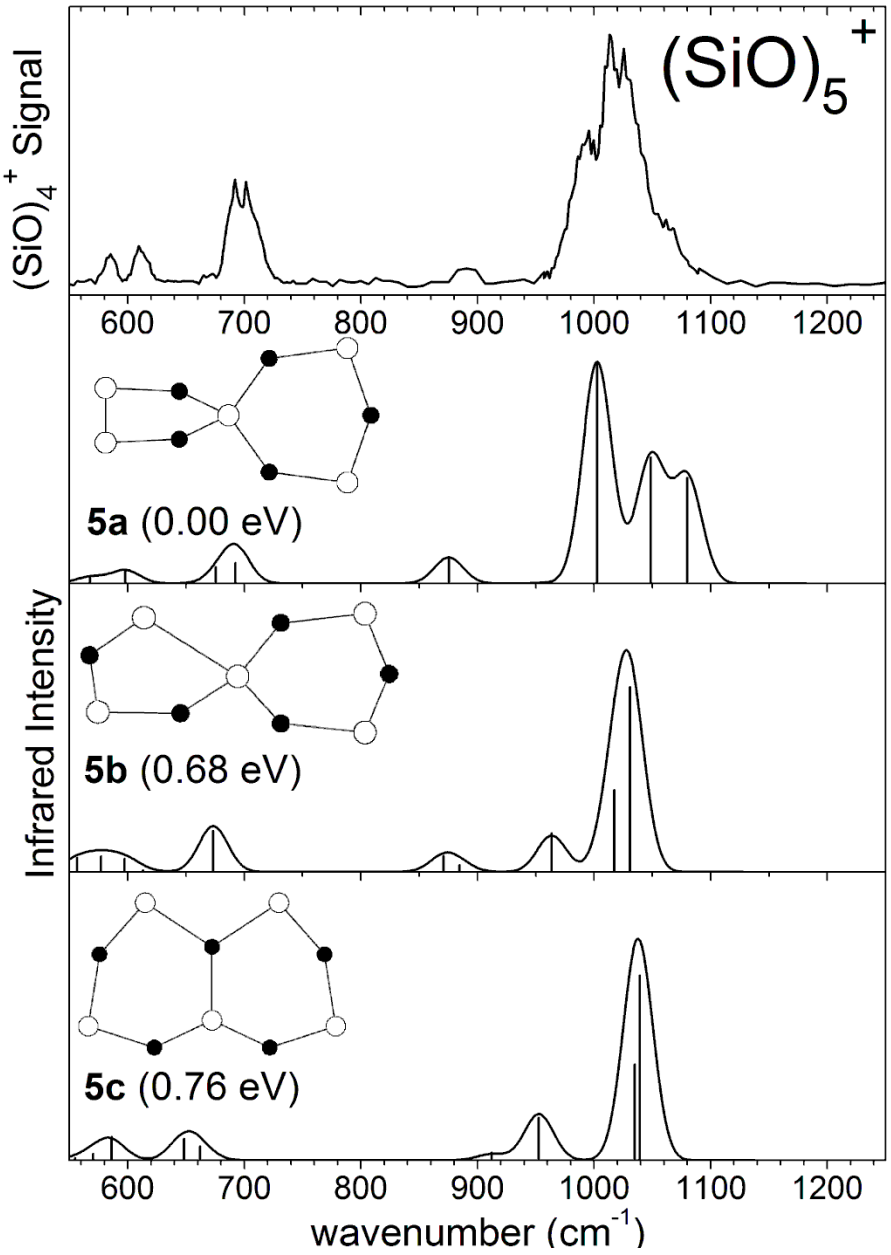

Figure 5.13 Experimental and calculated spectra for the $(SiO)_3^+$ cluster. The experimental IRMPD spectrum (top panel) was recorded by measuring the intensity of the $(SiO)_2^+$ fragment. Calculated (B3LYP) structure and linear absorption spectra for the three lowest energy isomers are shown in lower panels. Black and white circles represent oxygen and silicon atoms respectively. The calculated stick spectra were convoluted with a Gaussian line function (25 cm^{-1} FWHM).

The absence of other fragments suggests that the clusters were not composed of O_2 molecules adsorbed onto silicon clusters. The spectra in the top panels of Figures 5.11-5.13 represent the intensity of the $(SiO)_{n-1}^+$ fragment signal as a function of IR frequency. Each spectrum shows two or more bands between 900 and 1100 cm^{-1}, and additional features between 600 and 700 cm^{-1}. For each $(SiO)_n^+$ cluster, the three lowest energy isomers found from electronic structure calculations are presented in the three lower panels of Figures 5.11-5.13 along with their calculated IR spectra and relative energies. Animations of selected vibrational modes are included as supplemental material. We also calculated dissociation energies for SiO loss from each cluster, finding values of 2.92, 2.55 and 2.83 eV for $(SiO)_3^+$, $(SiO)_4^+$ and $(SiO)_5^+$ respectively. Fragmentation of these clusters thus requires on the order of 20 IR photons.

The $(SiO)_3^+$ spectrum in the top panel of Figure 5.11 shows three intense peaks at 590, 930, and 1080 cm^{-1}, labeled A, B, and C, respectively, and broader, weaker features between 800 and 900 cm^{-1} and around 1000 cm^{-1}. Bands A and B are close to those seen in the matrix IR spectrum of neutral Si_3O_3 at 631.5 and 972.6 cm^{-1}; these frequencies have been assigned to degenerate *E'* stretching vibrations, for a structure comprising a six-membered ring with alternating Si-O bonds and D_{3h} symmetry.[17,19]

Our calculations find that while the lowest energy structure of $(SiO)_3^+$, structure 3a, is a planar ring, it is less symmetric than the neutral, with C_{2v} rather than D_{3h} symmetry. The calculated frequency at 600 cm^{-1} for a Si-O-Si stretch matches that of peak A. In the simulation, the lower symmetry for the cation splits the higher frequency degenerate vibrations into a doublet at 830 and 914 cm^{-1}. In addition, a O-Si-O bend vibration becomes IR active at the lower symmetry, yielding an intermediate third peak at 845 cm^{-1}. It thus appears that peak A comes from structure 3a, and while the match between peak B and C and the simulated peaks is far from perfect, the frequencies and intensities of the simulated peaks depend strongly on the extent of distortion from D_{3h} symmetry in the cation. In fact, the cation most likely experiences either dynamic or static Jahn-Teller distortion, leading to inaccurate frequencies from the type of harmonic analysis used in our simulated spectra.

Contributions from low-lying other isomers must also be considered. The lower panels in Figure 5.11 show simulated spectra from the "book" isomer (3b) at 0.39 eV, and the "kite" (3c) at 0.41 eV. The most intense feature in the simulated spectrum for the kite structure at 1130 cm^{-1} is close to the experimental peak C; this frequency corresponds to the antisymmetric stretch vibration of the O atom in the “tail” of the kite. The book structure 3b has a strong transition at 890 cm^{-1}, close to the experimental peak B. There are strong transitions in the 700-850 cm^{-1} region of the simulated spectrum of these isomers that are not seen in the experiment, arguing against additional contributions from these structures. However, since deviations from the linear absorption intensities are not uncommon for this type of IRMPD spectroscopy and the presence of isomer 3c cannot be completely ruled out.

We thus attribute the $(SiO)_3^+$ spectrum to originate mainly from structure 3a, with the caveat that a more sophisticated vibrational analysis is needed to confirm our assignment.

The $(SiO)_4^+$ experimental spectra (top panel, Figure 5.12) shows five broad features centered around 700, 870, 930, 1040, and 1100 cm^{-1}. The lowest energy $(SiO)_4^+$ isomer, structure 4a, found in our calculations comprises a central Si atom tetrahedrally coordinated to four oxygen atoms and shared between a four and a five-membered ring. The larger ring contains a 2.98 Å Si-Si bond, which is presumably a rather weak interaction given that the equilibrium bond length in Si_2 is 2.246 Å.[24] The next isomer, 4b, lying 0.21 eV higher in energy, has a SiO unit common to a six- and a four-membered ring. This structure is a bridged version of the single buckled ring isomer which was found to be 0.54 eV higher in energy. This last isomer was found to be the minimum structure on the neutral surface,[10-13,15,16] and also resembles the lowest energy structure, 3a, calculated for $(SiO)_3^+$ in Figure 5.11. The calculated peak at 1090 cm^{-1} for structure 4a and the three peaks at 840, 920, and 1010 cm^{-1} for structure 4b match peaks in the experimental spectra, suggesting that we are observing signal from both isomers. Note that the lower frequency peaks at 750 and 650 cm^{-1} for 4a and 4b, respectively, overlap with the broad experimental feature covering 600-750 cm^{-1}. Contributions of multiple isomers may account for the more congested appearance of the $(SiO)_4^+$ experimental spectra compared to the two other clusters studied under the same conditions.

The electronic structure calculations show that the peak at 1090 cm^{-1} from structure 4a corresponds to antisymmetric stretch motion of the O atoms in the larger ring, while the smaller peak around 750 cm^{-1} is from antisymmetric stretching of the O atoms in the smaller ring. The higher frequency vibration is similar to the "kite tail" vibration in structure 3c. In structure 4b, the peaks at 1016 and 924 cm^{-1} correspond to the antisymmetric and symmetric stretch motion of the oxygen atoms in the larger ring, while the peaks at 840 and 647 cm^{-1} are associated with the doubly and triply coordinated oxygen atoms of the smaller ring.

The $(SiO)_5^+$ experimental spectrum in Figure 5.13 exhibits a doublet around 600 cm^{-1}, a more intense peak (or two peaks) at 700 cm^{-1}, a weak feature at 890 cm^{-1}, and three or four intense overlapped features between 970 and 1100 cm^{-1}. The lowest energy calculated structure, 5a, has a tetrahedrally-coordinated Si atom common to a four-membered and six-membered ring, with a 2.96Å Si-Si bond in the smaller ring. In order of descending frequency, the three major calculated peaks for 5a correspond to antisymmetric O atom stretching in the five-membered ring, antisymmetric O atom stretching in the six-membered ring, and bending motion of the two O atoms in the larger ring adjacent to the Si atom. The calculated energy of 5a is substantially lower than that of structures 5b (0.68 eV) and 5c (0.76 eV), which are also double-ring structures with Si and SiO cores, respectively. Structure 5b resembles 5a except that the central Si is bonded to a Si atom in the five-membered ring instead of an O atom. The 2.63Å Si-Si bond in 5b is also significantly shorter than in 5a. In contrast to the situation for the smaller clusters, the $(SiO)_5^+$ experimental spectrum is matched

reasonably well by that of the lowest energy calculated structure, consistent with the larger energy gap relative to the next lowest-energy structures. However the presence of the 5b and 5c isomers cannot be ruled out since their calculated spectra also agree relatively well with the experiment.

5.2.5 Discussion

There are several noteworthy trends in the experimental spectra. First, both experiment and theory indicate that the energetics of the considered cation isomers and even their ordering are different than their neutral counterparts. For neutral $(SiO)_3$, as discussed above, the lowest energy calculated structure by Lu *et al.*[10] is a planar ring with the next lowest, a "kite" structure, lying 1.523 eV higher. For the cation, the kite structure 3c lies only 0.41 eV above the ring, which is still found to be the lowest energy isomer, even if it is distorted in the cation. The preferred structures for $(SiO)_4^+$ and $(SiO)_5^+$ both contain a central, tetrahedrally-coordinated silicon atom bound to four oxygen atoms and a Si-Si bond on the periphery, and these structures account for some if not all of the experimental spectral features. In contrast, the lowest energy calculated structure for $(SiO)_4$ is a non-planar ring similar to 4c, for which there is little evidence in the experimental spectrum. For neutral $(SiO)_5$, the lowest energy structure looks like 5b, while 5a, the apparent cation ground state, lies 0.39 eV higher. The significance of this result is that there is a central Si-Si bond in 5b but not 5a, and in neutral clusters; this bond is predicted to evolve into a segregated Si_n core in larger clusters.[11,12]

Secondly, while we have assigned the *n*=3 and 5 to single cation isomers, two cation isomers are required to fit the *n*=4 spectrum. This result may reflect the isomer energetics, in that the calculated gap between the lowest and second lowest energy isomers is considerably smaller for *n*=4 than for the other clusters, resulting in more excited isomer population for *n*=4. Nonetheless, the apparent contribution of multiple $(SiO)_4^+$ isomers suggests that the cluster populations are well out of thermal equilibrium, given an ion temperature of ~70 K. The structural differences between the two isomers are significant, and the clusters most likely have a complex potential energy landscape with substantial barriers to isomerization, so thermalization of the ions to room temperature in the ion guide may not be sufficient to overcome the barriers separating individual isomers. As a result, each isomer may act as a separate chemical species in the trap and cool to the bottom of its corresponding local minimum on the potential energy landscape. In an extensive study of vanadium oxide cluster ions,[25] little evidence was found for the presence of multiple isomers using a similar cluster production / cooling scheme, indicating the barriers to isomerization in small SiO cluster cations may be significantly greater than those in vanadium oxide cluster ions.

5.2.6 Conclusions

In conclusion, we have measured the first gas-phase IR spectra of silicon monoxide cations $(SiO)_n^+$, n = 3-5, using IRMPD spectroscopy in the 550-1250 cm^{-1} frequency range. Comparison with the characteristic absorption regions identified by electronic structure calculation indicates that the cations have different structures than their neutral counterparts. However, exploration of the lower frequency region (300-600 cm^{-1}) as well as rare-gas tagging might be necessary to pinpoint the exact structure of these species. It will also be of interest to perform experiments and electronic structure calculations on larger cluster cations to see if a Si_n central core eventually arises, since its presence would facilitate the formation of enriched silicon and silicate structures from silicon monoxide clusters. Such a mechanism could be involved in the transformation of SiO molecules to silicon-containing structures in the interstellar medium.[11] Calculations on larger clusters may require a comprehensive search of the potential energy surface using a genetic algorithm to make sure that the global minimum is found, similar to the case of $Al_8O_{12}^+$ [26].

References

1) D. A. Williams and E. Herbst, *Surf. Sci.* **500** (1-3), 823 (2002).
2) A. Tamanai, H. Mutschke, J. Blum, and G. Meeus, *Astrophys. J.* **648** (2), L147 (2006).
3) A. N. Witt, K. D. Gordon, and D. G. Furton, *Astrophys. J.* **501** (1), L111 (1998).
4) V. G. Zubko, T. L. Smith, and A. N. Witt, *Astrophys. J.* **511** (1), L57 (1999).
5) H. P. Gail and E. Sedlmayr, *Astron. and Astrophys.* **166** (1-2), 225 (1986).
6) H. P. Gail and E. Sedlmayr, *Faraday Disc.* **109**, 303 (1998).
7) N. Wang, Y. H. Tang, Y. F. Zhang, C. S. Lee, and S. T. Lee, *Phys. Rev. B* **58** (24), 16024 (1998).
8) R. Q. Zhang, Y. Lifshitz, and S. T. Lee, *Adv. Mater.* **15** (7-8), 635 (2003).
9) Y. F. Zhang, Y. H. Tang, N. Wang, D. P. Yu, C. S. Lee, I. Bello, and S. T. Lee, *Appl. Phys. Lett.* **72** (15), 1835 (1998).
10) W. C. Lu, C. Z. Wang, V. Nguyen, M. W. Schmidt, M. S. Gordon, and K. M. Ho, *J. Phys. Chem. A* **107** (36), 6936 (2003).
11) A. C. Reber, P. A. Clayborne, J. U. Reveles, S. N. Khanna, A. W. Castleman, and A. Ali, *Nano Lett.* **6** (6), 1190 (2006).
12) R. Q. Zhang, M. W. Zhao, and S. T. Lee, *Phys. Rev. Lett.* **93** (9), 095503 (2004).
13) P. V. Avramov, I. Adamovic, K. M. Ho, C. Z. Wang, W. C. Lu, and M. S. Gordon, *J. Phys. Chem. A* **109** (28), 6294 (2005).
14) R. Q. Zhang, T. S. Chu, and S. T. Lee, *J. Chem. Phys.* **114** (13), 5531 (2001).
15) J. R. Chelikowsky, *Phys. Rev. B* **57** (6), 3333 (1998).
16) T. S. Chu, R. Q. Zhang, and H. F. Cheung, *J. Phys. Chem. B* **105** (9), 1705 (2001).
17) J. S. Anderson and J. S. Ogden, *J. Chem. Phys.* **51** (10), 4189 (1969).
18) J. S. Anderson, J. S. Ogden, and M. J. Ricks, *Chem. Commun.* (24), 1585 (1968).
19) J. S. Ogden, *Spectrochim. Acta A* **33** (12), 1059 (1977).
20) L. S. Wang, S. R. Desai, H. Wu, and J. B. Nichloas, *Z. Phys. D* **40** (1-4), 36 (1997).
21) D. Oepts, A. F. G. van der Meer, and P. W. van Amersfoort, *Infrared Phys. Technol.* **36** (1), 297 (1995).
22) J. Oomens, B. G. Sartakov, G. Meijer, and G. von Helden, *Int. J. Mass. Spectrom.* **254** (1-2), 1 (2006).

23) M. J. Frisch, G. W. Trucks, H. B. Schlegel*et al.*, Gaussian 03, Revision C.02 (Gaussian, Inc, Wallingford, CT, 2004).

24) K. P. Huber and G. Herzberg, *Molecular spectra and Molecular Structure IV: Constants of Diatomic Molecules*. (Van Nostrand-Reinhold, New York, 1977).

25) K. R. Asmis and J. Sauer, *Mass Spect. Rev.* **26** (4), 542 (2007).

26) M. Sierka, J. Döbler, J. Sauer, G. Santambrogio, M. Brümmer, L. Wöste, E. Janssens, G. Meijer, and K. R. Asmis, *Angew. Chem. Int. Ed.* **46** (18), 3372 (2007).